UiT The Arctic University of Norway

Department of Physics and Technology

Label-free super-resolution optical microscopy

Nikhil Jayakumar

A dissertation for the degree of Philosophiae Doctor November 2023

Contents

List of Figures

Motivation

What we observe is not nature itself, but nature exposed to our method of questioning.

-Werner Heisenberg

Our life has evolved under the sunlight. This enables a light optical microscope to study life with minimal invasion. Despite this inherent advantage, the wave nature of light has restricted its applicability for discerning features to the range of a few hundred nanometers $\approx$ 200 nm. This limit

$$d = \lambda/2NA \tag{1}$$

was identified by Ernst Abbe as arising due to the diffraction of light. In addition to the problem of diffraction-limited spatial resolution, poor-contrast plagues the imaging process of biological specimens like cells. These two challenges are typically mitigated by resorting to fluorescence microscopy. The molecular specificity offered by fluorescent molecules and the incoherent nature of their emission enables high-contrast imaging. Plus, by exploiting the intrinsic or induced photo-kinetics of these molecules, a number of fluorescence-based techniques have evolved over the years that routinely achieve resolution well below the Abbe limit stated above. But despite the overwhelming success of fluorescence microscopy, cell biologists opine that altering the natural state of the cell through the use of fluorescence dyes is not the preferred way to study life processes. This sentiment underlines the necessity to develop label-free techniques that circumvent the diffraction-limit.

Different label-free imaging approaches have evolved over the years, that generate images well below 200 nm. One such approach in improving the spatial resolution is through near-field optics. The principle behind near-field optics is to utilize the higher spatial frequencies of the diffracted light. For e.g., the higher spatial frequencies of the sample that do not propagate into the far-field can be collected by probing the sample in the near-field, thereby generating an image with a much higher spatial resolution. Looking at Abbe's diffraction-limit mentioned earlier, this could be interpreted as increasing the numerical aperture (NA) of the system. Another powerful approach is through the use of electron microscopes, where a very high resolution can be achieved, thanks to the ultra-short wavelength (λ) associated with an electron. However, both these

techniques have limited applicability while imaging live biological specimens. The implication of this limitation is an open problem in optics for a student to look into!

This thesis titled "Label-free super-resolution optical microscopy" provides an optical solution to the problem of far-field label-free diffraction-limited microscopy. The thesis reports relevant works carried out during the graduate studies, in a sequential manner. At the onset of the PhD, I was given an opportunity to work on quantitative phase microscopy and waveguide-based microscopy. The concepts I learnt from these two domains helped in developing ideas that provided insights about how label-free super-resolution microscopy can be experimentally demonstrated. In this thesis, focus will be on waveguide-based microscopy.

In paper 1 which is included in this thesis as Chapter 3, the aim was to perform super-resolution fluorescence microscopy using intensity-fluctuation algorithms. Instead of using the intrinsic fluctuations of the fluorophores, the idea was to artificially induce fluctuations by using a waveguide. After the completion of this work, the next question was to see if label-free super-resolution can be performed based on the concepts developed in the previous work, i.e., artificially induced fluctuations by waveguides in tandem with intensity-fluctuation algorithms to achieve super-resolution. This was explored in paper 2 which is included in this thesis as Chapter 4. The conclusion from this work was that high-contrast imaging of even weakly scattering biological specimens such as liposomes and extra-cellular vesicles can be performed with high-contrast. The developed technique is abbreviated cELS and is explained in Chapter 4. However, coherence of the scattered light prevents application of intensity-fluctuation algorithms in label-free regime to gain resolution more than the Abbe limit. Based on the above-mentioned findings, paper 3 which is included in this thesis as Chapter 5, develops the concepts and experimentally demonstrates label-free super-resolution. The developed technique is abbreviated EPSLON and is detailed in Chapter 5.

Thesis overview

Here, Chapter 1 and Chapter 2 supplements the concepts mentioned/utilized in the published articles provided in Chapters 3 - 5. Chapter 6 provides the global conclusion of the thesis and also provides cues to future research directions. The thesis is structured as follows:

- Chapter 1: Fundamentals
  Via Maxwell equations (Section 1.1), basics of diffraction of light (Section 1.2) and diffraction-limited resolution (Section 1.3) are explained. Then Sections 1.4 and 1.5 gives an overview about imaging using microscopes. Section 1.6 then focuses on the final image generated at the camera plane based on the coherence of the light. Next, Section 1.7 explains how an initially incoherent light source becomes coherent with propagation. Section 1.8 explains light scattering, i.e., describes how samples interact with the illuminating field. In this thesis, optical waveguides are used for imaging

and therefore, the samples to be imaged are placed on top of the core-cladding interface of waveguides. Hence, Section 1.9 describes the basics of optical waveguides. Finally, some of the state-of-the-art fluorescence-microscopy techniques (Section 1.10) and label-free microscopy techniques (Section 1.11) are elaborated. Thus, the concepts elaborated in Chapter 1 help in understanding the physical mechanism behind the problem of poor-contrast and diffraction-limited resolution in optical microscopes and, the concepts developed in this thesis for attacking these problems.

- Chapter 2: Experimental setup
  This chapter provides an overview of how to employ waveguides for microscopy. A schematic of the experimental setup employed as part of this thesis work is provided. Steps taken such as waveguide cleaning, polishing and sample preparation on waveguides to perform microscopy are elaborated.

- Chapter 3:
  Paper 1: This chapter initially provides a gist of the first research work included in this thesis. The work is titled ' On-chip TIRF nanoscopy by applying Haar wavelet kernel analysis on intensity fluctuations induced by chip illumination'. The published manuscript is also attached along with this chapter.

- Chapter 4:
  Paper 2: This chapter provides a gist of the work titled ' Multi-moded high-index contrast optical waveguide for super-contrast high-resolution label-free microscopy'. The published manuscript is attached along with this chapter.

- Chapter 5:
  Paper 3: The chapter provides a gist of the work titled ' Label-free incoherent super-resolution optical microscopy.' The archived manuscript is attached along with this chapter.

- Chapter 6:
  This chapter summarizes the research works included in this thesis and provides cues to future research directions.

Research works

The research works carried out during the course of the PhD is included in this section. I was given an opportunity to work on quantitative phase microscopy and optical-waveguide based microscopy at the start of my PhD. The concepts I learnt along the way, helped me in my research to cross-pollinate and extend ideas to develop solutions for problems such as poor-contrast and diffraction-limited resolution in optical microscopy. Among the works mentioned below, articles where my name is mentioned in bold indicates first author or joint first authorship. The three papers highlighted in cobalt are included in this thesis. They include waveguide-based super-resolution fluorescence microscopy, waveguide-based high-contrast label-free microscopy and waveguide-based super-resolution label-free microscopy. These three works are included in this thesis and are elaborated in Chapters 3, 4 and 5 respectively.

Optical waveguide-based microscopy

Fluorescence microscopy using waveguides

- **Jayakumar, Nikhil**, Øystein I. Helle, Krishna Agarwal, and Balpreet Singh Ahluwalia. "On-chip TIRF nanoscopy by applying Haar wavelet kernel analysis on intensity fluctuations induced by chip illumination." Optics Express 28, no. 24 (2020): 35454-35468.
- Boninsegna, Matteo, **Nikhil Jayakumar**, Firehun Tsige Dullo, Peter AG McCourt, Thomas Huser, Balpreet Singh Ahluwalia, and Antoni Homs Corbera. "Waveguide chip coupled with microfluidics enables super-resolution live-cell imaging." In Novel Optical Systems, Methods, and Applications XXIII, vol. 11483, pp. 166-173. SPIE, 2020.
- Priyadarshi, Anish, Firehun Tsige Dullo, Deanna Lynn Wolfson, Azeem Ahmad, Nikhil Jayakumar, Vishesh Dubey, Jean-Claude Tinguely, Balpreet Singh Ahluwalia, and Ganapathy Senthil Murugan. "A transparent waveguide chip for versatile total internal reflection fluorescence-based microscopy and nanoscopy." Communications Materials 2, no. 1 (2021): 85.

Label-free microscopy using waveguides

- **Jayakumar, Nikhil**, Firehun T. Dullo, Vishesh Dubey, Azeem Ahmad, Florian Ströhl, Jennifer Cauzzo, Eduarda Mazagao Guerreiro et al. "Multi-moded high-index contrast optical waveguide for super-contrast high-resolution label-free microscopy." Nanophotonics 11, no. 15 (2022): 3421-3436.

- **Jayakumar, Nikhil**, Firehun T. Dullo, Jean-Claude Tinguley, Krizia Sagini, Alicia Llorente, and Balpreet Singh Ahluwalia. "Label-free incoherent super-resolution optical microscopy." arXiv preprint arXiv:2301.03451 (2023).

Quantitative phase microscopy

- **Jayakumar, Nikhil**, Azeem Ahmad, Dalip Singh Mehta, and Balpreet Singh Ahluwalia. "Sampling Moiré method: a tool for sensing quadratic phase distortion and its correction for accurate quantitative phase microscopy." Optics Express 28, no. 7 (2020): 10062-10077.

- Cauzzo, Jennifer, **Nikhil Jayakumar**, Balpreet Singh Ahluwalia, Azeem Ahmad, and Nataša Škalko-Basnet. "Characterization of liposomes using quantitative phase microscopy (QPM)." Pharmaceutics 13, no. 5 (2021): 590.

- Ahmad, Azeem, Vishesh Dubey, Nikhil Jayakumar, Anowarul Habib, Ankit Butola, Mona Nystad, Ganesh Acharya, Purusotam Basnet, Dalip Singh Mehta, and Balpreet Singh Ahluwalia. "High-throughput spatial sensitive quantitative phase microscopy using low spatial and high temporal coherent illumination." Scientific reports 11, no. 1 (2021): 15850.

- Ahmad, Azeem, **Nikhil Jayakumar**, and Balpreet Singh Ahluwalia. "Demystifying speckle field interference microscopy." Scientific Reports 12, no. 1 (2022): 10869.

Conference papers

- **Jayakumar, Nikhil**, Firehun T. Dullo, Jean Claude Tinguley, Hong Mao, Krizia Sagini Alicia Llorente, Balpreet Singh Ahluwalia,. "EPSLON: Towards far-field label-free optical nanoscopy." Focus on Microscopy (FOM), Porto, 2023.

- **Jayakumar, Nikhil**, Balpreet Singh Ahluwalia, and Firehun T. Dullo. "Photonic chip for high-contrast and high-resolution label-free optical microscopy of nano-particles." In 2022 IEEE Photonics Conference (IPC), pp. 1-2. IEEE, 2022.

- Dullo, Firehun Tsige, Karolina Milenko, Nikhil Jayakumar, and Balpreet Singh Ahluwalia. "On-chip structured illumination microscopy (cSIM) with large imaging area." In 2022 IEEE Photonics Conference (IPC), pp. 1-2. IEEE, 2022.

- Ahmad, Azeem, Nikhil Jayakumar, Ankit Butola, Vishesh Dubey, Dalip Singh Mehta, and Balpreet Singh Ahluwalia. "High space-bandwidth product with high spatial phase sensitivity in single-shot digital holographic microscopy." In Digital Holography and Three-Dimensional Imaging, pp. W2B-5. Optica Publishing Group, 2019.

Chapter 1

Fundamentals

1.1 Maxwell equations

Maxwell's equations are invoked to elaborate the light-matter interactions described in this thesis. The macroscopic Maxwell equations can be written in the following form [1]:

$$\vec{\nabla} \times \vec{E}(\vec{r},t) = -\frac{\partial \vec{B}(\vec{r},t)}{\partial t} \tag{1.1}$$

$$\vec{\nabla} \times \vec{H}(\vec{r},t) = \vec{j}_{makr}(\vec{r},t) + \frac{\partial \vec{D}(\vec{r},t)}{\partial t} \tag{1.2}$$

$$\vec{\nabla} \cdot \vec{D}(\vec{r},t) = \rho_{ext}(\vec{r},t) \tag{1.3}$$

$$\vec{\nabla} \cdot \vec{B}(\vec{r},t) = 0 \tag{1.4}$$

where, $\vec{E}(\vec{r},t)$ is the electric field with units V/m, $\vec{H}(\vec{r},t)$ is the magnetic field with units A/m, $\vec{B}(\vec{r},t)$ is the magnetic flux density with units Vs/m^2, $\vec{D}(\vec{r},t)$ is the electric flux density with units As/m^2, $\rho(\vec{r},t)$ is the external charge density with units As/m^3 and, $\vec{j}_{makr}(\vec{r},t)$ is the macroscopic current density with units A/m^2.
The auxiliary equations are given by

$$\vec{D}(\vec{r},t) = \epsilon_0 \vec{E}(\vec{r},t) + \vec{P}(\vec{r},t) \tag{1.5}$$

$$\vec{H}(\vec{r},t) = \frac{[\vec{B}(\vec{r},t) - \vec{M}(\vec{r},t)]}{\mu_0} \tag{1.6}$$

where, $\vec{P}(\vec{r},t)$ is the dielectric polarization with units As/m^2, $\vec{M}(\vec{r},t)$ is the magnetic polarization with units Vs/m^2, ϵ_0 is the vacuum permittivity $\approx 8.854 \times$

10^{-12} As/Vm, μ_0 is the vacuum permeability $= 4 \times \pi \times 10^{-7}$ Vs/Am and, c $= \frac{1}{\sqrt{\mu_0 \epsilon_0}}$ is the speed of light in vacuum.

Now, the instantaneous magnitude and direction of power flow of an electromagnetic wave through an area is defined by the Poynting vector, $\vec{S}(\vec{r},t) = \vec{E}_{real}(\vec{r},t) \times \vec{H}_{real}(\vec{r},t)$, where $\vec{E}_{real}$ and $\vec{H}_{real}$ are the real valued electric and magnetic fields. However, due to the rapid fluctuations of the optical field, $\approx 10^{14}$ Hz, a time averaged intensity is measured experimentally [2, 3].

$$< \vec{S}(\vec{r},t) >= \frac{1}{T} \int_0^T \vec{S}(\vec{r},t')dt' \tag{1.7}$$

For monochromatic fields, Eqn. (1.7) reduces to $< \vec{S}(\vec{r},t) >= \frac{1}{2}\,\mathrm{Re}[\vec{E}(\vec{r}) \times \vec{H}^*(\vec{r})]$. It implies that phase information of the fields is lost during an intensity measurement, such as when a camera is used in optical microscopy.

1.2 Diffraction of light

This section helps to understand how information of an object encoded in a light beam changes with propagation. The propagation of light in a linear, homogeneous, isotropic, dispersive media is considered to understand the diffraction of light. For brevity, monochromatic beam propagation is assumed so that only diffraction needs to be considered, and dispersive effects of the medium can be disregarded. To develop an intuition for the various physical phenomena described in this thesis, Fourier transform is frequently utilized. For e.g., spatial effects like diffraction of light is treated in the spatial frequency domain.

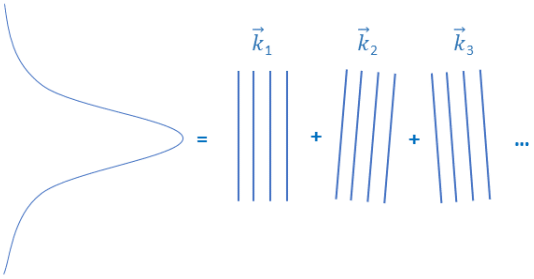

Figure 1.1: A beam can be described as a superposition of plane waves propagating at different directions.

$$\vec{E}(\vec{r},t) = \int_{-\infty}^{+\infty} \tilde{\vec{E}}(\vec{k}) \exp\Big[i(\vec{k}.\vec{r} - \omega t)\Big] d^3k \tag{1.8}$$

Eqn. (1.8) means that in the spatial frequency domain[1] , a beam can be considered as a superposition of plane waves with different wave vectors, i.e., different propagation directions, $\vec{k}_i$, as shown in Fig. 1.1. The medium considered here has no free charges or currents, i.e., the source terms $\vec{j}_{makr}(\vec{r},t)$ and $\rho_{ext}(\vec{r},t)$ in Eqn. 1.2 and Eqn. 1.3 respectively are set to zero. Now taking the curl of Eqn. 1.1 in temporal frequency domain[2], we arrive at $\vec{\nabla}(\vec{\nabla}.\widetilde{\vec{E}}(\vec{r},\omega)) - \nabla^2\widetilde{\vec{E}}(\vec{r},\omega) = i\omega\mu_0\widetilde{\vec{H}}(\vec{r},\omega)$. Since $\vec{\nabla}\cdot\widetilde{\vec{E}}(\vec{r},\omega)) = 0$, the equation reduces to the Helmholtz equation:

$$\nabla^2\widetilde{\vec{E}}(\vec{r},\omega) + \frac{\omega^2}{c^2}\epsilon(\omega)\widetilde{\vec{E}}(\vec{r},\omega) = 0 \tag{1.9}$$

where, relative permittivity $\epsilon(\omega) = 1 + \chi(\omega)$ and $\chi(\omega)$ is the susceptibility function. An ansatz for Eqn. (1.9) is $\widetilde{\vec{E}}(\vec{r},\omega) = \widetilde{\vec{E}}(\omega)exp(i\vec{k}.\vec{r})$. From Eqn.1.3, it implies that the wave is transversal, $\vec{k} \perp \widetilde{\vec{E}}(\omega)$. So the equation that needs to be solved using this ansatz is $\left[-k^2 + \frac{\omega^2}{c^2}\epsilon(\omega)\right]\widetilde{\vec{E}}(\omega) = 0$. Since $\widetilde{\vec{E}}(\omega) = 0$ is a trivial solution, the possible solution is

$$\begin{aligned}\vec{k}^2 = k^2 = k_x^2 + k_y^2 + k_z^2 &= \frac{\omega^2}{c^2}\epsilon(\omega) \\ &= \alpha^2 + \beta^2 + \gamma^2\end{aligned} \tag{1.10}$$

which is the dispersion relation. $k_x = \alpha, k_y = \beta$ and $k_z = \gamma$ are the spatial frequencies of the wave, $k(\omega) = \frac{\omega}{c}\sqrt{\epsilon(\omega)} = \frac{\omega}{c}\hat{n}(\omega)$ and $\hat{n}(\omega)$ is the complex refractive index. The conclusion is that the above-mentioned ansatz, plane waves, is a solution to Maxwell's equations in this media only if the dispersion relation is satisfied.

For simplicity, Eqn. (1.9) is reduced to the scalar Helmholtz equation which is exact for linearly polarized one-dimensional beams but an approximation in two-dimensional case [3]. Plugging Eqn. 1.10 into Eqn.1.9, we arrive at the scalar Helmholtz equation:

$$\nabla^2 u(\vec{r},\omega) + k^2(\omega)u(\vec{r},\omega) = 0 \tag{1.11}$$

Now, the problem to be solved is the following: given an initial field distribution $u(x,y,0)$ in a plane $z = 0$, we want to compute the field $u(x,y,z)$ at a plane z as shown in Fig. 1.2. To solve this problem, we switch to the spatial frequency domain. Due to the dispersion relation in Eqn. 1.10, a two-dimensional Fourier transform of the scalar fields is performed. The Fourier transform of the field is calculated as $u(\vec{r}) = \iint_{-\infty}^{+\infty} U(\alpha,\beta;z)exp[i(\alpha x + \beta y)]d\alpha d\beta$. This helps to

[1]The inverse Fourier transform is then described as $\widetilde{\vec{E}}(\vec{k},t) = (\frac{1}{2\pi})^3 \int_{-\infty}^{+\infty} \vec{E}(\vec{r})\exp\left[i(\vec{k}.\vec{r} - \omega t)\right]d^3r$

[2]Fourier transform in the temporal frequency domain is defined as $\tilde{\vec{E}}(\vec{r},\omega) = \frac{1}{2\pi}\int_{-\infty}^{+\infty}\vec{E}(\vec{r},t)\exp(i\omega t)dt$. This definition helps to replace $\frac{\partial}{\partial t}$ with $-i\omega$.

[3]Fundamentals of Modern Optics, Winter Semester 2015/16, Prof. Thomas Pertsch, Abbe School of Photonics, Friedrich-Schiller-Universität Jena.

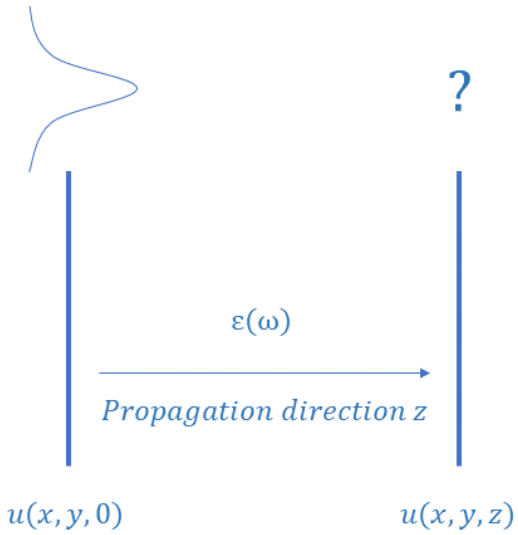

Figure 1.2: Given an initial field distribution $u(x, y, 0)$. The field propagates to a plane z in a medium with relative permittivity $\epsilon(\omega)$. The problem is to calculate the field $u(x, y, z)$.

transform Eqn. 1.11 into an algebraic equation. The physical meaning of such a transformation is that it helps to decompose the initial field into a superposition of different plane waves as shown in Fig. 1.1.

$$\begin{aligned} \left[\frac{d^2}{dz^2} + k^2 - \alpha^2 - \beta^2\right] U(\alpha, \beta; z) = 0 \\ \left[\frac{d^2}{dz^2} + \gamma^2\right] U(\alpha, \beta; z) = 0 \end{aligned} \tag{1.12}$$

General solution of Eqn. (1.12) is

$$U(\alpha, \beta; z) = U_1(\alpha, \beta) exp[i\gamma(\alpha, \beta)z] + U_2(\alpha, \beta) exp[-i\gamma(\alpha, \beta)z] \tag{1.13}$$

Looking at Eqn. (1.13), two types of solutions can be identified depending on the values of γ.

1. Homogeneous waves
   $\gamma^2 \geq 0$ where $\gamma = \sqrt{k^2 - \alpha^2 - \beta^2}$. This means that $\alpha^2 + \beta^2 \leq k^2$. It implies $\vec{k}$ is real. This equation could be interpreted as follows: α and β are restricted to a circle with radius k. It implies that the angle with respect to the z-axis, a reference axis system, is small. This is shown schematically in Fig. 1.3. The wave vector of the field, $\vec{k}$, is propagating at an angle θ with respect to the z-axis.

2. Evanescent waves
   $\gamma^2 < 0$ where $\gamma = \sqrt{k^2 - \alpha^2 - \beta^2}$. This means that $\alpha^2 + \beta^2 > k^2$. It

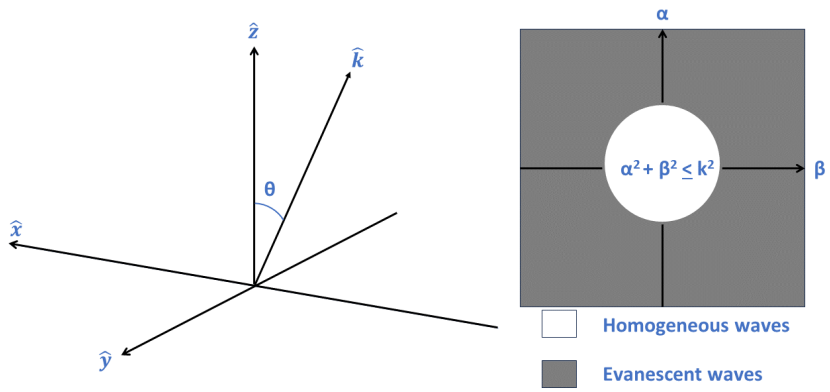

Figure 1.3: A wave vector propagates along $\hat{k} = \frac{\vec{k}}{|k|}$ making an angle θ with respect to the z-axis as shown. The magnitude of $\vec{k}$ in the α-β plane is shown by the white circle. The outer grey area represents the region where non-propagating or evanescent waves waves arise, $\alpha^2 + \beta^2 > k^2$. Higher spatial frequencies of the sample are contained in this grey region. They do not propagate into the far-field, leading to diffraction-limited resolution.

implies $\vec{k}$ is complex. From Eqn. (1.13), in the space $z > 0$, exponentially growing waves appear for the solution $exp(-i\gamma z)$. This is not a valid physical solution and hence, the solution shown in Eqn. (1.13) can be written as

$$U(\alpha, \beta; z) = U_1(\alpha, \beta) exp[i\gamma(\alpha, \beta)z] \tag{1.14}$$

We perform an inverse Fourier transform to get the fields in the real space at plane z:

$$u(\vec{r}) = \iint_{-\infty}^{+\infty} U(\alpha, \beta; z) exp[i(\alpha x + \beta y)] d\alpha d\beta \tag{1.15}$$

Plugging Eqn. (1.14) into Eqn. (1.15) we arrive at the final solution:

$$u(\vec{r}) = \iint_{-\infty}^{+\infty} U_1(\alpha, \beta) exp[i\gamma(\alpha, \beta)z] exp\left[i(\alpha x + \beta y)\right] d\alpha d\beta \tag{1.16}$$

Eqn. (1.16) calculates the the diffracted field distribution at a plane z. The initial field angular spectrum is a superposition of different homogeneous and evanescent waves, i.e., plane waves. These waves propagate along the propagation axis accumulating different phase, to give rise to the diffracted field. The interpretation of Eqn. 1.16 is as follows.

- $\iint_{-\infty}^{+\infty} d\alpha d\beta$
  Superposition of homogeneous and evanescent waves
- $exp[i(\alpha x + \beta y)]$
  excited plane waves

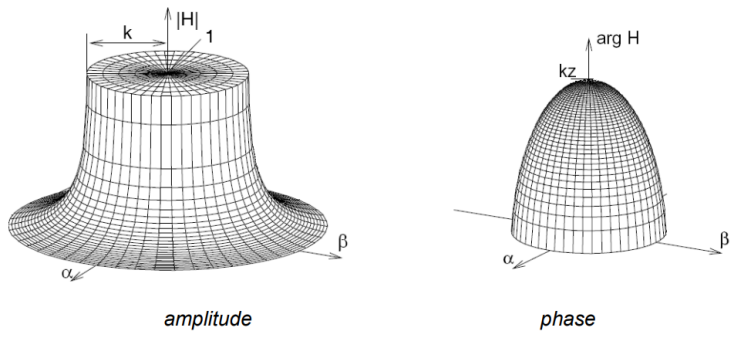

Figure 1.4: Amplitude and phase of complex transfer function as a function of spatial frequencies is shown. This figure is taken from [4].

- $U_1(\alpha, \beta)$
  coefficients of the excited plane waves
- $exp[i\gamma(\alpha, \beta), z]$
  phase accumulated by excited states with propagation distance z

The term $exp[i\gamma(\alpha, \beta), z] = H[\alpha, \beta; z]$ is referred to as the complex transfer function. The effects of the complex transfer function on homogeneous and evanescent waves is described below.

1. Homogeneous waves, i.e., $\alpha^2 + \beta^2 \leq k^2$
   $|H[\alpha, \beta; z]| = |exp[i\gamma(\alpha, \beta)z]| = 1$ and $\arg\left(exp[i\gamma(\alpha, \beta)z]\right) \neq 0$.
   .It means that the homogeneous waves merely accumulate phase upon propagation, $exp[i\sqrt{k^2 - \alpha^2 - \beta^2}z]$, while the amplitude remains unchanged.
2. Evanescent waves i.e., $\alpha^2 + \beta^2 > k^2$
   $|H[\alpha, \beta; z]| = |exp[i\gamma(\alpha, \beta)z]| = exp[-z\sqrt{\alpha^2 + \beta^2 - k^2}] < 1$ and
   $\arg\left(exp[i\gamma(\alpha, \beta)z]\right) = 0$.
   It means that evanescent waves decay in amplitude with increasing distance 'z', while keeping its phase constant.

1.3 Diffraction-limited resolution

Now, it is imperative to understand when evanescent waves arise. This helps understand the reason for diffraction-limited resolution. Let the electric field distribution immediately after a sample is described using Eqn. (1.16). The complex transfer function $H[\alpha, \beta; z]$ now helps to calculate the field distribution at a distance z, say where a microscope objective is situated. For low spatial frequencies of the sample, γ is real. Therefore, these frequencies propagate with

[4] Fundamentals of Modern Optics, Winter Semester 2015/16, Prof. Thomas Pertsch, Abbe School of Photonics, Friedrich-Schiller-Universität Jena.

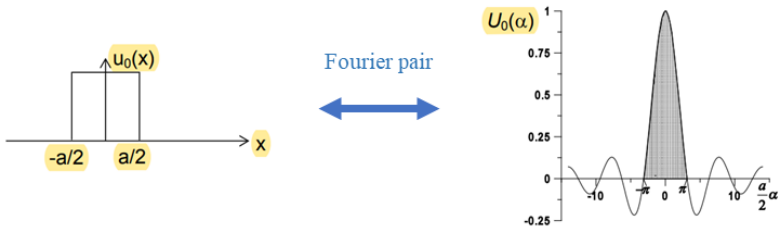

Figure 1.5: One-dimensional slit: $u(x) = 1$ for $|x| \leq \frac{a}{2}$ and $u(x) = 0$ elsewhere. Its Fourier transform $U(\alpha) = sinc(\frac{a}{2}\alpha)$ is shown alonside. The first zero of the function $U(\alpha)$ arises when $\frac{a}{2}\alpha = \pi$.

just a phase accumulation $exp[i\gamma(\alpha, \beta)z]$. High spatial frequencies, i.e., large angles θ with respect to z-axis as shown in Fig.1.3 , make γ imaginary, and so the plane waves becomes exponentially decaying along the z-axis, $exp(-\gamma z)$.
To develop an intuition for the above-mentioned concepts, a simplified example of light passing through a one-dimensional slit with width a units is shown. Fourier spectrum of waves emanating from this slit is $U(\alpha) = sinc(\frac{a}{2}\alpha)$. This is shown in Fig. 1.5. As can be seen, the central peak in the Fourier spectrum contains most of the information. Now, based on the concepts developed earlier, it is seen that evanescent waves arise when $\alpha^2 > k^2$. Or in other words , only when $\frac{2\pi}{a} < k = \frac{2\pi}{\lambda}n$, will propagating waves arise. This means that sub-wavelength features, $a < \frac{\lambda}{n}$, excite exponentially decaying evanescent waves. It implies a maximum cut-off spatial frequency $\rho_{max} = \sqrt{\alpha^2 + \beta^2} \leq \left|\vec{k}\right|$, which can propagate into the far-field. As a result, a conventional microscope objective cannot detect these rapidly decaying fields containing information about sub-wavelength features. In addition, the detection objective has a maximum angle of light it can collect, termed numerical aperture NA for the objective. It again limits the cut-off frequency admitted into the system, $\rho_{max} \sin\theta_{max}$, where θ_{max} is the maximum angle with respect to normal the objective can admit. Hence, it can be concluded that

- Information about sub-wavelength features of the sample are carried by evanescent waves. They decay in amplitude rapidly and do not propagate into the far-field.
- Finite aperture size of detection system limits the bandwidth of frequencies admitted into the system.

As a result, a far-field imaging system fails to create an exact replica of the input at the output due to loss in information. This gives rise to diffraction-limited resolution in optical imaging systems.

1.4 Imaging using a microscope

In this thesis, a 4f optical system is used for imaging. Hence, in this section, field distributions at different locations in a 4f setup is calculated using the concepts described in Section 1.2.

Earlier, it was seen that only those spatial frequencies lying within a circle, $\alpha^2 + \beta^2 \leq k^2$, propagate into the far-field. As a result, $\gamma = \sqrt{k^2 - \alpha^2 - \beta^2} \approx k - \frac{\alpha^2+\beta^2}{2k}$. Therefore, the modified real-valued transfer function is shown in Eqn.1.17. Such an approximation is called a Fresnel approximation.

$$H(\alpha, \beta; z) \approx exp(ikz) exp\left[-i\frac{\alpha^2 + \beta^2}{2k}z\right] = H_F(\alpha, \beta; z) \tag{1.17}$$

Translated to real space, the real-valued transfer function reads, Eqn. (1.18)

$$h_F(x, y; z) = \frac{-ik}{2\pi z} exp\left(ikz\left[1 + \frac{x^2 + y^2}{2z^2}\right]\right) \tag{1.18}$$

Now, a 4f optical system works as an optical relay: the sample is placed at the front focal plane of the first lens and the image is formed at the back focal plane of the second lens. For ease of calculation, a thin lens is considered [4]. The function of a lens is to transform a spherical wave into a plane wave, i.e.,

$$\frac{-i}{\lambda f} exp(ikf) exp\left[i\frac{k}{2f}(x^2 + y^2)\right] t_L(x, y) = \frac{-i}{\lambda f} exp(ikf)$$

Therefore, the transfer function, $t_L(x, y)$, of the lens is given by Eqn. (1.19)

$$\begin{aligned} t_L(x, y) &= exp\left[-i\frac{k}{2f}(x^2 + y^2)\right] \\ T_L(\alpha, \beta) &= -i\frac{\lambda f}{(2\pi)^2} exp\left[i\frac{f}{2k}(\alpha^2 + \beta^2)\right] \end{aligned} \tag{1.19}$$

Firstly, field distribution at the image plane of a single lens 2f system is analyzed. The field distribution after propagation through the lens can be calculated as follows:

- The sample is located at the focal plane of the lens, f units in front of the lens. Object spectrum is given by $U(\alpha, \beta)$.
- This spectrum then propagates a distance f before interacting with the lens, $U_-(\alpha, \beta; f) = U(\alpha, \beta) H_F(\alpha, \beta; f)$.
- Interaction with the thin lens is then given by $U_+(\alpha, \beta; f) = T_L(\alpha, \beta) * U_-(\alpha, \beta; f)$, where $*$ represents convolution.
- The field just after the lens $U_+(\alpha, \beta; f)$ propagates to the image plane, $U(\alpha, \beta; 2f) = H_F(\alpha, \beta; f) U_+(\alpha, \beta; f)$.

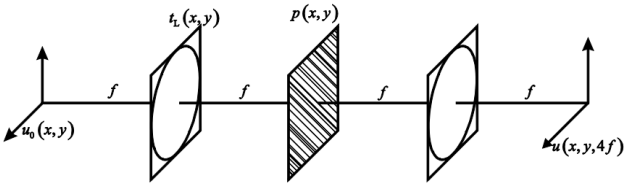

Figure 1.6: Schematic of 4f optical setup. This figure is taken from [5].

- Taking Fourier back transform to get back to real space, the field distribution at the image plane is calculated to be Eqn. (1.20). The interesting observation is that the field at the image plane is the Fourier transform of the field at the sample plane [2, 5]. This property of a lens gives a key to manipulating the spectrum of the sample.

$$u(x,y;2f) = -i\frac{(2\pi)^2}{\lambda f} exp(2ikf) U_0\left[\frac{k}{f}x, \frac{k}{f}y\right] \tag{1.20}$$

Building upon these concepts, the 4f setup is analyzed. From the properties of Fourier transform, it can be shown that sequential application of Fourier transform gives back the original function albeit with inverted co-ordinates [ref], i.e., $\mathcal{F}[\mathcal{F}g(x)] = g(-x)$. Therefore, a second lens can be inserted to perform an inverse Fourier transform optically and generate an image of the sample. A schematic of a 4f optical setup is shown in Fig. 1.6. $u(x,y)$ is the initial field distribution at the front focal plane of a thin lens. The transmission function of the thin lens is $t_L(x,y)$. The thin lens performs a Fourier transform of the initial field at its back focal plane. A transmission mask $p(x,y)$, placed at the back focal plane of the first thin lens and the front focal plane of the second thin lens, can be used to manipulate the Fourier spectrum of the initial field. The second thin lens helps to perform a back Fourier transform at its back focal plane and retrieve the field, $u(x,y,4f)$. Typically in microscopy these days, a digital camera is placed at the back focal plane of the second lens and helps to generate the image of the sample, $< u(x,y,4f) >_t$, where $<>_t$ represents time averaging by the camera. [6] The use of a transmission mask helps to model the constraints in the system. For e.g., optical filtering can be demonstrated by having a finite-sized aperture as the transmission mask. The field distribution at the back focal plane of the second thin lens is found to be 1.21.

$$u(-x,-y,4f) \sim \iint_{-\infty}^{\infty} P\left[\frac{k}{f}(x'-x), \frac{k}{f}(y'-y)\right] u_0(x',y')dx'dy' \tag{1.21}$$

[5] Fundamentals of Modern Optics, Winter Semester 2015/16, Prof. Thomas Pertsch, Abbe School of Photonics, Friedrich-Schiller-Universität Jena.

[6] In addition, the pixel size of the camera also affects the final resolution of the image. By using appropriate magnification, the sampling frequency using the detector must be two times the highest spatial frequency transmitted into the imaging system, as per the Nyquist sampling criteria.

Translated to Fourier space, it means that the field spectrum at $4f$ is given by the product of the Fourier transform of the initial field and Fourier transform of the mask. Or in other words, the response function of the system is proportional to Fourier transform of the mask.
Consider an infinite transmission mask, $p = 1$. Its Fourier transform is then $\delta(x - x')\delta(y - y')$. Then the field distribution $u(-x, -y, 4f) \sim u(x, y)$. If instead, a finite aperture is used as the transmission mask:

$$p(x, y) = \begin{cases} 1 & , x^2 + y^2 \leq (D/2)^2 \\ 0 & , \text{elsewhere} \end{cases} \tag{1.22}$$

The field distribution at plane $z = 4f$ is given by Eqn. (1.23).

$$u(-x, -y, 4f) \sim \iint_{-\infty}^{\infty} \frac{J_1\left[\frac{kD}{2f}\sqrt{(x' - x)^2 + (y' - y)^2}\right]}{\left[\frac{kD}{2f}\sqrt{(x' - x)^2 + (y' - y)^2}\right]} u(x', y')dx'dy' \tag{1.23}$$

Fourier Transform of the circular function is the two dimensional Bessel function of the first kind. Now Eqn. (1.23) shows that each point of the object $u(x', y')$ is convolved with the Bessel function. It implies that the image is a "blurred" version of the input. Optical resolution according to Lord Rayleigh is defined as,"two images are just resolvable when the center of the diffraction pattern of one is directly over the first minimum of the diffraction pattern of the other." First zero of this Bessel function in Eqn. (1.23) arises when $\frac{kD}{2f}\Delta r = 1.22\pi$. Defining $\frac{D}{2f}$ as numerical aperture NA of the system, the Rayleigh resolution limit of the system is defined in Eqn. (1.24).

$$\Delta r = \frac{0.61\lambda}{NA} \tag{1.24}$$

Using optical engineering techniques, the Rayleigh criteria can be changed. Therefore, a physically motivated, hard-limit [6] called Abbe-limit is used in microscopy, Eqn. (1.25). This limit gives a precise statement about which information of the sample passes into the microscope. For head-on illumination, Abbe found that the best achievable resolution is λ/NA. This situation corresponds to the 0^{th}, +1 and -1 orders of scattered light off a diffraction grating entering the back-aperture of a microscope objective as shown in Fig. 1.7. Abbe realized that for an image of the diffraction grating to be generated, only two orders are necessary. This means that using an oblique illumination, Fig.1.7, an image of the grating can still be generated and two times gain in resolution in principle can be achieved.

$$\Delta r = \frac{\lambda}{2NA} \tag{1.25}$$

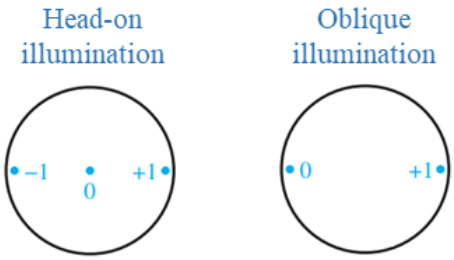

Figure 1.7: The circle represents the back-aperture of a microscope objective. The scattered diffraction orders off the sample, for head-on and oblique illumination is schematically shown. For e.g., consider a diffraction grating with a grating pitch Δr. From grating theory, the angles of the diffracted orders can be calculated as $\Delta r(\sin\theta_i + \sin\theta_r) = m\lambda$, where θ_i is the illumination angle with respect to normal, θ_r is the refracted angle with respect to the normal, λ is the wavelength of light used and m is an integer. $\theta_i = 0$ which corresponds to head-on illumination, m = 1 corresponds to the 1^{st} diffracted order and therefore, $\Delta r = \lambda/\sin\theta_r$. For oblique illumination, when $\theta_i = \theta_r = \theta$, then $\Delta r = \frac{\lambda}{2\sin\theta}$, the famous Abbe-limit.

1.5 Imaging system definition

For brevity, the $4f$ imaging setup described in Section 1.4, is treated as a " black-box", implying that the response of the system can be defined mathematically by just using the transmission mask function $p(x, y)$. Let $g_{in}(x_1, y_1) = u(x, y, 0)$ be the input to the black-box at (x_1, y_1), S represents transformation operator of the system and $g_{out}(x_2, y_2)$ be the output of the system at (x_2, y_2). This can be defined mathematically as in Eqn. (1.26) [7].

$$g_2(x_2, y_2) = S[g_1(x_1, y_1)] \tag{1.26}$$

As seen in Section 1.4, the system consists of free-space propagator $h_F(x, y; z)$, shown in Eqn. (1.18) and the lens transfer function $t_L(x, y)$, Eqn.1.19. These are linear operations and therefore, the system S is a linear operator[7]. Hence, invoking the sifting property of delta functions, Eqn.1.26 can be rewritten as shown in Eqn. (1.27).

$$\begin{aligned} g_2(x_2, y_2) &= S\left[\iint_{-\infty}^{\infty} g_1(\zeta, \eta)\delta(x_1 - \zeta, y_1 - \eta)d\zeta d\eta\right] \\ g_2(x_2, y_2) &= \iint_{-\infty}^{\infty} g_1(\zeta, \eta)S[\delta(x_1 - \zeta, y_1 - \eta)]d\zeta d\eta \end{aligned} \tag{1.27}$$

[7] An operator L is defined as linear if the following two properties are satisfied:

- $L[aU] = aLU$, where a is a constant and U is the unknown and
- $L[U_1 + U_2] = LU1 + LU_2$, where U_1 and U_2 are unknowns.

The response of the system at (x_2, y_2) for an input delta function at (ζ, η) is defined as the impulse response of the system, Eqn. (1.28).

$$h(x_2, y_2; \zeta, \eta) = S\left[\delta(x_1 - \zeta, y_1 - \eta)\right] \tag{1.28}$$

For a linear invariant system, Eqn. (1.28) can be modified and plugged into Eqn. (1.27) to arrive at Eqn. (1.29).

$$g_2(x_2, y_2) = \iint_{-\infty}^{\infty} g_1(\zeta, \eta) h(x_2 - \zeta, y_2 - \eta) d\zeta d\eta \tag{1.29}$$

Eqn. (1.29) is the convolution operation and can be written in shorthand notation as $g_2 = g_1 * h$. This is the result shown earlier in Eqn. (1.21). Translated to Fourier space, this can be written as shown in Eqn. (1.30).

$$G_2(\alpha, \beta) = H(\alpha, \beta) G_1(\alpha, \beta) \tag{1.30}$$

Here $H(\alpha, \beta)$ is defined as the transfer function of the system and accounts for effects of the system in spatial frequency domain.

1.6 Image formation: role of coherence of light

As seen in Section 1.4, the Abbe-limit arises by considering image formation as an interference phenomenon. Abbe found out that interference between the diffracted orders give rise to the image plane intensity distribution. This concept of interference naturally invokes the concept of coherence of light and therefore, in this section coherence of scattered light in imaging is analyzed.

Coherence means statistical similarity. This is important since all optical fields undergo random fluctuations [3]. For e.g., field from thermal light sources, light emitting diodes, lasers etc. all exhibit fluctuations. Coherence helps to quantify these fluctuations, i.e., it is a measure of statistical similarity of these field fluctuations at two or more points [8].

Assuming a narrow band temporal spectrum, the impulse response function is approximately same at all wavelengths [7]. The field $U_i(u, v)$ at the image plane coordinates (u, v) is then given by Eqn. (1.31).

$$U_i(u, v; t) = \iint_{-\infty}^{\infty} d\zeta d\eta h(u - \zeta, v - \eta) U(\zeta, \eta; t - \tau) \tag{1.31}$$

Here τ is the time taken by the fields to propagate from (ζ, η) to (u, v). Now the image intensity is given by $I_i(u, v) = \left\langle |U_i(u, v; t)|^2 \right\rangle$. Assuming that within the region where the impulse response function is non-zero, the time delays between the different fields can be neglected [7]. Therefore, the intensity at the image plane is given by Eqn. (1.32).

$$I_i(u, v) = \iint_{-\infty}^{\infty} d\zeta_1 d\eta_1 \iint_{-\infty}^{\infty} d\zeta_2 d\eta_2 h(u - \zeta_1, v - \eta_1) h^*(u - \zeta_2, v - \eta_2) J_g(\zeta_1, \eta_1; \zeta_2, \eta_2) \tag{1.32}$$

where $J_g(\zeta_1, \eta_1; \zeta_2, \eta_2) = \langle U(\zeta_1, \eta_1; t) U^*(\zeta_2, \eta_2; t) \rangle$, measures similarity of fields at two spatial locations on the object. For the case of perfectly coherent illumination, the fields at the two object points differ only by a complex constant. Therefore, Eqn. (1.32) can be modified as shown in Eqn. (1.33).

$$I_i(u, v) = \left| \iint_{-\infty}^{\infty} h(u - \zeta, v - \eta) U(\zeta, \eta) d\zeta d\eta \right|^2 \tag{1.33}$$

In shorthand notation, Eqn. (1.33) can be written as $I_i = |h * U|^2$. Next, for the perfectly incoherent case, the phases of the fields at the two object points vary randomly. This can be represented mathematically as $\langle U(\zeta_1, \eta_1; t) U^*(\zeta_2, \eta_2; t) \rangle = \kappa I_g(\zeta_1, \eta_1) \delta(\zeta_1 - \zeta_2, \eta_1 - \eta_2)$, where κ is a constant. Therefore, Eqn.1.32 can be modified for the perfectly incoherent case and written as shown in Eqn. (1.34).

$$I_i(u, v) = \kappa \iint_{-\infty}^{\infty} |h(u - \zeta, v - \eta)|^2 I_g(\zeta, \eta) d\zeta d\eta \tag{1.34}$$

In shorthand notation, Eqn. (1.34) can be written as $I_i = |h|^2 * I_g$, where I_g is the ideal image intensity without any blurring. Translated to spatial frequency domain, Eqn. (1.33) and Eqn. (1.34) can be written in shorthand notation as shown below, where $H = \mathcal{F}(h)$ and $G = \mathcal{F}(U)$.

- Coherent imaging
  $\mathcal{F}[I_i] = [HG] * [H^* G^*]$
- Incoherent imaging
  $\mathcal{F}[I_i] = [H * H^*][G * G^*]$

Now, it is interesting to consider the imaging performance of coherent and incoherent imaging systems based on contrast and two-point resolution. A simplified example helps to understand the concepts. Let an object with amplitude transmittance $\cos\left(2\pi \tilde{f} \zeta\right)$ be imaged in both coherent and incoherent imaging modes, where $f_0/2 < \tilde{f} < f_0$. This is shown in Fig. 1.8. As can be seen from Fig. 1.8, contrast of the image of the object is better in coherent case than in incoherent. Now, consider an object with amplitude transmittance $\left|\cos\left(2\pi \tilde{f} \zeta\right)\right|$. This means that frequency of amplitude transmission is now $2\tilde{f}$. This is beyond the cut-off frequency of the coherent transfer function but within the incoherent transfer function cut-off frequency. Hence, such an object will not be visible when imaged in coherent case. Therefore, this object is imaged better in incoherent case. Based on these arguments, it can be concluded that the amplitude transmission function of the object actually decides whether the object will be imaged with a better contrast in either coherent or incoherent mode.

Next, performance of coherent and incoherent imaging based on two-point resolution is considered. In Eqn. (1.23), it was seen that a point on the object gives rise to a Bessel function of the first kind intensity distribution in the image plane. According to Rayleigh resolution limit, Eqn.1.24, another point on the

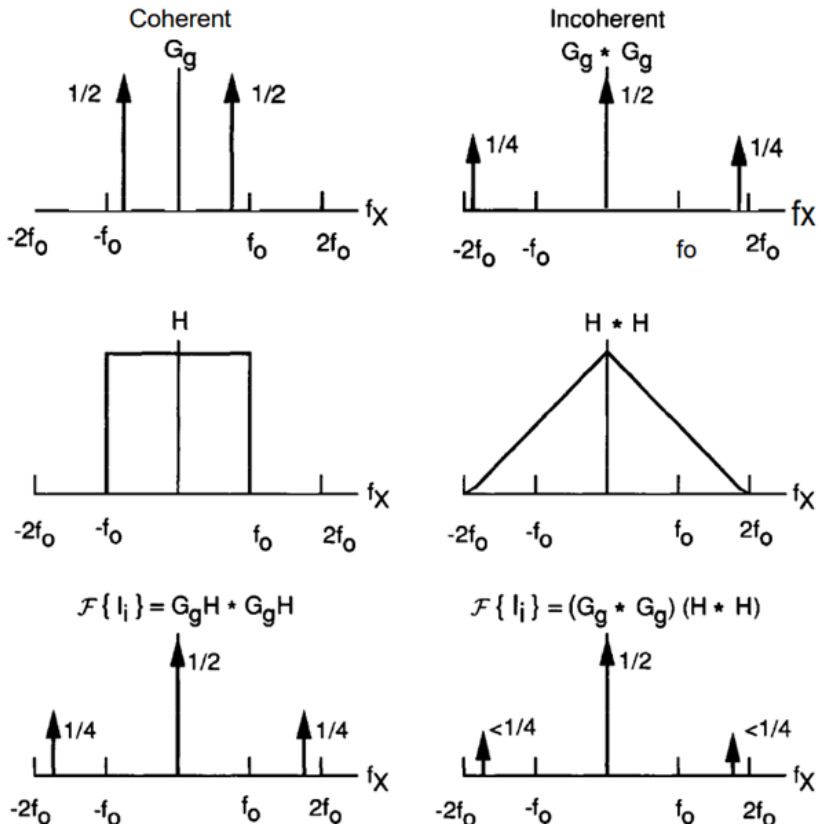

Figure 1.8: Comparison between coherent and incoherent imaging of object with amplitude transmittance $\cos\left(2\pi\tilde{f}\zeta\right)$. This figure is taken from [7].

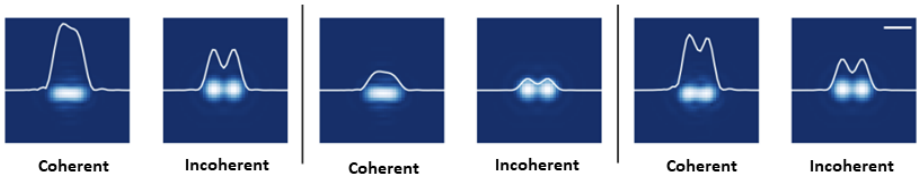

Figure 1.9: This simulation provides a comparison between two particles when they scatter coherently and when they scatter incoherently. Simulation of two 150 nm sized particles, separated by a distance of 350 nm, scattering coherently and incoherently. The scattered wavelength is 500 nm and numerical aperture of the collection objective is set as 1. The three columns correspond to three different phase differences between the scattered light in case of coherent imaging. The line plot indicates the intensity variation along the horizontal axis where the particles are located. Scale bar 500 nm.

object plane lying on the first minima of the Bessel function, i.e., separated by the Rayleigh limit, will appear resolved in the image plane. However, in case there is coherence or similarity between the fields from these two object points, then based on the phase difference between the fields superimposing at the image plane, the image plane intensity distribution will vary. Hence, similar to the contrast scenario seen earlier, there is no preferred imaging method to achieve the best resolution [7, 9]. This concept where phase of the scattered light influences the final generated image is shown in Fig. 1.9.

1.7 Propagation of correlation

It is interesting to note that, correlation i.e., coherence or phase relationship between emissions at two locations is a function of propagation distance [10]. To understand this, the general phenomena of interference of light is considered as shown in Fig. 1.10. Light from two points $P(\vec{r}_1)$ and $P(\vec{r}_2)$ overlap on a screen at $P(\vec{r})$. The distances $R_1 = t_1/c$ and $R_2 = t_2/c$ are the distances traversed by the fields from P_1 and P_2 on the aperture to reach the screen at P. Here $R_1 = t_1/c$ and $R_2 = t_2/c$, where t_1 and t_2 are the times taken by the fields to reach the screen from the apertures. The averaged intensity at the screen $P(\vec{r})$ is then given by Eqn. (1.35).

$$< I(\vec{r},t) >= |K_1|^2 < I(\vec{r_1},t) > +|K_2|^2 < I(\vec{r_2},t) > +2\mathcal{R}[K_1^* K_2 \Gamma(\vec{r}_1,\vec{r}_2,t_1-t_2)] \tag{1.35}$$

In Eqn. (1.35), K_1 and K_2 are complex constants, the mutual coherence function $\Gamma(\vec{r}_1,\vec{r}_2,t_1,t_2) = < U^*(\vec{r_1},t_1)U(\vec{r_2},t_2) >$ and $U(\vec{r_1},t_1)$, $U(\vec{r}_2,t_2)$ are the fields emanating from the aperture. By convention, this mutual coherence function is normalized and used, called the complex degree of coherence $\gamma(\vec{r}_1,\vec{r}_2,t_2-t_1) = \gamma(\vec{r}_1,\vec{r}_2,\tau)$ and $0 \leq |\gamma(\vec{r}_1,\vec{r}_2,\tau)| \leq 1$. Now let's see how this coherence function changes as the field propagates. This was first figured out by Wolf [10]. If $U(\vec{r_1},t_1)$ is a Cartesian component of the electric field, then the field component

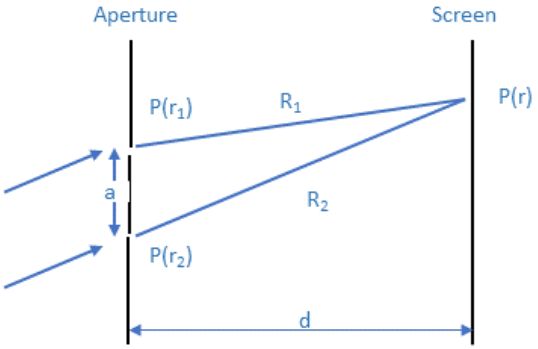

Figure 1.10: Interference phenomenon. Field from two points $P(\vec{r}_1)$ and $P(\vec{r}_2)$, separated by a distance a units, after traversing a distance R_1 and R_2 units overlap on a screen at $P(\vec{r})$.

will satisfy the wave equation as shown in Eqn. (1.36).

$$\nabla^2 U(\vec{r_1}, t_1) = \frac{1}{c^2} \frac{\partial^2 U(\vec{r_1}, t_1)}{\partial t^2} \tag{1.36}$$

Taking the complex conjugate of Eqn. (1.36) to arrive at Eqn. (1.37).

$$\nabla^2 U^*(\vec{r_1}, t_1) = \frac{1}{c^2} \frac{\partial^2 U^*(\vec{r_1}, t_1)}{\partial t^2} \tag{1.37}$$

Then it can be shown that the correlation function $\Gamma(\vec{r}_1, \vec{r}_2, \tau)$ satisfies two wave equations as shown in Eqn. (1.38).

$$\begin{aligned} \nabla_1^2 \Gamma(\vec{r}_1, \vec{r}_2, \tau) &= \frac{1}{c^2} \frac{\partial^2 \Gamma(\vec{r}_1, \vec{r}_2, \tau)}{\partial \tau^2} \\ \nabla_2^2 \Gamma(\vec{r}_1, \vec{r}_2, \tau) &= \frac{1}{c^2} \frac{\partial^2 \Gamma(\vec{r}_1, \vec{r}_2, \tau)}{\partial \tau^2} \end{aligned} \tag{1.38}$$

In Eqn. (1.38), ∇_1^2 and ∇_2^2 are the Laplacian operators with respect to $\vec{r}_1$ and $\vec{r}_2$ respectively. The wave nature of Eqn. (1.38) implies that correlations can be gained with propagation [7, 10].

1.8 Light scattering

In Secion 1.6, it was seen that contrast and resolution depends on the transmission properties of the sample under investigation. Therefore, in this section, light-matter interaction is analyzed. In optical microscopy, which is the topic of this thesis, visible light is used to illuminate the sample under consideration. When light illuminates the sample, the oscillating electric field sets the electrons of the sample also in motion. The accelerating electrons then generate

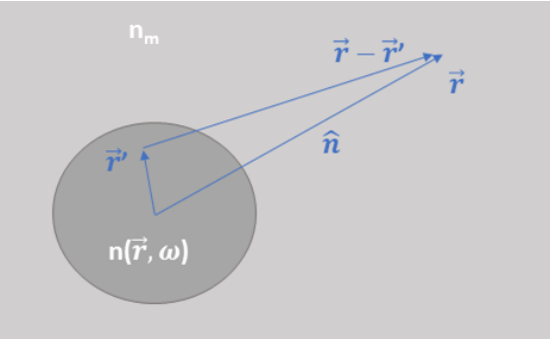

Figure 1.11: A sample of refractive index $n(\vec{r},\omega)$ is embedded in a medium of refractive index n. An observation point in the far-field is chosen is at a distance $|\vec{r}|$ units along the unit vector $\hat{n}$, where the scattered field from a scattering location $\vec{r'}$ is measured.

an electromagnetic radiation, referred to as the scattered light. This scattered light has the same frequency as the excitation light in case of linear media. For simplicity, scalar fields are assumed and the problem setting is shown in Fig. 1.11.

An incident scalar field $u_i(\vec{r},\omega)$ illuminates a sample with refractive index $n(\vec{r},\omega)$, which is embedded in a medium with refractive index n_m. The scattered scalar field by the sample is $u_s(\vec{r},\omega)$. Neglecting the time dependence of the fields, the total field $u(\vec{r})$ propagating through the sample is given by the homogeneous Helmholtz equation in Eqn. (1.39).

$$[\nabla^2 + k^2 n^2]u(\vec{r}) = 0 \tag{1.39}$$

This equation can be rewritten as a non-homogeneous Helmhotz equation as shown in Eqn. (1.40):

$$[\nabla^2 + k_m^2]u(\vec{r}) = -f(\vec{r})u(\vec{r}) \tag{1.40}$$

where, $k_m = kn_m$, $f(\vec{r}) = k_m^2\left[\frac{n^2(\vec{r})}{n_m^2} - 1\right]$ is referred to as the scattering potential [11]. Also, the incident field satisfies the scalar Helmholtz equation, Eqn. (1.41). This corresponds to situation where there is no sample.

$$\left[\nabla^2 + k_m^2\right] u_0(\vec{r}) = 0 \tag{1.41}$$

Eqn. (1.41) has plane wave solutions as shown in Eqn. (1.42), where $\hat{s}$ is the unit vector along the propagation direction of the incident wave vector k_m.

$$u_0(\vec{r}) = E_0 exp(ik_m \hat{s}.\vec{r}) \tag{1.42}$$

Based on the above equations, Eqn. (1.40) can be written as follows in Eqn. (1.43).

$$[\nabla^2 + k_m^2]u_s(\vec{r}) = -f(\vec{r})u(\vec{r}) \tag{1.43}$$

Then the total field detected at $\vec{r}$ can be found by employing the Green's function, Eqn. (1.44).

$$u(\vec{r}) = u_0(\vec{r}) + \int_V d^3r' G(\vec{r} - \vec{r'}) f(\vec{r'}) u(\vec{r'}) \tag{1.44}$$

where $\int_V$ stands for volume integration, $G(\vec{r} - \vec{r'})$ is Green's function and is the impulse response of the system, similar to the definition in Eqn. (1.28). The linear system operator here is $S = \nabla^2 + n_m^2 \frac{\omega^2}{c^2}$, which implies $[\nabla^2 + k_m^2] G(\vec{r} - \vec{r'}) = -\delta(\vec{r} - \vec{r'})$. A suitable ansatz for Green's function in Eqn. (1.44) is, $G(\vec{r} - \vec{r'}) = \frac{exp(ik_m|\vec{r} - \vec{r'}|)}{4\pi|\vec{r} - \vec{r'}|}$ [1].

In optical microscopy, the microscope objective is typically placed in the far-field as seen in the 4f-setup seen in Section 1.4. This helps to approximate the Green's function in the far-field as shown in Eqn. (1.45). The far-field detection implies that high spatial frequencies of the sample are lost upon propagation and not collected by the microscope objective.

$$G(\vec{r} - \vec{r'}) = \frac{1}{4\pi r} exp[ik_m r] exp(-ik_m \hat{n}.\vec{r'}) \tag{1.45}$$

For brevity, let incident wave vector $k_m \hat{s} = \vec{k}_i$ and scattered wave vector $k_m \hat{n} = \vec{k}_s$. Therefore, plugging in Eqn. (1.42) and (1.45) into Eqn. (1.44), we arrive at Eqn. (1.46).

$$u(\vec{r}) = E_0 exp[i\vec{k}_i.\vec{r}] + \frac{exp[ik_m r]}{4\pi r} \int_V d^3r' exp(-i\vec{k}_s.\vec{r}) f(\vec{r'}) u(\vec{r'}) \tag{1.46}$$

Born series is used to solve equations of the type shown in Eqn. (1.46). If, $u_s << u_i$, then total field, $u(\vec{r'}) = u_i(\vec{r'}) + u_s(\vec{r'})$ inside the integral can be approximated as $u(\vec{r'}) \approx u_i(\vec{r'})$ [12]. This is known as the first Born approximation. Then the integral in Eqn. (1.46) exhibits a Fourier transform operation on the scattering potential $f(\vec{r'})$, with the conjugate variable momentum transfer defined as $\vec{\kappa} = \vec{k}_i - \vec{k}_s$.

$$\begin{aligned} u(\vec{r}) &= u_0(\vec{r}) + \int_V d^3r' G(\vec{r} - \vec{r'}) f(\vec{r'}) u_0(\vec{r'}) \\ u(\vec{r}) &= E_0 exp[i\vec{k}_i.\vec{r}] + E_0 \frac{exp[ik_m r]}{4\pi r} \int_V d^3r' exp[i\vec{\kappa}.\vec{r'}] f(\vec{r'}) \end{aligned} \tag{1.47}$$

The physical interpretation of Eqn. (1.47): $u(\vec{r})$ is where the detector is placed, for example in optical microscopy, a microscope objective. The first term on the right hand side of the equation is the incident plane wave. Inside the integral, the plane wave u_0 shakes the potential f at location $\vec{r'}$. The Green's function then propagates this information from $\vec{r'}$ to the detector location $\vec{r}$. The total field at location $\vec{r}$ is the sum of the incident field $u_0(\vec{r})$ and scattered field $u_s(\vec{r})$, arising due to interaction of the incident field with the potential.

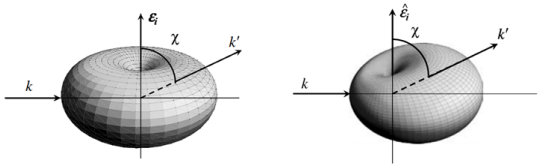

Figure 1.12: Scattering cross-section with an incident light beam, $\vec{\mathcal{E}}_i$, polarized along $\hat{\mathcal{E}}_i$. The incident wave vector is shown by $\vec{k}$ and the scattered wave vector $\vec{k}'$. χ is the angle between the electric field and the scattered field. This figure is taken from [13].

Richer information can be obtained if vectorial field equations are employed for light scattering. Fig. 1.12 shows the scattering cross-sections, which is related to scattered fields, for linearly polarized light in case of Born approximation. For e.g., when the wavelength is much larger than the size of the particle with radius 'a', the light scattering phenomenon is defined as Rayleigh scattering, and it shows a $1/\lambda^4$ and a^6 dependence. The implication of this result is that blue light whose frequency is roughly twice that of red light will be scattered approximately sixteen times stronger and therefore, the sky appears blue. And as particle size increases, the scattering cross-section becomes anisotropic as shown [13].

1.9 Optical waveguides

In this thesis waveguide-based microscopy is discussed, i.e., biological samples scatter light after getting illuminated by evanescent waves of optical waveguides. So what are these optical waveguides? Optical waveguides are structures that confine light and guide the optical power along its length. To understand how light is guided in these structures, Maxwell equations are invoked. In this thesis, dielectric waveguides are used and therefore, the modal analysis of a dielectric waveguide is considered in this section.

For dielectrics, the external charge density $\rho_{ext}(\vec{r},t)$, and macroscopic current density $\vec{j}_{makr}(\vec{r},t)$, in Eqn. 1.3 and Eqn. 1.2 respectively, are set to zero. A real valued dielectric constant is assumed which depends only on the transverse coordinate x, i.e., $\epsilon(\vec{r}) = \epsilon(x)$ and the material is lossless. This allows the use of ansatz in Eqn. (1.48) [14]. A schematic of such a light guiding structure is shown in Fig. 1.13.

$$\begin{aligned} \vec{E}(\vec{r}) &= \vec{E}_0(x) exp[i(\omega t - \beta z)] \\ \vec{H}(\vec{r}) &= \vec{H}_0(x) exp[i(\omega t - \beta z)] \end{aligned} \tag{1.48}$$

The physical interpretation of such an ansatz shown in Eqn. (1.48) is that a fixed field profile, $\vec{E}_0(x)$, propagates along the length of the waveguide accumulating only a phase, $exp(-i\beta z)$. Substituting the anstaz in Eqn. (1.48) into Maxwell equations for the dielectric structure, the TE and TM mode solutions are arrived

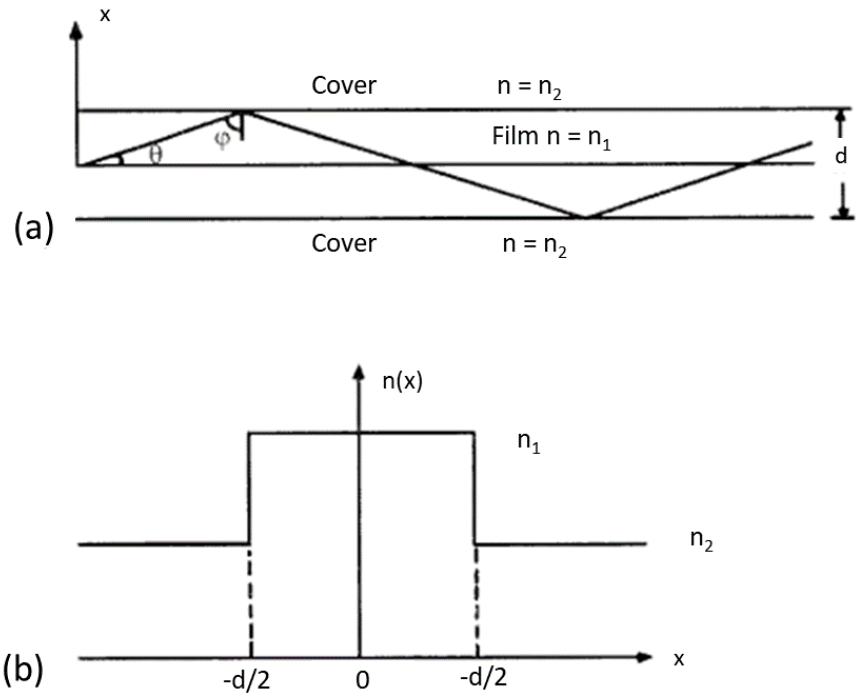

Figure 1.13: (a) Film waveguide with core refractive index n_1 sandwiched between a cover with a lower refractive index n_2. (b) Refractive index variation as a function of x is plotted. The thickness of the film waveguide is d units. This figure is taken from [14].

at, as shown in Eqn. (1.49) and Eqn. (1.50) respectively.

$$\begin{aligned} i\beta E_y &= -i\omega\mu_0 H_x \\ \partial E_y/\partial x &= -i\omega\mu_0 H_z \\ -i\beta H_x - \partial H_z/\partial x &= i\omega\epsilon_0 n^2(x) E_y \end{aligned} \tag{1.49}$$

$$\begin{aligned} i\beta H_y &= i\omega\epsilon_0 n^2(x) E_x \\ \partial H_y/\partial x &= i\omega\epsilon_0 n^2(x) E_z \\ -i\beta E_x - \partial E_z/\partial x &= -i\omega\mu_0 H_y \end{aligned} \tag{1.50}$$

The aim is now to determine the propagation constant β. For the TE modes, this could be found out by rearranging Eqn. (1.49) to arrive at Eqn. (1.51).

$$\begin{aligned} d^2E_y/dx^2 + \kappa^2 E_y = 0;\ |x| < d/2;\ Film \\ d^2E_y/dx^2 - \gamma^2 E_y = 0;\ |x| > d/2;\ Cover \end{aligned} \tag{1.51}$$

In Eqn. (1.51), $\kappa^2 = k_0^2 n_1^2 - \beta^2$ and $\gamma^2 = \beta^2 - k_0^2 n_2^2$, with vacuum wave number $k_0 = \omega/c$ and $\epsilon(x) = n^2(x)$. This definition helps to identify guided and decaying waves in the film and in the cover regions respectively. A similar set of equations can also be obtained for the TM modes involving $H_y(x)$ component, by rearranging Eqn. (1.50). The solutions for $E_y(x)$ and $H_y(x)$ must correspond to real fields, i.e., inside the core the fields should guide power along the length of the waveguide and, outside the core, the fields should vanish at infinity. This implies, $n_2^2 < \frac{\beta^2}{k_0^2} < n_1^2$. Therefore, the field profiles assume the form shown in Eqn. (1.52).

$$E_y(x) = \begin{cases} A\cos\kappa x + B\sin\kappa x & ;|x| < -d/2; \text{Film} \\ Cexp(\gamma x) & ;\ x < -d/2;\ \text{Cover} \\ Dexp(-\gamma x) & ;\ x > d/2;\ \text{Cover} \end{cases} \tag{1.52}$$

In Eqn. (1.52), the constants A, B, C and D can be determined by evaluating the boundary conditions, i.e., tangential fields must be continuous across the boundary. In addition, due to symmetry of refractive index distribution, $n^2(-x) = n^2(x)$, and since the operator in Eqn. (1.52) is linear, symmetric and anti-symmetric modal solutions satisfy Eqn. (1.51) [14]. For e.g., the TE symmetric mode distribution is shown in Eqn. (1.53).

$$E_y(x) = \begin{cases} A\cos\kappa x & ;\ |x| < -d/2; \\ Cexp(-\gamma|x|) & ;\ |x| > +d/2 \end{cases} \tag{1.53}$$

Now, if the values of the propagation constant are determined, then the field profiles have been figured out. Finding the propagation constants in non-trivial geometries such as rib or strip geometries which are employed in this thesis, are difficult and require Maxwell equation solvers such as COMSOL. However,

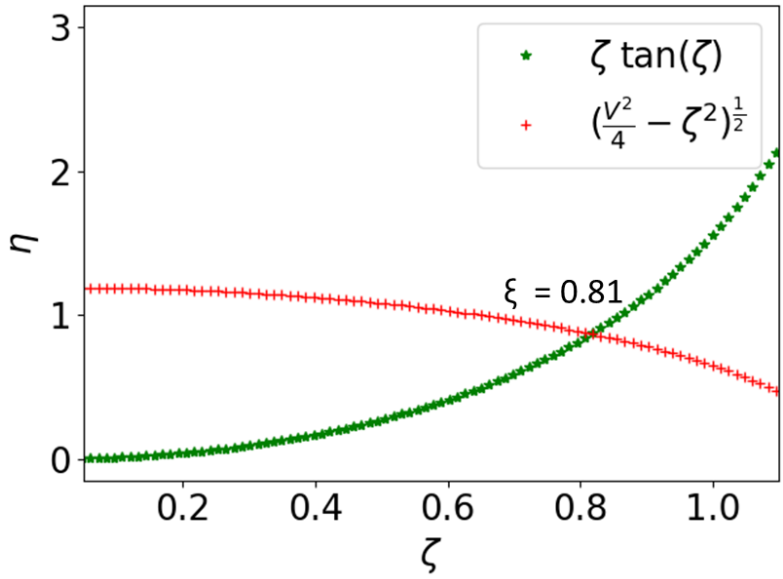

Figure 1.14: Green curve shows the left hand side of Eqn. (1.54) and red curve shows the right hand side of Eqn. (1.54) plotted as a function of ζ. The point of intersection of the curves dictates the propagation constants of the waveguide.

for the slab waveguide geometry considered here, Fig. 1.13, a transcendental equation can be obtained from Eqn. (1.53), and is shown in Eqn. (1.54).

$$\zeta \tan(\zeta) = (\frac{1}{4}V^2 - \zeta^2)^{1/2} \tag{1.54}$$

Similarly, for the anti-symmetric TE mode, Eqn. (1.55) shows the transcendental equation.

$$-\zeta \cot \zeta = (\frac{1}{4}V^2 - \zeta^2)^{1/2} \tag{1.55}$$

In Eqn. (1.54) and 1.55, $\zeta = \frac{\kappa d}{2}$, $\frac{\gamma d}{2} = (\frac{1}{4}V^2 - \zeta^2)^{1/2}$ and $V = k_0 d(n_1^2 - n_2^2)^{1/2}$. V is referred to as the dimensionless waveguide parameter. The graphical solution of Eqn. (1.54) of a waveguide with $n_1 = 1.503$, $n_2 = 1.500$ and $d = 4\ \mu m$ excited at 1000 nm is shown in Fig. 1.14. For this geometry, $V \approx 2.3$ and the curves in Eqn. (1.54) intersect at $\zeta \approx 0.81$. Therefore, the effective index of this TE mode is $n_{eff} = \beta/k_0 \approx 1.5016$. By increasing the dimensionless waveguide parameter V, i.e., by using a shorter wavelength or by increasing the film-cover index contrast, more number of modes can be guided. For example, if the same waveguide is excited at 500 nm, then $V \approx 4.7$ and the same waveguide can now support a symmetric TE mode with effective index, $n_{eff} \approx 1.5023$, and an anti-symmetric TE mode with effective index, $n_{eff} \approx 1.501$.

Now, to calculate the power guided by these modes, time averaged Poynting vector defined in Eqn. 1.7 is employed for the TE mode defined in Eqn. (1.53).

Calculating $< \vec{S} >_x$ along the x-axis leads to zero, implying that no power is transmitted along the x-axis on an average. This is because of the $\frac{\pi}{2}$ rad phase difference between the electric and magnetic fields in the plane perpendicular to the direction of propagation [15]. This implies that the exponentially decaying fields carry no net power away from the surface of the waveguide. The implication of this in waveguide microscopy is that the excitation light, i.e., guided light, does not reach a camera placed along the x-axis. These concepts are exploited in waveguide-based fluorescence and label-free microscopy and are elaborated in the upcoming sections. On the other hand, along the length of the waveguide, a non-zero time averaged Poynting vector,$< \vec{S} >_z$, is obtained. This implies that power is guided along the length of the waveguide via these modes.

In waveguide-based microscopy, the evanescently decaying field is what illuminates the sample. The evanescent field provides a highly oblique illumination to the sample placed on top of the core-cladding interface of the waveguide. The exponentially decaying nature of these fields, seen in Eqn. (1.52) and Eqn. (1.53), imply that the illumination strength decreases with increasing distance from the core. Typically the penetration depth of the evanescent field is defined as distance at which the field drops off to $\frac{1}{e}$ of its value at the core. By solving the transcendental equation in Eqn. (1.54), the penetration depth, $1/\gamma$, of the symmetric mode can be obtained. For e.g., in case of a slab waveguide with silica core of thickness 450 nm and cladding layers of fluorinated material CYTOP [16], $n_1 \approx 1.42$ and $n_2 \approx 1.34$, the penetration depth at 488 nm is calculated to be ≈ 200 nm. For the same waveguide geometry and excitation wavelength, if only the core material is changed to Silicon Nitride Si_3N_4, $n_1 \approx 2$, then the penetration depth is ≈ 60 nm.

1.10 Fluorescence microscopy

The scattering potential, described in Section 1.8, of biological specimens like individual cells, is poor due to minimal index contrast between the cell and its surrounding media [12]. This implies that in label-free optical microscopy of biological specimens, poor contrast is an issue. The other challenge is that of diffraction-limited resolution due to the inability of the system to capture the higher spatial frequencies of the sample, as described in Section 1.3. What it implies is that imaging weakly scattering specimens in their native state at high-contrast and high-resolution with visible light can be challenging. This is where fluorescence microscopy comes in handy and has over the years become a popular tool to study life at high-contrast and resolution [18].

In fluorescence microscopy, the area of interest is made to fluoresce. A simple model to describe fluorescence is shown in Fig. 1.15. Fluorescence is an inelastic scattering phenomenon, i.e., an incident illuminating field induces photoluminescence in fluorophores. The emitted light has a longer wavelength, i.e., Stoke shifted with respect to the incident light. This emission process is typically described using a Jablonski diagram, Fig. 1.15. Then, by using ap-

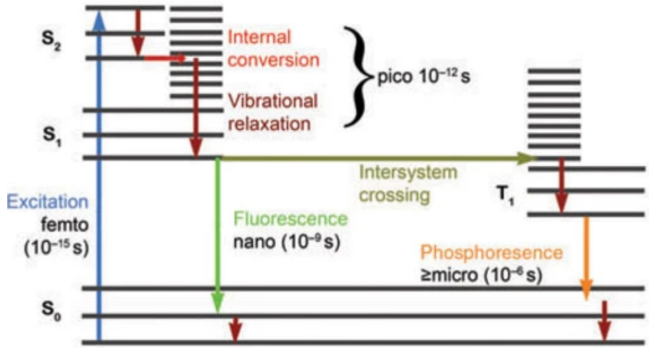

Figure 1.15: Jablonski diagram explaining fluorescence phenomenon. The energy states of the fluorophore are represented by the black horizontal lines and the black arrow points along increasing energy. The blue arrow on the left indicates the excitation light, causing an electronic transition from ground state S_0 to second electronic excited state S_2. This absorption process is fast and takes place on the order of femtoseconds. Now the excited electron can undergo non-radiative internal conversions or vibrational relaxations which take place on the order of picoseconds. This brings the electron back to the lowest level of the first electronic excited state S_1. From there via fluorescence, the excess energy is dissipated in the form of light, on the order of 10^{-9} to 10^{-7} seconds and the electron reaches the electronic ground state. As energy difference between S_0 and lowest vibrational state of S_1 is smaller than absorbed photon, the emitted fluorescence is Stoke shifted. Another possibility is that the excited electron can undergo intersystem crossing and enter into a long-live excited Triplet state T_1. This process takes place on the order of 10^{-8} to 10^{-3} seconds. There it can undergo non-radiative vibrational relaxations to reach the lower vibrational energy level of the excited triplet state. From there, the electron can undergo radiative phosphorescence and reach the ground state, which takes place on the order of $> 10^{-6}$ seconds. This figure is taken from [17].

propriate optical filters, the incident light is cut-off and only the Stoke shifted light is allowed to reach the camera. This ensures imaging of specific areas of the cell with high-contrast, as the background light is eliminated by the spectral filters and the speckle noise is mitigated due to random phase relationship between the different fluorescent molecules. A specific example where fluorescence microscopy helps image cellular structures with high-contrast is shown in Fig. 1.16. In addition to enabling high-contrast imaging, these molecules can be assumed to emit incoherently for moderate labeling densities [19, 20]. These properties are utilized by fluorescence-based super-resolution algorithms to circumvent the diffraction-limit. As a result, a number of techniques have evolved over the years that exploit linear or non-linear properties of fluorescent molecules [21] to circumvent the Abbe diffraction limit, Eqn. (1.25). For e.g., STimulated Emission Depletion STED [22], Photo-Activated Localization Microscopy PALM [23], nonlinear structured illumination microscopy [24] etc., utilize nonlinearity in fluorescent emission [25] to achieve optical resolution well below 100 nm. On the other hand, intensity-fluctuation based techniques that utilize the intrinsic temporal intensity-fluctuations in the emission profile of fluorescent molecules [26–32], and structured illumination microscopy [33,34] exploit the linear emission properties of these fluorescent molecules to circumvent the diffraction-limit.

In this thesis, intensity-fluctuation based algorithms and structured illumination microscopic techniques are employed to go beyond the diffraction-limit. Hence, a brief overview of these techniques is presented.
Firstly, we will look at intensity-fluctuation based techniques, especially how conventional super resolution optical fluctuation imaging SOFI [27] gains resolution [27]. Conventional SOFI utilizes the intrinsic blinking of fluorescent molecules to achieve super-resolution. For independently emitting molecules, the random phase relationship between the emissions of the different molecules gives rise to a linear imaging system in intensity, i.e., camera plane intensity is linearly related to the fluorescent molecule density. This randomness in emission helps SOFI differentiate between the emissions from different molecules from an image stack exhibiting intensity-fluctuations. The working principle of SOFI can be better understood using Eqn. (1.56) and 1.57 below. For e.g., if there are N independently emitting stationary fluorescent molecules with a constant molecular brightness ϵ_k and a time dependent fluctuation $s_k(t)$ that accounts for the photokinetics of the molecule, then the camera plane intensity, $F(\vec{r},t)$, is given by Eqn.1.56, where $U(\vec{r})$ is the point spread function of the system.

$$F(\vec{r},t) = \Sigma_{k=1}^{N} U(\vec{r}-\vec{r}_k)\epsilon_k s_k(t) \tag{1.56}$$

Eqn. (1.56) is the diffraction-limited wide-field fluorescence image. Neglecting the cross-correlation terms [8] due to random phase-relationship between the

[8] For simplicity, emission from two fluorescent molecules are considered. Molecule 1 has an emission profile, say $exp[i(\phi_1(t)]$ and emission from molecule 2 is $exp[i(\phi_2(t)]$. The time dependence in the phase argument accounts for the randomness in emission. The time averaged intensity will give a cross-correlation term $\cos[\phi_2(t) - \phi_1(t)]$. If the emissions from the two

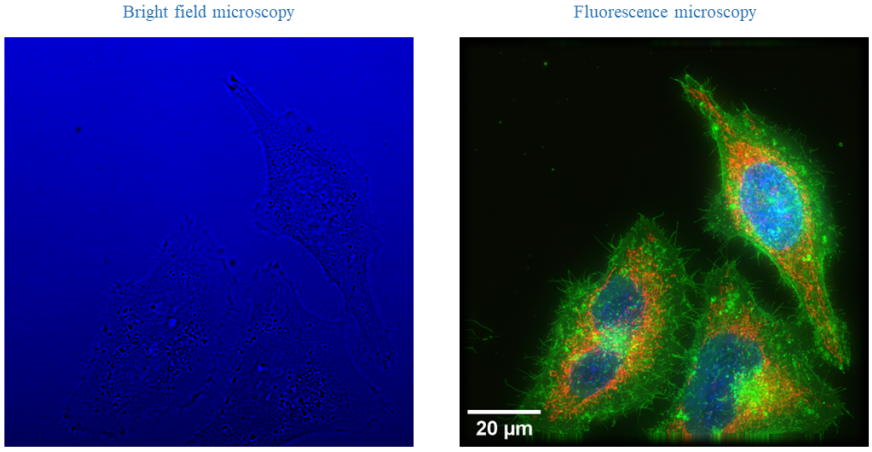

Figure 1.16: Comparison between HeLa cells imaged in bright-field and fluorescence mode. The cells are barely visible in bright-field configuration. To visualize them with high-contrast, the same cells are stained and imaged using fluorescence microscopy: nucleus is labeled with Hoechst and is seen in blue, mitochondria is labeled with Mitotracker Red and is seen in red and plasma membrane is labeled with Cell Mask Oragne and seen in green. Scale bar 20 μm.

emitting molecules, the second-order auto correlation function of the intensity-fluctuation function is calculated as in Eqn. (1.57).

$$G_2(\vec{r},\tau) = \Sigma_k U^2(\vec{r}-\vec{r}_k)\epsilon_k^2 < \delta s_k(t+\tau)\delta s_k(t) > \tag{1.57}$$

where $\delta s(t) = s(t) - < s(t) >$. Eqn. (1.57) is the SOFI image for a particular time lag τ. The resolution gain in the SOFI image in Eqn. (1.57) over the diffraction-limited image in Eqn. (1.56), is due to the non-linearity of the correlation function in Eqn. (1.57), i.e., the usage of a squared point spread function $U^2(\vec{r})$, as illustrated in Fig. 1.17. In principle, this provides a two-times resolution gain over the diffraction-limit for the 2^{nd} order SOFI reconstruction [35]. Recently, intensity-fluctuations have been induced via illumination beams, such as by illuminating the sample using speckle patterns [36–38] to generate super-resolved images using SOFI.

Next, the working principle of Structured Illumination Microscopy SIM [33, 34] is elaborated. As the name implies, the illumination beam profile is modified to circumvent the Abbe diffraction limit in Eqn. (1.25). Typically in SIM, two coherent beams are superimposed at the sample plane in space and time, to generate a sinusoidal intensity distribution. To understand the resolution gain mechanism in SIM, Eqn. (1.58) to Eqn. (1.59) and Fig. 1.18 is provided. A sample fluorescence distribution $S(\vec{r})$ is illuminated with a structured beam $I_{\theta,\phi}(\vec{r})$ and imaged onto a camera, The point spread function of the system is

molecules are independent with respect to one another, then the argument of the correlation term will still be a function of time and therefore, tends to zero on time averaging.

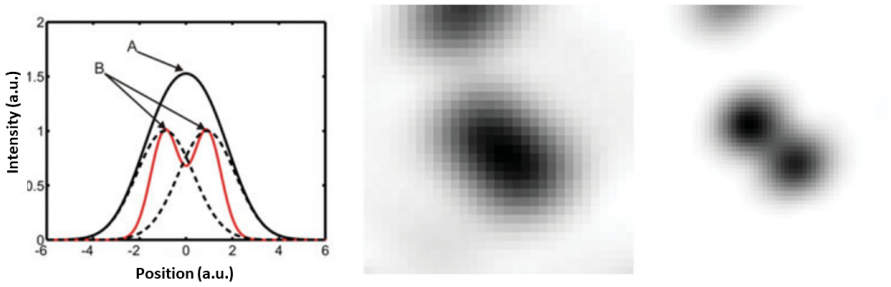

Figure 1.17: Non-linearity of correlation function helps gain resolution in SOFI. The red curve shows the correlation values. The black dotted curve shows signal from a single emitter only. The black curve labeled 'A' is sum signal from the two emitters and 'B' indicates points of highest correlation. The middle figure shows an experimental image of two unresolved quantum dots. The right figure shows its corresponding SOFI image, where a clear gain in resolution is observed. This figure is taken from [39].

$H(\vec{r})$ and $N(\vec{r})$ accounts for noise in the captured image. Then the captured image can be described as shown in Eqn. (1.58), [40].

$$D_{\theta,\phi}(\vec{r}) = [S(\vec{r})I_{\theta,\phi}(\vec{r})] * H(\vec{r}) + N(\vec{r}) \tag{1.58}$$

If $I_{\theta,\phi}(\vec{r}) = I_0[1-\frac{m}{2}\cos 2\pi\vec{p}_\theta.\vec{r}+\phi]$, where I_0 is the maximum value of sinusoidal illumination profile, $\vec{p}_\theta = (p\cos\theta, p\sin\theta)$ is the illumination spatial frequency vector, θ gives orientation of the illumination, ϕ is phase of illumination pattern and m is the modulation factor. Then spatial Fourier transform of Eqn. (1.58) results in Eqn. (1.59).

$$\tilde{D}_{\theta,\phi}(\vec{k}) = \frac{I_0}{2}[\tilde{S}(\vec{k}) - \frac{m}{2}\tilde{S}(\vec{k}-\vec{p}_\theta)e^{-i\phi} - \frac{m}{2}\tilde{S}(\vec{k}+\vec{p}_\theta)e^{i\phi}]\tilde{H}(\vec{k}) + \tilde{N}(\vec{k}) \tag{1.59}$$

The physical interpretation of Eqn. (1.59) is that the captured image is a sum of three images. This is illustrated schematically in Fig. 1.18. By acquiring three images with three different illumination phases ϕ, the acquired image can be disentangled and the higher-spatial frequencies can be restored to its appropriate positions. For isotropic resolution enhancement, the pattern orientation, θ, can be changed and a final image with a higher-resolution than the diffraction-limited image can be generated. The resolution of the final reconstructed image will be $\frac{1}{\frac{2NA_{ill}}{\lambda_{ill}}+\frac{2NA_{det}}{\lambda_{det}}}$, where $\lambda_{ill/det}$, $NA_{ill/det}$ are the illumination/detection wavelengths and numerical aperture [6].

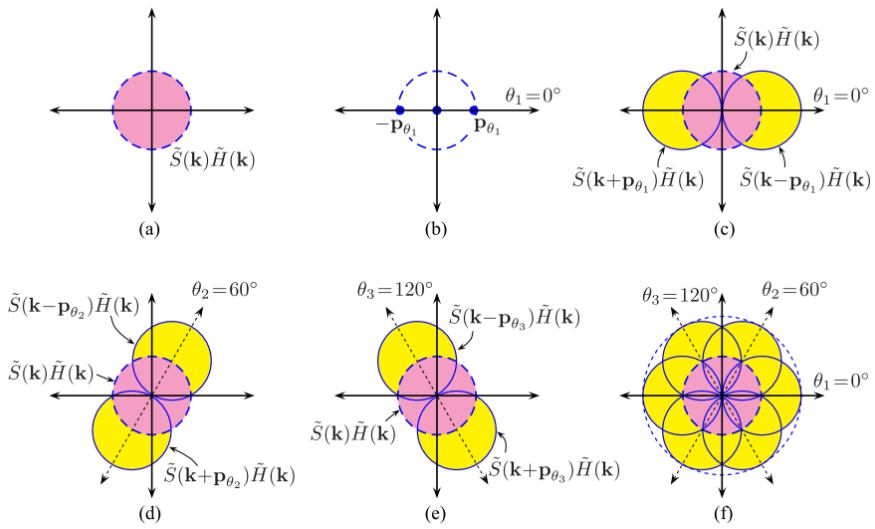

Figure 1.18: SIM reconstruction in reciprocal space is illustrated. (a) Diffraction-limited image contains sample information limited by the optical transfer function $\tilde{H}(\vec{k})$. (b) Frequency domain representation of the intensity distribution, at $\theta = 0°$, of the illumination beam with respect to $\tilde{H}(\vec{k})$. (c, d, e) Schematic representation of Eqn. (1.59) for $\theta = 0°$, $\theta = 60°$ and $\theta = 120°$ is shown. The yellow crescent shaped regions correspond to higher-spatial frequencies of the sample that are now low passed into the pass-band of the system. (f) The higher spatial frequencies that got low passed into the pass-band are separated and restored to its appropriate positions to finally generate a super-resolved image of the sample. This figure is taken from [40].

1.11 Label-free microscopy

Biological samples like cells and tissues are mostly transparent at visible wavelengths and are commonly referred to as phase objects [41]. The refractive index contrast of live cells with its surrounding media is typically 0.01 - 0.05 [42, 43]. What this implies is that these biological specimens can be considered as weakly scattering potentials, and therefore, imaging them in the presence of an overwhelming incident light is challenging. This allows to invoke the first-order Born approximation, described in Section 1.8, and thereby show that light transmitted by a biological sample can be represented as $u(x,y) = |u|exp[i\phi(x,y)] \approx |u|[1+i\phi(x,y)]$ [44], where $\phi(x,y)$ is the phase delay associated with a light beam passing through the sample. This implies that a camera collecting this light, generates an image with minimal modulations in intensity as shown in the bright-field image in Fig. 1.16. A number of techniques have evolved over the years that render these weakly scattering specimens visible with high-contrast. For e.g., phase contrast microscopy [45], quantitative phase microscopy [41], differential interference contrast [46], rotating coherent scattering microscopy [47], interferometric scattering microscopy [48], optical waveguides [16, 49–52], Fourier ptychography [53], dark-field microscopy [54] etc. These techniques help image biological specimens with high-contrast but with diffraction-limited resolution. The different optical techniques for circumventing the Abbe limit in label-free microscopy include near-field scanning optical microscopy [55], negative index or left handed materials [56], applying fluorescence based super-resolution algorithms by exploiting the auto-fluorescence properties of biological samples [57], using a nonlinear propagation medium for self-induced structured illumination [58], employing micro-spheres [59], optical super-oscillation techniques [60] etc. However, their applicability in bio-imaging has been limited due to respective experimental challenges. Therefore, state-of-the-art (SOTA) techniques in life-sciences still rely on conventional microscopy involving dielectric lenses and linear imaging media. These SOTA techniques can be categorized into three, based on their working principle to enhance the resolution:

- Technique 1: techniques that rely on the concept of synthetic aperture of coherently scattering specimens using free-space optics [47, 61–64].
- Technique 2: techniques that rely on the concepts of synthetic aperture/spatial frequency shift for coherently scattering specimens using chip-based solutions [49, 51, 65, 66].
- Technique 3: techniques that use fluorescence-based super-resolution algorithms to coherently scattering specimens [57, 67].

Some of the abovementioned techniques push resolution well below 200 nm. However, these techniques are still diffraction-limited in Abbe's sense, $\lambda/(NA_{ill}+NA_{det})$, where λ is wavelength of the detected light, NA_{ill} and NA_{det} are numerical aperture of illumination and detection objectives. This is attributed to coherence of scattered light off the sample [6]. In fluorescence microscopy,

the fluorescent molecules emit spatially incoherently. This means that these molecules will respond only to variations in intensity of the illuminating beam, i.e., a structured illumination induces intensity variations at the sample plane which is exploited by the SIM reconstruction algorithm. This is in contrast to coherently scattering specimens, where any phase shift in illumination beam will induce phase shifts in the scattered light off the sample and therefore, differences in the final generated image. This is further explained as follows. Invoking the first-order Born approximation for biological samples, scattered field off the sample obeys Eqn. (1.43). Spatial Fourier transform of Eqn. (1.43) with an illuminating plane wave, $u(\vec{r}) = exp(i\vec{k}_i.\vec{r})$, results in a scattered field spectrum proportional to $\tilde{F}(\vec{k} - \vec{k}_i)$, where $\tilde{F}(\vec{k})$ is the Fourier transform of the scattering potential $f(\vec{r})$. This means that a change in phase $\vec{k}_i$ of the illuminating field, causes a change in the sampled spectrum of the sample and thus, the differences in the image arising due to differences in obliquity of the illumination. This is the reason why fluorescence-based algorithms like SIM [40], applied to coherently scattering specimens do not gain any more resolution than what is already accessible via oblique illumination [68]. The final resolution is determined by Abbe's limit for oblique illumination, Eqn. 1.25. Due to similar arguments, the coherence of the scattered light also restricts the usage of intensity-fluctuation-based algorithms. In addition, interference of coherently scattered light at the camera plane can lead to artefacts in the reconstructed image, if intensity-fluctuation algorithms are applied to coherent imaging [52].

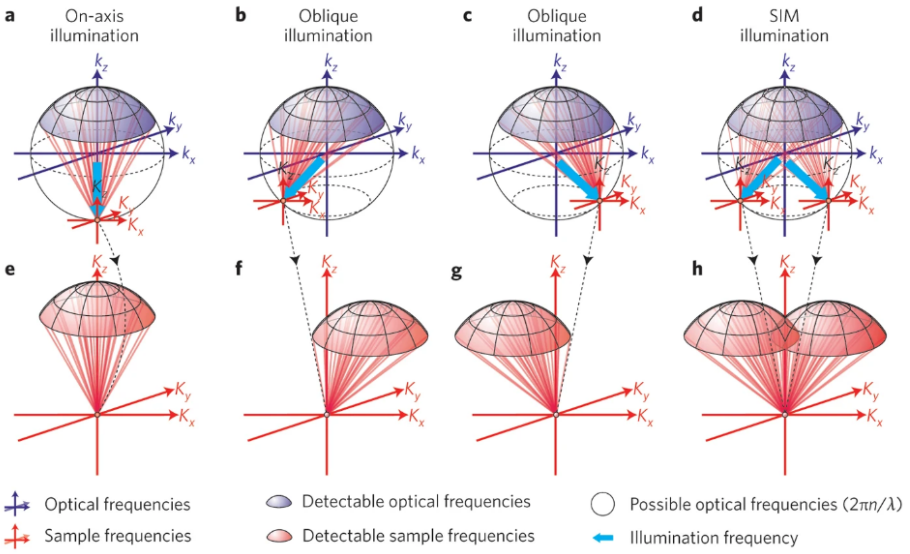

Figure 1.19: (a - d) Illumination wave-vector is represented by the blue arrow. The illumination wave vector interacts with the sample which scatters light as explained in Section 1.8. The scattered light is represented by the hollow black sphere. Only a part of this scattered light is admitted into the numerical aperture of the system. The numerical aperture of the system is shown by the purple spherical cap. (e - g) The spatial frequencies of the sample admitted into the numerical aperture of the system are shown by the red spherical cap. Differences in (e) on-axis and (f, g) off-axis illumination show the differences in the sample spatial frequencies admitted into the imaging system. (h) Structured illumination on a coherently scattering sample provides the same information as separately illuminating the coherently scattering specimen with two oblique illuminations. This figure is taken from [68].

Chapter 2

Waveguide microscopy

Of late, optical waveguides are being increasingly employed in fluorescence [38, 69–77] and label-free microscopy [16, 52, 78]. This is because these optical waveguides can cater to the two major challenges in microscopy, i.e., contrast and resolution, albeit for two-dimensional imaging due to evanescently decaying nature of the illuminating field. In an ideal waveguide, the decoupled illumination and detection scheme helps cut-off the incident light and allows only the scattered light off the sample to reach the camera, thus enabling high-contrast imaging [16, 52]. In addition, the higher refractive index of the dielectric core, plus the various on-chip beam-shaping options, help in super-resolution fluorescence microscopy [69, 70] and high-resolution label-free microscopy [49, 51].

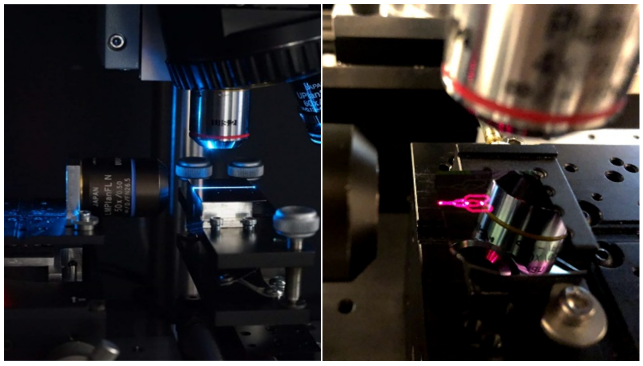

Figure 2.1: Laser at 488 nm, blue light, and at 640 nm, red light, is confined and guided by Si_3N_4 waveguides. These waveguides support guidance with tolerable losses over a few hundred nanometers in the visible spectrum. In addition, they allow complex on-chip beam shaping without necessitating the need for additional beam splitters and mirrors, that can make the experimental setup cumbersome.

2.1 Experimental setup

At this point, it is worth comparing the working principles of fluorescence and label-free optical waveguide based microscopy, which is central to this thesis. The experimental setup shown in Fig. 2.2(a) is similar in both waveguide-based fluorescence and label-free microscopy, except for minor changes which will be highlighted in their respective chapters. In this thesis, high-index contrast dielectric waveguides made of Tantalum pentoxide Ta_2O_5 and silicon nitride Si_3N_4 in rib and strip geometries as shown in Fig. 2.2(b) are employed. The sample to be imaged in both fluorescence and label-free mode is placed on top of the core-cladding interface of the waveguide.

As seen in Fig. 2.2, laser is coupled into a single mode fiber and collimated. This collimated light is linearly polarized using a polarizer and guided using a mirror onto the back focal plane of a coupling objective, Olympus LMPanFL $50\times/0.5$ NA. The coupling objective is mounted on a Thorlabs 3-axis stage, XYZ Nano stage. This coupling objective focuses the laser light onto the front facet of a waveguide, shown within the red dotted box which is also blown-up and shown alongside in the red box. The waveguide is mounted on a 2/3-axis Thorlabs translation stage. The coupled laser light excites predominantly the different TE modes in the waveguide that gets guided along the length of the waveguide, as shown in Fig.2.1. As light gets guided along the length of the waveguide, it also sets up an evanescent field along the core-cladding interface of the waveguide. This field interacts with the sample placed on the core-cladding interface of the waveguide.

In fluorescence microscopy, the drop in evanescent field strength ensures that only the fluorescent molecules which are within the penetration depth of the field emit with sufficient strength. Since the fluorescent molecules emit incoherently, they are not sensitive to the illumination phases but to the illumination intensity. The illumination intensity at each point in such multi-moded waveguides is modulated based on the interference between the different guided modes. This ensures a linear relationship between sample plane fluorophore concentration and image plane intensity.

On the other hand, in label-free microscopy, any index perturbation within the penetration depth of the evanescent field will scatter light into the camera, i.e., specificity is compromised as opposed to fluorescence microscopy. Also, due to coherence between the scattered fields, camera plane intensity is non-linearly related to particle concentration. The strength of this scattered field is a function of the scattering potential of the sample.

The scattered light is now collected by an imaging objective and imaged onto the camera via a combination of tube lens and emission filters. In fluorescence microscopy, spectral filters are used to allow the Stoke shifted light from the fluorescent molecules to reach the camera. Thus, a fluorescent image can be regarded as a map of the location of these fluorescent molecules. In label-free microscopy, typically the spectral filters are absent. The scattered light off the sample is relayed onto the camera via the imaging objective and tube lens. Fig.

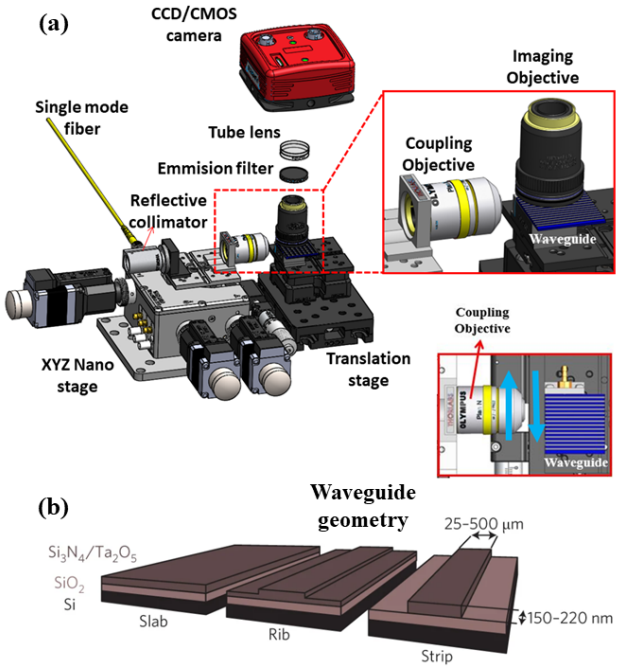

Figure 2.2: (a) Waveguide-based microscopy experimental setup in reflection mode is provided. (b) Different waveguide geometries are shown. The core is made of high-index material like Si_3N_4 or Ta_2O_5. Various core widths and thickness are available, core width is in the range of 25 - 500 μm m is available in rib and strip geometry and thickness is about 150 - 200 nm. Figire (b) is taken from [69].

2.2 gives a general overview of a waveguide-based microscopy setup in reflection geometry.

2.2 Waveguide chip preparation

The wafer is cleaved according to the user requirement to obtain chips . The chip may host various waveguides such as straight, four-arm, SIM chips etc. The cleaved wafers can have crooked edges. This can affect the coupling of light into the waveguide. Therefore, the waveguides are polished so that their edges are smooth. Polishing is done as follows. Silicon carbide papers are used to spin-polish the front facets of the chips, spinning speeds are typically set to 4000 rotations per minute on the machine. The choice of thickness of the grinding papers is decided after visual inspection of the facets of the chip under an optical microscope. For e.g., a typical chip is cleaved using a 5 μm sheet for 2 minutes, followed by a 1 μm for 1 minute and 0.5 μm for 3 minutes. The time and thickness of the sheets are decided after visual inspection, goal is to

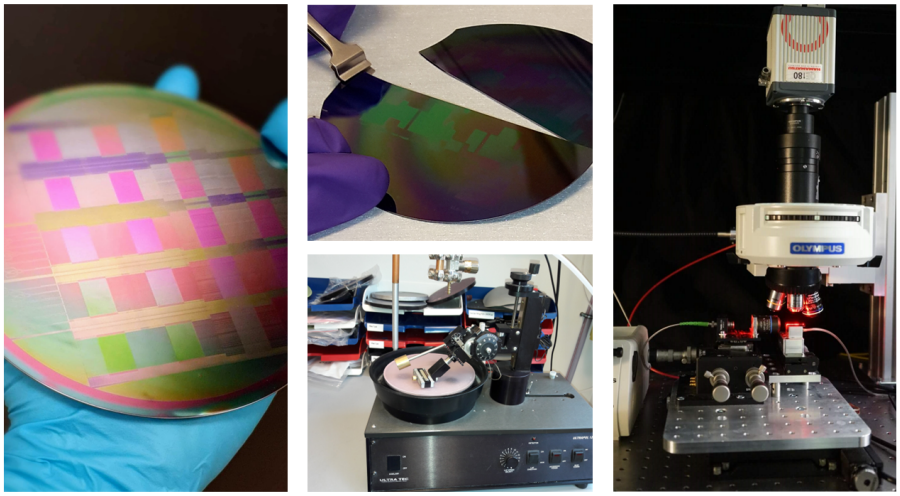

Figure 2.3: This figure shows some of the steps involved once wafers are recieved from the foundry. A wafer hosts several waveguide chips and is cleaved to the required shape. The cleaved wafer chips are then polished to achieve optimal coupling before being used for microscopy.

ensure a smooth coupling facet. After cleaving and polishing, the next step is to clean the chips so as to remove all the dirt on the chip which can adversely affect imaging. These steps are shown in Fig. 2.3.

The chips are completely immersed in 1% Hellmanex solution, which is heated on a hot place at 70° C for 10 minutes. To ensure a thorough cleaning, it is advisable to use cotton swabs to gently swipe the waveguide surface every few minutes. After 10 minutes, the chips are taken out of the hot bath and washed using distilled water, isopropanol and acetone. Compressed Nitrogen is used to dry the chips.

The biological samples are placed on top of the waveguide within a polydimethylsiloxance (PDMS) chamber. The desired thickness of the PDMS chamber is approximately 150 μm. This thickness is chosen so as to be compatible with the working distances of high NA objectives. It is prepared by mixing Sylgard 184 in a ratio of 10:1. The mixture is kept in a vacuum chamber for approximately 10 minutes to ensure no bubbles are present. The mixture weighing 1.7 grams is placed at the center of 100 mm $\times$ 15 mm sterilized petri-dishes. The dish is placed on a spin coater with the following settings: 20 seconds at 900 rpm and an acceleration of 75 rpm/s. After this, the petri-dishes are placed on a hot plate at 50° C for at least two hours. Curing is done and the PDMS can be cut into desired shapes and placed on top of the core-cladding interface of the waveguide.

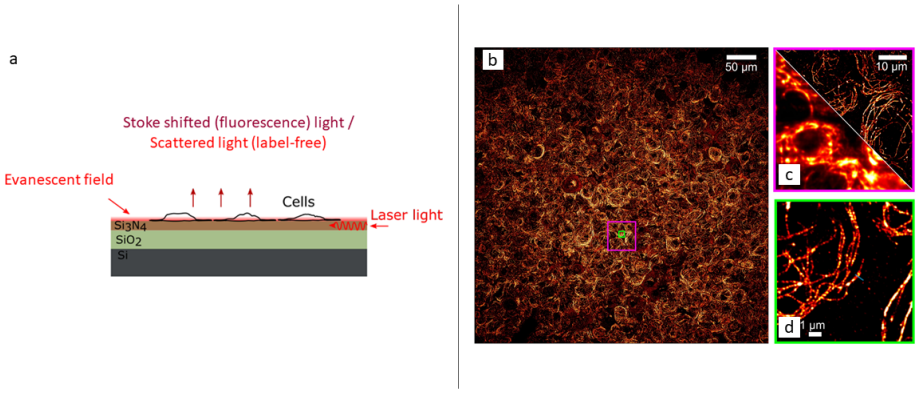

Figure 2.4: (a) Laser is coupled into a waveguide, whose core is made of Si_3N_4 on Silicon (Si) substrate with an additional buffer layer of SiO_2. To satisfy boundary conditions, the guided field generates an evanescent field that interacts with the biological cells placed on top of the core. The evanescent field excites fluorescent molecules in fluorescence microscopy or scatters off due to index-perturbations within the sample in label-free microscopy. The evanescently decaying nature of the fields ensures that only a thin section of the sample close to the core is imaged with high-contrast. (b) The illumination area is limited by the dimensions of the imaging area. This figure shows a large field-of-view super-resolved image of tubulin filaments in rat liver sinusoidal endothelial cells labeled with Alexa 647. Scale bar 50 μm. (c) Magnified image of the pink box shown in the large field-of-view. Both diffraction-limited and super-resolved images of the same region of interest are shown. Scale bar 10 μm. (d) Magnified super-resolved image of the green box shown in the large field-of-view image is provided, scale bar 1 μm. This figure is taken from [80].

2.3 Waveguides in microscopy

An obvious question would be why waveguides should be employed in microscopy, given the popularity of objective-based total internal reflection (TIRF) microscopy [79]. An immediate response would be that in waveguides, the imaging area is limited by the waveguide imaging area and not by the illumination objective, shown in Fig. 2.4(a). Such an imaging platform can be used to perform super-resolution imaging over large field-of-view, for e.g., 0.5 mm x 0.5 mm as demonstrated in [80]. This is shown in Fig. 2.4(b). Another response would be that the illumination profile in a waveguide is uniform over larger areas, as opposed to a Gaussian intensity distribution while employing a conventional TIRF objective lens. This is illustrated in Fig. 2.5. In addition, due to the decoupled illumination/detection scheme in waveguide-based microscopy, imaging of weakly scattering specimens can be performed with high-contrast. This is because the overwhelming illuminating light is cut-off, and only the scattered light off the sample reaches the camera. As a result, the same sample can be imaged with a higher-contrast as opposed to bright-field microscopy. Recently, these waveguide chips are compatible to perform super-resolution imaging us-

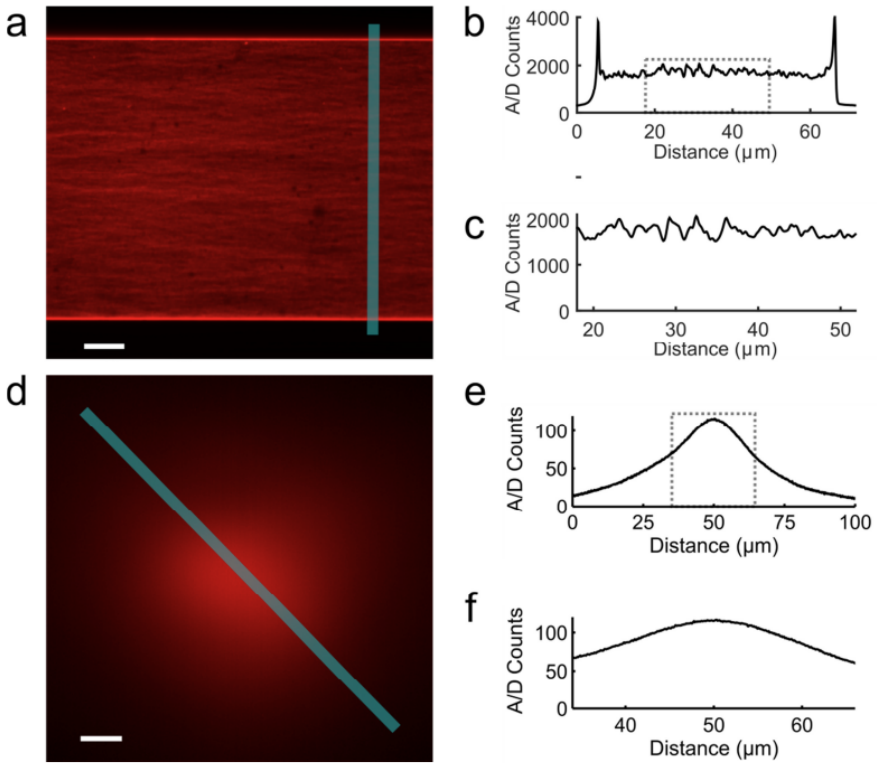

Figure 2.5: (a) Diffraction-limited image of homogeneity in waveguide illumination is provided. For this experiment, a waveguide surface is labeled with fluorescent dye. The diffraction-limited image is generated by taking an average of 200 frames, each frame is due to a different combination of modes overlapping within the same field of view which is achieved by scanning the piezo along the input facet of the waveguide. (b) Modulation in intensity along the bold line in the diffraction-limited image of the waveguide surface is shown by the line profile. (c) The modulation depth, ignoring the edges is shown and is $\approx$ 16 %. (d) Illumination beam profile of a ring-TIRF illumination on an OMX V4 Blaze System is shown. (e) The line profile of intensity variation along the bold line in the illumination beam profile is provided. (e, f) The illumination profile within which the modulation in intensity is $\approx$ 16 % is about 18 μm $\times$ 18 μm. Scale bar 10 μm. This figure is taken from [69].

ing a 3D printed microscope and a cellphone camera, thus providing a cheap solution [81]. All these have kindled an interest in waveguide-based microscopy systems.

Several works involving waveguide microscopy have spurted up over the last two decades. Both fluorescence [71, 73] and label-free microscopy [16, 52] have been demonstrated using waveguides. In addition, groups have experimented with different core materials as well: Si_3N_4 [52, 71, 72, 82], Ta_2O_5 [38, 77, 83], photoresist polymer layer [84], polymethylmethacrylate [73], fluorinated polymer [50], Aluminium oxide [49], Titanium dioxide [66], Gallium phosphide [65] etc. In this thesis, Si_3N_4 and Ta_2O_5 are used as the core material. The refractive index of these materials in the visible range is ≈ 2. The core-cladding interface at the imaging area has an index contrast of ≈ 0.6 since typically the sample to be imaged is immersed in water or glycerol. This larger index difference as compared to polymer waveguides as in [16], helps in a stronger decay of the evanescent field as discussed in Section 1.9. The higher core index helps generate smaller speckles or interference patterns. This property is utilized to perform super-resolution fluorescence imaging as shown in [38, 69, 70]. The higher index core also helps in high-resolution label-free imaging [51, 65, 66]. This is because the highly oblique illumination helps transmit higher spatial frequencies of the coherently scattering sample into the pass-band of the objective [52, 62, 68, 85]. Thus, both label-free and fluorescence-based super-resolution techniques have been demonstrated on the chip. In this thesis, Ta_2O_5 core waveguide is utilized for fluorescence-based super-resolution imaging, Si_3N_4 core waveguide for high-contrast label-free imaging and subsequently utilizing the Si_3N_4 core waveguide for label-free super-resolution microscopy. These works are detailed in the upcoming chapters: Chapter 3 focuses on waveguide-based super-resolution fluorescence microscopy, Chapter 4 focuses on waveguide-based high-contrast label-free microscopy and Chapter 5 details waveguide-based label-free super-resolution microscopy.

Chapter 3

Paper 1: Waveguide-based super-resolution fluorescence microscopy

On-chip TIRF nanoscopy by applying Haar wavelet kernel analysis on intensity fluctuations induced by chip illumination

Research question

Optical waveguides with a high-index contrast and large width, support multiple modes to guide power along its length. These modes can generate speckle-like interference patterns when they superimpose along the length of the waveguides. If these speckle patterns can be temporally varied, will the fluctuations in intensity so induced be compatible with intensity-fluctuation based algorithms like SOFI to circumvent the Abbe limit? This problem is addressed in the attached paper titled, ' On-chip TIRF nanoscopy by applying Haar wavelet kernel analysis on intensity fluctuations induced by chip illumination'.

Aim: The aim of this work is to circumvent Abbe's optical diffraction limit by resorting to waveguide-based fluorescence microscopy.

Method: For this, dielectric optical waveguide made of Tantalum Pentoxide, Ta_2O_5 with core refractive index $n_1 \approx 2$, is employed to illuminate the fluorescently labeled sample. Typically, wide waveguides are employed in bio-imaging applications. Such waveguides have a large V number, as discussed in Section 1.9. It implies that these waveguides support multiple modes to guide power along its length. These modes overlap as they propagate, and generate multi-mode interference (MMI) patterns. Therefore, in addition to the intrinsic photokinetics of the fluorescent molecules, in this work it is investigated if such MMI patterns can be employed to induce intensity-fluctuations that can be utilized by intensity-fluctuation based algorithms like SOFI to go beyond Abbe's diffraction-limit. [27].

Fixed PTk2 cells and fixed mercel cell carcinoma cells (MCC13) are imaged.

Tubulin structures in PTk2 and actin filaments in MCC13 are fluorescently labeled for imaging. These samples are placed on the core-cladding interface of a Ta_2O_5 waveguide inside a polydimethylsiloxane (PDMS) chamber of thickness ≈ 150 μm sealed with a cover slip. Continuous wave lasers (660 nm Cobolt Flamenco, 561 nm Cobolt Jive) are used to excite the modes in the waveguide. For PTk2 cells, imaging is performed at 660 nm excitation wavelength, and for MCC13 cells the waveguide is excited at 561 nm. The coupling objective, mounted on a piezo-stage, is oscillated along the input facet of the waveguide. This will excite different modes in the waveguide with different amplitudes. These modes overlap to generate MMI patterns, as shown in Fig. 5 of the attached paper. Now, as the piezo stage is oscillated, different MMI patterns will be generated, which will induce intensity variations at the sample plane, illustrated schematically in Fig. 3.1. The fluorescent molecules emit a Stoke shifted light in proportion to the illumination intensity. At each scan location of the piezo, using spectral filters, only the Stoke shifted light is acquired by a sCMOS camera. Therefore, an image stack exhibiting fluctuations in intensity is generated by oscillating the coupling objective along the input facet of the waveguide. This image stack is used to generate the final super-resolved image.

Observations and Solution: The acquired fluorescent images were initially given as input to SOFI. Though the averaged diffraction-limited image was devoid of any illumination artifacts, the reconstructed super-resolved SOFI image showed artifacts, which is a consequence of the non-uniform illumination arising due to the MMI patterns. Therefore, the initial observation was that these MMI patterns are not suited for resolution gain when applied in tandem with SOFI. Hence, the next task was to understand if this induced correlation arising out of MMI patterns can be avoided.

The schematic of the proposed solution is shown in Fig. 3.1. The idea is to introduce spatio-temporal sparsity by pre-processing the diffraction-limited image stack using a pre-processing method called Haar Wavelet Kernel (HAWK) [86]. SOFI relies on incoherence in emission between different fluorescent molecules to go beyond the diffraction-limit, as explained in Section 1.10. However, in waveguide microscopy, when the fluorescent molecules are illuminated by the MMI patterns of the straight waveguide, it can induce correlation in emission between the molecules. As a result, SOFI fails to resolve regions with high mutual correlation and can thus lead to artifacts in the final image. HAWK pre-processing helps mitigate this issue by generating a sparse image stack with more number of frames than the input via temporal band-pass filtering, thus aiding in reducing the correlation in emission by the MMI patterns. This is elaborated in Supplementary section S1 - S3 in the attached manuscript.

Results: HAWK pre-processing helps to introduce sparsity in the diffraction-limited image stack. This data stack when used as input for SOFI generated an image with reduced artifacts as well as resolution enhancement. This is shown in Fig. 3.2.

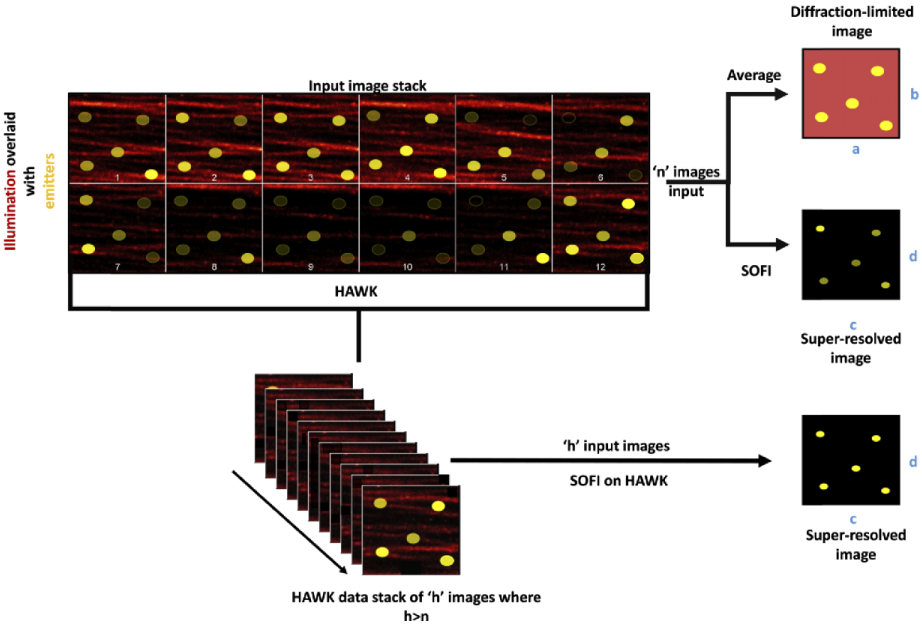

Figure 3.1: Schematic of the proposed solution: Fluorescent emitters shown in yellow are illuminated by the MMI patterns of a highly multi-moded waveguide. The coupling objective is oscillated along the input facet of the waveguide to generate different MMI patterns that will induce intensity-fluctuations in the fluorescent emitters in addition to their intrinsic photokinetics. The data stack of 'n' images with dimensions 'a x b ' pixels, is processed using SOFI which gives rise to artifact-ridden super-resolved image with dimensions 'c x d '. To alleviate this issue, the data stack is pre-processed using HAWK. HAWK helps generate a spare data set of 'h' images with '$h > n$', which is given as input to SOFI. This helps alleviate the artefacts in the super-resolved image arising due to the non-uniform illumination pattern. This figure is taken from [38].

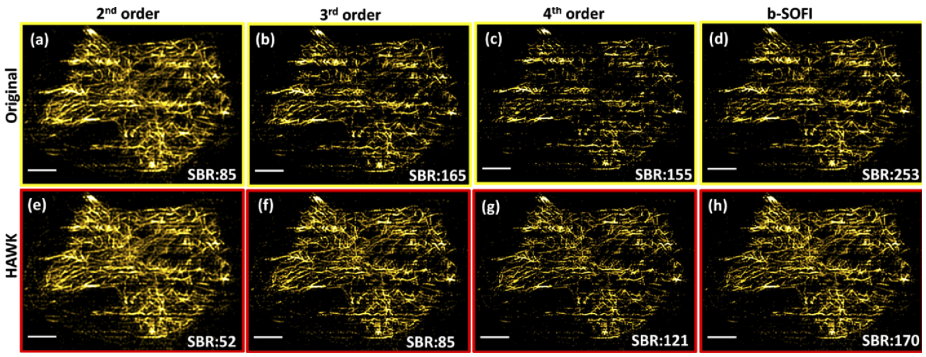

Figure 3.2: Super-resolved chip-based SOFI imaging, orders 2 to 4, of tubulin filaments in PTk2 cells is shown. (a-d) The yellow outline indicates SOFI reconstructions of diffraction-limited image stacks without any HAWK processing. Here the artifacts due to MMI patterns is clearly visble. (e-h) The red outline indicates SOFI reconstructions of diffraction-limited image stacks with HAWK processing. HAWK pre-processing prior to the application of SOFI helps to alleviate the issue of artifacts arising due to non-uniform illumination of the MMI patterns. This figure is taken from [38].

Conclusion and future outlook: It has been demonstrated that the MMI patterns in multi-moded waveguides can be used to induce intensity-fluctuations, which can then be utilized by SOFI to achieve super-resolution. The advantage of using chip-based Total Internal Reflection Fluorescence (TIRF) as opposed to conventional TIRF is the generation of images with large field-of-view [69]. However, non-uniform illumination of the MMI patterns can induce artifacts in the reconstructed image. This can be alleviated by a pre-processing algorithm called HAWK, available as a Fiji plugin. The HAWK processed images when used as input to SOFI, helped generated super-resolved images with reduced artifacts and improved resolution.

This pilot project provides a solution to minimize artefacts arising out of correlation in illumination. The solution helps chip-based imaging platforms to be used in tandem with intensity-fluctuation techniques like SOFI, i.e., generate super-resolved images over a large field-of-view with a few hundred images. However, the drawback is that HAWK pre-processing generates an image stack larger than the input dataset. Therefore, processing such a large dataset using SOFI is a computationally intensive task. Another solution to minimize artefacts arising due to correlation in illumination is by using special waveguide geometries like four-arm crossing waveguide. This is explored in Chapters 4 and 5, and the artefacts in super-resolved images arising due to MMI patterns in straight waveguides are shown to be minimized by employing four-arm crossing waveguides and algorithms like SACD [32]. In addition, a simulation analysis is provided to study the influence of MMI patterns on SOFI reconstruction, Supplementary Fig. (3 - 6) in the attached paper in Chapter 5.

Author contribution: NJ carried out the research study and prepared the manuscript. OIH provided the experimental data used for the analysis. KA initiated and supervised the study. BSA supervised and funded the project. All authors commented on the manuscript.

Research Article | Vol. 28, No. 24 / 23 November 2020 / Optics Express 35454
Optics EXPRESS

On-chip TIRF nanoscopy by applying Haar wavelet kernel analysis on intensity fluctuations induced by chip illumination

NIKHIL JAYAKUMAR,[1,3] ØYSTEIN I. HELLE,[1] KRISHNA AGARWAL,[1] AND BALPREET SINGH AHLUWALIA[1,2,4]

[1]Department of Physics and Technology, UiT The Arctic University of Norway, Tromsø 9037, Norway
[2]Department of Physics, Indian Institute of Technology Delhi, Hauz Khas, New Delhi 110016, India
[3]nik.jay.hil@gmail.com
[4]balpreet.singh.ahluwalia@uit.no

Abstract: Photonic-chip based TIRF illumination has been used to demonstrate several on-chip optical nanoscopy methods. The sample is illuminated by the evanescent field generated by the electromagnetic wave modes guided inside the optical waveguide. In addition to the photokinetics of the fluorophores, the waveguide modes can be further exploited for introducing controlled intensity fluctuations for exploitation by techniques such as super-resolution optical fluctuation imaging (SOFI). However, the problem of non-uniform illumination pattern generated by the modes contribute to artifacts in the reconstructed image. To alleviate this problem, we propose to perform Haar wavelet kernel (HAWK) analysis on the original image stack prior to the application of (SOFI). HAWK produces a computational image stack with higher spatio-temporal sparsity than the original stack. In the case of multimoded non-uniform illumination patterns, HAWK processing breaks the mode pattern while introducing spatio-temporal sparsity, thereby differentially affecting the non-uniformity of the illumination. Consequently, this assists nanoscopy methods such as SOFI to better support super-resolution, which is otherwise compromised due to spatial correlation of the mode patterns in the raw image. Furthermore, applying HAWK prior to SOFI alleviates the problem of artifacts due to non-uniform illumination without degrading temporal resolution. Our experimental results demonstrate resolution enhancement as well as reduction in artifacts through the combination of HAWK and SOFI.

1. Introduction

In far-field optical microscopy, the diffraction of light limits the ability of the system to image two adjacent point sources distinctly to $\backsim$ 200 nm. This is referred to as the resolution limit of the optical system. The theoretical resolution limit of an optical microscope is approximately $\frac{\lambda}{2NA}$, where λ is the wavelength of fluorescent emission and NA is the numerical aperture of the optical system. A lot of features and physiological processes of interest lie below this resolution limit and hence, medical solutions to real-world problems require a resolution beyond this barrier. Different imaging methodologies such as near-field scanning methods [1,2] and electron microscope (EM) [3,4] supports much better resolution. Near-field methods are challenging as it requires bringing the probe close to the target and EM are incompatible with live cell imaging applications. Therefore, the invention of fluorescence based far-field super-resolution optical microscopy, commonly referred to as optical nanoscopy has gained popularity during the last two decades. Fluorescence microscopy methods are live cell compatible and allows selective imaging of cellular components via molecule-specific labeling in both fixed and living samples. High specificity, live-sample compatibility and visualization of structures below the resolution limit make fluorescence based optical nanoscopy popular among biologists [5].

For applications where high contrast imaging close to the membrane surface is required with reduced photo-toxicity and excellent optical sectioning, total internal reflection fluorescence

#403804 https://doi.org/10.1364/OE.403804
Journal © 2020 Received 27 Jul 2020; revised 10 Oct 2020; accepted 11 Oct 2020; published 9 Nov 2020

Optics EXPRESS

(TIRF) microscopy is employed [6]. Conventionally, a high numerical aperture (N.A.) and a high magnification TIRF lens is used in TIRF microscopy, which limits the field of view (FoV). Recently, it was demonstrated that photonic-chip based TIRF microscopy enables TIRF imaging over large FoV and supports scalable resolution and FoV [7]. Furthermore, it was demonstrated that waveguide platforms fabricated using high refractive index contrast (HIC) materials are attractive as it can generate high intensity in the evanescent field [8]. The core of the optical waveguide is made of a high-refractive index material, with a top and a bottom cladding layer of lower refractive index material, and guides visible light due to total-internal reflection (TIR) at the core-cladding interface. The TIR of light at the core-cladding interface is accompanied with the generation of an evanescent field that exponentially decays in the cladding region. The limited penetration depth of the evanescent field from the core-cladding interface helps prevent out-of-focus light when harnessed for fluorescence excitation of a specimen lying on the chip surface. As a result, several imaging methods have been implemented using waveguide platforms over the past few years – direct stochastic optical reconstruction microscopy (*d*STORM) [7,9], resonance Raman spectroscopy [10], points accumulation in nanoscale topography (PAINT) [11], Fourier ptychography [12], beam shaping and steering in free space [13] etc. For bio-imaging applications, wide waveguides (50-500 μm) are used and the field of view is limited by the imaging microscope objective. Such waveguides support multiple optical electromagnetic wave modes, where each mode represents an eigen solution of the wave propagation equation for the waveguide. These multiple modes can superimpose leading to multimode interference (MMI) in the waveguide core. This results in a non-homogenous evanescent field intensity distribution leading to uneven excitation of fluorescently labeled biological samples placed on top of the waveguide. However, by taking an average of several images, each image taken under a different combination of modes, a reduced modulation in intensity across the imaging area is obtained [14]. The different combination of modes can be generated by scanning the incident light spot on the input facet of the waveguide. However, the scanning process deteriorates the temporal resolution. Single mode waveguides can alleviate the problems caused by MMI, but due to the narrow width needed to excite the single mode, a long adiabatic taper would be needed to expand the mode for very wide waveguides (e.g. 500 μm). Using the adiabatic taper approach, the cross-section of the structure is gradually changed along the propagation direction of the light such that coupling of energy from the lower order mode into higher order modes is inhibited [15]. However, it poses challenges such as shadowing effects which are difficult to avoid [16]. These shadowing effects manifest as dark bands parallel to the direction of propagation of light and arise mainly due to strong localized scattering from the waveguide surface. The scattering could also arise due to material impurities or refractive index variations of the sample or in the waveguide itself. In this aspect, multiple mode illumination is advantageous as each mode illuminates any local region in the sample from different directions and reduces the shadowing effect.

Many studies nowadays revolve around the development and usage of intensity fluctuation-based algorithms which can improve spatial resolution over optical resolution limited fluorescence microscopy and temporal resolution over single molecule localizations methods. The spatio-temporal sparsity required by single molecule localization (SML) techniques [17,18] for a reliable reconstruction demands large number of images and high laser power [5]. On the other hand, intensity fluctuation-based algorithms overcome these constraints but at the cost of relatively poorer spatial resolution than SML. Super-resolution optical fluctuation imaging (SOFI) [19], multiple signal classification algorithm (MUSICAL) [20], super-resolution radial fluctuations (SRRF) [21], entropy based super-resolution imaging (ESI) [22], sparsity based super-resolution correlation microscopy (SPARCOM) [23], Bayesian analysis of blinking and bleaching (3B) [24] can help generate super-resolved images using image stacks acquired from standard optical microscopes by using conventional fluorophores and nominal laser powers. These algorithms resort to higher order statistical analysis of intensity fluctuations from an emitter, a fluorophore molecule, as a function of time to generate super-resolved images.

Optics EXPRESS

In this article, we investigate the usage of one of the intensity fluctuation algorithms, namely SOFI, on waveguides to generate super-resolved images. In waveguide TIRF imaging, the intensity values recorded by a camera are the product of fluorophore distribution and the MMI pattern of the evanescent field. The fluctuations arise due to the intrinsic photokinetics of the fluorescent molecule and temporally varying non-uniform MMI pattern. These fluctuations which manifest as a change in intensity value at a particular pixel of a camera, can be localized to within subpixel precisions computationally using algorithms such as SOFI. However, it is observed that even though the average diffraction-limited image shows insignificant evidence of these MMI patterns, SOFI reconstructions provide prominent evidence of the non-uniform illumination, thereby hindering a reliable reconstruction. To alleviate this problem we investigate the usage of Haar wavelet kernel analysis (HAWK) [25] prior to applying SOFI. HAWK is a preprocessing algorithm that helps generate spatio-temporal sparse data sets via temporal band-pass filtering of the original data set. This helps in breaking the correlation in illumination pattern arising out of the MMI patterns. Supplement 1 gives insights into the relationship between the transform levels of HAWK and temporal frequency of emitters. Thus, a detailed experimental and mathematical analysis is illustrated in this article to generate chip based TIRF super-resolved images with minimized artifacts at high temporal resolution.

2. Methods

2.1. Experimental setup

In the chip-based microscope used in this paper, the core of the waveguide is made of a high refractive index (n) material, Tantalum pentoxide with n=2.1. Total internal reflection at the low refractive index boundary results in a 100-150 nm deep evanescent wave that exponentially decays away from the waveguide surface [7]. A CW laser (660 nm Cobolt Flamenco, 561 nm Cobolt Jive) coupled to a single mode fiber is focused on the waveguide input face using a fiber-collimator and a microscope objective lens (Olympus LMPlanFL N, 50X/0.5 NA), allowing for end-facet coupling of light on the planar waveguide structure. The in-coupling optics are mounted on a piezo-electric XYZ translation stage. Using the high precision piezoelectric translation stage, the coupling optics can be shifted transversally along the waveguide input facet as shown by the blue arrows in Fig. 1(a), causing a spatial re-distribution of the guided modes. By shifting the MMI patterns in time, darker regions can also be illuminated and an average intensity distribution with reduced modulations across the entire waveguide area can be achieved. The fluorescently labeled sample is placed on top of the waveguide chip and excited via the evanescent field. The emitted Stoke shifted light from regions tagged by the fluorescent molecules is collected by an upright microscope fitted with emission filters and a sCMOS camera (Hamamatsu C11440-42U30). The experimental setup and waveguide TIRF concept are shown in Fig. 1(a) and 1(b).

2.2. Imaging configurations

The experimental results on chip-based intensity fluctuation imaging of tubulin in fixed PTk2 cells and actin in fixed merkel cell carcinoma cells (MCC13) are provided in this article. An image sequence of 300 frames for PTk2 cells and 500 frames for MCC13 cells is used as the input for the reconstruction algorithms. For PTk2 imaging, the waveguide is excited at 660 nm vacuum wavelength and images are acquired with an exposure time of 30 ms using an Olympus UPlanSApo 60X/1.2 NA water immersion objective referred to as the imaging objective. For MCC13 cells, the waveguide is excited using the 561 nm laser and images are acquired with an exposure time of 30 ms. The cells and aqueous imaging buffer are placed on top of the waveguide inside a polydimethylsiloxane (PDMS) chamber of $\backsim$ 150 μm thickness. The chamber is sealed with a # 1.5 thickness coverslip and imaged using the imaging objective from top as shown in Fig. 1(b).

Optics EXPRESS

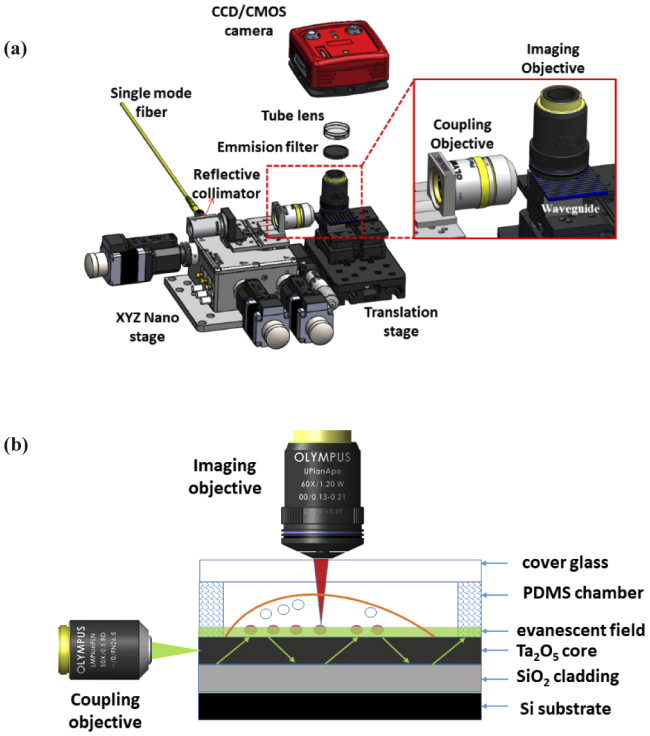

Fig. 1. Schematic diagram of chip-based imaging setup and waveguide TIRF concept. (a) Schematic diagram of waveguide based TIRF imaging is presented here. (b) A microscope objective (50X/0.5NA), referred to as coupling objective, is used to focus light into the core of a waveguide. The light is guided along the length of the waveguide via total internal reflection, shown using the green arrows. The fluorescently labeled sample to be imaged is placed on the top of the waveguide core. The evanescent field generated along the surface of the core as a consequence of total internal reflection illuminates a thin section of the sample in contact with the surface via the evanescent field. Only the fluorescent molecules (shown in red) in contact with the evanescent field are excited. The red shifted light emitted by the fluorescent molecules are collected by a collection objective. Waveguide TIRF approach dissociates the excitation and detection paths enabling scalable field-of-view.

2.3. SOFI and HAWK in the context of chip-based imaging

Conventionally, the photokinetics of fluorescent molecules are exploited by fluctuation based algorithms for the generation of super-resolved images. Photokinetics in fluorescent molecules may arise due to blinking of the molecules as exploited in SML techniques or due to intrinsic spontaneous emission of molecules of the fluorescently labeled sample. As a consequence of photokinetics, the number of photons emitted by a fluorescent molecule in a given time duration is given by a probability density function, rather than a constant number, and manifests as changes in intensity values over time. The concept of photo kinetics in fluorescent molecules is depicted in Fig. 2. In waveguide TIRF experiments, the fluctuations necessary to apply intensity fluctuation based algorithms arise from the intrinsic photokinetics of the molecules as well due to the external oscillating illumination scheme employed. A better insight may also be obtained via the experiments presented in Supplement 1, see sections S2 and S3 and Fig. (S1-S3).

The photokinetics of the fluorescent molecules should scale with the excitation intensity. The excitation intensities used for the experiments presented in this manuscript fall into sufficiently

Optics EXPRESS

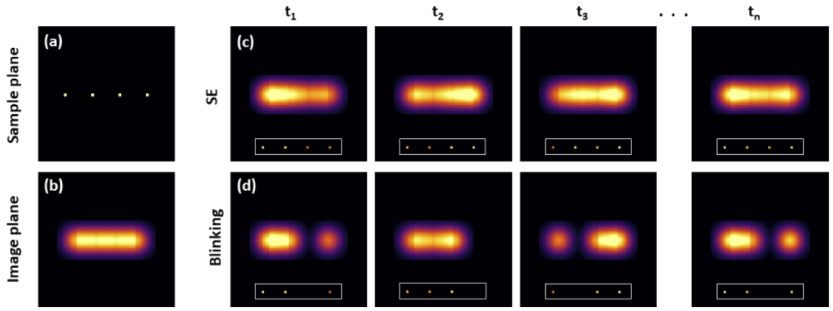

Fig. 2. Photokinetics panel. The different frames represents the images of four fluorophores recorded by the camera, generated due to convolution of the system PSF with the fluorophore shape in the sample plane. (a) Four emitters in the sample plane. (b) Image of the four emitters formed on the camera. The different frames acquired by the camera at different times $t_1, t_2 \ldots t_n$ are shown, where the time intervals are in the order of 10^{-3} s. The absorption of light by the fluorescent molecules takes place in the order of 10^{-12} to 10^{-15} s. The excited molecules may then relax to the ground state via radiative or a non-radiative transfer. The fluctuations necessary for generating super-resolved images may arise due to the following: (c) Spontaneous emission which is the intrinsic intermittent emission of the fluorophores, (d) blinking (on/off) of the fluorophores. The insets, not drawn to scale, in (c-d) show the corresponding intensity distribution of the four emitters in the sample plane.

low regime so as not to induce long dark states. The typical intensities needed to induce strong blinking in molecules like that required in *d*STORM is about 1-10kWcm^{-2} [7]. For the experiments presented in this manuscript, the intensity levels were not quantified but were sufficiently low as photobleaching did not happen even after recording 600 frames and the excitation intensity was maintained a constant at the input facet of the waveguide. As mentioned in Supplementary Table 1 of Ref. [7], the intensities with which diffraction limited images are acquired are typically of the order of 0.01kW/ cm^{-2}. Therefore, it can be safely assumed that the excitation intensities fall within this range.

A second order auto-correlation function may be expressed as shown in Eqn. (1) [19,26]

$$G_2(\boldsymbol{r},\ \zeta) = \sum_{i,j=1}^{N} PSF(\boldsymbol{r}-\boldsymbol{r}_i)\cdot PSF(\boldsymbol{r}-\boldsymbol{r}_j)\cdot \varepsilon_i \cdot \varepsilon_j \cdot \langle \delta s_i(t+\zeta)\delta s_j(t)\rangle_t \tag{1}$$

where N is the number of emitters, PSF($\mathbf{r}$) is the point spread function of the system, $\boldsymbol{\varepsilon}_{i,j}$ is the constant brightness of the ith and jth fluorescent molecules, $s_{i,j}(t)$ is the time-dependent fluctuation of these molecules, $\delta s_{i,j}$ quantifies the fluctuations over zero-mean and $\langle \cdots \rangle_t$ represents time averaging. If there is no correlation between the different emitters the above auto correlation function can be simplified to a 2nd order auto-cumulant function (n=2), see Eq. (2), and the pixel values in a SOFI image correspond to the cumulant values of the intensity distribution.

$$G_2(\boldsymbol{r},\ \zeta) = \sum_{i=1}^{N} PSF^2(\boldsymbol{r}-\boldsymbol{r}_i)\cdot \varepsilon_i^2 \cdot \langle \delta s_i(t)\delta s_i(t+\zeta)\rangle_t \tag{2}$$

Equation (2) may be understood as pixel values in a SOFI image depending on the weighting terms ε_i^2 and $\langle \delta s_i(t)\delta s_i(t+\zeta)\rangle_t$. It implies that a SOFI image communicates about brightness and degree of correlation of temporal fluctuations in photon emissions from an emitter. A higher degree of fluctuation will yield a higher weighting factor and will be better visible in the SOFI reconstruction. This also implies that emitters with weaker weighting factors may get masked in the presence of brighter emitters. In the conventional application of SOFI, the resolution gain is achieved by assuming that a single emitter is spatio-temporally correlated with only itself. If the emission between the different emitters are mutually independent, then Eq. (2) can be

Optics EXPRESS

invoked which leads to squaring of the PSF that will ensure super-resolution unlike the correlation function described by Eq. (1). Higher order cumulants may be employed to further enhance the resolution. A variation of SOFI, namely b-SOFI (balanced-SOFI) [27], may be utilized to avoid the masking of weaker emitters, which linearizes the brightness to provide good contrast images without the weak emitters getting masked [22]. The SOFI reconstructions in this article are carried out using the MATLAB code, © 2012 Marcel Leutenegger et al., École Polytechnique Fédérale de Lausanne, under the GNU General Public License. In this article 2^{nd}, 3^{rd}, 4^{th} order and b-SOFI reconstructions are performed for one dataset for comparing their performances. Otherwise, generally b-SOFI is used for other experiments. The different orders of the SOFI reconstructions correspond to the different orders of the cumulants employed by the algorithm.

Using the waveguide platform for imaging, the fluorescent molecule fluctuations are controlled by the evanescent field distribution in each frame as shown in Fig. 3. In each frame, the fluorescence is proportional to the excitation light intensity it receives as a consequence of the MMI pattern. The non-uniformity in illumination leads to correlation between the different fluorophores. This evanescent field illumination of fluorophores is analogous to random speckle illumination used in [28]. It implies that the assumption of no cross-correlation between different fluorophores as mentioned in [19] is violated. The non-uniform illumination induces correlation between the different fluorophores. This correlation between the emitters due to MMI patterns will modify the pixel values in the SOFI image according to Eq. (1). Therefore, the resolution

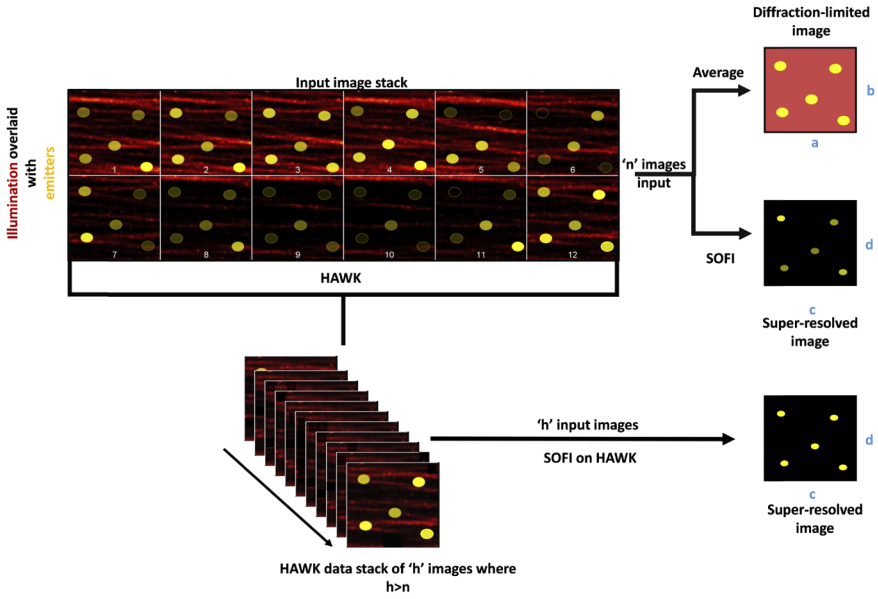

Fig. 3. Schematic representation of chip-based intensity fluctuation analysis. The fluctuations arising from the MMI pattern and the intrinsic fluctuation (SE) of the molecules are recorded in an image stack containing 'n' frames, with each frame of (a × b) pixels. The image stack of 'n' frames is duplicated and also preprocessed using HAWK. SOFI operates on both the original and HAWK data stack of diffraction-limited images to produce a super resolved image of (c × d) pixels where c > a and d > b. The non-uniform illumination leads to artifact generation in the super-resolved images generated using SOFI. These artifacts can be minimized by preprocessing the image stack with HAWK before applying SOFI. A detailed insight about the influence of HAWK on emitters exhibiting different temporal frequencies is presented in the supplementary sections S1 and S2.

Optics EXPRESS

enhancement achieved using SOFI on images acquired using a waveguide platform is analogous to resolution gain as in S-SOFI [28] after invoking contribution of the cross-correlation terms.

HAWK (Haar wavelet kernel) analysis is a pre-processing algorithm that helps introduce computational sparsity into the original image stack via Haar wavelet transform (HWT). The intensity trace of a particular pixel over 'n' frames of the unprocessed image stack is expressed as a column vector A(t). Its transform intensity trace B(t') is synthesized as $B(t') = H \cdot A(t)$, where H is the Haar matrix. Then a filter of level m is applied to B(t'), where m denotes the level of the Haar wavelet transform. This is achieved by setting to zero all the elements of B(t') that do not belong to that particular level m of the Haar matrix. The filtered pixel intensity trace is obtained via the inverse HWT and is given by $C^m(t) = H^T \cdot B^m(t')$, where the inverse HWT is given by $H^{-1} = H^T$. Then a cropping procedure is applied as detailed in Ref. [25]. This process of transform-filter-inverse transform is performed on all the pixels of the image for the desired number of filter levels and the resulting image sequences are appended together to produce the Haar transformed data set. A comparison on the influence of different filter levels on SOFI reconstructions is explained in Supplement 1 section S4 and Fig. S4. The application of filter levels and cropping procedure introduces zeros into the pixel intensity trace. In the case of chip-based imaging, this process helps to break correlation arising out of the non-uniform illumination. The breaking of correlation computationally leads to reduced pixel values in the SOFI image, thereby preventing masking of weaker emitters. The detailed theory describing the HAWK method can be found in [25] and in the supplementary section S1. For all the experiments described in this article, the option ''Separate'' was selected in the Fiji plugin for HAWK processing and filter level $m = 3$ was used. This option separates positive and negative values into two stacks and redresses the negative values to positive before appending them together. A comparison between SOFI reconstructions on HAWK data stack after using the two different options ''Separate'' and ''Absolute'' is also provided in the supplementary section in Fig. S5.

3. Results and discussion

3.1. HAWK helps break correlation and reduce average value of intensity trace per pixel

An analogy between MMI in waveguides and speckle formation in free space optics is drawn. The high coherence of laser light gives rise to speckle phenomena and one of the methods of suppressing the speckle contrast is to image through a rotating diffuser [29]. The laser light is incident on a diffuser and light coming out of the diffuser is imaged on a camera. In this experiment, a diffuser is rotated sequentially from 1° to 360° in steps of 1° and an image of the speckle pattern is acquired after each 1° rotation. To illustrate the applicability of HAWK technique in reducing the overall average intensity value of the speckles, the original and HAWK data stacks are averaged in intensity as shown in Fig. 4(b1-b2). Then the average value per column, i.e., along y-axis in Fig. 4, of the so obtained averaged images of size (432 × 432) pixels is calculated and is plotted in Fig. 4(c1) respectively. It can be seen from Fig. 4(c1) that through the introduction of HAWK the averaged image has a lower intensity value per pixel.

In waveguides, through the introduction of temporal sparsity HAWK helps to break the correlation arising out of MMI illumination. As can be seen from Fig. 4(c1) the average value per pixel is also reduced after the application of HAWK. This aids SOFI in reconstructing emitters exhibiting weaker fluctuations in the original data stack. However, this may reduce the signal-to-background ratio of the final reconstructed image. To study the influence of HAWK on breaking correlation in illumination, the MMI patterns of a waveguide are imaged. For this analysis, a 200 μm Tantalum pentoxide (Ta_2O_5) waveguide is coated with Alexa Fluor 647. A stack of 40 images is recorded. Each image is acquired with an exposure time of 30 ms as the coupling objective oscillates along the input facet of the waveguide while still maintaining coupling as described in Fig. 3. The image stack so acquired is duplicated into two. One stack is

Optics EXPRESS

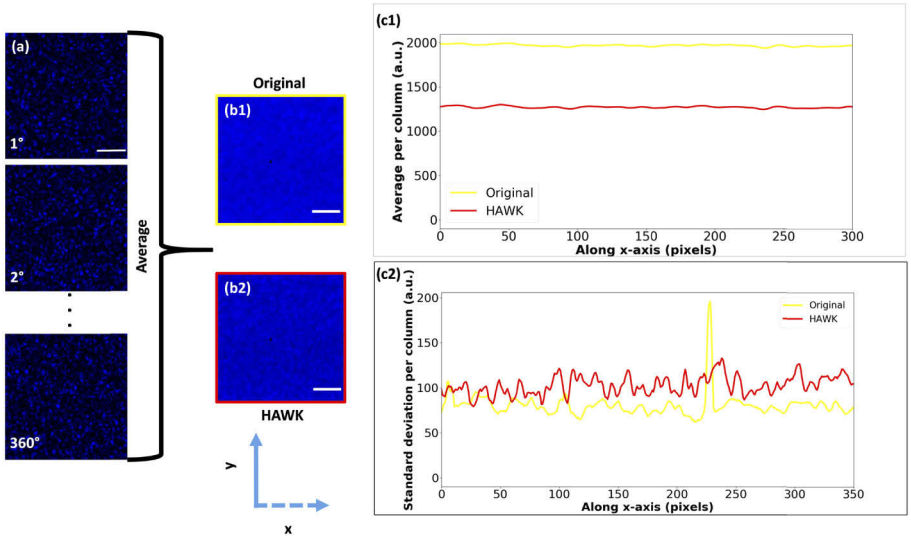

Fig. 4. (a) The images of the speckles recorded after each 1° rotation of the diffuser is shown. A total of 360 images, of size 432 × 432, pixels are recorded corresponding to 360° rotation of the diffuser. (b1) Average intensity image of the original data stack and (b2) average intensity image of the HAWK data stack. (c1) Average value per column of the averaged original and HAWK data stacks. (c2) Standard deviation per column of the averaged original and HAWK data stacks. The dotted x-axis indicates the direction along the length of the waveguide and y-axis indicates the direction along the columns of the image. Scale bar 8 μm.

averaged in intensity using Fiji. The other stack is pre-processed using HAWK at level 3 and then averaged in intensity. Figure 5(a) represents an image stack of 40 frames acquired by oscillating the coupling objective. Figure 5(b1-b2) represents average images of the original and HAWK data stack respectively. The average value and standard deviation of each column of the original and HAWK intensity-averaged images shown in Fig. 5(b1-b2) are calculated and shown in the plots Fig. 5(c1-c2) respectively. The yellow and red vertical arrows in Fig. 5(b1-b2) indicate the direction, i.e. along the columns of the image, in which average and standard deviation of the averaged image are calculated for original and HAWK data set respectively. The dotted arrows indicate the direction along the length of the waveguide. Similar to Fig. 4(c1), it can be seen that through the introduction of HAWK the averaged image has a lower intensity value per pixel for waveguide illumination as shown in Fig. 5(c1). The reduction in the standard deviation along the columns as depicted in Fig. 5(c2) signifies a more uniform illumination.

3.2. *Chip based TIRF imaging*

Tubulin filaments in PTk2 cells labeled using Alexa Fluor 647 is imaged in waveguide TIRF mode. The coupling objective, mounted on a piezo stage as shown in Fig. 1., is oscillated while sustaining coupling. A stack of 300 images is acquired at 30 ms per frame using a sCMOS camera.

An average diffraction-limited TIRF image is generated from the initial image stack of 300 frames. This is shown in Fig. 6(a). HAWK introduces artificial temporal sparsity and helps in depopulating densely packed regions, for example the green box shown in Fig. 6(a). The effect of HAWK in depopulating densely packed regions is explained experimentally in section S3 of Supplement 1. The initial data stack of 300 frames is used to generate a HAWK level 3 data set of 1778 frames. Since SOFI relies on fluctuations for super-resolution, it is imperative to quantify the strength of the fluctuations. The standard deviation over the data stack at a particular

Optics EXPRESS

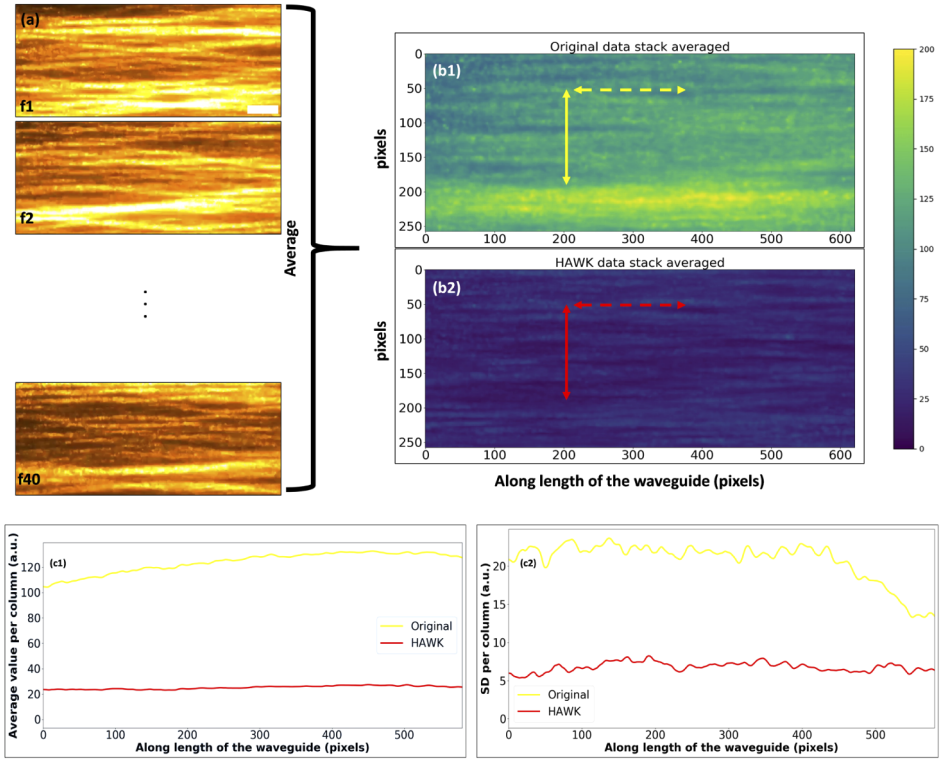

Fig. 5. (a) Image stack of 40 frames acquired by oscillating the coupling objective. (b1) Average image of the original data stack, (b2) average image of the HAWK data stack. The vertical complete arrows indicate the direction of the columns and dotted horizontal arrows indicate the direction of rows,i.e., along the length of the waveguide. (c1) Average value and (c2) standard deviation (SD) of the columns of the original and HAWK averaged images. Scale bar 8 μm.

pixel gives a measure of the strength of the fluctuations at that particular pixel. If a pixel hosts an emitter it shows fluctuations over time which are recorded in the image stack. Therefore, to quantify the strength of the fluctuations, the ratio of standard deviation to average for each pixel is computed over all the frames. This is done for both the initial data stack of 300 frames and HAWK data of 1778 frames and is shown in Fig. 6(d) and Fig. 6(e) respectively, and is referred to as fluctuation map in this article.

It can be seen from Fig. 6(b) that b-SOFI masks the weaker emitters due to the uneven illumination. But HAWK helps in preventing this masking of weaker emitters by breaking the correlation through the introduction of temporal sparsity. The effect is evident in b-SOFI reconstruction of the HAWK data set shown in Fig. 6(c). This can be understood from the fluctuation maps shown in Fig. 6(d-e). The fluctuation map of the original data stack shows the presence of very strong fluctuations from certain emitters. Even when b-SOFI is applied on such a data stack it leads to masking of the weaker emitters, i.e. emitters lying in the dark region of the MMI patterns over a longer course of time. However, the fluctuation map of the HAWK data stack reveals that by breaking the correlation between successive frames, HAWK decreases the average value. After the application of HAWK, the pixels will have a reduced value and an increase in the ratio of standard deviation to mean. An increase in standard deviation over mean means an increase in fluctuation in intensity in each pixel and from Eq. 2. it is known that the pixel value of a SOFI image depends on fluctuations over mean. As a result, a pixel hosting an emitter will show more fluctuations and consequently more intensity in the SOFI reconstructed

Optics EXPRESS

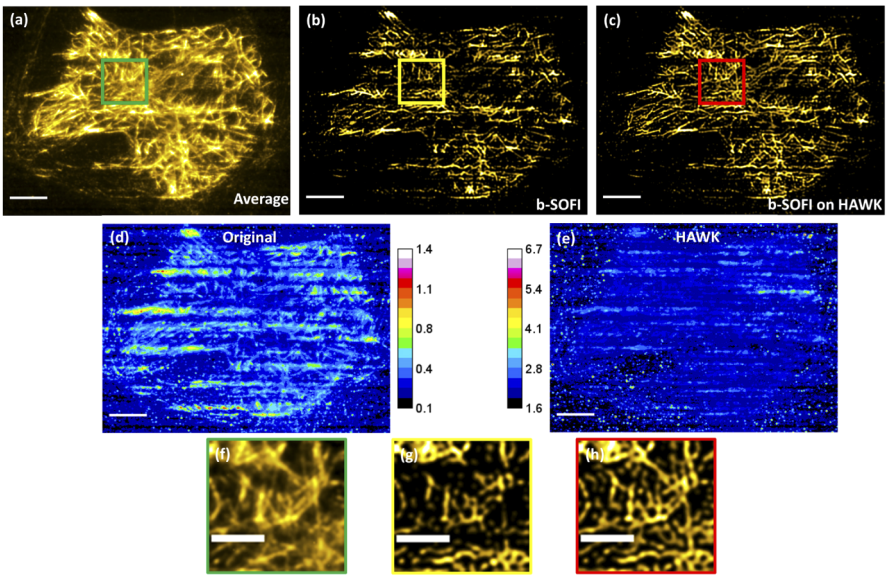

Fig. 6. Chip based TIRF images of tubulin in PTk2 cells. (a) Diffraction-limited TIRF image of tubulin in PTk2 cells generated by averaging an image stack of 300 frames. (b) b-SOFI reconstruction of original data stack (c) b-SOFI reconstruction of HAWK data stack. Ratio of standard deviation to average plot of (d) original data stack of 300 frames and (e) HAWK level 3 data stack of 1778 frames. The calibration bar quantifies the ratio of standard deviation to average taken for each pixel over all the frames. This ratio quantifies the strength of fluctuations in intensity over the average intensity. Blown up image of (f) green box shown in diffraction limited image, (g) yellow box shown in b-SOFI reconstruction of the original data stack and (h) red box shown in b-SOFI reconstruction of the HAWK data stack. Scale bars: (a-e) 8 μm and (f-h) 4 μm.

image than a pixel without an emitter. Therefore, even the weaker emitters can be picked up by b-SOFI after HAWK thereby leading to a more reliable reconstruction. The magnified images shown in Fig. 6(f-h) highlight its experimental verification.

The SOFI reconstructions on the original data set of 300 frames are given in Fig. 7(a-d) and the corresponding SOFI reconstructions on HAWK level 3 data set of 1778 frames is shown in Fig. 7(e-h). The resolution assessed using Fourier Ring Correlation, FRC, is shown in Fig. 7(i-l). Local FRC resolution is calculated for Fig. 7(d) and Fig. 7(h) and is shown in supplementary section as Fig. S6. It is seen that SOFI reconstructions on HAWK data set yielded a better resolution and a more reliable reconstruction by preventing the masking of the weaker emitters. However, there is a tradeoff, as the signal to background ratio is lower for the HAWK data set.

To showcase the strength of TIRF-imaging over large area using waveguide chip-based imaging platform for SOFI, MCC13 cells stained for actin are imaged using a LUCPLFLN 20X/0.45 NA microscope objective. The average intensity image of the data stack of 500 frames acquired using 20X/0.45 NA is shown in Fig. 8(a). A smaller region of interest, enclosed by the blue box in Fig. 8(a), within the large field-of-view captured using the low magnification objective is then imaged using a 60X/1.2 NA water immersion objective. To enhance the resolution of the images acquired using the 20X/0.45 NA objective, b-SOFI reconstructions are carried out on the original and HAWK data stack and shown in Fig. 8(c) and Fig. 8(d) respectively. The results shown in Fig. 8 opens up the possibility of generating super-resolved images using SOFI with minimized artifacts over large field-of-views.

Optics EXPRESS

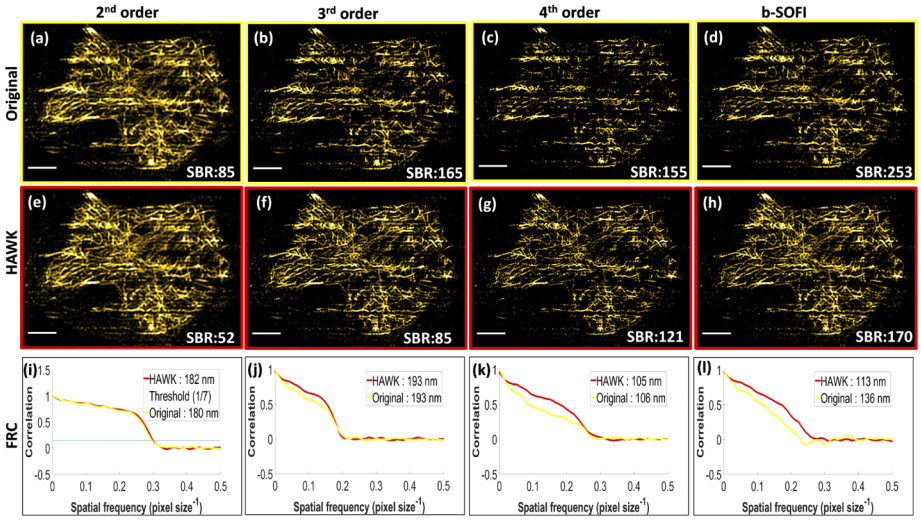

Fig. 7. Chip based SOFI imaging. SOFI reconstructions on original data set of 300 frames is shown by (a-d), enclosed within yellow frames. The orders of SOFI used for this purpose are (a) 2nd order, (b) 3rd order, (c) 4th order and (d) b-SOFI. SOFI reconstructions on HAWK data set of 1778 frames is shown by (e-h), enclosed within red frames. The SOFI orders used for reconstruction are (e) 2nd order, (f) 3rd order, (g) 4th order and (h) b-SOFI. Signal to background ratio (SBR) of the image is provided in the bottom right corner. The resolutions of the different reconstructions are quantified using FRC for (i) 2nd, (j) 3rd, (k) 4th and (l) b-SOFI. The FRC resolution values are provided as insets in the FRC plots. All the reconstructions are displayed here after scaling down using bilinear interpolation in Fiji. Scale bar 8 μm.

Optics EXPRESS

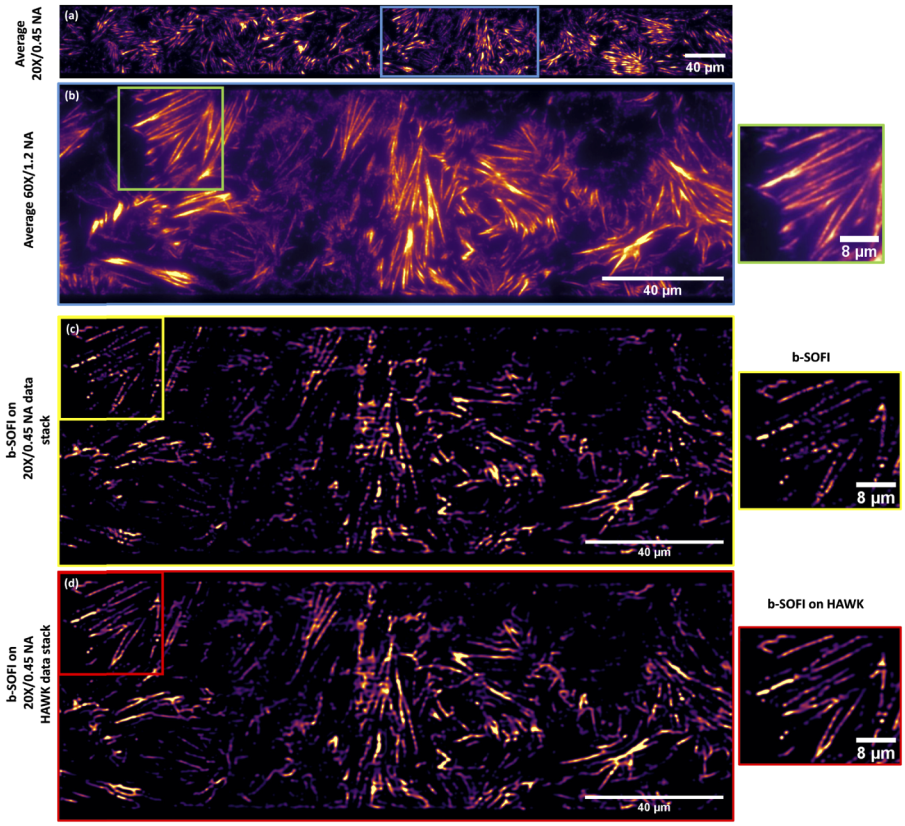

Fig. 8. Chip based SOFI imaging of MCC13 cells stained for actin (AF 555 phalloidin). (a) Diffraction limited TIRF image generated by averaging an image stack of 500 frames acquired using 20X/0.45 NA. The region shown inside the green box is (b) imaged using a 60X/1.2NA water immersion objective and shown enclosed in a purple frame, (c) reconstructed using b-SOFI on the original data set of 500 frames acquired using 20X/0.45 NA and shown enclosed in a yellow frame with FRC resolution of 299 nm, and (d) reconstructed using b-SOFI on the HAWK data set of 2978 frames for 20X/0.45 NA and is shown enclosed in a red box with FRC resolution of 241 nm. Scale bars: 40 µm and 8 µm for the magnified regions.

Optics EXPRESS

4. Conclusion

The employment of SOFI on chip-based imaging platforms helps gain resolution over a large field-of-view. It was observed that many of reconstruction artifacts are not due to SOFI, rather due to the on-chip illumination scheme employed. Wide waveguide generates an uneven distribution of the evanescent field arising due to multiple modes propagating simultaneously in the waveguide. To overcome this challenge, application of HAWK on the image stack prior to the application of SOFI has proven to be useful. In particular, the challenges associated with the masking of the weaker emitters showed improvements. Though the artifacts are not completely eliminated they have been minimized. Future work will focus on designing multi-mode waveguide structures with Y-junctions as shown in Ref. [30] to generate an almost uniform evanescent field illumination. We are also investigating the fact that a better labeling strategy of the cells, i.e. by minimizing the bleeding of dyes into the background, might help in improving the SBR lost after the application of HAWK. Our preliminary results suggest that the concept of application of HAWK to minimize the artifacts arising due to MMI patterns in waveguides can also be extended to other algorithms like MUSICAL, super-resolution method based on auto-correlation two-step deconvolution (SACD) [31] etc.

As compared to chip-based SMLM approaches [7,11], chip-based SOFI is an effective technique to generate super-resolved images with relatively higher temporal resolution. Waveguide platform has been previously used TIRF microscopy on living cells [14] and super-resolution imaging of fixed cell using SMLM method [9]. Future work will focus on super-resolution imaging of living cells exploiting chip-based SOFI. As chip-based SOFI needs similar number of images, a few hundred images, as acquired in chip-based TIRF, the method is suitable for live cell imaging application. Furthermore, chip-based SOFI can easily be integrated with other on-chip optical functions such as on-chip Raman spectroscopy [32–34], waveguide trapping [35–38], optical phase tomography [39–41] and others.

Funding

European Research Council (804233); H2020 Marie Skłodowska-Curie Actions (SEP-210382872); H2020 Marie Skłodowska-Curie Actions (31147, MSCA_ITN: 31147).

Acknowledgements

The authors would like to thank Dr. Deanna Wolfson, Dr. Firehun T Dullo, Dr. Azeem Ahmad, Dr. Vishesh Dubey and Sebastian Acuna for their valuable inputs during the course of this work. The publication charges for this article have been funded by a grant from the publication fund of Universitetet i Tromsø.

Disclosures

B.S.A. have applied for patent GB1606268.9 for chip-based optical nanoscopy. B.S.A and O.I.H. are co-founders of the company Chip NanoImaging AS, which commercializes on-chip super-resolution microscopy systems.

See Supplement 1 for supporting content.

References

1. G. Binnig, C. F. Quate, and C. Gerber, "Atomic force microscope," Phys. Rev. Lett. **56**(9), 930–933 (1986).
2. E. Betzig and J. K. Trautman, "Near-field optics: microscopy, spectroscopy, and surface modification beyond the diffraction limit," Science **257**(5067), 189–195 (1992).
3. D. McMullan, "Scanning electron microscopy 1928–1965," Scanning **17**(3), 175–185 (2006).

Optics EXPRESS

4. Eva Nogales and Sjors HW Scheres, "Cryo-EM: a unique tool for the visualization of macromolecular complexity," Mol. Cell **58**(4), 677–689 (2015).
5. L. Schermelleh, A. Ferrand, T. Huser, C. Eggeling, M. Sauer, O. Biehlmaier, and G. P. Drummen, "Super-resolution microscopy demystified," Nat. Cell Biol. **21**(1), 72–84 (2019).
6. M. L. Martin-Fernandez, C. J. Tynan, and S. E. D. Webb, "A 'pocket guide'to total internal reflection fluorescence," J. Microsc. **252**(1), 16–22 (2013).
7. R. Diekmann, Ø. I. Helle, C. I. Øie, P. McCourt, T. R. Huser, M. Schüttpelz, and B. S. Ahluwalia, "Chip-based wide field-of-view nanoscopy," Nat. Photonics **11**(5), 322–328 (2017).
8. S. Gaugiran, S. Gétin, J.-M. Fedeli, G. Colas, A. Fuchs, F. Chatelain, and J. Dérouard, "Optical manipulation of microparticles and cells on silicon nitride waveguides," Opt. Express **13**(18), 6956–6963 (2005).
9. Ø. I. Helle, D. A. Coucheron, J.-C. Tinguely, C. I. Øie, and B. S. Ahluwalia, "Nanoscopy on-a-chip: super-resolution imaging on the millimeter scale," Opt. Express **27**(5), 6700–6710 (2019).
10. D. A. Coucheron, D. N. Wadduwage, G. Senthil Murugan, P. T. So, and B. S. Ahluwalia, "Chip-Based Resonance Raman Spectroscopy Using Tantalum Pentoxide Waveguides," IEEE Photonics Technol. Lett. **31**(14), 1127–1130 (2019).
11. A. Archetti, E. Glushkov, C. Sieben, A. Stroganov, A. Radenovic, and S. Manley, "Waveguide-PAINT offers an open platform for large field-of-view super-resolution imaging," Nat. Commun. **10**(1), 1267–1269 (2019).
12. F. Ströhl, I. S. Opstad, J.-C. Tinguely, F. T. Dullo, I. Mela, J. W. Osterrieth, B. S. Ahluwalia, and C. F. Kaminski, "Super-condenser enables labelfree nanoscopy," Opt. Express **27**(18), 25280–25292 (2019).
13. M. Lahrberg, F. T. Dullo, and B. S. Ahluwalia, "Photonic-chip based free space beam shaping and steering for advanced optical microscopy application," OSA Continuum **3**(2), 359–378 (2020).
14. J.-C. Tinguely, Ø. I. Helle, and B. S. Ahluwalia, "Silicon nitride waveguide platform for fluorescence microscopy of living cells," Opt. Express **25**(22), 27678–27690 (2017).
15. Y. Fu, T. Ye, W. Tang, and T. Chu, "Efficient adiabatic silicon-on-insulator waveguide taper," Photonics Res. **2**(3), A41–A44 (2014).
16. B. Agnarsson, S. Ingthorsson, T. Gudjonsson, and K. Leosson, "Evanescent-wave fluorescence microscopy using symmetric planar waveguides," Opt. Express **17**(7), 5075–5082 (2009).
17. R. E. Thompson, D. R. Larson, and W. W. Webb, "Precise nanometer localization analysis for individual fluorescent probes," Biophys. J. **82**(5), 2775–2783 (2002).
18. Eric Betzig, George H. Patterson, Rachid Sougrat, O. Wolf Lindwasser, Scott Olenych, Juan S. Bonifacino, Michael W. Davidson, Jennifer Lippincott-Schwartz, and Harald F. Hess, "Imaging intracellular fluorescent proteins at nanometer resolution," Science **313**(5793), 1642–1645 (2006).
19. T. Dertinger, R. Colyer, G. Iyer, S. Weiss, and J. Enderlein, "Fast, background-free, 3D super-resolution optical fluctuation imaging (SOFI)," Proc. Natl. Acad. Sci. **106**(52), 22287–22292 (2009).
20. K. Agarwal and R. Macháň, "Multiple signal classification algorithm for super-resolution fluorescence microscopy," Nat. Commun. **7**(1), 13752–9 (2016).
21. N. Gustafsson, S. Culley, G. Ashdown, D. M. Owen, P. M. Pereira, and R. Henriques, "Fast live-cell conventional fluorophore nanoscopy with ImageJ through super-resolution radial fluctuations," Nat. Commun. **7**(1), 12471–9 (2016).
22. I. Yahiatene, S. Hennig, M. Müller, and T. Huser, "Entropy-based super-resolution imaging (esi): From disorder to fine detail," ACS Photonics **2**(8), 1049–1056 (2015).
23. Yonina Eldar, Mordechai Segev, Oren Solomon, and Maor Mutzafi, "Sparsity-based super-resolution correlation microscopy," U.S. Patent Application 16/484,123, filed January 2, 2020.
24. S. Cox, E. Rosten, J. Monypenny, T. Jovanovic-Talisman, D. T. Burnette, J. Lippincott-Schwartz, G. E. Jones, and R. Heintzmann, "Bayesian localization microscopy reveals nanoscale podosome dynamics," Nat. Methods **9**(2), 195–200 (2012).
25. R. J. Marsh, K. Pfisterer, P. Bennett, L. M. Hirvonen, M. Gautel, G. E. Jones, and S. Cox, "Artifact-free high-density localization microscopy analysis," Nat. Methods **15**(9), 689–692 (2018).
26. T. Dertinger, A. Pallaoro, G. Braun, S. Ly, T. A. Laurence, and S. Weiss, "Advances in superresolution optical fluctuation imaging (SOFI)," Q. Rev. Biophys. **46**(2), 210–221 (2013).
27. S. Geissbuehler, N. L. Bocchio, C. Dellagiacoma, C. Berclaz, M. Leutenegger, and T. Lasser, "Mapping molecular statistics with balanced super-resolution optical fluctuation imaging (bSOFI)," Opt. Nanoscopy. **1**(1), 4 (2012).
28. M. Kim, C. Park, C. Rodriguez, Y. Park, and Y.-H. Cho, "Superresolution imaging with optical fluctuation using speckle patterns illumination," Sci. Rep. **5**(1), 1–5 (2015).
29. Goodman and W. Joseph, *Introduction to Fourier optics* Roberts and Company Publishers, 2005.
30. Ø. I. Helle, F. T. Dullo, M. Lahrberg, J.-C. Tinguely, O. G. Hellesø, and B. S. Ahluwalia, "Structured illumination microscopy using a photonic chip," Nat. Photonics **14**(7), 431–438 (2020).
31. Weisong Zhao, Jian Liu, Chenqi Kong, Yixuan Zhao, Changliang Guo, Chenguang Liu, Xiangyan Ding, Xumin Ding, Jiubin Tan, and Haoyu Li, "Faster super-resolution imaging with auto-correlation two-step deconvolution," arXiv preprint arXiv:1809.07410 (2018).
32. W. Lee, P. Muñoz-Galindo, I. Hegeman, Y.-S. Yong, M. Dijkstra, S. M. García-Blanco, and H. L. Offerhaus, "Study on multiple waveguide platforms for waveguide integrated Raman spectroscopy," OSA Continuum **3**(5), 1322–1333 (2020).

Optics EXPRESS

33. P. Løvhaugen, B. S. Ahluwalia, T. R. Huser, and O. G. Hellesø, "Serial Raman spectroscopy of particles trapped on a waveguide," Opt. Express **21**(3), 2964–2970 (2013).
34. Ashim Dhakal, Ananth Z. Subramanian, Pieter Wuytens, Frédéric Peyskens, Nicolas Le Thomas, and Roel Baets, "Evanescent excitation and collection of spontaneous Raman spectra using silicon nitride nanophotonic waveguides," Opt. Lett. **39**(13)(13), 4025–4028 (2014).
35. Ø. I. Helle, B. S. Ahluwalia, and O. G. Hellesø, "Optical transport, lifting and trapping of micro-particles by planar waveguides," Opt. Express **23**(5), 6601–6612 (2015).
36. S. Kawata and T. Tani, "Optically driven Mie particles in an evanescent field along a channeled waveguide," Opt. Lett. **21**(21), 1768–1770 (1996).
37. O. G. Hellesø, P. Løvhaugen, A. Z. Subramanian, J. S. Wilkinson, and B. S. Ahluwalia, "Surface transport and stable trapping of particles and cells by an optical waveguide loop," Lab Chip **12**(18), 3436–3440 (2012).
38. B. S. Schmidt, A. H. Yang, D. Erickson, and M. Lipson, "Optofluidic trapping and transport on solid core waveguides within a microfluidic device," Opt. Express **15**(22), 14322–14334 (2007).
39. G. Yurtsever, N. Weiss, J. Kalkman, T. G. van Leeuwen, and R. Baets, "Ultra-compact silicon photonic integrated interferometer for swept-source optical coherence tomography," Opt. Lett. **39**(17), 5228–5231 (2014).
40. S. Schneider, M. Lauermann, P.-I. Dietrich, C. Weimann, W. Freude, and C. Koos, "Optical coherence tomography system mass-producible on a silicon photonic chip," Opt. Express **24**(2), 1573–1586 (2016).
41. Z. Wang, H.-C. Lee, D. Vermeulen, L. Chen, T. Nielsen, S. Y. Park, A. Ghaemi, E. Swanson, C. Doerr, and J. Fujimoto, "Silicon photonic integrated circuit swept-source optical coherence tomography receiver with dual polarization, dual balanced, in-phase and quadrature detection," Biomed. Opt. Express **6**(7), 2562–2574 (2015).

Supplemental Document

Optics EXPRESS

On-chip TIRF nanoscopy by applying Haar wavelet kernel analysis on intensity fluctuations induced by chip illumination: supplement

NIKHIL JAYAKUMAR,[1,3] ØYSTEIN I. HELLE,[1] KRISHNA AGARWAL,[1] AND BALPREET SINGH AHLUWALIA[1,2,4]

[1]*Department of Physics and Technology, UiT The Arctic University of Norway, Tromsø 9037, Norway*
[2]*Department of Physics, Indian Institute of Technology Delhi, Hauz Khas, New Delhi 110016, India*
[3]*nik.jay.hil@gmail.com*
[4]*balpreet.singh.ahluwalia@uit.no*

Supplement DOI: https://doi.org/10.6084/m9.figshare.13077950

Parent Article DOI: https://doi.org/10.1364/OE.403804

On-chip TIRF nanoscopy by applying Haar wavelet kernel analysis on intensity fluctuations induced by chip illumination : supplemental document

S1. *HAWK transform*

Consider the situation of a single pixel which has an intensity trace of 4 frames. This data stack of 4 frames in general may be represented as $\begin{pmatrix} a \\ b \\ c \\ d \end{pmatrix}$. The corresponding transformed intensity $\begin{pmatrix} p \\ q \\ r \\ s \end{pmatrix}$ trace can be obtained after multiplication with a 4×4 Haar matrix as shown below.

$$\begin{bmatrix} \frac{1}{2} & \frac{1}{2} & \frac{1}{2} & \frac{1}{2} \\ \frac{1}{2} & \frac{1}{2} & -\frac{1}{2} & -\frac{1}{2} \\ \frac{1}{\sqrt{2}} & -\frac{1}{\sqrt{2}} & 0 & 0 \\ 0 & 0 & \frac{1}{\sqrt{2}} & -\frac{1}{\sqrt{2}} \end{bmatrix} \begin{pmatrix} a \\ b \\ c \\ d \end{pmatrix} = \begin{pmatrix} \frac{a+b+c+d}{2} \\ \frac{a+b-c-d}{2} \\ \frac{a-b}{\sqrt{2}} \\ \frac{c-d}{\sqrt{2}} \end{pmatrix} = \begin{pmatrix} p \\ q \\ r \\ s \end{pmatrix}$$

The next step is to apply the desired filter level *m*. The possible values of *m* are integers in the range 1 to $\log_2 N$, where *N* is the total number of frames in the original data stack. The filtered pixel intensity trace can be calculated by applying the condition $H^{-1} = H^T$ to get the resultant vector $\begin{pmatrix} F1 \\ F2 \\ F3 \\ F4 \end{pmatrix}$.

$$\begin{bmatrix} \frac{1}{2} & \frac{1}{2} & \frac{1}{\sqrt{2}} & 0 \\ \frac{1}{2} & \frac{1}{2} & -\frac{1}{\sqrt{2}} & 0 \\ \frac{1}{2} & -\frac{1}{2} & 0 & \frac{1}{\sqrt{2}} \\ \frac{1}{2} & -\frac{1}{2} & 0 & -\frac{1}{\sqrt{2}} \end{bmatrix} \begin{pmatrix} p \\ q \\ r \\ s \end{pmatrix} = \begin{pmatrix} \frac{p}{2}+\frac{q}{2}+r/\sqrt{2} \\ \frac{p}{2}+\frac{q}{2}-r/\sqrt{2} \\ \frac{p}{2}-\frac{q}{2}+s/\sqrt{2} \\ \frac{p}{2}-\frac{q}{2}-s/\sqrt{2} \end{pmatrix} = \begin{pmatrix} F1 \\ F2 \\ F3 \\ F4 \end{pmatrix} = \begin{pmatrix} a \\ b \\ c \\ d \end{pmatrix}$$

For m = 1 the resultant vector is:

$$\begin{pmatrix} F1 \\ F2 \\ F3 \\ F4 \end{pmatrix} = \begin{pmatrix} \frac{(a-b)}{2} \\ \frac{-(a-b)}{2} \\ \frac{(c-d)}{2} \\ \frac{-(c-d)}{2} \end{pmatrix}$$

For m = 2 the resultant vector is:

$$\begin{pmatrix} F1 \\ F2 \\ F3 \\ F4 \end{pmatrix} = \begin{pmatrix} \frac{(a+b)}{4} - \frac{(c+d)}{4} \\ \frac{(a+b)}{4} - \frac{(c+d)}{4} \\ \frac{-(a+b)}{4} + \frac{(c+d)}{4} \\ \frac{-(a+b)}{4} + \frac{(c+d)}{4} \end{pmatrix}$$

The resultant vectors are then appended together to get the HAWK processed data stack. HAWK plugin in Fiji takes the desired filter level m as input from the user. After processing using HAWK, the negative values in the processed data stack are redressed positive or the positive and negative values are separated into two stacks and negative values are redressed positive. For the experiments presented in this manuscript, the latter condition is chosen with filter level $m = 3$.

S2. *A simple numerical example to illustrate the effect of the transform levels of HAWK*

To understand the influence of HAWK on the original image stack, consider a temporally varying signal such as $\begin{pmatrix} a \\ b \\ c \\ d \end{pmatrix} = \begin{pmatrix} 100 \\ 10 \\ 15 \\ 12 \end{pmatrix}$. This intensity trace is an example of a pixel lying on the border of a bright-dark band of the MMI pattern. The intensity trace of a pixel over time varies in proportion with the illumination intensity as the MMI pattern shifts transversally. The transformed traces for this particular pixel are $\begin{pmatrix} 45 \\ -45 \\ 1.5 \\ -1.5 \end{pmatrix}$ for $m = 1$ and $\begin{pmatrix} 20.75 \\ 20.75 \\ -20.75 \\ -20.75 \end{pmatrix}$ for $m = 2$. It can be seen that if the original data stack is used for SOFI reconstruction, this particular pixel will be rendered dim in the SOFI reconstructed image compared to pixels lying on a bright fringe. But after processing with HAWK the transformed intensity trace can lead to a higher pixel value in the SOFI reconstructions thereby aiding in alleviating the reconstruction artifacts due to the MMI pattern.

Similarly, an emitter lying on a bright band of the MMI pattern over the entire sequence of four frames can be represented as $\begin{pmatrix}100\\86\\95\\90\end{pmatrix}$. This corresponds to an emitter exhibiting fluctuations with low temporal frequency. The transformed traces for such a pixel are $\begin{pmatrix}7\\-7\\2.5\\-2.5\end{pmatrix}$ for $m = 1$ and $\begin{pmatrix}0.25\\0.25\\-0.25\\-0.25\end{pmatrix}$ for $m = 2$. The non-linear response of SOFI images to brightness is therefore reduced after HAWK which helps prevent masking of the weaker emitters.

Lastly, let us consider an emitter exhibiting high temporal fluctuations. It can be represented as $\begin{pmatrix}100\\16\\95\\10\end{pmatrix}$. The corresponding transform traces are $\begin{pmatrix}42\\-42\\42.5\\-42.5\end{pmatrix}$ for $m = 1$ and $\begin{pmatrix}2.75\\2.75\\-2.75\\-2.75\end{pmatrix}$ for $m = 2$. It can be seen that a highly fluctuating signal is represented predominantly by $m = 1$ filter while low temporal frequency information of emitters is retained by the higher order filter levels. Therefore, by appropriately choosing the filter level the artifacts generated by SOFI due to MMI patterns can be alleviated via HAWK processing. Ideally the correct filter level has to ensure that all the emitters get adequately represented in the reconstructed image.

S3. *HAWK helps depopulate regions with higher fluorophore density and increases the fluctuations*

The next challenge for SOFI is in reconstructing those regions of the sample, which have high fluorophore density. A high fluorophore density yields lower fluctuations, which in turn leads to a lower pixel value in the SOFI reconstructions. This is experimentally demonstrated by Fig. S1. For this particular experiment, Alexa Fluor 647 is coated on a Tantalum pentoxide waveguide surface. Images are acquired every 30 ms in epi-fluorescence mode. A region with a high density of fluorophores as shown in Fig. S1 is chosen and the ratio of standard deviation to average over 300 frames is calculated. The same data stack of 300 frames is then processed using HAWK and the ratio of standard deviation to average is again calculated. The filter level $m = 3$ is chosen so as to match with the experimental particulars described in the main article. It can be seen that the ratio of standard deviation to average increased two orders of magnitude for this experiment after the application of HAWK.

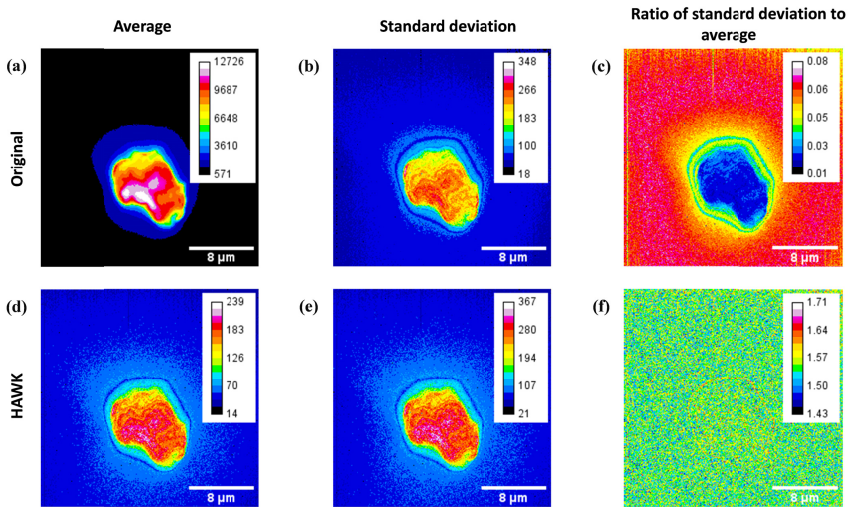

Fig. S1: Influence of HAWK on densely packed fluorophores. (a) Average of 300 frames. (b) Standard deviation over 300 frames. (c) Ratio of standard deviation to average over 300 frames. (d) Average of 1778 frames after HAWK processing. (e) Standard deviation of 1778 frames generated using HAWK. (e) Ratio of standard deviation to average of 1778 frames generated using HAWK. Scale bar 8 µm.

While imaging in waveguide TIRF mode, the fluctuations necessary for performing a SOFI reconstruction may arise from the intrinsic photokinetics of the fluorescent molecules as well as due to the oscillating nature of the illuminating scheme employed. To see which effect dominates, the following two experiments were performed. A uniform layer of Alexa Fluor 647 is coated on a Tantalum pentoxide waveguide and imaged as described in Section 2.1 of the main text.

In the first experiment, the coupling objective was held stationary and a stack of 300 frames were acquired. It means that the fluctuations recorded in the image stack arise only due to the intrinsic photokinetics of the fluorescent molecules. The results are presented in Fig. S2. For the second experiment, the coupling objective was manually oscillated and a sequence of 300 images were acquired during this process. Now the intensity trace of the pixels in the image frames so recorded will have fluctuations arising due to the intrinsic photokinetics of the fluorescent molecules as well as due to the oscillating nature of the illumination. The experimental results are presented in Fig. S3.

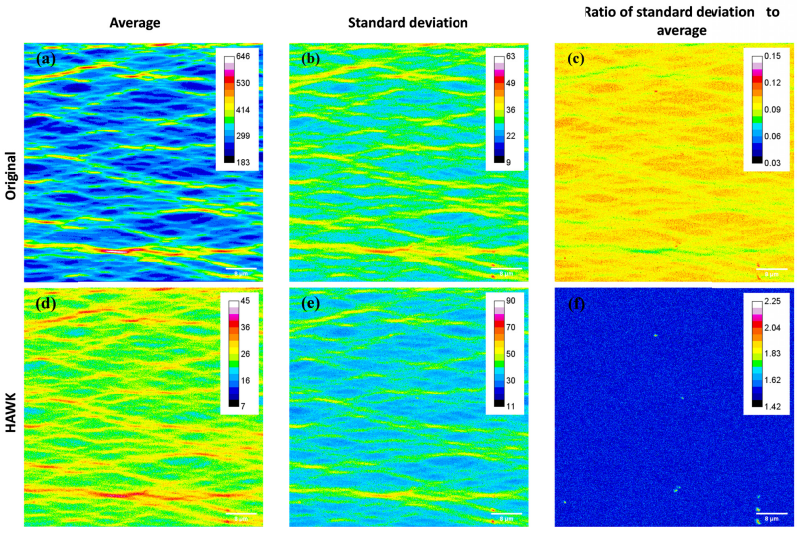

Fig. S2: Fluctuations due to intrinsic photokinetics in waveguide TIRF mode. (a) Average TIRF image of 300 frames. (b) Standard deviation over 300 frames. (c) Ratio of standard deviation to average of the original data stack of 300 frames. (d) Average TIRF image of HAWK processed data stack of 1778 frames. (e) Standard deviation over 1778 frames. (f) Ratio of standard deviation to average of the HAWK processed data stack of 1778 frames. Scale bar 8 µm.

It is seen from Fig. S2(c) and S2(f) that the ratio of standard deviation to average increased after the application of HAWK on the original data stack of 300 frames. Also, it can be seen from Fig. S2(c) and Fig. S3(c) that the fluctuations have been enhanced because of the oscillating illumination scheme employed.

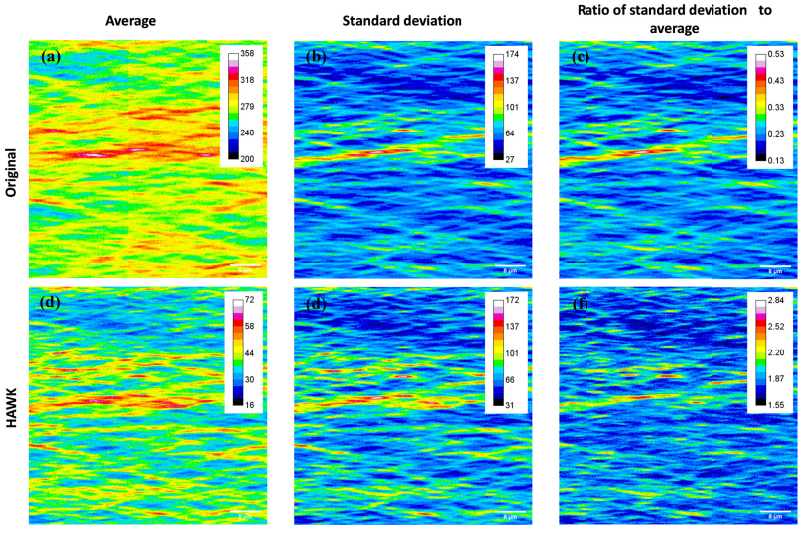

Fig. S3: Fluctuations due to intrinsic photokinetics and oscillating nature of illumination. (a) Average TIRF image of 300 frames. (b) Standard deviation over 300 frames. (c) Ratio of standard deviation to average of the original data stack of 300 frames. (d) Average TIRF image of HAWK processed data stack of 1778 frames. (e)

Standard deviation over 1778 frames. (f) Ratio of standard deviation to average of the HAWK processed data stack of 1778 frames. Scale bar 8 µm.

The inferences from these experiments is that in waveguide TIRF imaging mode, fluctuations arising due to photokinetics and waveguide illumination are present. It is also seen that HAWK helps in increasing the ratio of standard deviation to average in waveguide TIRF imaging mode and in regions with high density of fluorophores as shown in Fig. S1. It means that the necessity of averaging out the modes to generate a uniformly illuminated image can be exploited by HAWK to enhance intensity fluctuations even in regions having high density of fluorophores, thereby alleviating the reconstruction artifacts of SOFI due to MMI patterns.

S4. *Effect of different transformation levels of HAWK on the reconstruction quality*

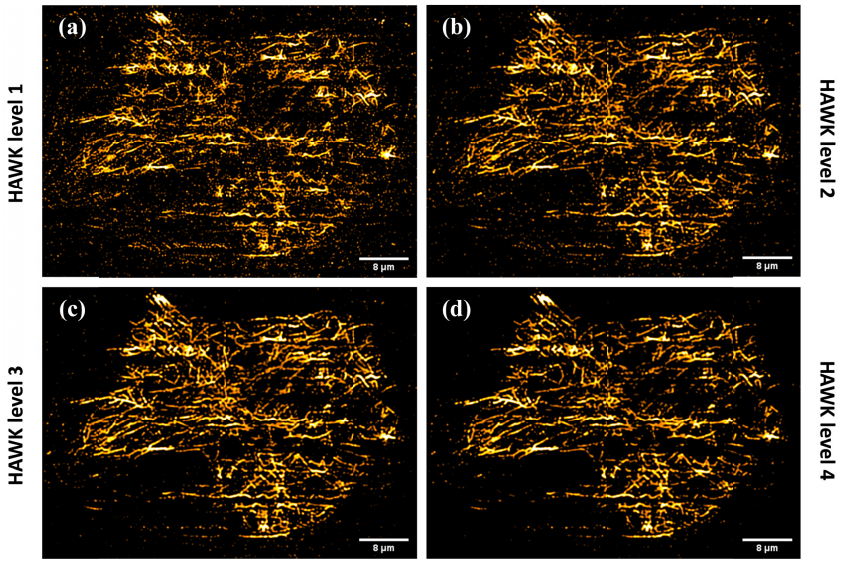

Fig. S4: Influence of HAWK filter levels on 4th order SOFI reconstruction. 4th order SOFI reconstructions on (a) HAWK data stack with $m = 1$, (b) HAWK data stack with $m = 2$, (c) HAWK data stack with $m = 3$ and (d) HAWK data stack with $m = 4$. Scale bar 8 µm.

Fig. S4 portrays the effect of HAWK filter levels on SOFI reconstructions. It can be seen that the HAWK data stack with $m = 3$ gave the best 4th order SOFI reconstruction. At low filter levels such as $m = 1$, the high temporal frequency content is more dominant as explained in Section 1.2. At higher filter levels, the low frequency information will also get adequately represented in the image stack. At even higher filter levels like $m = 4$ and above we expect the emitters exhibiting low temporal frequency with high intensity to be predominantly represented after the SOFI reconstructions due to the non-linear brightness scaling of SOFI. In this manuscript, $m = 3$ gave the best reconstruction.

S5. *Effect of the method of separation of negative values available in HAWK Fiji plugin on SOFI reconstruction*

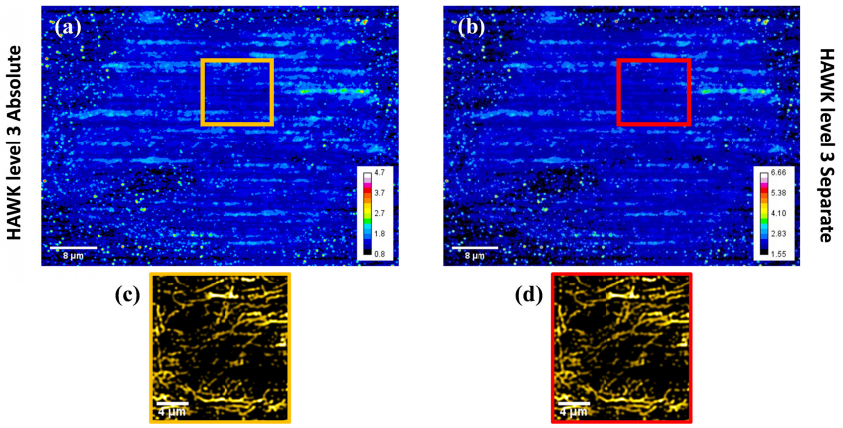

Fig. S5: Ratio of standard deviation to average on (a) HAWK data stack with absolute option used, (b) HAWK data stack with ‘‘separate’’ option used. 4th order SOFI reconstruction carried out on (c) HAWK data stack enclosed by the yellow box, (d) HAWK data stack enclosed by the red box. Scale bars: (a-b) 8 µm and (c-d) 4 µm.

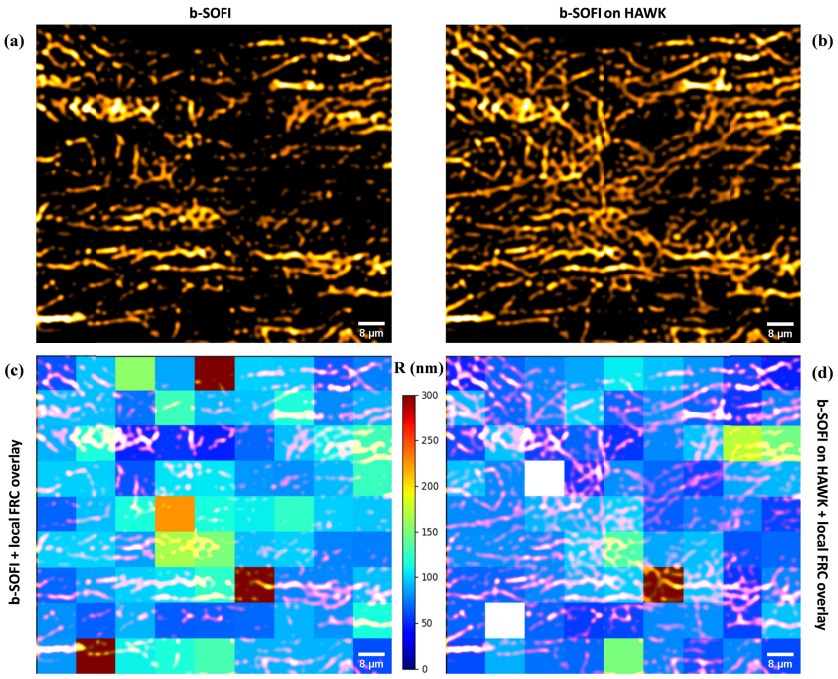

Fig. S6: Local FRC resolution for the data of Fig. 7. (a) b-SOFI reconstruction of the original data stack. (b) b-SOFI reconstruction on HAWK data stack. (c) Local FRC resolution R(nm) computed for 100 × 100 pixels on b-SOFI reconstruction of original data stack with b-SOFI reconstruction overlaid. (d) Local FRC resolution computed for 100 × 100 pixels on b-SOFI reconstruction of HAWK data stack with b-SOFI on HAWK reconstruction overlaid. The local FRC images are rescaled using bilinear interpolation before overlaying them with b-SOFI reconstructions. The pure white pixels indicate regions where local FRC failed to give a value. Scale bar: 8 µm.

Chapter 4

Paper 2: Waveguide based high-contrast label-free microscopy

Multi-moded high-index contrast optical waveguide for super-contrast high-resolution label-free microscopy

Research question

There are two questions that led to the start of this project:

- In microscopy, rotating diffusers are used to reduce speckle noise associated with coherent light sources [87, 88]. By drawing an analogy between rotating diffusers and temporally varying MMI patterns in waveguides, Fig. 4 and Fig. 5 in the manuscript in Chapter 3, can speckle noise be mitigated to perform waveguide-based label-free imaging?
- If speckle noise can be mitigated, then can the MMI patterns be used to induce intensity-fluctuations in unlabeled samples as described in Chapter 3, and thereby generate label-free super-resolved images using intensity-fluctuation algorithms?

Therefore, the problem that is being addressed is that of generation of high-contrast label-free images using waveguides and subsequently generating super-resolved label-free images using the so acquired dataset. This problem is addressed in the attached paper titled, ' Multi-moded high-index contrast optical waveguide for super-contrast high-resolution label-free microscopy'.

Aim: The aim of this work is to first generate high-contrast label-free images of biological samples using optical waveguides and subsequently, circumvent Abbe's optical diffraction limit .

Method: For this, dielectric optical waveguide made of Silicon Nitride, Si_3N_4 with core refractive index $n_1 \approx 2$, is employed to illuminate the unlabeled sample. By utilizing temporally varying MMI patterns in multi-moded waveguides,

it is investigated if an analogy can be drawn with rotating diffusers to generate high-contrast label-free images. Subsequently, the generation of super-resolved label-free images using a so-acquired dataset is investigated. The technique developed is abbreviated cELS, which stands for chip-based Evanescent Light Scattering.

To mitigate the coherent speckle noise in microscopy setups that use lasers, rotating diffusers are employed. The working principle is to average several speckle patterns within the integration time of the camera, which helps in generating an image with reduced speckle noise [8]. In waveguide-based microscopy, the different MMI patterns correspond to the speckle patterns that get generated when coherent light passes through a diffuser. To ensure several speckle/MMI patterns get averaged within the integration time of the camera, a galvo scan mirror is employed. The galvo scan oscillation rate of 1013 Hz gave the optimal results and was arrived at after many iterations. The galvo scan helps excite different MMI patterns in the waveguide, as shown in Fig. 4.1, i.e., different modes that get excited, get coherently scattered off the sample onto the camera, as the galvo scans the input facet of the waveguide. The camera exposure time is set at 30 ms. This ensures that within the integration time of the camera, several MMI patterns get averaged and thus, helps mitigate speckle noise and generate a single diffraction-limited image, shown experimentally in Fig. 4.1. This is explained mathematically in Section 3.2 of the attached manuscript.

Now to employ intensity-fluctuation algorithms, an image stack exhibiting fluctuations in intensity is acquired as mentioned above. The galvo oscillation and camera acquisition is not synchronized, this implies that each image acquired by the camera will be due to illumination of the sample with a different set of modes. This image stack is then given as input to an intensity-fluctuation based reconstruction algorithm. In this thesis, MUSICAL algorithm [31] is chosen.

Coherent Laser (Cobolt Flamenco 660) is used to excite modes at vacuum wavelength 660 nm in the waveguide. The laser light which is coupled onto a single mode fiber is collimated and directed towards a galvo mirror. The collimated light from galvo falls on the back aperture of the coupling objective 50X/0.5 NA. The coupling objective MO_1 focuses the coherent light onto the input facet of the waveguide which is mounted on a high-precision piezo-electric XYZ translation stage. The unlabeled sample is placed inside a cover-slip sealed polydimethylsiloxane (PDMS) chamber of thickness ≈ 150 μm, on top of the core-cladding interface of the waveguide. The excited modes guide power along the length of the waveguide and interact with the sample using their evanescent tails. The sample scatters this evanescent field into the far-field, i.e., the higher spatial frequencies of the sample get convolved with the illumination spatial frequencies and get low-passed into the pass-band of the objective, as described in Section 1.8, also shown schematically in Fig. 1b and explained in Section 3.1 in the attached paper. The scattered light is relayed onto the camera via a 4f setup, collection objective MO_2 collects the scattered light. It allows the coherently scattered light to reach the scientific camera Hamamatsu C13440-20CU. The experimental setup is shown in Fig. 4.2.

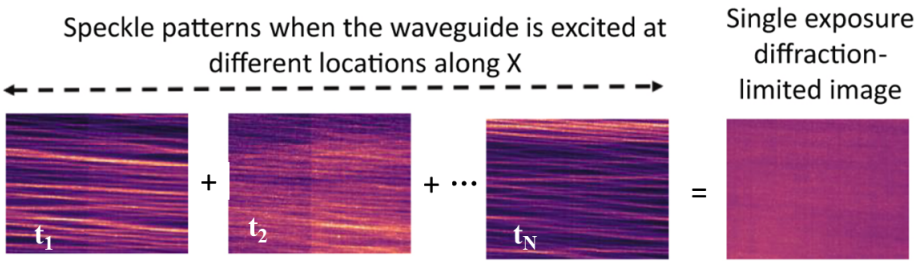

Figure 4.1: Scanning the input facet of the waveguide excites different MMI patterns. When these patterns are added on an intensity-basis, it will help mitigate the speckle noise [89]. In this experiment, within the integration time of the camera, many speckle patterns are added on an intensity basis to generate a single diffraction-limited image with minimized speckle noise. As the galvo scans across the input facet of the waveguide, it excites different modes with different amplitudes. These modes superimpose to generate the MMI patterns. The camera sees an averaged intensity image, i.e., sum of many MMI patterns. This figure is taken from [52].

Observations: Each optical mode in the waveguide, described in Section 1.9, can be decomposed into two plane waves propagating at angles $\pm\ \theta_m$, where m corresponds to the m^{th} mode in the waveguide propagating at angle $\pm\theta_m$ with respect to the propagation axis. This is illustrated in Fig. 2 in the attached paper in this chapter and explained in detail in Section S2 of the supplementary text of the attached paper. What this means is that each mode illuminates the sample with a different obliquity. Due to coherence of the scattered light, the scattered light off the sample can superimpose and interfere. For e.g., if two unlabeled particles are illuminated by the coherent evanescent waves of the waveguide, the image registered by the camera will look different for different illuminating MMI patterns. This is shown in Fig. 4.2. The scattered light off the two particles can interfere constructively and appear as a single blob of light, or interfere destructively and appear as two distinct particles. This is in contrast to two incoherently emitting fluorescent objects. Therefore, applying intensity-fluctuation techniques can induce artifacts in the reconstructed image. Besides, it does not give any resolution improvement over Abbe's diffraction-limit in Eqn. 1.25. Hence, the application of intensity-fluctuation techniques can only result in contrast enhancement and a seemingly improved resolution. The usage of MMI patterns in waveguides help to suppress speckle noise. However, to achieve super-resolution using intensity-fluctuation techniques, the emission between the particles must incoherent.

Results: High-contrast images of weakly scattering specimens like HeLa cells (Fig. 6 in the attached paper), liposomes (Fig. 3b - 3e in the attached paper), extra-cellular vesicles (Fig. 3f in the attached paper) and nanobeads (Fig. 3a, Fig.4, Fig. 5 in the attached paper) are demonstrated using high-index contrast

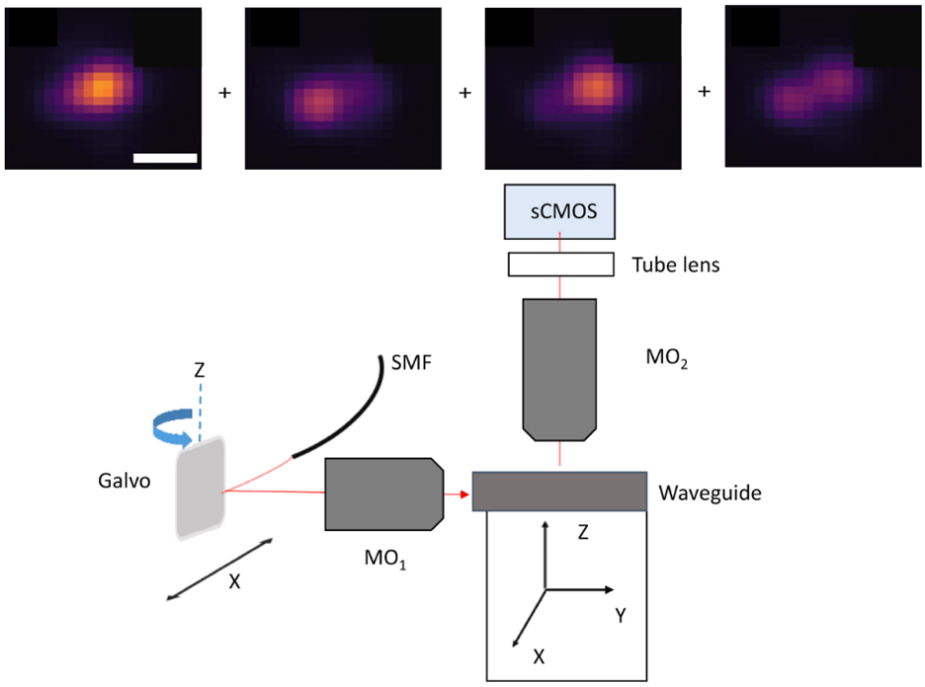

Figure 4.2: Coherent scattering of light leads to different images of the same field-of-view under different oblique illuminations. This is attributed to nonlinear mapping between the coherently scattered field and image-plane intensity. In the figure, experimental results of imaging of two 100 nm gold nano-particles using a multi-moded waveguide is shown. The simulation analysis of coherent imaging using waveguides is shown in Fig. 1.9. Scale bar 2 μm.
The schematic of the experimental setup of cELS is shown below. Laser light is coupled into a single mode fiber SMF, collimated and directed towards a galvo mirror which is free to rotate along the z-axis. The galvo steers the collimated light onto the back-focal plane of MO_1. MO_1 then focuses this light onto the input facet of a waveguide mounted on a translation stage. The unlabeled sample placed on the core-cladding interface of the waveguide scatters the coherent light, which is collected by another microscope objective MO_2. The collected light is realyed onto a scientific camera via a tube lens. This figure is taken from [52].

multi-moded waveguides. This is achieved by summing up speckle patterns on an intensity basis to suppress speckle noise. Thus, cELS enables high-contrast imaging of weakly scattering specimens. cELS for imaging of HeLa cells is shown in Fig. 4.3. Fig. 4.3 shows correlative cELS and TIRF images of the same field-of-view.

Conclusion and future outlook: cELS enables high-contrast label-free imaging using high-index contrast optical waveguides. This is accomplished by summing up many speckle/MMI patterns on an intensity basis at the camera plane, which is realized experimentally by employing a galvo scan as described in the Methods section. This work also explains the physical mechanism of how the multiple modes propagating in the waveguide contribute to the final image formation.

Future work should look into restoring the spatial frequencies of the sample to its exact location in the spatial frequency domain, similar to [66]. This is because the higher spatial frequencies of the sample get low-passed into the pass-band of the objective when the sample interacts with the evanescent waves at the core-cladding interface of the waveguide. As a result, the image gener-

ated may have artefacts as the spatial frequencies of the sample are not restored to their original position. Also, super-resolution could not be achieved due to the coherent nature of the scattered light. Hence, the idea developed from this project is that if the two particles can be made to emit incoherently in label-free mode, then fluorescence-based techniques like SIM and SOFI can be applied in the label-free regime to circumvent the Abbe limit in Eqn. 1.25. This is explored in Chapter 5.

Author contributions: NJ conceptualized the idea and designed the experiments along with BSA. FTD designed the waveguide chip and mask for fabrication. NJ, FTD, VD, and AA were involved in sample preparation. NJ performed the experiments and analyzed the data. JC and NSB provided the liposome samples. EMG and OS provided the vesicle samples. NJ worked on the theory with inputs from FS, KA and BSA. NJ wrote the manuscript and all authors commented on the manuscript. KA and BSA supervised the project.

Research Article

Nikhil Jayakumar, Firehun T. Dullo, Vishesh Dubey, Azeem Ahmad, Florian Ströhl, Jennifer Cauzzo, Eduarda Mazagao Guerreiro, Omri Snir, Natasa Skalko-Basnet, Krishna Agarwal and Balpreet Singh Ahluwalia*

Multi-moded high-index contrast optical waveguide for super-contrast high-resolution label-free microscopy

https://doi.org/10.1515/nanoph-2022-0100
Received February 22, 2022; accepted June 8, 2022;
published online June 20, 2022

Abstract: The article elucidates the physical mechanism behind the generation of superior-contrast and high-resolution label-free images using an optical waveguide. Imaging is realized by employing a high index contrast multi-moded waveguide as a partially coherent light source. The modes provide near-field illumination of unlabeled samples, thereby repositioning the higher spatial frequencies of the sample into the far-field. These modes coherently scatter off the sample with different phases and are engineered to have random spatial distributions within the integration time of the camera. This mitigates the coherent speckle noise and enhances the contrast (2–10) × as opposed to other imaging techniques. Besides, the coherent scattering of the different modes gives rise to fluctuations in intensity. The technique demonstrated here is named chip-based Evanescent Light Scattering (cELS). The concepts introduced through this work are described mathematically and the high-contrast image generation process using a multi-moded waveguide as the light source is explained. The article then explores the feasibility of utilizing fluctuations in the captured images along with fluorescence-based techniques, like intensity-fluctuation algorithms, to mitigate poor-contrast and diffraction-limited resolution in the coherent imaging regime. Furthermore, a straight waveguide is demonstrated to have limited angular diversity between its multiple modes and therefore, for isotropic sample illumination, a multiple-arms waveguide geometry is used. The concepts introduced are validated experimentally via high-contrast label-free imaging of weakly scattering nanosized specimens such as extra-cellular vesicles (EVs), liposomes, nanobeads and biological cells such as fixed and live HeLa cells.

Keywords: coherence of light; high throughput imaging; high-contrast label-free imaging of nano carriers and biological cells; intensity fluctuation algorithms; label-free microscopy; multi-moded high-index contrast waveguide.

1 Introduction

Label-free microscopy circumvents the need for exogenous contrast agents. However, this gives rise to challenges such as poor contrast and low resolution while performing far-field label-free microscopy of weakly scattering biological specimens. Diffraction-limited resolution arises due to the inability to capture high spatial frequencies of the specimen in the far-field, whereas poor contrast in the optical regime is attributed to a weak scattering signal in comparison to the illuminating light. Moreover, illuminating these samples with a highly coherent light source like a laser can lead to speckle formation, degrading the image quality [1]. Hence, the key idea in this paper is to describe mathematically the physical mechanism and demonstrate experimentally how a high-index contrast multi-moded

*Corresponding author: Balpreet Singh Ahluwalia, Department of Physics and Technology, UiT The Arctic University of Norway, Tromsø 9037, Norway; and Department of Clinical Science, Intervention and Technology, Karolinska Insitute, 17177 Stockholm, Sweden,
E-mail: balpreet.singh.ahluwalia@uit.no
Nikhil Jayakumar, Vishesh Dubey, Azeem Ahmad, Florian Ströhl and Krishna Agarwal, Department of Physics and Technology, UiT The Arctic University of Norway, Tromsø 9037, Norway,
E-mail: nik.jay.hil@gmail.com. https://orcid.org/0000-0003-3671-0058 (N. Jayakumar)
Firehun T. Dullo, Department of Microsystems and Nanotechnology, SINTEF Digital, Gaustadalleen 23C, 0373 Oslo, Norway
Jennifer Cauzzo and Natasa Skalko-Basnet, Department of Pharmacy, Faculty of Health Sciences, UiT The Arctic University of Norway, Tromsø 9037, Norway
Eduarda Mazagao Guerreiro and Omri Snir, Department of Clinical Medicine, UiT The Arctic University of Norway, Tromsø 9037, Norway

optical waveguide helps mitigate the abovementioned challenges in label-free microscopy.

High-contrast label-free images of weakly scattering specimens typically use holographic interferometric setups [2–4], holographic noninterferometric setups [5, 6], sequential illumination of the sample and iterative stitching in Fourier space [7, 8], multiple 2D holographic measurements for 3D reconstruction of refractive index of the sample via inverse scattering [9], multiple intensity-only measurements for tomographic reconstruction [10, 11], a physical stop to block background light [12], phase-rings [13] etc. Most of these techniques illuminate the entire volume of the sample, require multiple frames for reconstructing the final image or/and typically use incoherent white light or LED [14] as the light source which has lower photon degeneracy [2]. On the other hand, sources with higher photon degeneracy like lasers can generate coherent artifacts. This problem can be mitigated via optical sectioning of the sample, as in total internal reflection microscopy [15]. A typical way of generating an evanescent wave illumination is using a total internal reflection fluorescence (TIRF) objective [16]. Rotating Coherent Scattering microscopy (ROCS) [17] uses an evanescent field generated by a diode laser passed through a rotating diffuser to illuminate the sample from all azimuthal directions. However, a high magnification/numerical aperture (N.A.) TIR objective lens (e.g., 60–100× > 1.33 N.A.) is typically used in ROCS, thus limiting the field-of-view (FoV). Another approach to generating evanescent fields and over larger areas is via an optical waveguide, i.e., a photonic chip [18–26]. Previous chip-based label-free microscopy works use an incoherent white light source [23], fluorescent nanowire ring illumination [24], index-matched waveguide geometry [25], polymer fluorescent films [26], Fourier Ptychography via single-mode waveguide [27] etc. to suppress stray light that is detrimental while imaging weakly scattering specimens. However, in this article, a high index contrast optical waveguide guiding laser along its length is demonstrated as a feasible secondary light source for superior contrast and high-resolution imaging of weakly scattering specimens. As opposed to other label-free waveguide techniques which require multiple images with complicated optical setup [27], incoherent light source or/and in combination with index-matched waveguides [23–26], here in this work a high-index contrast multi-moded waveguide guiding a coherent laser light is engineered as a partially coherent secondary light source for single-shot imaging with superior contrast.

Through this work, which uses the experimental setup shown in Figure 1(a), the following concepts are proposed: (1) Multi-moded optical waveguide as a partially coherent light source, (2) physical mechanism of high-contrast label-free image formation using a multi-moded waveguide, (3) feasibility of employing intensity fluctuation algorithms [28], typically used in fluorescence microscopy, to utilize fluctuations in intensity induced by the multiple modes [29] coherently scattering off the sample and (4) for isotropic sample illumination, a four-arm crossing waveguide is used to mitigate the challenge of limited angular diversity between the modes of a straight waveguide. An overview of waveguides, modes and fabrication of the chips is given in Supplementary sections S1-S4 and Figures S(1)–S(4). A comparison between the different chip-based label-free works is provided in Table 1 of the supplementary material. In addition, this approach based on photonic chips offers several advantages: (1) the decoupled illumination and detection scheme allows only the scattered light off the sample to reach the camera. A comparison between the different illumination schemes is given in Figure S5 of the supplementary material. (2) The use of high refractive index waveguide material ($n \approx 2$) enables accessing higher spatial frequencies of the sample [30], see Figure 1(b), that are typically inaccessible using conventional free-space bulk optics approach or using index-matched waveguide geometries [25]. The high index core, $n_{\text{eff}} = 2$, reduces the speckle size that can be formed to about $2\pi/(k_e + k_{out})$, where $k_e = 2\pi.n_{\text{eff}}/\lambda_{vac}$, $k_{out} = 2\pi.\text{N.A.}/\lambda_{vac}$, n_{eff} is the effective index of mode, k_e is the magnitude of the incident evanescent wave vector, k_{out} defines the passband of the microscope and λ_{vac} is the vacuum wavelength [31]. (3) The addition of multiple modes within the integration time of the camera helps suppress speckle noise as shown in Figure 1(c). (4) Any perturbation in the index at the core-cladding interface scatters light into the microscope objective (MO) as shown in Figure 1(d). (5) The use of a coherent light source like a laser helps focus very high-power into thin waveguide geometries. The lack of specificity in label-free imaging and consequently multiple scattering issues are mitigated by the evanescent field excitation of the low-loss high refractive index material thin (150 nm) waveguides. This provides excellent optical sectioning to about less than 100 nm and high field intensities [32], as shown in Figure 1(e). As opposed to index-matched optical waveguides [25], a thin (150 nm) high-refractive index contrast Si_3N_4 waveguide as used in this work significantly enhances the intensity in the evanescent field, with up to 10–15% of the mode power flux

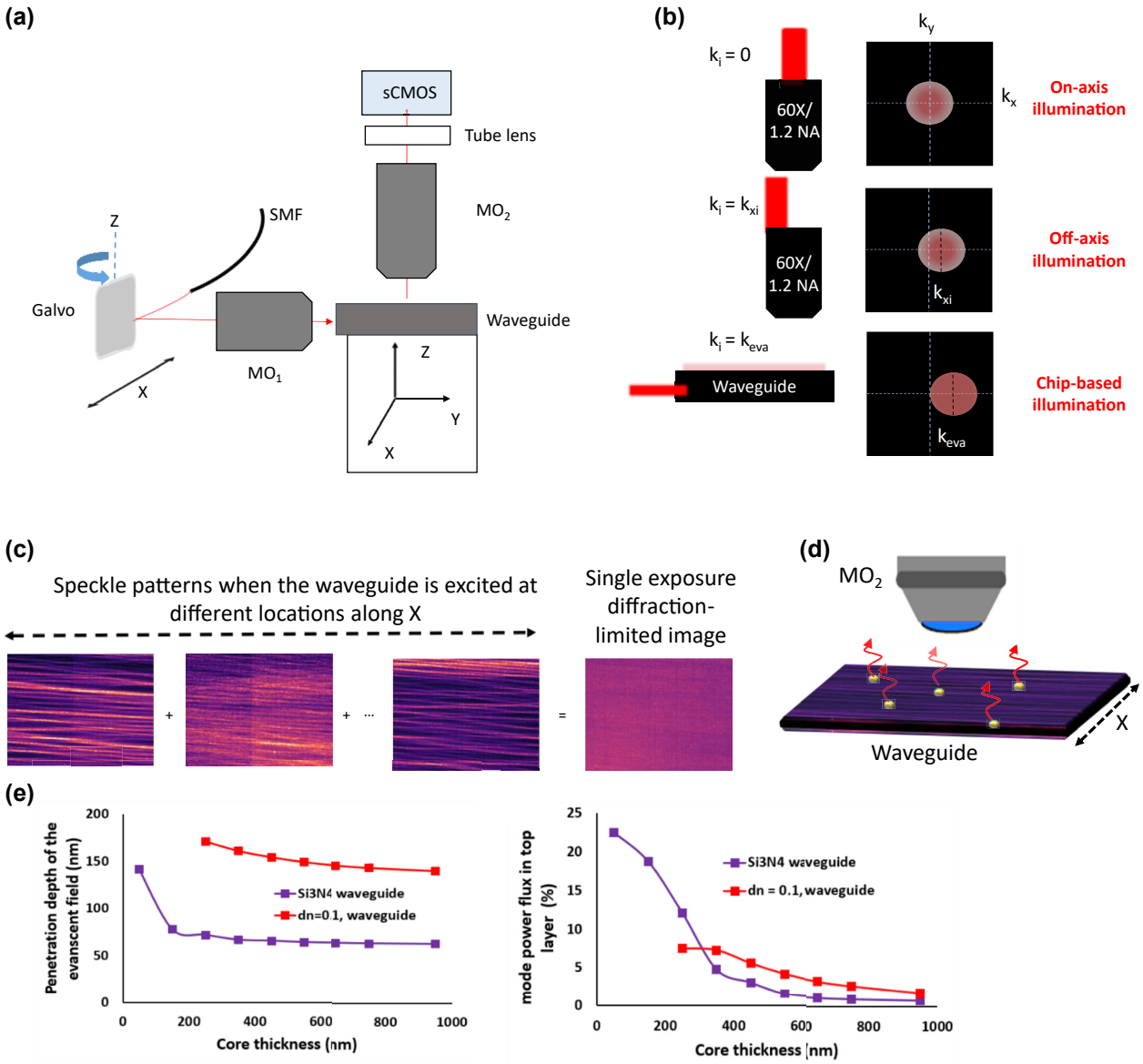

Figure 1: Basic concepts of cELS.
(a) Schematic of cELS experimental setup. (b) Influence of obliquity of illumination in Fourier domain (k_x–k_y domain). Three different cases corresponding to on-axis epi-illumination ($k_i = 0$), off-axis epi-illumination ($k_i = k_{xi}$) and waveguide chip-based illumination ($k_i = k_{eva}$) and the corresponding object spectrum they sample are shown. Flat-field like illumination provided by high-refractive index chip provides access to the higher sample spatial frequencies. (c) The addition of multiple speckle patterns at the camera plane helps suppress the speckle noise. (d) Schematic representation of an optical waveguide supporting several guided modes and some scattering objects that convert the evanescent waves into scattering waves is also given. (e) The penetration depth and field intensity of a TE1 mode of Si_3N_4 high index core ($\Delta n \approx 0.5$) waveguide and an index matched waveguide ($\Delta n \approx 0.1$) are provided here.

present in the evanescent field, Figure 1(e). A high-index waveguide thus enables both the collection of higher spatial frequencies and generates high field intensity that are crucial while imaging nano-sized weakly scattering objects. This work utilizing the coherent scattering of the multiple modes of the waveguide to mitigate the coherent speckle noise is referred to as chip-based evanescent light scattering (cELS).

2 Optical setup and imaging conditions

The schematic of cELS experimental setup is shown in Figure 1(a). The coherent laser (Cobolt Flamenco 660) light, $\lambda_{vac} = 660$ nm, is coupled into a single mode fiber that delivers collimated light via a collimator onto a galvo

mirror which is free to rotate along the z-axis. The galvo helps steer this light onto the back focal plane of a microscope objective (Olympus LMPanFL N 50×/0.5 NA), MO_1. MO_1 focuses the incident collimated light onto the input facet of a waveguide. This configuration enables scanning of the incident light on the input facet of the waveguide, exciting different sets of guided modes for each incident location. The waveguide is mounted on a high-precision piezo electric XYZ-translation stage. The sample to be imaged is placed on top of the waveguide core. The evanescent light that interacts with the sample, gets scattered and is collected by a microscope objective MO_2. Via a 4f setup, the scattered light is imaged onto an sCMOS camera (Hamamatsu C13440-20CU). The exposure time of the camera for the different experiments presented in this article is typically about 30 ms. The galvo oscillation rate is set at 1013 Hz for the waveguide widths used in this experiment, a prime number, which causes a spatial redistribution of the excited modes within the exposure time of the camera. Throughout this article, experiments have been carried out using a silicon nitride (Si_3N_4) waveguide. The fabrication of Si_3N_4 waveguide and the preparation, characterization, and labeling strategies of biological samples such as liposomes, EVs and cells are given in Sections S4–S7 of the supplementary material.

3 Theory of image formation in cELS

The theory section provided here and in the Supplementary Material focuses on mainly three concepts: (1) transmitting near-field information to far-field, (2) waveguide as a partially coherent light source and (3) multiple modes induce fluctuations in intensity that aid in the generation of high-contrast images.

3.1 Near-field information to far-field

If an ideal waveguide without any sample is imaged, no light will reach the camera plane. However, any perturbation in the refractive index at the core-cladding interface can scatter photons into the camera [28]. The physical mechanism behind the conversion of nonpropagating evanescent waves into propagating waves may be understood from the following simplified illustration [31, 33]. A two-dimensional sample is illuminated by an incident field $E(x, y, z)$. Let us represent the two-dimensional Fourier transform of this field by $\tilde{E}(\alpha, ß; z)$ where α, β and γ are spatial frequencies with respect to x, y and z axis respectively, i.e., propagation vector $\vec{k} = \alpha\hat{x} + ß\hat{y} + \gamma\hat{z}$. The magnitude of the wave vector of a waveguide mode is $\frac{2\pi}{\lambda_{vac}} n_{eff}$, where n_{eff} is the effective mode index. The evanescent wave vector corresponds to the largest spatial frequency components of the field. This field interacts with a thin sample placed at $z = 0$. The sample may be represented by a transmission function $T(x, y)$. Invoking the Born approximation, just after the thin sample the field becomes [31]

$$E_{sample}(x, y; 0) = T(x, y)\, E(x, y; 0) \tag{1}$$

By the property of Fourier transform, Eq. (1) may be represented alternatively as the convolution of the two signals in the spatial frequency domain as

$$\tilde{E}_{sample}(\alpha', ß'; 0) = \iint_{-\infty}^{\infty} \tilde{E}(\alpha, ß; 0)\, \hat{T}(\alpha - \alpha', ß - ß')\, d\alpha dß \tag{2}$$

But the illuminating field may be represented via the sifting property of the delta function as follows

$$\tilde{E}(\alpha, ß; 0) = \iint_{-\infty}^{\infty} \tilde{E}(\tilde{\alpha}, \tilde{ß}; 0)\, \delta(\tilde{\alpha} - \alpha, \tilde{ß} - ß)\, d\tilde{\alpha} d\tilde{ß} \tag{3}$$

Combining Eqs. (2) and (3) the spatial frequencies of the sample represented by $\hat{T}(\alpha, ß)$ gets convolved with the spatial frequencies of the incident field. Or in other words, if a mode of an evanescent field is represented by $\delta(\alpha_{eva}, ß_{eva})$, then the electric field just after the thin sample contains the shifted object spectrum $\hat{T}(\alpha - \alpha_{eva}, ß - ß_{eva})$, where α_{eva} and $ß_{eva}$ are the spatial frequencies of the evanescent wave illuminating the sample. This is illustrated in Figure 1(b). If the shifted version of the function falls within the passband of the microscope, those high spatial frequencies of the object will reach the camera plane. Thus, sub-diffraction limit sized features are captured using cELS due to the high n_{eff} of the waveguide core that is typically not accessible with conventional objective based illumination schemes or index-matched waveguide geometries.

3.2 Waveguide as a partially coherent light source

In conventional bright field imaging, the incident light $E_i(\boldsymbol{r}, t)$ and the light scattered off the sample $E_s(\boldsymbol{r}, t)$ reach the camera. The total complex scalar field at the camera plane is $E_T(\boldsymbol{r}, t) = E_i(\boldsymbol{r}, t) + E_s(\boldsymbol{r}, t)$. For weakly scattering specimens, the only modulation in the total field will be in its phase. But the intensity registered by the camera, $I(\boldsymbol{r}, t)$, will have no phase information and hence poor contrast, where $\langle\rangle$ represents time averaging. But while imaging

using waveguides, only scattered light off the sample gets detected, i.e., $E_T(\boldsymbol{r},t) = E_s(\boldsymbol{r},t)$. Therefore, the point will be visible with enhanced contrast as a bright spot on a dark background.

Consider two-point scatterers represented by $j = 1, 2$. The incident field induces Rayleigh dipoles [34] which radiate into the far-field. Let the field emitted by each emitter at the camera plane be given by $E_j(\boldsymbol{r},t) = E_0(\boldsymbol{r}) \exp\left[i\varphi_j(\boldsymbol{r},t) - i\omega t\right]$. Here we assume that the scatterers are identical, i.e., the radiated fields have the same amplitude. The total field intensity averaged over the integration time of the camera is then represented as [35]

$$I(\boldsymbol{r},t) = 2\left|E_0(\boldsymbol{r})\right|^2 + 2\left|E_0(\boldsymbol{r})\right|^2 \langle\cos(\chi(\boldsymbol{r},t))\rangle \tag{4A}$$

where

$$\chi(\boldsymbol{r},t) = \varphi_1(\boldsymbol{r},t) - \varphi_2(\boldsymbol{r},t) \tag{4B}$$

First, let us consider the situation of coherent illumination. Although the phases $\varphi_1(\boldsymbol{r},t)$ and $\varphi_2(\boldsymbol{r},t)$ are a function of time, the phase difference $\chi(\boldsymbol{r},t)$ is time-invariant and can be simply represented as $\chi(\boldsymbol{r})$. The cosine term in Eq. (4A) becomes time invariant and therefore, the interference phenomenon is observed. On the contrary, in the case of incoherent illumination as in fluorescence imaging, the phase difference $\chi(\boldsymbol{r},t)$ is not time-invariant and the cosine term is a function of temporal variations. Since the phase fluctuations occur on a time scale much smaller than the integration time of the camera, the time-averaged cosine term tends to zero and therefore no interference is observed.

However, multi-moded illumination patterns inside the photonic waveguides presents a very interesting case. Let the electric fields emitted from the scatterers due to a particular mode "m" be represented as $E_{j,m}(\boldsymbol{r},t) = E_{0,m}(\boldsymbol{r}) \exp\left[i\varphi_{j,m}(\boldsymbol{r},t) - i\omega_m t\right]$, where the subscript m denotes the mode. Correspondingly, the subscript m may be introduced in $I_m(\boldsymbol{r},t)$ and $\chi_m(\boldsymbol{r})$ as well. Since the modes are coherent individually and with respect to each other, the time term in the function $\chi_m(\boldsymbol{r},t)$ is absent. At any given point in time t, due to galvo scanning, the mode combinations will be different. Representing the complex mode coefficients at a given time t as $a_m(t)$, the average intensity within a camera integration time due to all the mode combinations is given as

$$I(\boldsymbol{r},t) = \Big\langle 2\left|a_m(t)\right|^2 \left|E_{0,m}(\boldsymbol{r})\right|^2 + 2\left|a_m(t)\right|^2 \left|E_{0,m}(\boldsymbol{r})\right|^2 \cos\left(\chi_m(\boldsymbol{r}) - \alpha_m(t)\right)\Big\rangle \tag{5}$$

where $\alpha_m(t)$ represents the phase of $a_m(t)$. The presence of a time-varying cosine term $\cos(\alpha_m(t))$ which changes continuously with the galvo scan position implies that the average intensity shown in Eq. (5) is no longer coherent. However, it is also not strictly incoherent because the galvo scan times are comparable to the camera exposure time. To ensure that there is no strict correlation between the images acquired across different frames we set the galvo scan rate to a prime number. In essence, we realize a partially coherent illumination case per frame. Equation (5) may be understood as many speckle patterns getting added at the camera plane. As per the central limit theorem, the contrast of these speckles scales as $1/\sqrt{N}$ when added on an intensity basis, where N is the number of independent speckle patterns added [36]. This is illustrated schematically in Figure 1(c). In the experiments described here, the galvo oscillation rate is set at a prime number of 1013 Hz. The logic behind choosing a prime number can be understood as follows. During oscillation at each position of the galvo, a set of modes are excited in the waveguide that get coherently scattered off the sample onto the camera. Within one exposure time of the camera, the galvo would have oscillated ($0.030\ \text{s} \times 1013\ \text{Hz} \approx 31$) times and excited the modes. Due to a prime number setting, it will ensure that 31 distinct set of mode patterns or speckle patterns get averaged within the integration time of the camera. This condition will help suppress the speckle noise according to the Central Limit Theorem. Thus, the issue of coherent noise is mitigated via the usage of a multi-moded waveguide and galvo scanning, demonstrating a multi-moded waveguide as a partially coherent light source that enables high-contrast imaging.

3.3 Coherent scattering of modes enable super-contrast label-free imaging

Consider two particles "1" and "2" placed on top of the waveguide surface as shown in Figure 2(a). The input coherent laser light excites a few modes of the waveguide. These modes are described mathematically as given by Eq. (S3) in the supplementary material. So, any mode "m" may be decomposed into a pair of plane waves propagating at angles $\pm\theta_m$ with respect to the propagation direction, z-axis. For brevity only two such modes are shown in green and red in Figure 2. The tails of these modes extend into the cladding and polarize the particles "1" and "2". The particles then radiate into the far-field as described earlier. As per the first order Born approximation, the incident and scattered waves can be assumed to have the same phase [34]. Therefore, the phase difference between the scattered waves off the two particles will be dependent only on the positions of these particles on the waveguide.

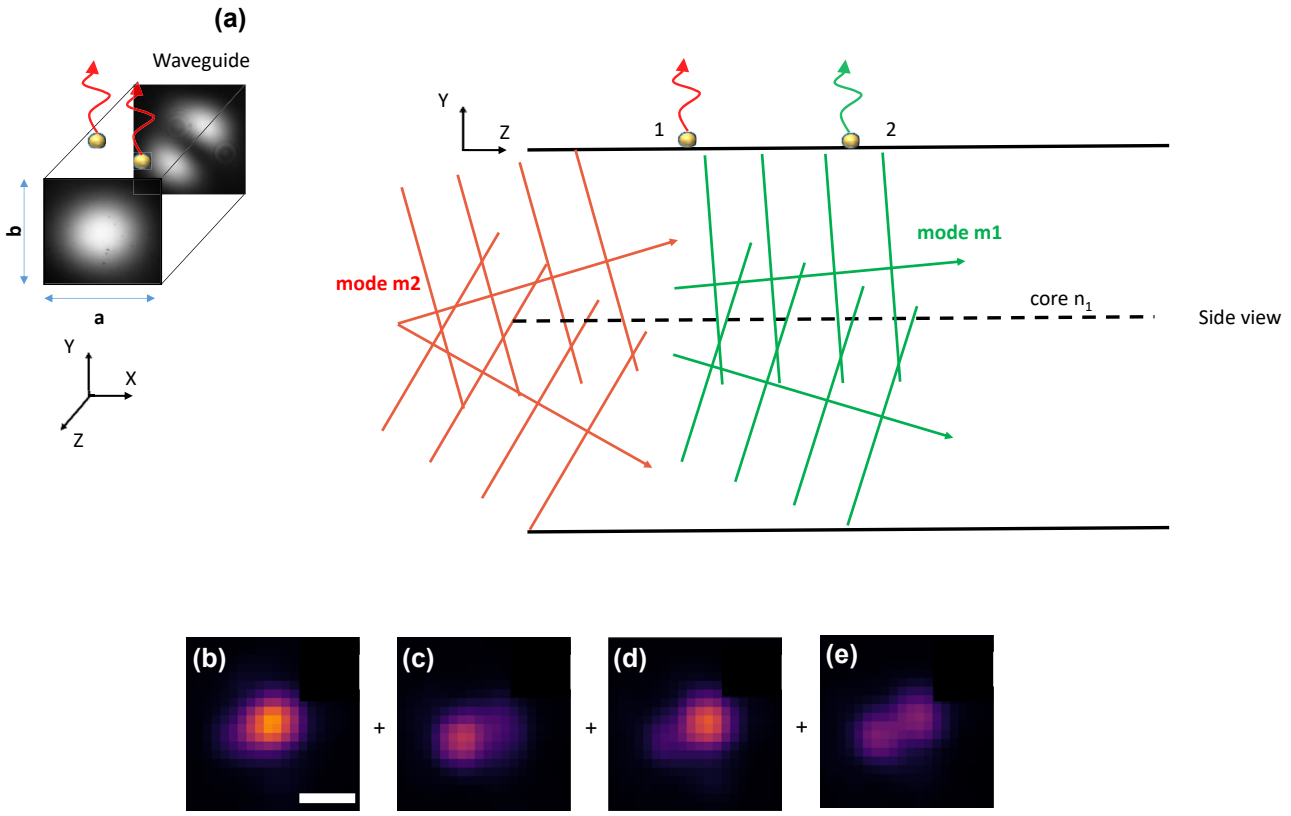

Figure 2: Theory of cELS image formation.
(a) A rectangular waveguide with transverse widths "*a*" and "*b*" units guiding power via fundamental and higher-order modes is shown. The two modes m1 and m2 are shown in green and red color respectively in the side view diagram. The modes are decomposed into a pair of plane waves propagating at discrete angles with respect to the optical axis along *z*. The evanescent tails of these guided modes polarize particles 1 and 2 placed on the surface and scatter into the far-field. (b–e) Experimental demonstration of the theory of image formation using a multi-moded waveguide. The images are of 100 nm gold nanoparticles imaged using a 10X/0.25 NA MO. The multi moded speckle pattern causes variations in the intensity of the coherently scattered light. Scale bar 2 µm.

Therefore, the imaging process may be described as follows.

Two particles separated by one Rayleigh distance = $0.61\lambda/\mathrm{NA}$, are located on a rectangular waveguide with transverse widths "*a*" and "*b*" units as shown in Figure 2. For $\lambda = 660$ nm and NA = 1.2., the two particles can then be assumed to be located at points with coordinates (0, $b/2$, 0) and ($0.508a$, $b/2$, 0). In the case of incoherent imaging, i.e., if particles "1" and "2" are fluorescent beads, they will be just resolved in an ideal microscope as per Rayleigh's resolution criteria. However, the coherent scattering off the particles by the multi-moded waveguide chip presents the following interesting scenarios in contrast the incoherent fluorescent imaging. This is listed below.

1. The two particles are illuminated by the same mode. For example, consider illumination with TE_{11} mode ($m = 1$, $n = 1$) which is described in Eq. (S3) of the supplementary text. Substituting the above-mentioned particle's location into Eq. (S3), the phase difference between the coherently scattered light reaching the detector will be approximately 1.6 radians. Due to interference between these coherently scattered fields as described by Eq. (4A), the particles will no longer be resolved as per Rayleigh's criteria. This contrasts with these two particles getting resolved as in the case of incoherent imaging.
2. The two particles are illuminated by say TE_{11} ($m = 1$, $n = 1$) and TE_{21} ($m = 2$, $n = 1$) mode. Substituting the abovementioned particle locations into Eq. (S3), the phase difference between the fields is seen to be $\boldsymbol{\pi}$ radians. As a result, the particles get resolved in label-free mode as per Rayleigh's criteria.

Now as the galvo oscillates to vary the illumination patterns in the waveguide, the complex mode coefficient $a_m(t)$ changes with time, hence, both the amplitude and phase of the scattered light change. An image stack so acquired over time exhibits fluctuations in intensity. This

is shown via the experimental results in Figure 2(b). As a result, image contrast can be enhanced by performing the average or standard deviation of such an image stack.

Naturally, the feasibility of employing intensity-fluctuation based algorithms to such an image stack exhibiting fluctuations in intensity is worth analyzing. These fluctuation-based algorithms are typically used in fluorescence microscopy to circumvent the diffraction limit. However, applying these fluorescence-based algorithms in the partial coherent imaging regime as in cELS presents some caveats [37]. In fluorescence microscopy, the fluorescent molecules which are typically a few nanometers in size emit independently and portray a linear mapping between the fluorophore concentration and image plane. But the partial coherent imaging nature of cELS implies that the sample plane concentration and image plane intensity obey a nonlinear relationship due to the interference term described in Eq. (5). This can lead to artificial sharpening and false localizations by the algorithm and hence, lead to artifacts in the reconstructed image. E.g., consider the scenario presented in case 1 above, where the particles are no longer resolvable as per Rayleigh's criteria. The algorithm may then localize to the point of maximum intensity which lies in between the two particles, thus leading to a false localization. However, if the particles are resolvable as per the scenario presented in case 2 above, the algorithm can artificially sharpen the image and lead to a seemingly improved contrast and resolution. The nonlinear sharpening effect can also lead to masking of regions with lower scattering intensity.

4 Results and discussion

The following imaging results are presented to validate the theory developed above: (a) 60 nm polystyrene nanobeads, (b) weakly scattering nanosized biological specimens like liposomes and extracellular vesicles, (c) fixed and live biological cells, (d) 100 nm gold nanoparticles imaged using dark-field and cELS microscopy and (e) application of intensity fluctuation algorithms on 100 nm polystyrene nanobeads. (a–d) validate superior contrast imaging and (e) verifies the feasibility of applying intensity fluctuation algorithms in label-free mode. Details of experimental parameters are provided in Supplementary material Table 2.

4.1 Weakly scattering specimens

Firstly, 60 nm polystyrene nanobeads are imaged to compare the performance of TIRF and cELS. Figure 3(a) shows the images of 60 nm polystyrene beads acquired in cELS and TIRF mode and the two images are in good agreement. The signal to background ratio (SBR) is higher for the cELS image. The Fourier transform of the TIRF image shows that higher spatial frequencies get attenuated faster which is the case for incoherent imaging. On the other hand, cELS is a partially coherent imaging technique and therefore, the contrast does not drop significantly even for the higher spatial frequencies which is expected for coherent imaging. Thus, cELS supports superior contrast imaging of nano-sized structures that have predominantly high spatial frequencies. The difference in the Fourier spectrum between the coherent and incoherent imaging is further discussed in Supplementary material section S2.

Next, we opted for samples that are both weakly scattering and are nanoscale in size, liposomes. The index contrast of liposomes with its surrounding is only about 0.04 [38] and the size of the liposomes used here is about 125 nm. This constitutes a weakly scattering specimen and hence, to detect these structures they are typically prepared including fluorescent molecules for fluorescence imaging. Due to their limited size, the fluorescence signal emitted by the structures is usually weak. But due to the use of high-index contrast waveguide material with a thin waveguide geometry (150 nm thick), the evanescent field intensity at the waveguide surface is high and decays rapidly, aiding in generating label-free images of such weakly scattering specimens with higher signal to background noise as opposed to TIRF. cELS image also shows the presence of a larger number of particles whereas the TIRF image of the same region of interest showed a fewer number of particles, see also Figure S6 of supplementary material. This could be attributed to bleaching out of the fluorescence or due to a very weak fluorescence signal. A similar behavior is also noted in Ref. [25].

In Figure 3(b)–(e), we compare the images of liposomes acquired using different light sources and in different modes. Here, both laser and pseudo-thermal light sources (PTS) are used in epi-illumination mode, and TIRF and cELS in the near-field illumination mode via a photonic-chip. A PTS is generated by passing a laser through a rotating diffuser to reduce the coherent noise [36] and such an illumination method is termed dynamic speckle illumination (DSI). As anticipated, the laser in the epi-fluorescence mode generates coherent noise that hinders label-free imaging of weakly scattering nano-object, Figure 3(b). The coherent noise, however, can be reduced using DSI. Even after addressing the coherent noise issue, the epi-configuration illumination mode generates a background signal comparable to that of the weakly scattered

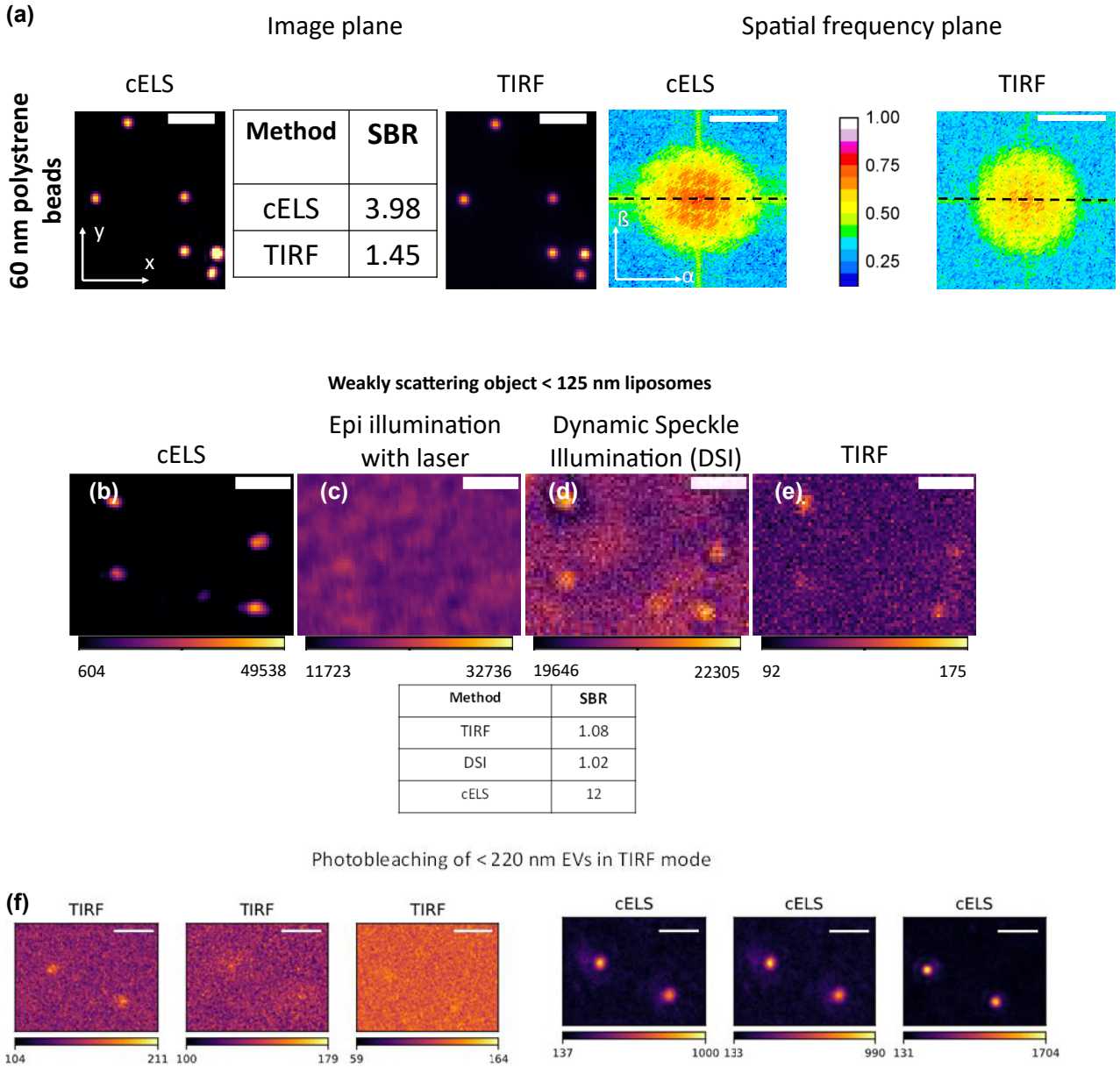

Figure 3: Experimental results of weakly scattering specimens.
(a) cELS and TIRF images of 60 nm polystyrene beads. The signal to background ratio (SBR) is given in the table and the Fourier transform of the beads imaged using cELS and TIRF is given alongside. Scale bar 2 μm in the image plane ($x-y$ plane) and 5 μm^{-1} in the spatial frequency plane ($\alpha-\beta$ plane). The colorbar shows the intensity variation along the dotted lines in the Fourier plane. (b) Liposomes of <125 nm in size imaged using epi-illumination laser mode, (c) TIRF mode, (d) Dynamic Speckle Illumination mode and (e) cELS are compared. The colorbar shows the pixel values of the images. The corresponding SBR is given in the table below. Scale bar 2 μm. (f) cELS and TIRF images of <225 nm sized extracellular vesicles (EVs). The TIRF image shows photo-bleaching with time whereas cELS allows long-term imaging of the EVs. A larger field-of-view image of EVs is provided in Supplementary article, Figure S7. The colorbar shows the pixel values of the images. Scale bar 2 μm.

light from the object, consequently reducing the contrast of the images. In TIRF, fluorescence tagging, and near-field excitation helps reduce out-of-focus light to improve the image contrast. However, this method still suffers from photo-bleaching, labeling nonuniformity and background fluorescence signal arising from unspecific labeling that are inherent to fluorescence-based approaches. Contrary to all these approaches, cELS generates superior contrast imaging of liposomes in label-free mode, which is devoid of bleaching issues as well, as shown next.

Figure 3(f) shows the time-lapse imaging of another weakly scattering object, <225 nm extra-cellular vesicles

(EVs). Photo-bleaching is a well-known problem in fluorescence microscopy and the bleaching of the fluorescence signal from EVs is depicted in the TIRF images. The fluorescent molecules bleach out over time in TIRF mode whereas cELS continued to generate high-contrast images of EVs even after photo-bleaching of its fluorescence. This demonstrates the time-lapse label-free imaging capability of cELS that would find application for imaging nano-sized biological structures like liposomes or EVs where the fluorescence signal will be limited. Also, cELS can be combined with image segmentation algorithms for estimating nano-particle density for different scattering intensities, as shown in Supplementary Figure S7.

Next, we demonstrate the competitive edge of cELS over incoherent epi-illumination methods. The decoupled illumination/detection paths of cELS configuration allow the use of a low magnification objective lens. This supports imaging of large areas without sacrificing the optical sectioning supported by the evanescent field. In Figure 4, 100 nm polystyrene beads are imaged in cELS and epi-illumination mode with both DSI and white light (WL) sources using a low magnification 20×/0.45N.A objective lens. The isolated nano-beads are not visible with DSI and WL. Only aggregated 100 nm beads are barely visible with DSI and white light sources. On the contrary, cELS provide high-contrast images even with 20×/0.45N.A. objective lens, thus enabling superior contrast imaging over large FoV. This is attributed to a multitude of factors like decoupled illumination/detection in dark-field mode, coherent scattering of multiple modes and use of high-index contrast waveguide material. The high effective index of the guided modes ($n_{\text{eff}} = 1.75$) scatters the dominant high spatial frequency components of the nano-sized samples. On the other hand, in epi-illumination mode, the illumination and detection schemes are coupled and both the light sources, i.e., spatially incoherent light (partially incoherent) for DSI and temporally incoherent light for WL fail to generate sufficient contrast. See Supplementary Figure S8 for scalable field of view imaging of 100 nm polystyrene beads in cELS mode using 25×/0.85NA and 60×/1.2NA MOs.

The resolution supported by cELS is $\lambda_{\text{vac}}/(n_{\text{eff}} +$ N.A.). While for other methods that use the same MO for illumination and collection, the resolution supported is

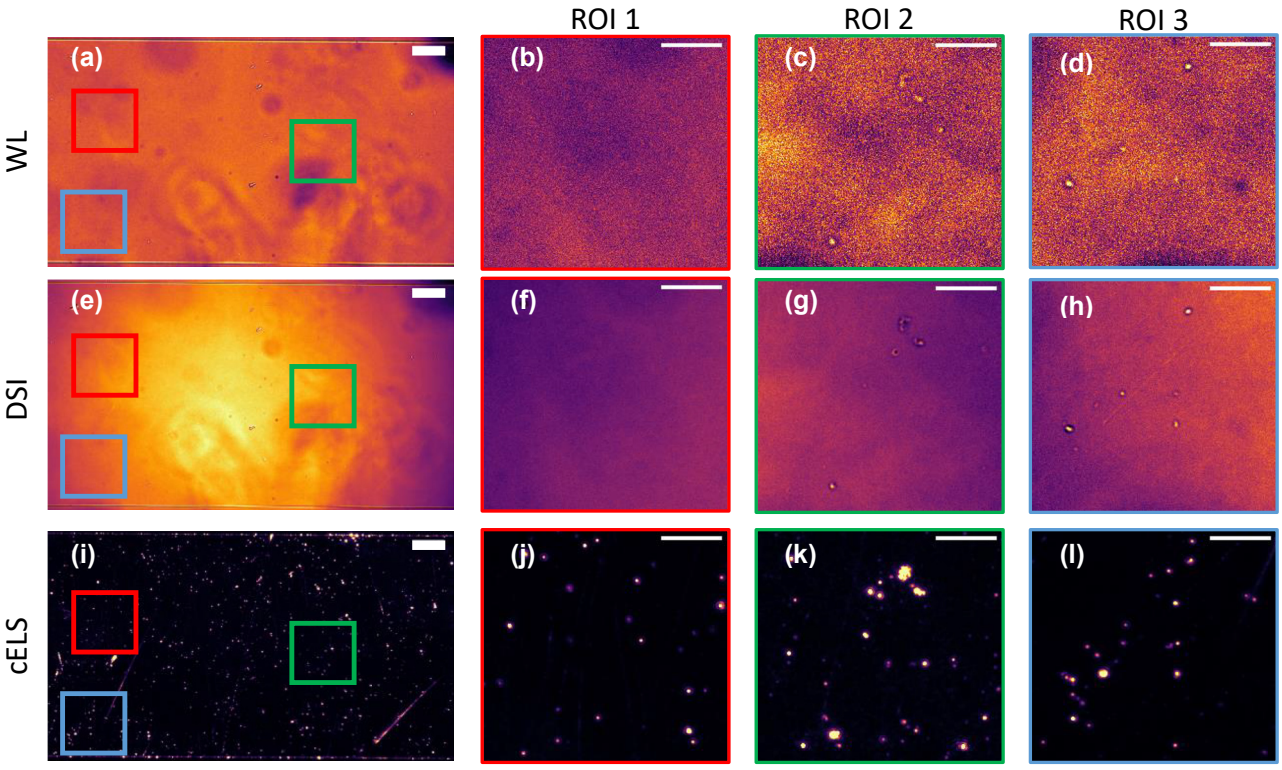

Figure 4: 100 nm polystyrene beads imaged using 20×/0.45NA with white light (WL), dynamic speckle illumination (DSI) and cELS. (a, e, i) 100 nm beads imaged using WL, DSI and cELS respectively. Scale bar 50 µm. A few regions of interest, ROI 1–3, with aggregated and sparse beads are chosen within the FoV enclosed by red, green and blue boxes which are blown up and displayed. (b, c, d) WL images of 100 nm beads, (f, g, h) 100 nm beads imaged in DSI mode and (j, k, l) 100 nm beads imaged using cELS. Scale bar 20 µm in the blown-up regions.

given by $\lambda_{vac}/2N.A.$ As n_{eff} is independent of the imaging objective lens, even with a lower N.A. MO, cELS enables high-contrast and higher resolution imaging. To validate this point experimentally, a comparison between dark-field (DF) microscopy and cELS is demonstrated in Figure 5. For this experiment, 100 nm gold nanoparticles (GNP) are imaged in cELS mode using a 10X/0.25 NA MO and in DF mode using a 10X/0.30 NA MO. In cELS, the camera acquisition time is set at 1 ms and an image stack of 100 images is acquired. Three different regions of interest in the acquired image stack are shown in Figure 5(a1)–(a3). The same regions of interest are also imaged using DF microscopy. The exposure time of the DF microscope is set at 100 ms for a fair comparison between the two techniques and the images are given in Figure 5(b1)–(b3). Comparing Figure 5(a1) and (b1), the beads contained within the red box are resolvable as two distinct beads in cELS method, as shown by the line plot in Figure 5(c). A similar improvement in performance of cELS over DF is visible in the green boxes shown in Figure 5(a2) and (b2). The corresponding Fourier spectrum of the images is also provided alongside each of the images. The difference in the spectrum is attributed to cELS being a partially coherent imaging technique while DF microscopy uses an incoherent white light source for imaging. Also, due to the use of coherent laser and high effective index of the guided modes, the scattering signal in cELS images is almost two orders of magnitude higher than the corresponding DF images.

4.2 cELS for imaging cells

Here the compatibility of cELS for bioimaging is demonstrated and compared with fluorescence imaging. Figure 6 compares cELS and TIRF images of a fixed HeLa cell. cELS imaging was performed at 660 nm excitation and detection. For TIRF imaging, the actin filaments were labeled at 532 nm excitation and the Stoke shifted signal was detected using a 595/40 nm band-pass filter. Three different boxes in red, yellow, and green are blown-up and shown alongside for both cELS and TIRF. The yellow box contains the nucleus of the cell. Typically, the nucleus of the cell accommodates many fluorophores. As a result, the fluorescence intensity even in TIRF mode will be high. This can obscure some of the features as opposed to cELS. cELS image shows more features as the nucleus is situated slightly above the cell membrane and hence the evanescent field scattering will be less. Next for regions outside the nucleus, the TIRF image exhibited a reduced contrast for the filament like structures which could be attributed to weak fluorescence intensity, nonuniform, and unspecific labeling. Being a label-free method would enable cELS to perform long duration live cell imaging without worrying about photo-bleaching. In Figure S9 of the supplementary material, epifluorescence, TIRF and cELS images of the same region of interest presented here are given. The dynamics of a living HeLa cell acquired in cELS mode is provided as a supplementary movie.

4.3 Sample illumination via four-arm crossing waveguide and application of fluorescence-based intensity-fluctuation algorithm to cELS

A multi-moded straight waveguide supports modes predominantly along a straight line. For the waveguide geometry shown in Figure S3 of the supplementary section, the angle the modes described by Eq. (S3) of the supplementary material make with respect to the optic axis (z-axis) is given by $\theta = \cos^{-1}\beta/kn_1$ [39]. The difference in θ between the first mode ($\beta = 1.75$) and say the twentieth mode ($\beta = 1.76$) is only about 5 degrees. This fact of limited angular diversity between the modes can also be understood from Figure S2 in supplementary section. It is known that the period of interference fringes is inversely proportional to the angle between the modes. The argument of the cosine function in Eq. (5) depends on the angle between the two interfering beams. Since the angle between the modes is small, the Fourier peaks of the cosine function are also located close to the origin, which is what is seen experimentally as shown in Figure S2. As a result, the enhancement in resolution is not isotropic. To mitigate this issue, a four-arm crossing waveguide is proposed, shown in Figure 7(a). The imaging region is highlighted by the green dotted lines in Figure 7(a) where several modes from the four-arms interfere. By illuminating the sample from several azimuthal orientations, the illumination frequencies become isotropic [27, 40–42]. This concept is illustrated experimentally in Figure 7(a) where 100 nm polystyrene beads are imaged using straight and four-arm junction waveguide. The images acquired using straight waveguides show the presence of coherent noise, predominantly along the direction of propagation of light. This is mitigated when illuminating the sample from all azimuthal directions as shown by the images of 100 nm polystyrene beads acquired using a four-arm crossing waveguide. Using a four-arm crossing waveguide, though we have more illumination frequencies illuminating the sample as shown in Figure S2 of the supplementary text, it is still not isotropic. Resolution enhancement will be predominantly along the direction of propagation of

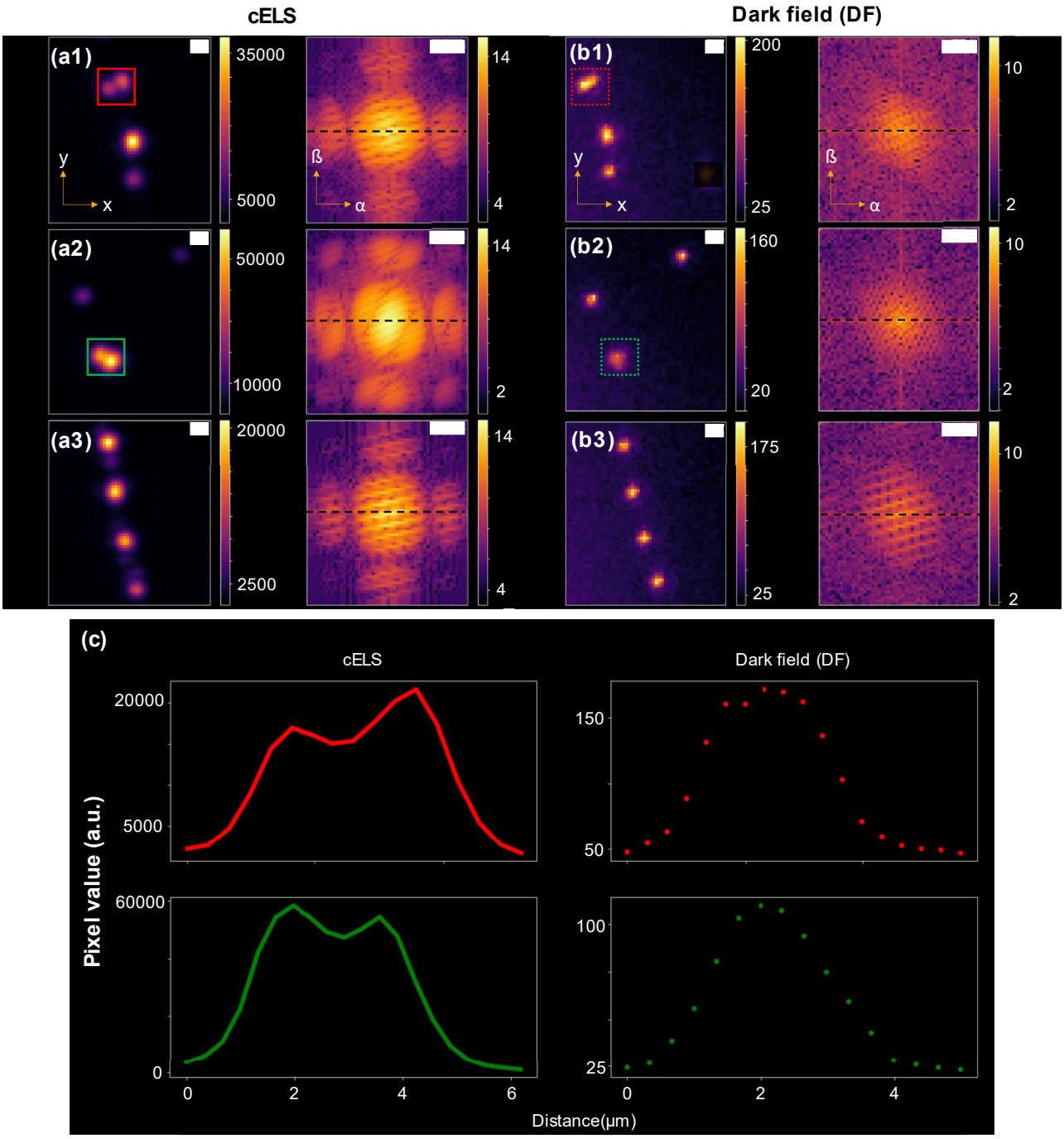

Figure 5: Comparison of 100 nm gold nanoparticles (GNP) imaged using cELS and dark-field (DF) microscopy. (a1)–(a3) Averaged image ($x-y$ plane) of 100 nm GNP of three different regions of interest imaged in cELS mode and acquired using a 10X/0.25 NA MO. Their corresponding Fourier spectrum ($\alpha-\beta$ plane) is shown alongside. (b1)–(b3) 100 nm beads imaged ($x-y$ plane) using a DF microscope with 10×/0.3 NA and their corresponding Fourier spectrum ($\alpha-\beta$ plane) is shown. The colorbars indicate the pixel values in the real image ($x-y$ plane). In the Fourier images ($\alpha-\beta$ plane) the colorbars indicate logarithm of the pixel values along the black dotted line. (c) Line plots of the cELS and DF images are shown. The line plots given by the red and green lines correspond to the boxes in (a1)–(a2) and are for the cELS images. The red and green dotted lines correspond to the dotted boxes in (b1)–(b2) and are for the DF images. To match the magnification between cELS and DF microscope, cELS images are bilinearly interpolated and displayed here. All the Fourier images are displayed on log scale for a better visualization. Scale bar 2 μm in real space and 500 mm^{-1} in Fourier space.

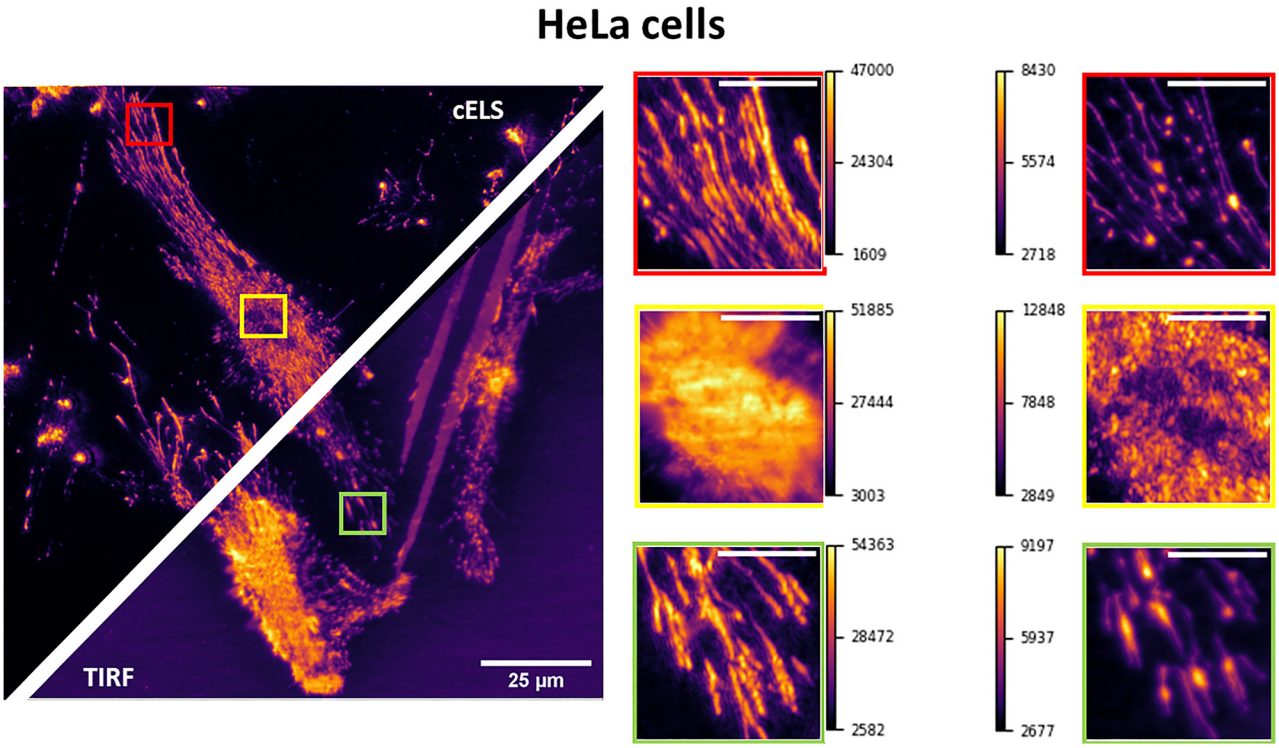

Figure 6: Comparison between cELS and TIRF images of Hela cells, scale bar 25 µm. Three different regions of interest enclosed by red, yellow, and green boxes are blown-up and provided alongside. The yellow box shows the nucleus region of the cell whereas the red and green boxes are the filaments, scale bar 8 µm. The color bars given alongside the magnified regions indicate the pixel values.

the light. To achieve isotropic resolution enhancement, the photonic-chip geometry used for structured illumination microscopy as in Ref. [30] needs to be adopted for cELS.

Next, we investigate the effect of MUltiple SIgnal Classification ALgorithm (MUSICAL) on the cELS data stack. MUSICAL helps extract sub-diffraction limit sized features from diffraction-limited image stacks like other intensity-fluctuation based fluorescence algorithms like SOFI (Super-resolution Optical Fluctuation Imaging) [43], SRRF (Super-Resolution Radial Fluctuations) [44], ESI (Entropy based Super-resolution Imaging) [45], 3B (Bayesian analysis of Blinking and Bleaching) [46], SACD (Super-resolution with Auto-Correlation two-step Deconvolution) [47]. Via singular value decomposition, MUSICAL decomposes the diffraction-limited image stack into spatial patterns in the shape of eigen-vectors and eigen values. Then based on the user input, the algorithm splits the eigen-vectors into two disjoint subsets – signal and noise to compute the final MUSICAL image which contains sub-diffraction limit sized features. For a more detailed analysis on MUSICAL, the readers may refer to [28].

The average diffraction-limited image of 100 nm polystyrene beads acquired in cELS mode is shown in Figure 7(a). Three different regions of interest from this diffraction-limited image are blown up and shown in Figure 7(b). The corresponding MUSICAL reconstructions are shown alongside. MUSICAL helps resolve beads better than the cELS image as explained earlier. However, caution must be exercised as artifacts could be introduced due to false localizations and artificial sharpening. The corresponding line profiles, green for cELS and red for MUSICAL on cELS, help illustrate the concepts explained.

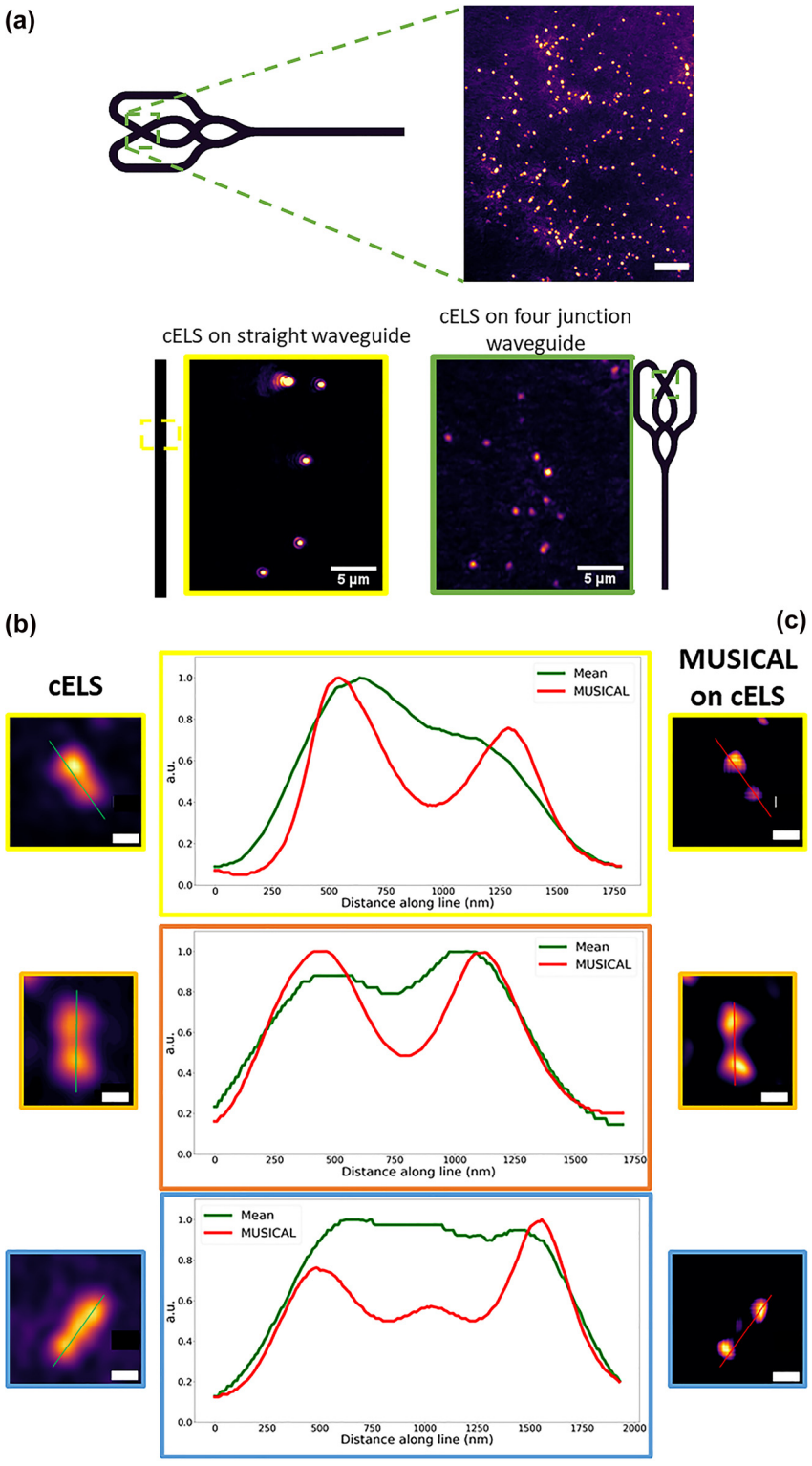

Figure 7: cELS on four arm junction waveguide and application of intensity fluctuation algorithm to cELS images.
(a) Four arm junction waveguide used for the experiments. 100 nm polystyrene beads imaged in cELS mode using a four-arm crossing waveguide is given, scale bar 10 µm. The green dotted box in the waveguide shows the imaging region. The use of a four-arm crossing waveguide mitigates the coherent scattering noise as shown by the images of 100 nm polystyrene beads imaged using straight and four crossing waveguides. Scale bar 5 µm. (b) Three different regions of interest of 100 nm polystyrene beads imaged in cELS mode. (c) The corresponding MUSICAL reconstruction is shown. A stack of 100 images is given as input for MUSICAL. Three separate regions of interest in yellow, orange, and blue boxes in cELS and the corresponding MUSICAL reconstructions are shown side by side. The line profiles of the regions are given as well. Scale bar 500 nm.

5 Conclusions

There already exists high-contrast label-free imaging techniques like waveguide-based techniques which use index-matched waveguides or/and incoherent light source for sample illumination [23–25], on-chip Fourier Ptychography using eight single moded waveguides for sample illumination [27], interferometric techniques that can achieve nanoscale sensitivity [48–55] etc. In this article we have demonstrated how a high-index contrast multi-moded waveguide can be used as a partially coherent light source for high-contrast imaging with enhanced resolution. We developed the theoretical framework and demonstrated experimental results of label-free super-contrast high-resolution optical microscopy method using a photonic-chip. The detection sensitivity of cELS depends on waveguide material impurities and surface roughness. However, silicon nitride based waveguides are complementary-metal-oxide-semiconductor (CMOS) compatible, which is a mature process. Therefore, we expect an improvement in detection sensitivity as has been demonstrated in Ref. [56].

It is important to mention that the mixing of high and low spatial frequency components at the image plane due to convolution between the object and illuminating field spectrum as explained earlier can lead to image distortions, see Supplementary section S5 for a more detailed discussion. And since the mixing of high frequency signals leads to the generation of moiré patterns which is finally collected by the microscope objective, sub-diffraction limit sized features of the sample will be enlarged more in the image plane [41, 42]. All these issues can distort the final image at the camera plane. However, owing to the nanoscale size of samples explored in this work (EVs, nanobead and liposomes), these issues are not significant.

Waveguide based imaging is an attractive imaging modality as has been demonstrated by the growing research in this field. Demonstrating label-free superior contrast and high-resolution imaging using waveguide-based imaging technology provides an attractive route to the field of label-free super-contrast high-resolution microscopy. Recently, an affordable waveguide-based 3D printed microscope has been used to image SARS-CoV-2 viroids [57]. Also, multi-modal imaging techniques by combining 3D structured illumination microscopy and ODT [58, 59], 3D quantitative phase imaging and SOFI [60] etc. have been demonstrated to provide complimentary information. Multi-modal imaging on chip of nano-sized viruses, exosomes, EVs and single-cell organisms such as microalgae and bacteria using cELS would be attractive applications, especially when combined with micro-fluidics [61]. We anticipate the results presented in this article will aid researchers in further developing the field of label-free super-contrast high-resolution microscopy.

Acknowledgments: The authors would like to thank all the staff at UiT for their support during the Covid19 times, Prof. Dr. Ulf Peschel of Friedrich Schiller University Jena, Sebastian Acuna Maldonado, Abhinanda Ranjit Punnakkal and Prof. Dr. Olav Gaute Hellesø of University of Tromsø for their valuable inputs.

Author contributions: NJ conceptualized the idea and designed the experiments along with BSA. FTD designed the waveguide chip and mask for fabrication. NJ, FTD, VD, AA was involved in sample preparation. NJ performed the experiments and analyzed the data. JC and NSB provided the liposome samples. EMG and OS provided the vesicles samples. NJ worked on the theory with inputs from FS, KA and BSA. NJ and BSA wrote the manuscript and all authors commented on the manuscript. KA and BSA supervised the project.

Research funding: This project has received funding from the European Union's Horizon 2020 research and innovation program under the Marie Skłodowska-Curie Grant Agreement No. 766181, project "DeLIVER". European Research Council (804233); H2020 Marie Skłodowska-Curie Actions (SEP-210382872); H2020 Marie Skłodowska-Curie Actions (31147, MSCA_ITN: 31147); Research Council of Norway (NANO 2021–288565); BIOTEK 2021 (BIOTEK 2021–285571).

Conflict of interest statement: The authors declare no conflicts of interest regarding this article.

Disclosures: B.S.A. have applied for patent GB1606268.9 for chip-based optical nanoscopy. B.S.A is the co-founder of the company Chip NanoImaging AS, which commercializes on-chip super-resolution microscopy systems.

References

[1] B. Redding, M. A. Choma, and C. Hui, "Speckle-free laser imaging using random laser illumination," *Nat. Photonics*, vol. 6, no. 6, pp. 355–359, 2012.

[2] Z. Wang, L. Millet, M. Mir, et al., "Spatial light interference microscopy (SLIM)," *Opt. Express*, vol. 19, no. 2, pp. 1016–1026, 2011.

[3] J. K. Zhang, Y. R. He, N. Sobh, and G. Popescu, "Label-free colorectal cancer screening using deep learning and spatial light interference microscopy (SLIM)," *APL Photonics*, vol. 5, no. 4, p. 040805, 2020.

[4] Y. K. Park, C. Depeursinge, and G. Popescu, "Quantitative phase imaging in biomedicine," *Nat. Photonics*, vol. 12, no. 10, pp. 578–589, 2018.
[5] Y. S. Baek and Y. K. Park, "Intensity-based holographic imaging via space-domain Kramers–Kronig relations," *Nat. Photonics*, vol. 15, no. 5, pp. 354–360, 2021.
[6] L. Waller, L. Tian, and B. George, "Transport of intensity phase-amplitude imaging with higher order intensity derivatives," *Opt. Express*, vol. 18, no. 12, pp. 12552–12561, 2010.
[7] J. Marrison, L. Räty, P. Marriott, and P. O'Toole, "Ptychography–a label free, high-contrast imaging technique for live cells using quantitative phase information," *Sci. Rep.*, vol. 3, no. 1, pp. 1–7, 2013.
[8] G. Zheng, R. Horstmeyer, and C. Yang, "Wide-field, high-resolution Fourier ptychographic microscopy," *Nat. Photonics*, vol. 7, no. 9, pp. 739–745, 2013.
[9] J. M. Soto, J. A. Rodrigo, and A. Tatiana, "Optical diffraction tomography with fully and partially coherent illumination in high numerical aperture label-free microscopy," *Appl. Opt.*, vol. 57, no. 1, pp. A205–A214, 2018.
[10] J. Li, A. C. Matlock, Y. Li, Q. Chen, C. Zuo, L. Tian, et al., "High-speed in vitro intensity diffraction tomography," *Adv. Photon.*, vol. 1, no. 6, p. 066004, 2019.
[11] G. Gbur and E. Wolf, "Diffraction tomography without phase information," *Opt. Lett.*, vol. 27, no. 21, pp. 1890–1892, 2002.
[12] A. Weigel, A. Sebesta, and P. Kukura, "Dark field microspectroscopy with single molecule fluorescence sensitivity," *ACS Photonics*, vol. 1, no. 9, pp. 848–856, 2014.
[13] F. Zernike, "How I discovered phase contrast," *Science*, vol. 121, no. 3141, pp. 345–349, 1955.
[14] Z. Liu, L. Tian, S. Liu, L. Waller, et al., "Real-time brightfield, darkfield, and phase contrast imaging in a light-emitting diode array microscope," *J. Biomed. Opt.*, vol. 19, no. 10, p. 106002, 2014.
[15] A. Priyadarshi, F. T. Dullo, D. L. Wolfson, et al., "A transparent waveguide chip for versatile total internal reflection fluorescence-based microscopy and nanoscopy," *Commun. Mater.*, vol. 2, no. 1, pp. 1–11, 2021.
[16] H. He and J. Ren, "A novel evanescent wave scattering imaging method for single gold particle tracking in solution and on cell membrane," *Talanta*, vol. 77, no. 1, pp. 166–171, 2008.
[17] D. Ruh, J. Mutschler, M. Michelbach, A. Rohrbach, et al., "Superior contrast and resolution by image formation in rotating coherent scattering (ROCS) microscopy," *Optica*, vol. 5, no. 11, pp. 1371–1381, 2018.
[18] W. Hickel and W. Knoll, "Optical waveguide microscopy," *Appl. Phys. Lett.*, vol. 57, no. 13, pp. 1286–1288, 1990.
[19] Ø. I. Helle, D. A. Coucheron, J. C. Tinguely, C. I. Øie, and B. S. Ahluwalia, "Nanoscopy on-a-chip: super-resolution imaging on the millimeter scale," *Opt. Express*, vol. 27, no. 5, pp. 6700–6710, 2019.
[20] J.-C. Tinguely, Ø. Ivar Helle, and B. Singh Ahluwalia, "Silicon nitride waveguide platform for fluorescence microscopy of living cells," *Opt. Express*, vol. 25, no. 22, pp. 27678–27690, 2017.
[21] I. S. Opstad, F. Ströhl, M. Fantham, et al., "A waveguide imaging platform for live-cell TIRF imaging of neurons over large fields of view," *J. Biophot.*, vol. 13, no. 6, p. e201960222, 2020.
[22] B. Agnarsson, A. B. Jonsdottir, N. B. Arnfinnsdottir, and K. Leosson, "On-chip modulation of evanescent illumination and live-cell imaging with polymer waveguides," *Opt. Express*, vol. 19, no. 23, pp. 22929–22935, 2011.
[23] D. J. Hill, C. W. Pinion, J. D. Christesen, and J. F. Cahoon, "Waveguide scattering microscopy for dark-field imaging and spectroscopy of photonic nanostructures," *ACS Photonics*, vol. 1, no. 8, pp. 725–731, 2014.
[24] X. Liu, C. Kuang, X. Hao, et al., "Fluorescent nanowire ring illumination for wide-field far-field subdiffraction imaging," *Phys. Rev. Lett.*, vol. 118, no. 7, p. 076101, 2017.
[25] B. Agnarsson, A. Lundgren, A. Gunnarsson, et al., "Evanescent light-scattering microscopy for label-free interfacial imaging: from single sub-100 nm vesicles to live cells," *ACS Nano*, vol. 9, no. 12, pp. 11849–11862, 2015.
[26] A. K. Engdahl, S. Belle, and T. C. Wang, "Large field-of-view super-resolution optical microscopy based on planar polymer waveguides," *ACS Photonics*, vol. 8, no. 7, pp. 1944–1950, 2021.
[27] F. Ströhl, I. S. Opstad, J. C. Tinguely, et al., "Super-condenser enables labelfree nanoscopy," *Opt. Express*, vol. 27, no. 18, pp. 25280–25292, 2019.
[28] K. Agarwal and R. Macháň, "Multiple signal classification algorithm for super-resolution fluorescence microscopy," *Nat. Commun.*, vol. 7, no. 1, pp. 1–9, 2016.
[29] N. Jayakumar, Ø. I. Helle, K. Agarwal, and B. S. Ahluwalia, "On-chip TIRF nanoscopy by applying Haar wavelet kernel analysis on intensity fluctuations induced by chip illumination," *Opt. Express*, vol. 28, no. 24, pp. 35454–35468, 2020.
[30] Ø. I. Helle, F. T. Dullo, M. Lahrberg, J. C. Tinguely, O. G. Hellesø, B. S. Ahluwalia, et al., "Structured illumination microscopy using a photonic chip," *Nat. Photonics*, vol. 14, no. 7, pp. 431–438, 2020.
[31] L. Novotny and B. Hecht, *Principles of Nano-Optics*, Cambridge, Cambridge University Press, 2012.
[32] R. Diekmann, Ø. I. Helle, C. I. Øie, et al., "Chip-based wide field-of-view nanoscopy," *Nat. Photonics*, vol. 11, no. 5, pp. 322–328, 2017.
[33] Y. Ben-Aryeh, "Tunneling of evanescent waves into propagating waves," *Appl. Phys. B*, vol. 84, no. 1, pp. 121–124, 2006.
[34] J. A. Kong, *Theory of Electromagnetic Waves*, New York, 1975.
[35] E. Wolf, *Introduction to the Theory of Coherence and Polarization of Light*, Cambridge, Cambridge University Press, 2007.
[36] J. W. Goodman, *Statistical optics*, New York, John Wiley & Sons, 2015.
[37] K. Wicker and R. Heintzmann, "Resolving a misconception about structured illumination," *Nat. Photonics*, vol. 8, no. 5, pp. 342–344, 2014.
[38] J. Cauzzo, N. Jayakumar, B. S. Ahluwalia, A. Ahmad, and N. Škalko-Basnet, "Characterization of liposomes using quantitative phase microscopy (QPM)," *Pharmaceutics*, vol. 13, no. 5, p. 590, 2021.
[39] A. A. Ghatak and K. Thyagarajan, *An Introduction to Fiber Optics*, Cambridge University Press, 1998.

[40] C. Pang, J. Li, M. Tang, et al., "On-chip super-resolution imaging with fluorescent polymer films," *Adv. Funct. Mater.*, vol. 29, no. 27, p. 1900126, 2019. https://doi.org/10.1002/adfm.201900126.

[41] M. Tang, X. Liu, Z. Wen, et al., "Far-field superresolution imaging via spatial frequency modulation," *Laser Photon. Rev.*, vol. 14, no. 11, p. 2020, 1900011. Available at: https://doi.org/10.1002/lpor.201900011.

[42] X. Hao, C. Kuang, Y. Li, X. Liu, et al., "Evanescent-wave-induced frequency shift for optical superresolution imaging," *Opt. Lett.*, vol. 38, no. 14, pp. 2455–2458, 2013.

[43] T. Dertinger, R. Colyer, G. Iyer, S. Weiss, J. Enderlein, et al., "Fast, background-free, 3D super-resolution optical fluctuation imaging (SOFI)," *Proc. Natl. Acad. Sci. USA*, vol. 106, no. 52, pp. 22287–22292, 2009.

[44] N. Gustafsson, S. Culley, G. Ashdown, D. M. Owen, P. M. Pereira, and R. Henriques, "Fast live-cell conventional fluorophore nanoscopy with ImageJ through super-resolution radial fluctuations," *Nat. Commun.*, vol. 7, no. 1, pp. 1–9, 2016.

[45] I. Yahiatene, S. Hennig, M. Mu¨ller, and T. Huser, "Entropy-based super-resolution imaging (ESI): from disorder to fine detail," *ACS Photonics*, vol. 2, no. 8, pp. 1049–1056, 2015.

[46] S. Cox, E. Rosten, J. Monypenny, et al., "Bayesian localization microscopy reveals nanoscale podosome dynamics," *Nat. Methods*, vol. 9, no. 2, pp. 195–200, 2012.

[47] W. Zhao, J. Liu, C. Kong, et al., "Faster super-resolution imaging with auto-correlation two-step deconvolution," arXiv preprint arXiv:1809.07410, 2018.

[48] M. Jin, S. J. Tang, J. H. Chen, et al., "1/f-noise-free optical sensing with an integrated heterodyne interferometer," *Nat. Commun.*, vol. 12, no. 1, pp. 1–7, 2021.

[49] G. De Wit, J. S. Danial, P. Kukura, M. I. Wallace, et al., "Dynamic label-free imaging of lipid nanodomains," *Proc. Natl. Acad. Sci. USA*, vol. 112, no. 40, pp. 12299–12303, 2015.

[50] R. W. Taylor, R. G. Mahmoodabadi, V. Rauschenberger, A. Giessl, A. Schambony, and V. Sandoghdar, "Interferometric scattering microscopy reveals microsecond nanoscopic protein motion on a live cell membrane," *Nat. Photonics*, vol. 13, no. 7, pp. 480–487, 2019.

[51] O. Avci, M. I. Campana, C. Yurdakul, and M. S. Ünlü, "Pupil function engineering for enhanced nanoparticle visibility in wide-field interferometric microscopy," *Optica*, vol. 4, no. 2, pp. 247–254, 2017.

[52] G. G. Daaboul, A. Yurt, X. Zhang, G. M. Hwang, B. B. Goldberg, M. S. Unlu, et al., "High-throughput detection and sizing of individual low-index nanoparticles and viruses for pathogen identification," *Nano Lett.*, vol. 10, no. 11, pp. 4727–4731, 2010.

[53] J. Ortega Arroyo, J. Andrecka, K. M. Spillane, et al., "Label-free, all-optical detection, imaging, and tracking of a single protein," *Nano Lett.*, vol. 14, no. 4, pp. 2065–2070, 2014.

[54] M. E. Kandel, K. W. Teng, P. R. Selvin, G. Popescu, et al., "Label-free imaging of single microtubule dynamics using spatial light interference microscopy," *ACS Nano*, vol. 11, no. 1, pp. 647–655, 2017.

[55] C. Yurdakul, O. Avci, A. Matlock, et al., "High-throughput, high-resolution interferometric light microscopy of biological nanoparticles," *ACS Nano*, vol. 14, no. 2, pp. 2002–2013, 2020.

[56] S.-J. Tang, S. Liu, X. C. Yu, Q. Song, Q. Gong, Y. F. Xiao, et al., "On-chip spiral waveguides for ultrasensitive and rapid detection of nanoscale objects," *Adv. Mater.*, vol. 30, no. 25, p. 1800262, 2018.

[57] B. Diederich, Ø. Helle, P. Then, et al., *Nanoscopy on the Chea (i)*, bioRxiv., 2020.

[58] S. Chowdhury, W. J. Eldridge, A. Wax, and J. A. Izatt, "Structured illumination multimodal 3D-resolved quantitative phase and fluorescence sub-diffraction microscopy," *Biomed. Opt. Express*, vol. 8, no. 5, pp. 2496–2518, 2017.

[59] S. Shin, D. Kim, K. Kim, and Y. Park, "Super-resolution three-dimensional fluorescence and optical diffraction tomography of live cells using structured illumination generated by a digital micromirror device," *Sci. Rep.*, vol. 8, no. 1, pp. 1–8, 2018.

[60] A. Descloux, K. S. Grußmayer, E. Bostan, et al., "Combined multi-plane phase retrieval and super-resolution optical fluctuation imaging for 4D cell microscopy," *Nat. Photonics*, vol. 12, no. 3, pp. 165–172, 2018.

[61] M. Boninsegna, N. Jayakumar, F. T. Dullo, et al., "Waveguide chip coupled with microfluidics enables super-resolution live-cell imaging," in *Novel Optical Systems, Methods, and Applications XXIII*, vol. 11483, California, USA, SPIE, 2020.

Supplementary Material: The online version of this article offers supplementary material (https://doi.org/10.1515/nanoph-2022-0100).

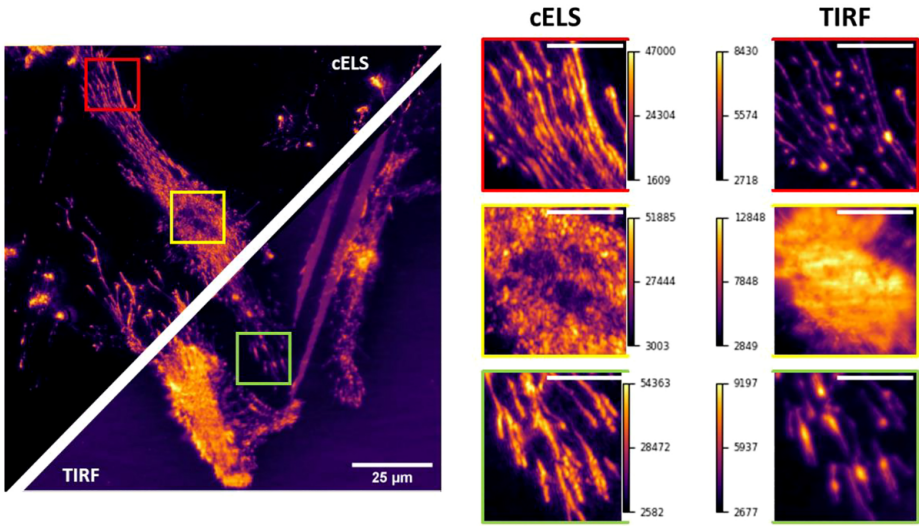

Figure 4.3: cELS and TIRF images of the same field-of-view are provided. In this experiment, HeLa cells are imaged in both cELS and TIRF configuration, scale bar 25 μm. cELS imaging is performed at 660 nm wavelength. For TIRF imaging, actin filaments of the HeLa cells are labelled and imaged at 532 nm excitation and emission is observed at 595/40 nm. Three regions of interest shown in red, yellow and green boxes are blown up and provided alongside, scale bar 8 μm. The colour bars provided alongside indicate the pixel values in cELS and TIRF images. In the yellow box, the nucleus of the cell is shown. As opposed to cELS, some of the features of the nucleus are lost in the TIRF image and are attributed to a dense population of fluorophores in the nucleus region of the cell.

Multi-moded high-index contrast optical waveguide for super-contrast high-resolution label-free microscopy

NIKHIL JAYAKUMAR,[1,6] FIREHUN T DULLO,[2] VISHESH DUBEY,[1] AZEEM AHMAD,[1] FLORIAN STRÖHL, [1] JENNIFER CAUZZO, [3] EDUARDA MAZAGAO GUERREIRO, [4] OMRI SNIR, [4] NATASA SKALKO-BASNET, [3] KRISHNA AGARWAL,[1] AND BALPREET SINGH AHLUWALIA[1,5,7]

[1] *Department of Physics and Technology, UiT The Arctic University of Norway, Tromsø 9037, Norway*
[2] *SINTEF Digital, Department of Microsystems and Nanotechnology, Gaustadalleen 23C, 0373 Oslo, Norway*
[3] *Department of Pharmacy, Faculty of Health Sciences, UiT The Arctic University of Norway, Tromsø 9037, Norway*
[4] *Department of Clinical Medicine, UiT The Arctic University of Norway, Tromsø 9037, Norway*
[5] *Department of Clinical Science, Intervention and Technology, Karolinska Insitute, 17177 Stockholm, Sweden*
[6]*nik.jay.hil@gmail.com*, [7]*balpreet.singh.ahluwalia@uit.no*

This document supplements the work described in the main article. The concept of modes, the theory behind the formation of images in cELS and the application of cELS to imaging is provided here.

S1. Optical modes in waveguides

Waveguide core material	Refractive index at 660 nm
Si_3N_4	2.0804
Ta_2O_5	2.2080
TiO_2	2.5607

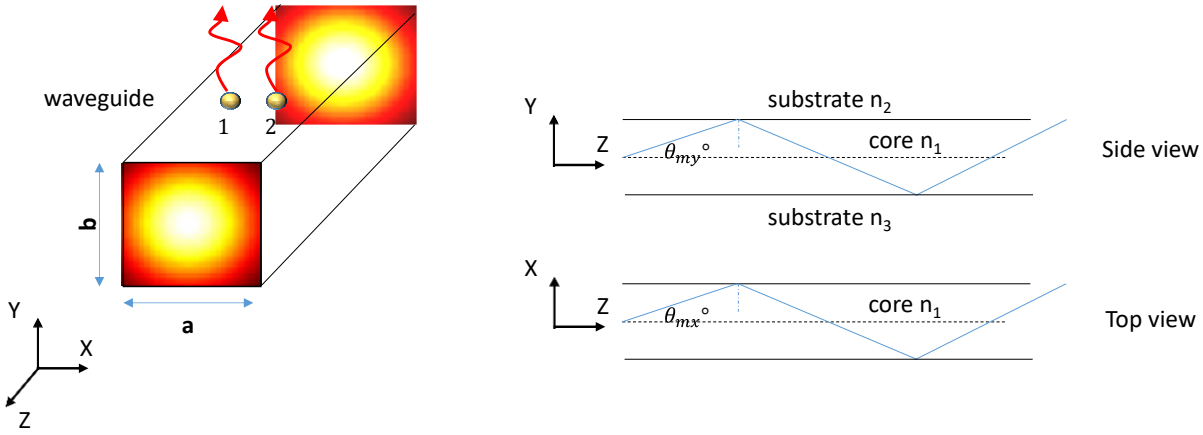

FIG. S1. Schematic of a rectangular waveguide with a Gaussian mode profile being guided along its length. The modes are field distributions that propagate keeping its transverse profile (x-y) intact. They merely accumulate a phase with distance 'z'. A waveguide supports discrete and not a continuum set of modes, ψ_m, and each mode is characterized by a discrete angle of propagation θ_m. Two-point particles, placed on the x-z plane, with a different refractive index scatters the evanescent field into the far-field.

Assume that the dielectric constant 'ϵ' depends only on the transverse co-ordinate, x, and y. It means that along z-axis, the modes will accumulate only a phase as it propagates along the length of the waveguide. This will help reduce Maxwell's equations to two independent sets of solutions called transverse electric (TE) and transverse magnetic modes. For TE modes the Helmholtz equation is given as

$$(\frac{d^2}{dx^2}+\frac{d^2}{dy^2})E_y + {k_0}^2\epsilon(x,y)E_y = ß^2E_y \qquad \text{(S1)}$$

where E_y is the y-component of the electric field, $k_0 = \omega/c$ is the free-space wave number and ß is the propagation constant of the mode. For comparison, the two-dimensional time-independent Schrödinger equation is given, where $V(x,y)$ is the potential, $\psi_{(x,y)}$ is the wavefunction and E is the energy of the particle.

$$\frac{-h^2}{2m}(\frac{d^2}{dx^2}+\frac{d^2}{dy^2})\psi_{(x,y)} + V(x,y)\psi(x,y) = E\psi(x,y) \qquad \text{(S2)}$$

For the waveguides used here the refractive index of the core n_1 is greater than that of the substrates. Now comparing Eqn. (S1) and (S2), the dielectric constant is similar to the potential function. Or it means that light gets attracted to areas of higher dielectric constant, i.e., light gets attracted towards the core for the waveguides considered here. The solution of Eqn. (S1) can be found to be oscillatory in nature inside the core and the boundary conditions at the core-cladding interface impose decaying behavior for the evanescent fields. Now for a rectangular dielectric waveguide with dielectric constant $\epsilon(x,y)$, the general Helmholtz equation when solved yields the following solutions.

$$\begin{aligned} E_x &\approx \cos\frac{m\pi x}{a}\sin\frac{n\pi y}{b}e^{-ißz} \\ E_y &\approx \sin\frac{m\pi x}{a}\cos\frac{n\pi y}{b}e^{-ißz} \\ H_x &\approx \sin\frac{m\pi x}{a}\cos\frac{n\pi y}{b}e^{-ißz} \\ H_y &\approx \cos\frac{m\pi x}{a}\sin\frac{n\pi y}{b}e^{-ißz} \end{aligned} \qquad \text{(S3)}$$

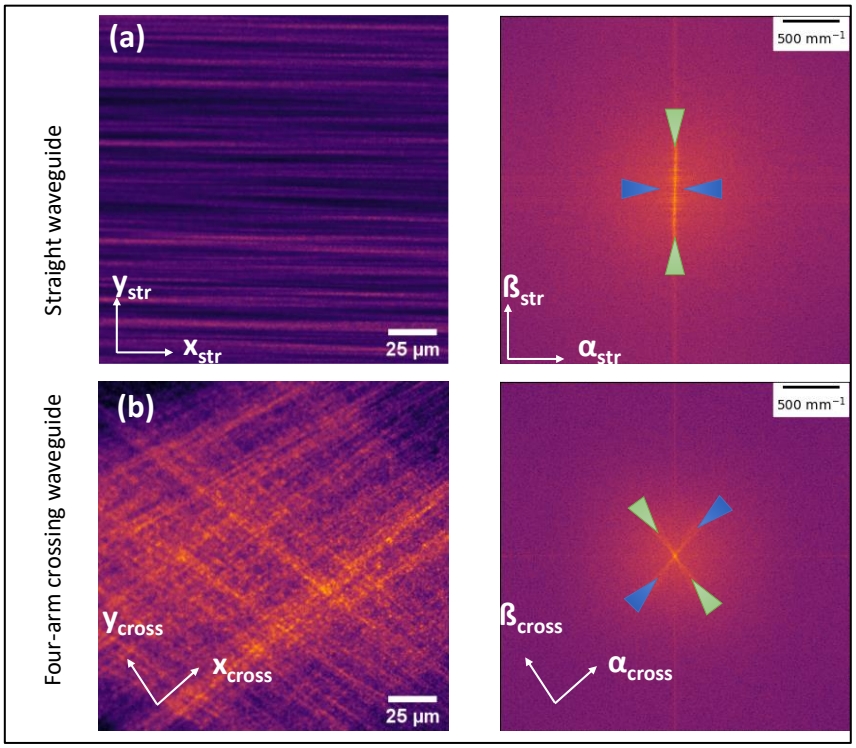

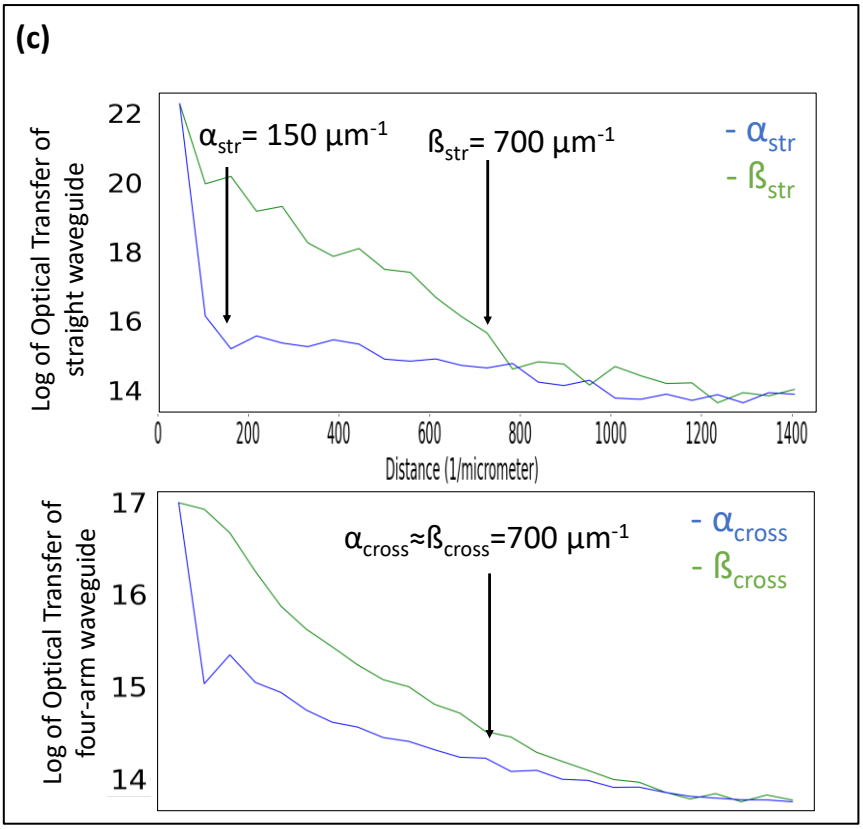

FIG. S2. The multiple modes overlap to produce speckle patterns. (a) The use of straight waveguides limits the illumination spatial frequencies to regions around the vertical axis, $ß_{str}$. This can be understood from the Fourier spectrum of the speckle pattern shown alongside. The blue and green triangles mark the cut-off frequency along the (α_{str}-$ß_{str}$) plane of the Fourier space for the straight waveguide. (b) To mitigate this issue and ensure isotropic sample illumination a four-arm crossing waveguide is proposed. Such an illumination geometry provides more illumination frequencies to the sample. This is demonstrated by the Fourier spectrum of the illumination frequencies shown alongside. The blue and green triangles mark the cut-off frequency along the (α_{cross}-$ß_{cross}$) plane of the Fourier space for the four-crossing waveguide. Scale bar 25 µm in real space images and 500 mm^{-1} in Fourier images. (c) The value of the Fourier spectrum along the blue and green triangles shown in (a) and (b) are plotted. Cut-off frequency along α_{str}-$ß_{str}$ of the straight waveguide and α_{cross}-$ß_{cross}$ of the four-arm crossing waveguide is marked.

The above equation constitutes the TE_{mn} modes where m = 0,1,2… and n = 0,1,2 etc. It implies that the modes are discrete and not continuous. Each of these modes can be also represented as a sum of two plane waves propagating at angles $\pm\theta$ with respect to the z-axis as shown in Fig. S1. These modes propagate along the length of the waveguide through the generation of evanescent waves at the core-cladding interface. The physical understanding of the generation of evanescent waves can be as follows. The incident wave vector $\overrightarrow{k_i} = \alpha_i\hat{x} + ß_i\hat{y} + \gamma_i\hat{z}$ strikes the core-substrate interface as shown in Fig. S1. The dispersion relation for the wave vector in the core is given by $\vec{k_i}^2 = \alpha_i^2 + ß_i^2 + \gamma_i^2$ and for the cladding is $\vec{k}_{cla}{}^2 = \alpha_{cla}^2 + ß_{cla}^2 + \gamma_{cla}^2$. The high index core squeezes the wave fronts at the interface. This implies that for phase matching at the core-cladding interface one of the wave vector components, $ß_{cla}$, of the cladding must become imaginary. This imaginary component of the wave vector leads to an exponential decay of the field away from the interface, i.e., along the y-axis in Fig. S1, and they are known as evanescent waves.

The discrete number of modes imply that there are discrete angles of propagation, and they can overlap in space and lead to speckles or multi-mode interference patterns as shown in Fig. S2. This makes the illumination profile non-uniform and speckle ridden. The Fourier spectrum of the illumination profile shows that in case of a straight waveguide, the illumination spatial frequencies are restricted along the k_y axis. As a result, isotropic resolution enhancement is not possible. Also, when intensity fluctuation based algorithms are applied on image stacks

acquired using straight waveguides, the fluctuations in intensity will be predominantly along the vertical axis, thereby restricting the resolution enhancement only along the vertical axis.

S2. Theory of image formation in cELS

Consider two particles '1' and '2' placed on top of the waveguide surface as shown in Fig. S3. The input coherent laser light excites a few modes inside the waveguide. For clarity only two of these modes are depicted in Fig. S3. As mentioned in Ref. [1], any mode 'm' may be decomposed into a pair of plane waves propagating at angle $\pm\theta_m$ with respect to the z-axis. Therefore, two modes are represented in green (mode m1) and red color (mode m2) propagating inside the core. The tails of these modes extend into the cladding and interact with the particles located there. The particles are polarized as a result and radiate into the far-field which is detected by the camera.

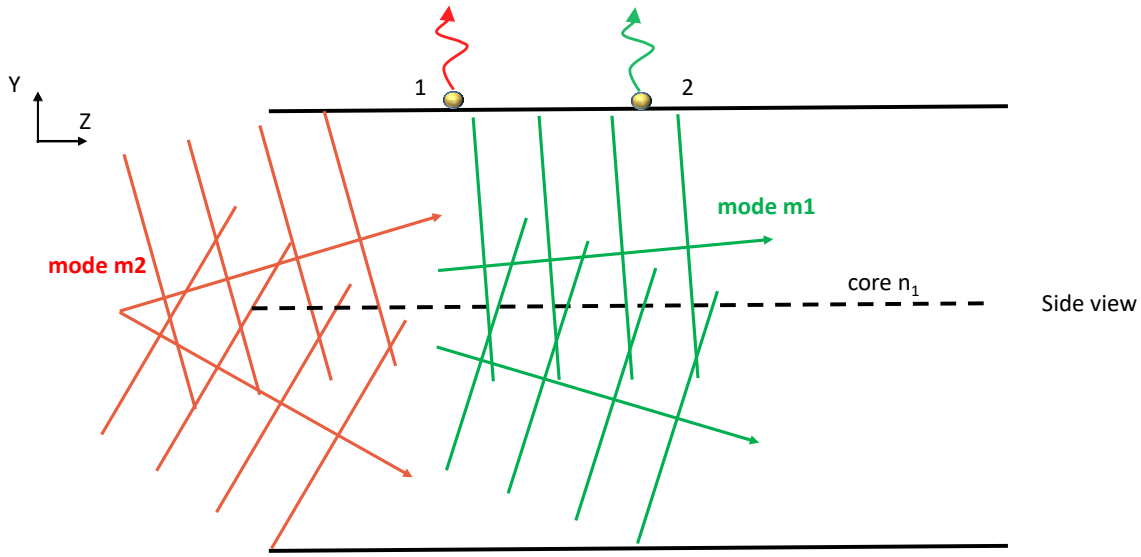

FIG. S3. Theory of cELS image formation. Two modes of the waveguide m1 and m2 are shown in green and red color respectively. The modes are decomposed into a pair of plane waves propagating at discrete angles with respect to the optical axis along z. The evanescent tails of these guided modes interact with particles 1 and 2 placed on the surface and as a result, light is scattered into the far-field.

Neglecting the vectorial aspect of light, let the scalar field generated by the two particles be $U_1(\boldsymbol{r},t) = a_1(\boldsymbol{r})e^{i\varphi_1(\boldsymbol{r},t)-i\omega t}$ and $U_2(\boldsymbol{r},t) = a_2(\boldsymbol{r})e^{i\varphi_2(\boldsymbol{r},t)-i\omega t}$. For simplicity assume that the two particles are identical and radiate with the same amplitude distribution, i.e., $a_1(\boldsymbol{r}) = a_2(\boldsymbol{r}) = a(\boldsymbol{r})$. The coherence lengths of waveguides have been experimentally calculated in Ref. [2] via the visibility of interference fringes. For silicon waveguides fabricated in standard CMOS foundry, the coherence lengths are found to be approximately 4.17 mm for rib and 1.6 mm for strip geometry [2] and it is about 27 m for phosphorous-doped core silica on silicon waveguides. The main source of fluctuations is attributed to variations in waveguide dimension and composition. These fluctuations manifest mainly in the phase of the light scattered by the particles and is accounted for by making the phase, $\varphi_j(\boldsymbol{r}) = \overrightarrow{k_j}.\overrightarrow{r}$, a function of time 't', i.e., $\varphi_j(\boldsymbol{r}) = \varphi_j(\boldsymbol{r},t)$, where j=1,2 represent the two particles described here. The total electric field $U_T(\boldsymbol{r},t)$ reaching the camera will be

$$U_T(\boldsymbol{r},t) = (U_1(\boldsymbol{r},t) + U_2(\boldsymbol{r},t)) \otimes h(\boldsymbol{r}) \quad \text{(S4)}$$

where $h(\boldsymbol{r})$ is the coherent transfer function of the optical system, $\otimes$ represents convolution operation and bold letters represent vectors. The spectrum of the total field reaching the camera may be computed as

$$\widetilde{U_T}(\boldsymbol{k},t) = \widetilde{U_1}(\boldsymbol{k},t)\tilde{H}(\boldsymbol{k}) + \widetilde{U_2}(\boldsymbol{k},t)\tilde{H}(\boldsymbol{k}) \quad \text{(S5)}$$

where $\widetilde{U_j}(\boldsymbol{k},t)$ is the Fourier transform of the amplitudes of the particles and $\widetilde{H}(\boldsymbol{k})$ is the amplitude transfer function. The Fourier transform of the fields $U_1(\boldsymbol{r},t)$ and $U_2(\boldsymbol{r},t)$ may be computed as $\widetilde{U_1}(\boldsymbol{k},t) = \tilde{A}(\boldsymbol{k}) \circledast \delta(\boldsymbol{k}-\boldsymbol{k_1}) = \tilde{A}(\boldsymbol{k_1})$ and $\widetilde{U_2}(\boldsymbol{k},t) = \tilde{A}(\boldsymbol{k}) \circledast \delta(\boldsymbol{k}-\boldsymbol{k_2}) = \tilde{A}(\boldsymbol{k_2})$. Substituting this result into Eqn. (S5) we can see that the shifted object spectrum field is low passed by the coherent transfer function. Now the instantaneous intensity in real space can be computed from Eqn. (S4) as follows

$$I_T(\boldsymbol{r},t) = [(U_1(\boldsymbol{r},t) + U_2(\boldsymbol{r},t)) \circledast h(\boldsymbol{r})].[(U_1{}^*(\boldsymbol{r},t) + U_2{}^*(\boldsymbol{r},t)) \circledast h^*(\boldsymbol{r})] \quad \text{(S6)}$$

In this work, we scanned the input facet of the waveguide with a galvo to generate different sets of guided mode inside the waveguide. This generates speckle patterns that get added up incoherently during the integration time of the camera at the detector plane. This can be represented mathematically as

$$\langle I_T(\boldsymbol{r},t)\rangle = I_1(\boldsymbol{r},t) + I_2(\boldsymbol{r},t) + \cdots = \textstyle\sum_n I_n(\boldsymbol{r},t) \quad \text{(S7)}$$

The final image generated by the camera is obtained as described by Eqn. (S7). To understand the Fourier transform of the cELS image generated, Eqn. (S6) may be Fourier transformed and then generalized for Eqn. (S7). Fourier transforming Eqn. (S6) gives

$$\tilde{I}_T(\boldsymbol{k},t) = \left[(\widetilde{U}_1(\boldsymbol{k},t) + \widetilde{U}_2(\boldsymbol{k},t)).\widetilde{H}(\boldsymbol{k})\right] \circledast \left[(\widetilde{U}_1{}^*(\boldsymbol{k},t) + \widetilde{U}_2{}^*(\boldsymbol{k},t)).\widetilde{H}^*(\boldsymbol{k})\right] \quad \text{(S8)}$$

Substituting for $U_j(\boldsymbol{r},t)$ in Eqn. (S8), it can be further reduced to the following form.

$$\tilde{I}_T(\boldsymbol{k},t) = \left[\tilde{A}(\boldsymbol{k_1}).\widetilde{H}(\boldsymbol{k}) + \tilde{A}(\boldsymbol{k_2}).\widetilde{H}(\boldsymbol{k})\right] \circledast \left[\tilde{A}^*(\boldsymbol{k_1}).\widetilde{H}^*(\boldsymbol{k}) + \tilde{A}^*(\boldsymbol{k_2}).\widetilde{H}^*(\boldsymbol{k})\right] \quad \text{(S9)}$$

where $\tilde{A}(\boldsymbol{k_1})$ and $\tilde{A}(\boldsymbol{k_2})$ represent the shifted Fourier spectrum of the two particles corresponding to the illumination fields exciting them, $\widetilde{H}(\boldsymbol{k})$ is the Fourier transform of the coherent transfer function and possess Hermitian symmetry, $\widetilde{H}(-\boldsymbol{k}) = \widetilde{H^*}(\boldsymbol{k})$. The spectrum of the final image obtained will then be given by adding the spectra described by Eqn. (S9). For ease of notation let $\tilde{P}(\boldsymbol{k}) = \tilde{A}(\boldsymbol{k_1}).\widetilde{H}(\boldsymbol{k})$ and $\tilde{Q}(\boldsymbol{k}) = \tilde{A}(\boldsymbol{k_2}).\widetilde{H}(\boldsymbol{k})$. Then Eqn. (S9) can rewritten as

$$\tilde{I}_T(\boldsymbol{k},t) = \tilde{P}(\boldsymbol{k}) \circledast \tilde{P}^*(\boldsymbol{k}) + \tilde{Q}(\boldsymbol{k}) \circledast \tilde{Q}^*(\boldsymbol{k}) + \tilde{P}(\boldsymbol{k}) \circledast \tilde{Q}^*(\boldsymbol{k}) + \tilde{P}^*(\boldsymbol{k}) \circledast \tilde{Q}(\boldsymbol{k}) \quad \text{(S10)}$$

For incoherent illumination the cross-terms in the above-mentioned equation, $\tilde{P}(\boldsymbol{k}) \circledast \tilde{Q}^*(\boldsymbol{k})$ and $\tilde{P}^*(\boldsymbol{k}) \circledast \tilde{Q}(\boldsymbol{k})$, will tend to zero on time averaging and therefore, becomes linear in intensity. Thus, Eqn. (S10) represents the spectrum for coherent illumination. The spectrum of the final image will be the sum of many individual spectrums represented by Eqn. (S10) as explained earlier.

The following interesting cases may be noted while illuminating with waveguide modes. As per first order Born approximation, the incident and scattered waves can be assumed to have the same phase [3]. Therefore, the phase difference between the scattered waves off the two particles can be assumed to be dependent only on the illuminating field, the phase of which varies with the position of the particles. This can be understood as follows. Consider the situation where the two particles depicted as in Fig. (S3) are illuminated by the same mode. The two particles are assumed to be located at a separation of Rayleigh distance = 0.61λ/NA, where NA is the numerical aperture of the microscope objective and λ is the wavelength of detected light. In the experiments presented here, λ = 660 nm and NA = 1.2. Therefore, the two particles can be assumed to be located along the x-axis at (0, b/2, 0) and (0.508a, b/2, 0). In case of incoherent illumination, i.e., if fluorescent particles are used, they will be just resolved as per Rayleigh's resolution criteria. However, in case of cELS the following cases may arise.

1. The two particles are illuminated by the same mode m1, see Fig. (S3). For example, consider illumination with TE_{11} mode (m=1, n=1). Substituting the particle's location into Eqn. (S3) it can be seen that the phase difference between the scattered light reaching the detector will be approximately 1.6 radians. It implies that the interference term will not cause as much dip in intensity as observed in Rayleigh resolution limit, which corresponds to a phase difference of $\boldsymbol{\pi}$ radians between the particles. It may be noted that the field equations given in Eqn. (S3) are the oscillatory solutions for the guided modes inside the core. For evanescent waves the same field distribution is obtained except for the fact that γ_i becomes complex, i.e., exponentially decaying along the z-axis.
2. The two particles are illuminated by say TE_{11} and TE_{21} mode. Then the phase difference between the particles from Eqn. (S3), is found to be $\boldsymbol{\pi}$ radians which corresponds to the particles being resolved as per Rayleigh's criteria. Hence, a much deeper dip in intensity is observed than in the previous case.

Within the exposure time of the camera, the galvo would have oscillated several times back and forth. In the experiments presented here the galvo oscillation rate is set as a prime number at 1013 Hz. The exposure time of the camera was typically set to 30 ms. It means that the galvo would have oscillated approximately 30 times back and forth within 30 ms. The phase of the light varies at a rate order of magnitude higher than the exposure time of the camera or the oscillation rate of the galvo. At each position of the galvo, it will excite a set of modes. The particles scatter the light that interferes at the camera plane. The galvo then moves to the next position and again the particles scatter light with a different phase difference between them as explained earlier. The final image generated by the camera at the end of it's integration time will be the sum of the different intensity distributions of the light scattered by particles. The phase difference between light scattered off by the particles due to multi-mode illumination can be assumed to have values ranging between $-\boldsymbol{\pi}$ and $+\boldsymbol{\pi}$ radians. Therefore, the final image formed at the camera plane can be considered a superposition of different speckle patterns with different phase differences, and thus resembling a random walk. This helps mitigate speckle noise as illustrated in [4].

S3. Role of coherence in image formation

The longitudinal coherence lengths of a light source may be deduced from Wiener-Khintchin theorem and is given by [5]:

$$\frac{1}{L_c} \approx \frac{2\sin^2\theta/2}{\lambda_0} + \frac{\Delta\lambda}{{\lambda_0}^2}\cos^2\theta/2 \qquad \text{(S10)}$$

where L_c is the longitudinal coherence length as a function of both angular and temporal spectrum, λ_0 is the center wavelength of the temporal spectrum of a source with temporal bandwidth $\Delta\boldsymbol{\lambda}$, $l_c \approx \frac{{\lambda_0}^2}{\Delta\lambda}$ is the temporal coherence length of the light source and θ is width of angular spectrum. The longitudinal coherence length gives the length over which the photons remain correlated. A similar expression as in Eqn. (S10) is also obtained for transverse coherence lengths [5]. The coherence volume of the field may be defined as the product of the transversal and longitudinal coherence lengths. Only photons within the coherence volume can interfere to generate a sustained interference pattern.

For the experiments presented in this article, cELS imaging have been carried out using a diode laser, Cobalt Flamenco 660 nm laser. The bandwidth of this laser is < 1 GHz as mentioned in the company website. This implies a coherence time of ≈ 159 ns. The exposure time of the camera is 30 ms and therefore, a number of different speckle patterns as described earlier will get generated within the integration time of the camera. As a result, the degree of coherence is not unity and therefore, using this laser itself some mitigation in speckle noise is achieved. In contrast, if fluorescence imaging is performed, for example such as TIRF mentioned in this article, a larger number of speckle patterns will get generated within the integration time of the camera. It means the use of fluorescence will yield a highly incoherent illumination. For example, if the bandwidth of fluorescence emission is 100 nm, then the coherence time of the laser can be shown to ≈ 3 fs. It means that more that 10^6

speckle patterns as compared to cELS imaging will get generated within the exposure time of the camera and therefore, more reduction in speckle noise is observed.

S4. Waveguide fabrication and characterization

The imaging platform is based on silicon nitride (Si_3N_4) waveguides on a silicon wafer, fabricated by low-pressure chemical vapor deposition and reactive-ion etching as detailed in [6]. Waveguide chips were produced at the Institute of Microelectronics Barcelona (IMB-CNM, Spain). Waveguide fabrication steps as follows: a 2µm thick silica layer was grown thermally on the silicon wafer, followed by deposition of silicon nitride layer via low-pressure chemical vapor deposition (LPCVD) at 800°C. The waveguide structures are then created via photolithography and reactive ion etching (RIE) to produce the required 2-D waveguides.

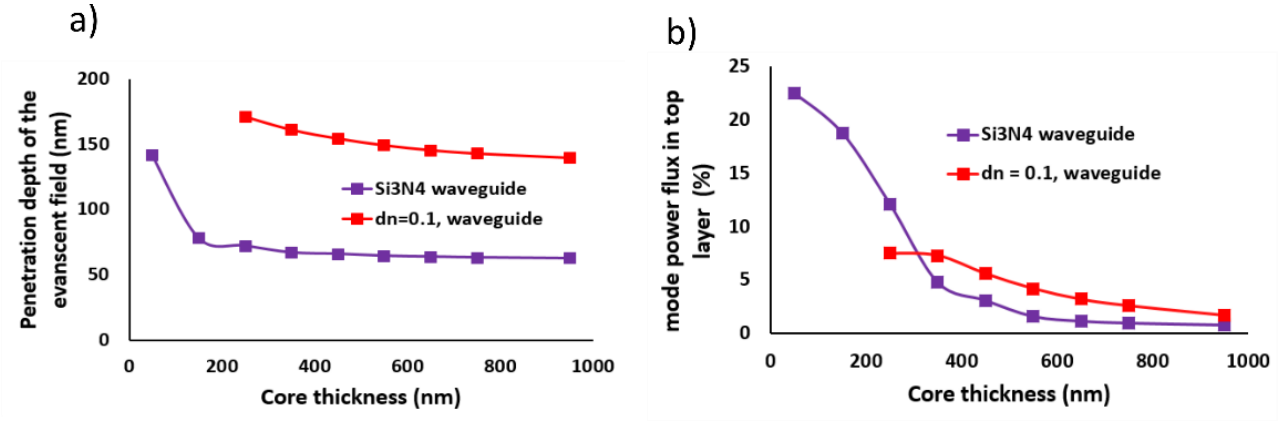

FIG. S4. The (a) penetration depth and (b) field intensity of a TE1 mode of Si_3N_4 high index core ($\Delta n \approx 0.5$) waveguide and an index matched waveguide ($\Delta n \approx 0.1$) are provided here.

Ref No. (Supp)	Title	Waveguide geometry and material	Excitation light for waveguide	Light registered by the camera
7	Optical Waveguide Microscopy	Planar geometry for the guiding structure. Two different core materials SiO_2 and solid polyelectrolyte (polymer) used.	Coherent laser light	Coherent laser light
8	Waveguide Scattering Microscopy for Dark-Field Imaging and Spectroscopy of Photonic Nanostructures (WSM)	Dielectric slab waveguide (standard microscope slides or coverslips used for imaging.)	Incoherent white light	Incoherent white light
9	Fluorescent Nanowire Ring Illumination for Wide-Field Far-Field Subdiffraction Imaging	Film waveguide (SiO_2, Al_2O_3 and TiO_2)	Fluorescent light emitted from nanowire rings (incoherent broadband light)	Fluorescent light (incoherent broadband light)

10	Evanescent Light-Scattering Microscopy for Label-Free Interfacial Imaging: From Single Sub-100 nm Vesicles to Live Cells	Planar core (SiO_2) with polymer cladding.	Coherent laser light	Coherent laser light
11	Super-condenser enables label-free nanoscopy	Si_3N_4 rib single moded waveguide	Coherent laser light	Coherent laser light

Table 1: Comparison between different on-chip label-free microscopy works.

S5. Liposomes preparation, characterization and labeling

Labeled liposomes were formulated with a mass ratio 100:1 comprising soy phosphatidylcholine (SPC, Lipoid S100, main lipid ingredient kindly provided by Lipoid GmbH, Ludwigshafen, Germany) and 1-myristoyl-2-{6-[(7-nitro-2-1,3-benzoxadiazol-4-yl)amino]hexanoyl}-sn-glycero-3- phosphocholine (fluorescently labeled phospholipid, obtained from Avanti Polar Lipids, Alabaster, AL, USA). The film hydration method was used to prepare a multilamellar/multivesicular dispersion. A methanol solution of both ingredients was subjected to gentle solvent removal (Büchi Rotavapor, Büchi Labortechnik, Flawil, Switzerland) and the thin film obtained was rehydrated by hand shaking to the final concentration of 10 mg/mL of SPC and 0.1 mg/mL of labeled lipid. Stepwise extrusion through polycarbonate membranes (Nucleopore®) of 800, 400 and 200 nm sieving sizes was performed for efficient size reduction of the vesicles [12]. Hence, dynamic light scattering was utilized for conventional characterization (Malvern Zetasizer Nano – SZ, Malvern Oxford, UK), obtaining Gaussian distributions for size (121±30 nm, with polydispersity index of 0.19±0.01) and zeta-potential (-9.39±3.3 mV, as estimation of the surface charge).

S6. EV preparation, characterization and labeling

Isolation of platelet-derived extracellular vesicles

Blood (50 ml) was collected from healthy volunteers into non-glass Vacuette tubes (6ml Z with no additive, Greiner Bio-One, Austria). Acidic citrate dextrose (ACD, 39 mM citric acid, 75 mM sodium citrate, 135 mM [D]-glucose, pH 4.5) buffer was added immediately to the tubes to prevent clotting. Platelet rich plasma (PRP) was generated by centrifuging the blood at 140gx for 15 min with no brakes. PRP was transferred to fresh tubes and ACD and 2.83 µM Prostaglandin E1 (PGE1, Sigma) were added and centrifuged at 900 gx for 15 min to pellet the platelets. Supernatant was discarded and platelets were resuspended in Ca^{2+} free Tyrode-HEPES buffer (137 mM NaCl, 0.3 mM NaH_2PO_4, 3.5 mM HEPES, 5.5 mM [D]-glucose, pH 7.35) and washed twice by centrifuging at 900 gx for 15 min. Platelet washes were carried out in the presence of PGE1 at 2.83 µM to prevent their activation. Once washed, platelets were resuspended in Tyrode buffer (137 mM NaCl, 0.3 mM NaH_2PO_4, 3.5 mM HEPES, 5.5 mM [D]-glucose, 1 mM $MgCl_2$, 2 mM $CaCl_2$, 3 mM KCl, pH 7.35) to a final concentration of $250x10^6$ platelets/ml. Platelets were stimulated with 20 mM thrombin receptor activator peptide 6 (TRAP6, Sigma) for 15 min at 37 °C with and EDTA 20 mM was added to stop the reactions. To remove platelets, samples were centrifuged at 2,500 gx for 15 min and platelet-free supernatants were collected and stored at -80 °C until use. To purify EVs, supernatants were thawed and centrifuged at 20,000 gx for 30 min at 4 °C. EV pellets were resuspended in 0.1V of particle free Dulbeco's Phosphate-buffered saline (DPBS, Sigma) and stained with 100 µl FITC-conjugated lactadherin (1.6 µM, Haematological Technologies). Importantly, to avoid sample contamination, FITC-

conjugated lactadherin was pre-filtered using an Ultrafree MC-GV filter (Merck Millipore, Ireland). Extracellular vesicles were incubated with FITC- conjugated lactadherin for 15 min on ice, in the dark. Excess stain was washed by centrifuging at 20,000 gx for 30 min, 4 °C. Supernatants were discarded and extracellular vesicles were resuspended in 120 µl particle free DPBS, and filtered in a Ultrafree MC-GV filter at 5,000 gx for 30 sec. The study of extracellular vesicles was approved by the regional committee for medical and health research ethics (REC North) and donors have sighed an informed consent.

S7. HeLa cell labeling

HeLa cells were grown in the culture media prepared in minimum essential medium (MEM) supplemented with 10% fetal bovine serum and 1% penicillin/streptomycin. The cells were seeded into the PDMS well chambers located on waveguide chip and kept in a standard humidified incubator at 37°C with 5% CO2 overnight. For live-cell imaging, the culture medium was aspirated and replaced with pre-warmed Live Cell Imaging Solution (Invitrogen) before imaging. For actin labeling, HeLa cells were fixed for ~15 minutes using 4% paraformaldehyde in PBS. Cells were then washed in PBS followed by incubation with 0.1% Triton X-100 in PBS for 10 minutes. The cells were further washed 3 times in PBS for a few minutes each time. Cells were then incubated with Atto-565 phalloidin (1:50 for in PBS for 90 minutes). The quantum yield and extinction coefficient of Atto-565 phalloidin is 0.90 and 120000 $cm^{-1}M^{-1}$ respectively.

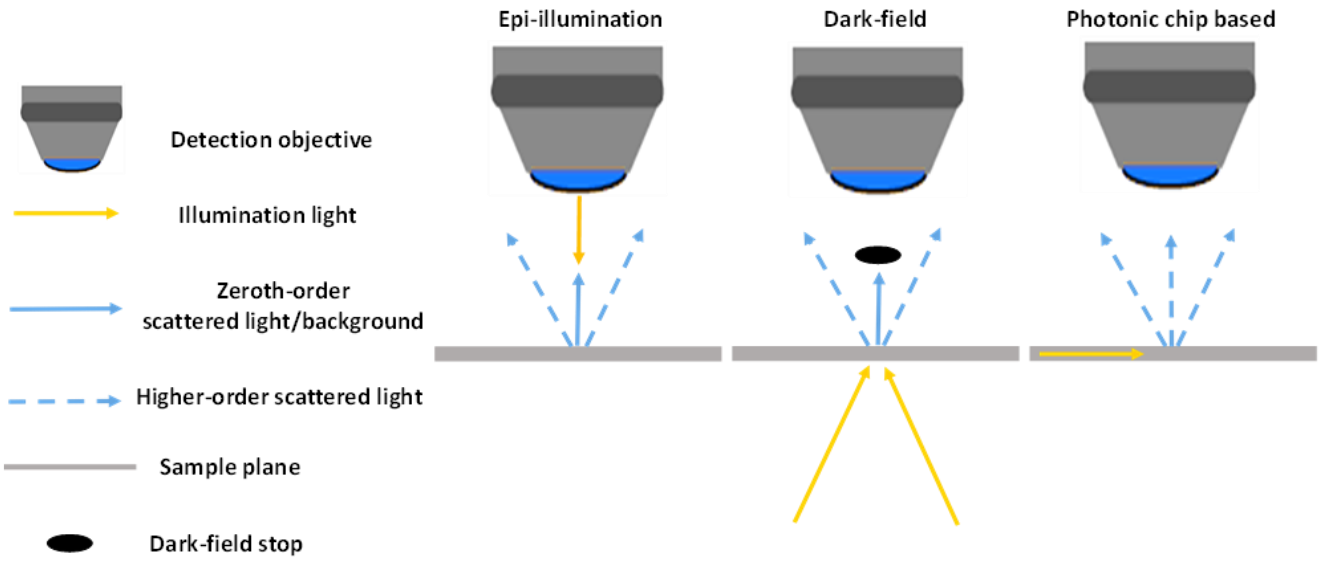

FIG.S5. Comparison between epi-illumination, dark-field and photonic-chip based illumination. Photonic-chip helps decouple the illumination and detection paths and caters to scalable field-of-view. The incident light is given in yellow and scattered light in blue.

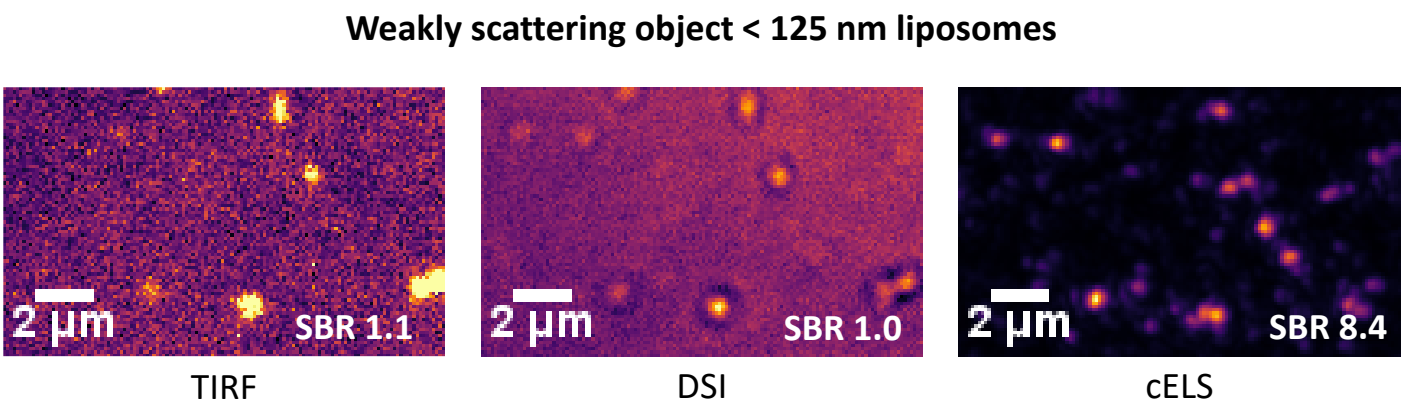

FIG. S6. TIRF, DSI and cELS images of < 125 nm liposomes. The signal to background ratio is also given as inset in the figure. cELS shows the presence of larger number of scattering particles as opposed to the other methods of illumination. Scale bar 2 µm.

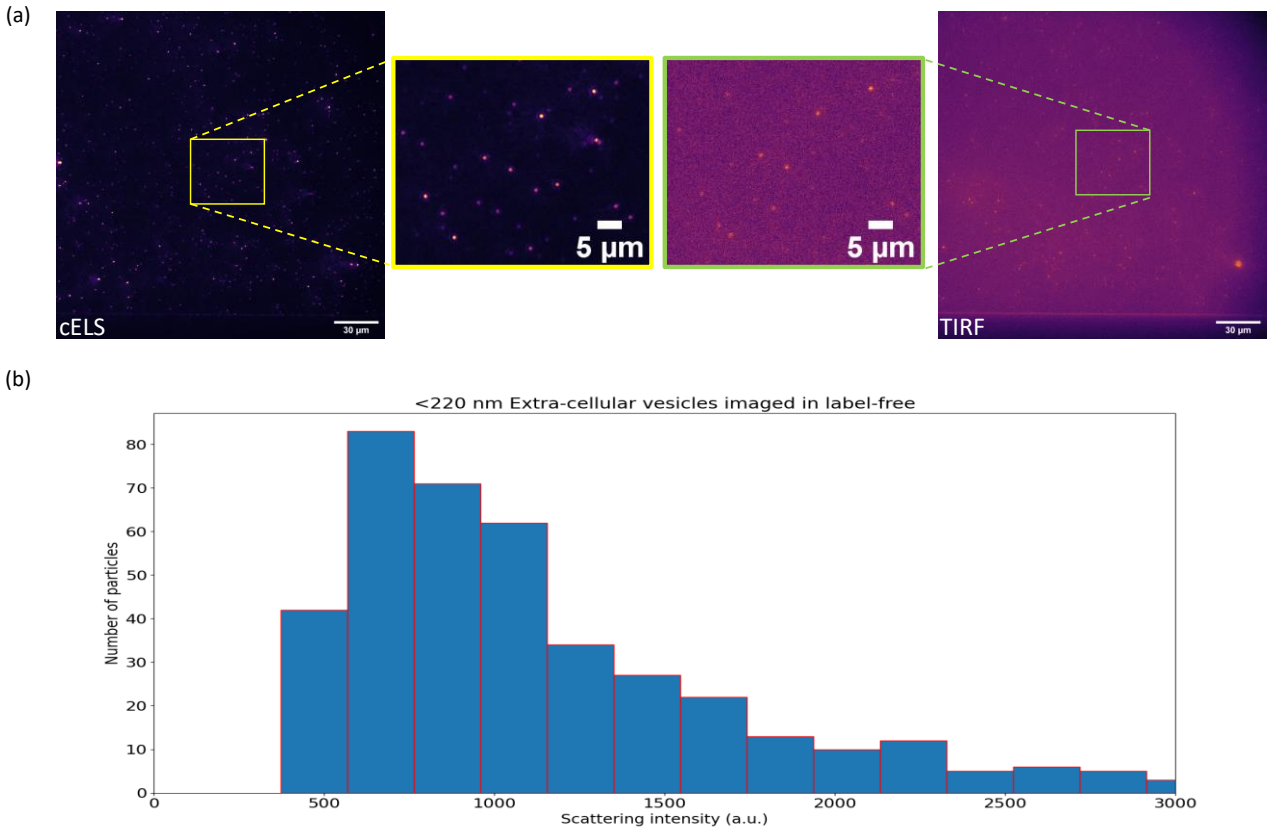

FIG. S7. < 220 nm Extra-cellular vesicles imaged in cELS and TIRF mode. (a) cELS and TIRF images of EV's. Scale bar 30 µm. Magnified regions are also shown alongside. Scale bar 5 µm. (b) Histogram showing number of particles versus scattering intensity for the cELS image shown in (a).

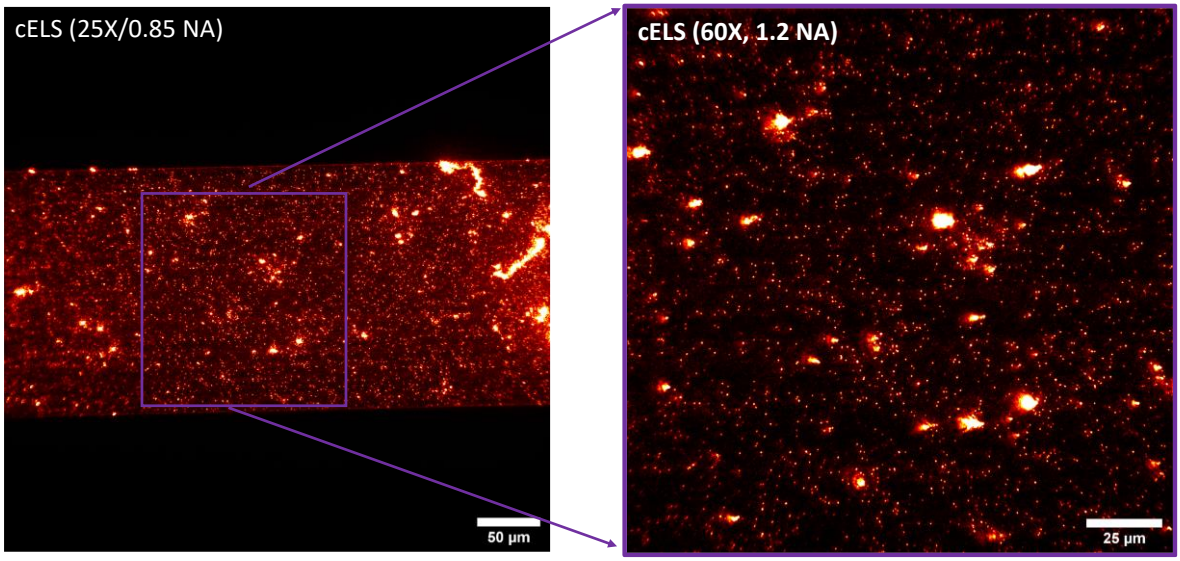

FIG. S8. Scalable field-of-view using cELS. Decoupling of illumination and detection paths enable scalable field-of-view as illustrated here. A larger field-of-view (shown on left) of 100 nm polystyrene beads is imaged using a 25X/0.85 NA microscope objective initially and then for higher resolution, a smaller field-of-view is imaged using a 60X/1.2 NA microscope objective.

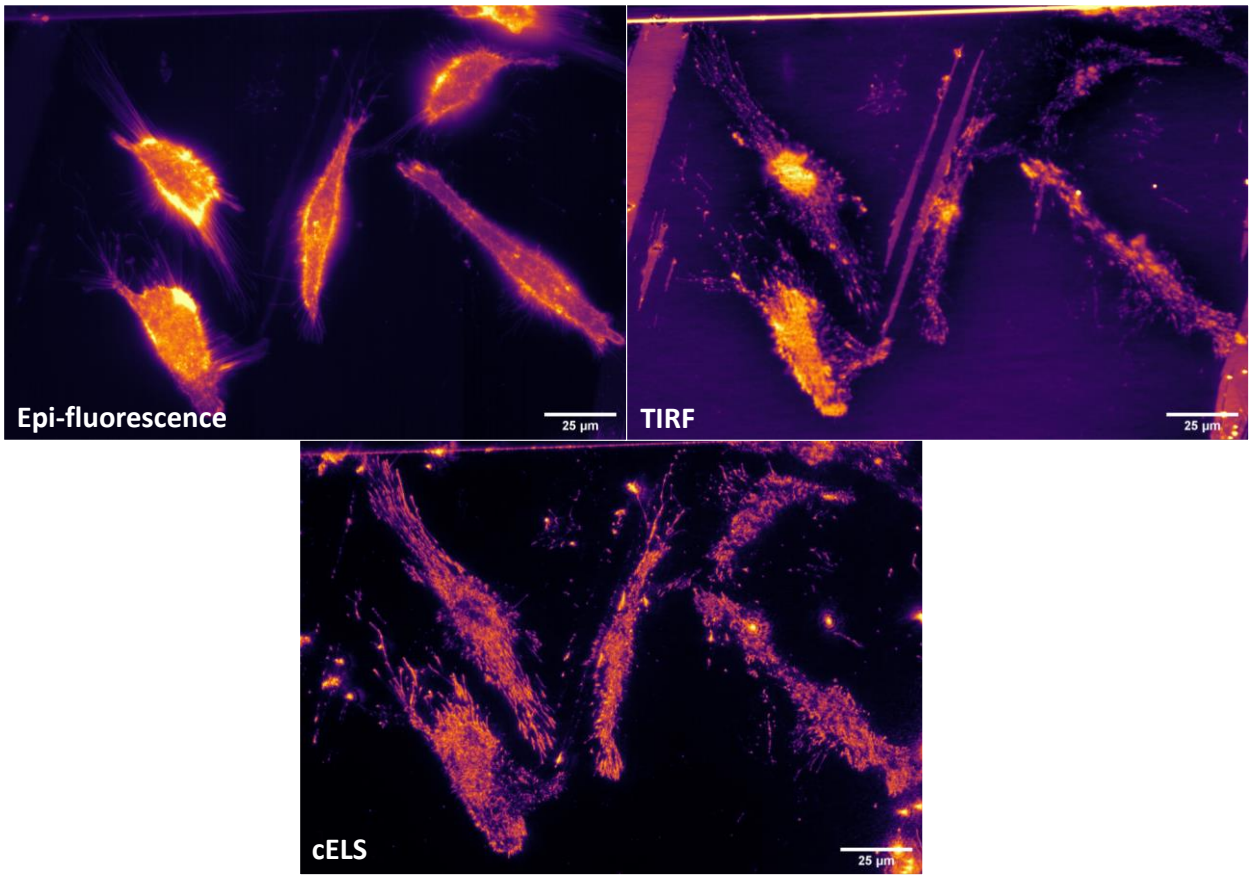

FIG. S9. Comparison between epi-fluorescence, TIRF and cELS images of Hela cells with the same field-of-view. Scale bar 25 µm.

Fig	Sample used	Experiment	Excitation λ	Detection λ	Exposure time	Filters used (LP –long pass, BP – band pass)	Additional comments
3(a)	60 nm polystyrene beads	cELS	660 nm	660 nm	30 ms	-	
		TIRF	532 nm	595 nm	50 ms	532 nm LP 595/40 nm BP	
3(b-e)	< 125 nm liposomes	Epi-illumination laser	660 nm	660 nm	30 ms	-	
		TIRF	488 nm	520 nm	200 ms	488 nm LP 520/35 nm BP	
		Epi-illumination spatially incoherent	660 nm	660 nm	30 ms	-	
		cELS	660 nm	660 nm	30 ms	-	
3(f)	< 225 nm extra-cellular vesicles	TIRF	488 nm	520 nm	100 ms	488 nm LP 520/35 nm BP	
		cELS	660 nm	660 nm	30 ms	-	
4	100 nm polystyrene beads	20X/0.45 NA (cELS, DSI, WL)	660 nm	660 nm	30 ms	-	

5	100 nm gold nanoparticles	cELS Dark-field	660 nm White light	660 nm White light	1 ms 100 ms		Stack of 100 images acquired in cELS mode for averaging. cELS performed using 10X/0.25NA and Dark-field using 10X/0.30 NA
6	Fixed Hela cells	cELS	660 nm	660 nm	30 ms	-	
		TIRF	532 nm	595 nm	50 ms	532 nm LP 595/40 nm BP	
7(b-c)	100 nm polystyrene beads	cELS/MUSICAL	660 nm	660 nm	30 ms	-	Stack of 100 images acquired in cELS mode used as input for MUSICAL. Threshold value for MUSICAL set at 0.8 and subpixelation at 10.

Table 2: Particulars of the experiments detailed in the main article.

S8. Image distortions due to convolution between evanescent wave illumination and sample spectrum

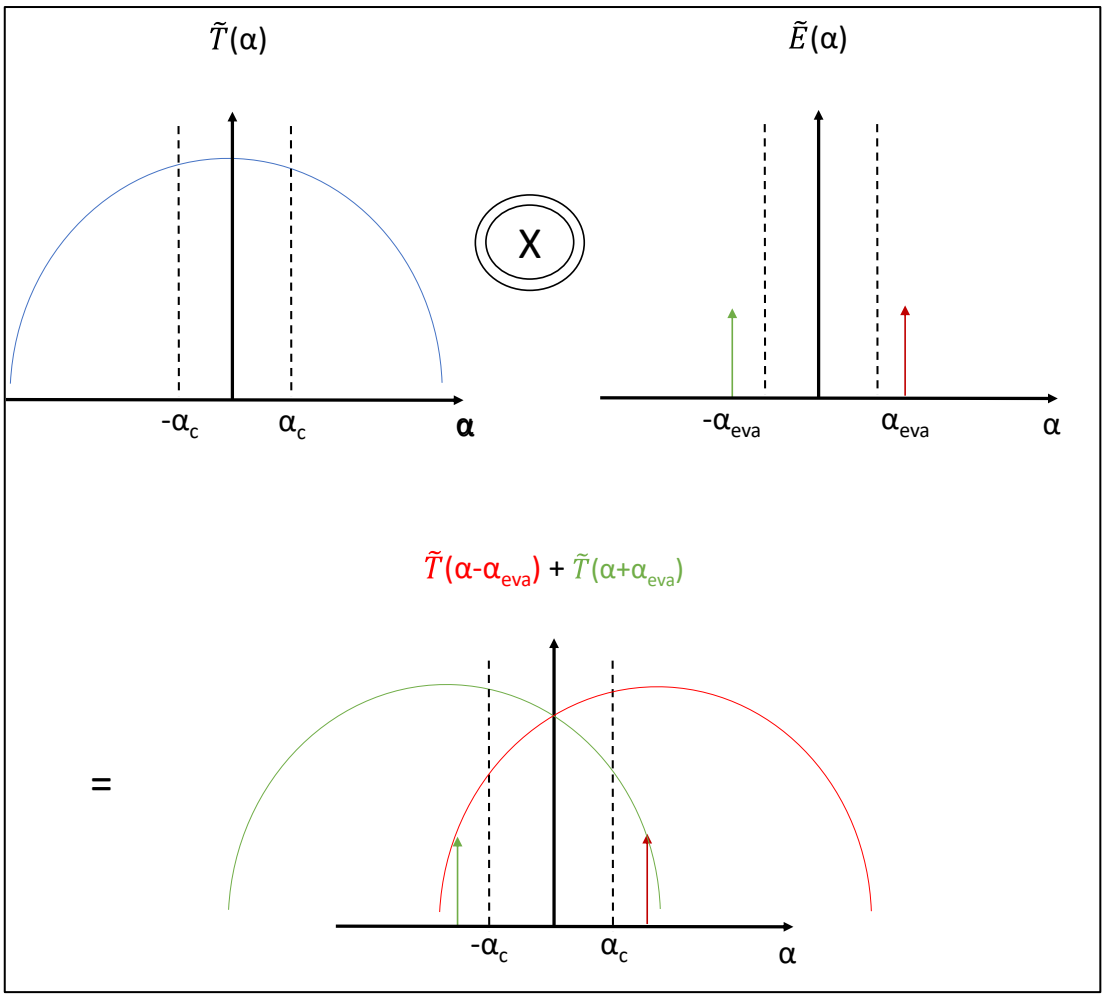

Fig.S10: Convolution between sample spectrum $\tilde{T}(\alpha)$ and illumination spectrum $\tilde{E}(\alpha)$, $\tilde{T}(\alpha) \otimes \tilde{E}(\alpha)$, shifts higher spatial frequencies of the sample into the pass-band of the microscope. Pass-band of the microscope is shown by the black dotted lines extending from $-\alpha_c$ to α_c. The illumination spectrum consists of two delta functions at $-\alpha_{eva}$ and α_{eva} shown by the green and red arrows respectively.

Consider we have a one-dimensional sample as shown by the ground truth image in Fig. S11. A Fourier decomposition of the ground truth image gives rise to three spatial frequencies with different Fourier weights as shown, only positive frequencies are shown here for brevity. When such a sample is illuminated by an evanescent wave, say α_{eva}=1 meter^{-1}, the higher spatial frequencies of the sample convolve with the high spatial frequency of the illuminating field and get heterodyned. This is shown in Fig. S(11b) where all the three spatial frequencies of the ground truth image get shifted to a lower frequency. If these frequencies are not shifted back to their original positions in the Fourier space, this can lead to distortions or deviations from the ground truth image. This is shown in Fig. S(11c). However, this issue will not be severe when imaging nano-sized specimens such as liposomes or EVs which predominantly contain high spatial frequencies.

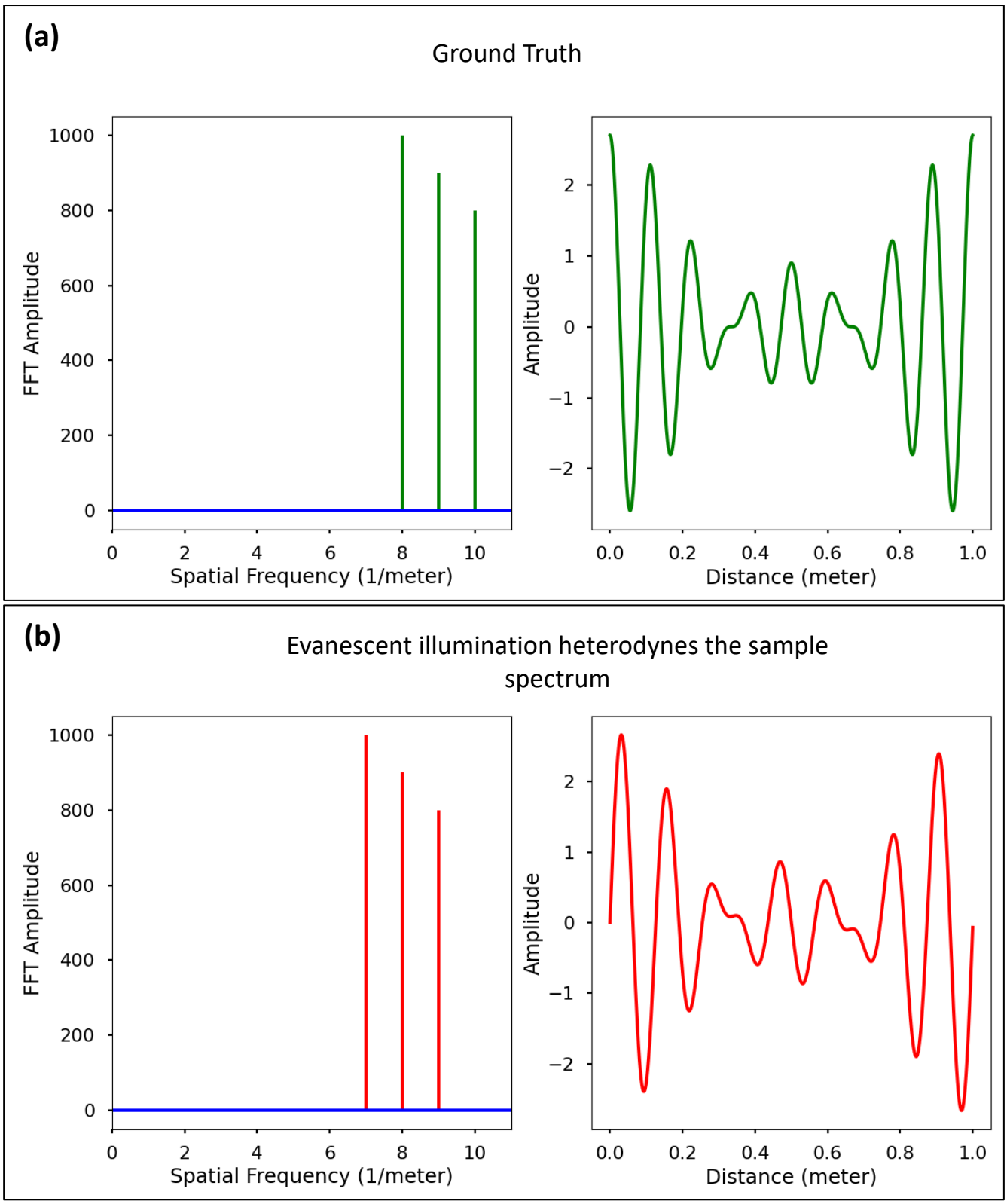
(a)
Ground Truth
FFT Amplitude
Spatial Frequency (1/meter)
Amplitude
Distance (meter)
(b)
Evanescent illumination heterodynes the sample spectrum
FFT Amplitude
Spatial Frequency (1/meter)
Amplitude
Distance (meter)

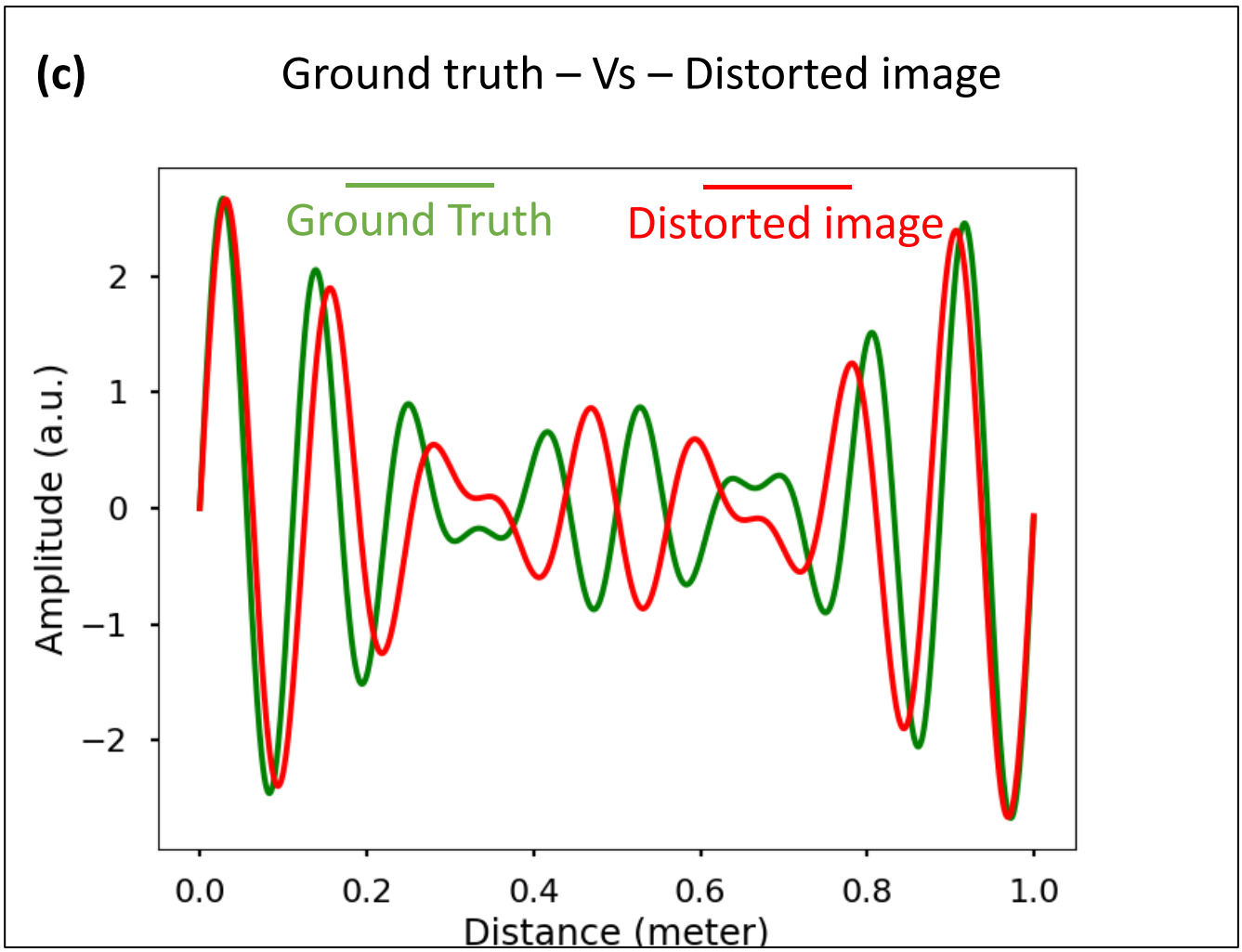

Fig. S11. (a) Ground truth image and its Fourier components. (b) Convolution of sample spectrum with an evanescent wave heterodynes the spatial frequencies of the sample spectrum, which can lead to distortions. The distorted image due to heterodyning and its Fourier components are shown. (c) Overlay of ground truth and the distorted images for visualization purpose.

References

1. GHATAK, AJOY AUTOR, et al. *An introduction to fiber optics*. Cambridge university press, 1998.
2. Yang, Yisu, et al. "Phase coherence length in silicon photonic platform." *Optics express* 23.13 (2015): 16890-16902.
3. Kong, Jin Au. "Theory of electromagnetic waves." *New York* (1975).
4. Goodman, Joseph W. *Statistical optics*. John Wiley & Sons, 2015.
5. Ryabukho, V. P., et al. "Wiener–Khintchin theorem for spatial coherence of optical wave field." *Journal of Optics* 15.2 (2013): 025405.
6. Prieto, Francisco, et al. "An integrated optical interferometric nanodevice based on silicon technology for biosensor applications." *Nanotechnology* 14.8 (2003): 907.
7. Hickel, Werner, and Wolfgang Knoll. "Optical waveguide microscopy." Applied physics letters 57.13 (1990): 1286-1288.
8. Hill, David J., et al. "Waveguide scattering microscopy for dark-field imaging and spectroscopy of photonic nanostructures." Acs Photonics 1.8 (2014): 725-731.
9. Liu, Xiaowei, et al. "Fluorescent nanowire ring illumination for wide-field far-field subdiffraction imaging." Physical review letters 118.7 (2017):076101.
10. Agnarsson, Bjorn, et al. "Evanescent light-scattering microscopy for label-free interfacial imaging: from single sub-100 nm vesicles to live cells." ACS nano 9.12 (2015): 11849-11862.
11. Ströhl, Florian, et al. "Super-condenser enables labelfree nanoscopy." Optics express 27.18 (2019): 25280-25292.
12. Cauzzo, Jennifer, et al. "Characterization of Liposomes Using Quantitative Phase Microscopy (QPM)." *Pharmaceutics* 13.5 (2021): 590.

Erratum

Nikhil Jayakumar, Firehun T. Dullo, Vishesh Dubey, Azeem Ahmad, Florian Ströhl, Jennifer Cauzzo, Eduarda Mazagao Guerreiro, Omri Snir, Natasa Skalko-Basnet, Krishna Agarwal and Balpreet Singh Ahluwalia*

Erratum to: Multi-moded high-index contrast optical waveguide for super-contrast high-resolution label-free microscopy

https://doi.org/10.1515/nanoph-2022-0500

After the publication of this article, the authors found that the yellow boxes (nucleus of the cell) in Figure 6 of the main article, corresponding to cELS and TIRF modalities, got swapped and is hereby corrected as:

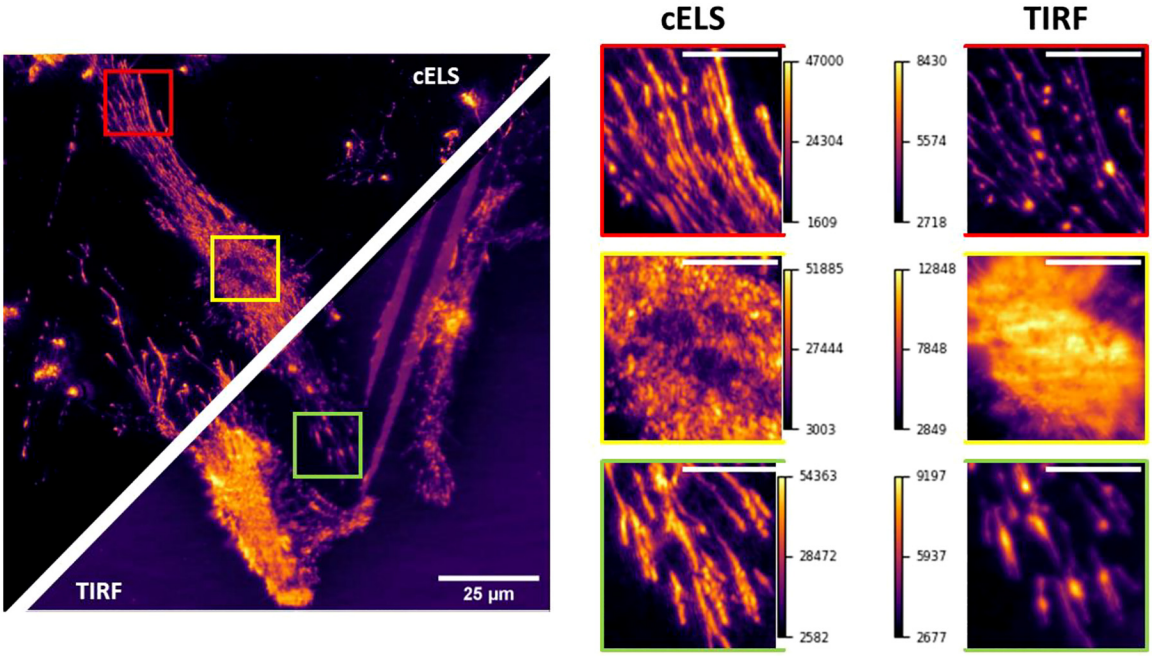

Figure 6: Comparison between cELS and TIRF images of Hela cells, scale bar 25 µm. Three different regions of interest enclosed by red, yellow, and green boxes are blown-up and provided alongside. The yellow box shows the nucleus region of the cell whereas the red and green boxes are the filaments, scale bar 8 µm. The color bars given alongside the magnified regions indicate the pixel values.

***Corresponding author: Balpreet Singh Ahluwalia**, Department of Physics and Technology, UiT The Arctic University of Norway, Tromsø 9037, Norway, E-mail: balpreet.singh.ahluwalia@uit.no
Nikhil Jayakumar, Vishesh Dubey, Azeem Ahmad, Florian Ströhl and Krishna Agarwal, Department of Physics and Technology, UiT The Arctic University of Norway, Tromsø 9037, Norway, E-mail: nik.jay.hil@gmail.com. https://orcid.org/0000-0003-3671-0058 (N. Jayakumar)
Firehun T. Dullo, Department of Microsystems and Nanotechnology, SINTEF Digital, Gaustadalleen 23C, 0373 Oslo, Norway
Jennifer Cauzzo and Natasa Skalko-Basnet, Department of Pharmacy, Faculty of Health Sciences, UiT The Arctic University of Norway, Tromsø 9037, Norway
Eduarda Mazagao Guerreiro and Omri Snir, Department of Clinical Medicine, UiT The Arctic University of Norway, Tromsø 9037, Norway

Chapter 5

Paper 3: Waveguide-based label-free super-resolution microscopy

Label-free incoherent super-resolution optical microscopy

Research question

Label-free super-resolution microscopy, i.e., circumventing the Abbe limit in Eqn. 1.25 using optical techniques is investigated. In Chapter 4, high-contrast imaging of weakly scattering specimens was demonstrated. It was also experimentally demonstrated that coherence of the scattered light from two particles in Fig. 4.2, prevents fluorescence-based super-resolution algorithms like SIM and intensity-fluctuation based algorithms from gaining resolution over the Abbe limit. This means that coherent illumination is not suitable to gain resolution using fluorescence-based algorithms.

Building upon the concepts in Chapter 4 and [68], the conclusion that can be drawn is that if by some means the two particles can be made to scatter with random phase relationship, then the image stack so acquired can be processed using these algorithms to achieve label-free super-resolution. What it means is that if tiny independent light sources can be used to illuminate the sample, then the scattered light from each object position can be considered to have a random phase relationship in emission from all other positions. However, in Section 1.7 it was seen that mutual coherence gains with increasing distance, i.e., correlation in emission between independent light sources increases with field propagation. This mandates the sample to be in near-field with respect to the illumination source. Hence, the research question can be summed up as follows:

- Can autofluorescence/photoluminescence (PL) in Si_3N_4 waveguides be regarded as an array of light sources that can be used for near-field illumination of unlabeled samples?

- Then, if PL of Si_3N_4 is used for near-field illumination of unlabeled samples, can fluorescence-based SIM and intensity-fluctuation algorithms be applied to achieve label-free super-resolution?

This problem is addressed in the attached paper titled, ' Label-free incoherent super-resolution optical microscopy'.

Aim: The aim of this work is to circumvent Abbe's optical diffraction limit by resorting to waveguide-based label-free microscopy.

Method: For this, dielectric optical waveguide made of Si_3N_4 with core refractive index $n_1 \approx 2$. The guided modes can induce PL in the core. This PL is used for near-field illumination of the unlabeled sample placed on the core-cladding interface of the waveguide. By exciting different MMI patterns, an image stack exhibiting intensity-fluctuations can be generated, which can then be used by fluorescence-based super-resolution algorithms to achieve label-free super-resolution. The technique is abbreviated EPSLON, which stands for Evanescently Decaying Photoluminescence Scattering enables Label-free Optical Nanoscopy.

To understand the concept of EPSLON, it is worth reviewing the experimental configurations used in the previous chapters. In Chapter 3, super-resolution fluorescence microscopy using optical waveguides made of Ta_2O_5 is demonstrated. The modes of the waveguide interact with a fluorescently labeled sample placed on the core-cladding interface. The fluorescent molecules absorb energy from the modes of the waveguide, emit Stoke shifted light which is then filtered using spectral filters to cut-off the illumination light and allow only the incoherent Stoke shifted light to reach the camera. Speckle suppression is naturally achieved due to incoherent nature of the Stoke shifted light. By scanning the piezo stage, the coupling objective scans the input facet of the waveguide. At each scan position of the waveguide, speckle/MMI patterns are generated due to different modes superimposing with different amplitudes and an image is acquired. These MMI patterns are varied to artificially induce intensity-fluctuations and an image stack so acquired is then processed to generate the final super-resolved image.

In Chapter 4, high-contrast label-free microscopy using optical waveguides made of Si_3N_4 is demonstrated. The modes of the waveguide interact with unlabeled sample placed on the core-cladding interface. The sample scatters the evanescently decaying field into the far-field which is then relayed onto a scientific camera. To suppress speckle noise arising due to coherence of the guided modes, within the integration time of the camera different MMI patterns are generated using a galvo scan scheme. This ensures that different MMI patterns get added on an intensity basis at the camera plane, helping suppress the speckle noise. Thus, high-contrast label-free images are generated.

In this chapter, unlabeled sample is placed on the core-cladding interface of a Si_3N_4 waveguide. Since bandgap energy of Si_3N_4 falls within the visible light frequency regime [90, 91], the guided modes can induce PL in the core.

This implies that the excitation wavelength induces a broadband PL in the core as shown in Fig. 5.1(a). This PL generated inside the core can illuminates the sample in transmission and near-field configuration, i.e., a part of the PL confined to the core due to total-internal reflection provides near-field illumination to the sample, while the remaining part illuminates the sample volume. The confined PL field can interact with the sample and get scattered into the far-field, Fig. 5.1(b). Then similar to Chapter 3, spectral filters are inserted in the tube-lens of the microscope. This ensures that the illuminating field that gets scattered off the sample is cut-off and only the incoherent PL reaches the camera. The experimental setup is shown in Fig. 5.1(c). This incoherent PL is a combination of both transmitted and confined PL field interacting with the sample. It is the confined PL field that is of interest since the transmitted PL will be visible as an omnipresent background throughout the core, while the confined PL scatters into the far-field only when there is an index perturbation at the core-cladding interface. Speckle suppression is naturally achieved due to the incoherent nature of the PL. This is experimentally demonstrated in Fig. 1g in the attached manuscript.

Now that label-free incoherent images can be generated, the next task is to induce intensity-fluctuations for SIM or intensity-fluctuation-based algorithms. For this, a piezo-stage is used to excite different MMI patterns in straight and four-arm waveguide geometries, and at each scan position along the input facet of the waveguide, an image is acquired. The image stack so acquired is then processed using fluorescence-based algorithms such as SACD [32] or BlindSIM [92] to generate label-free super-resolved images. Different waveguide geometries such as straight, four-arm and SIM chips are used in this work. In case of SIM chips, one-dimensional SIM is demonstrated. For this, two single mode waveguides overlap at the imaging area to generate well-defined interference fringes. The phase shift required for SIM algorithms is achieved by changing the index on one of the arms of the waveguide. This can be done by adding for e.g., ethanol to one arm which causes a relative phase shift between the interfering light beams. The geometries and their PL images with different MMI patterns are shown in Fig. 5.2. Simulation analysis to showcase how MMI patterns in waveguides can be used in tandem with intensity-fluctuation algorithms like SOFI or SACD to exploit the artificially induced fluctuations to gain resolution is provided in Supplementary Section 3 of the attached manuscript .

Observations and Solution: To verify the influence of coherence of the scattered light in EPSLON the following experiment is performed. Two particles on the core-cladding interface of the waveguide are imaged in coherent scattering, cELS Chapter 4, and incoherent scattering, EPSLON mode. The experimental setup used for both coherent and incoherent scattering configuration is shown in Fig. 5.1(c). The main difference with Chapter 4 is that in case of coherent scattering mode, spectral filters are removed in the tube lens to collect the coherently scattered light. The experimental observation is shown in Fig. 5.3. The phase relationship between the scattered fields are lost in case of EPSLON, leading to identical images for the different illumination phases. This is

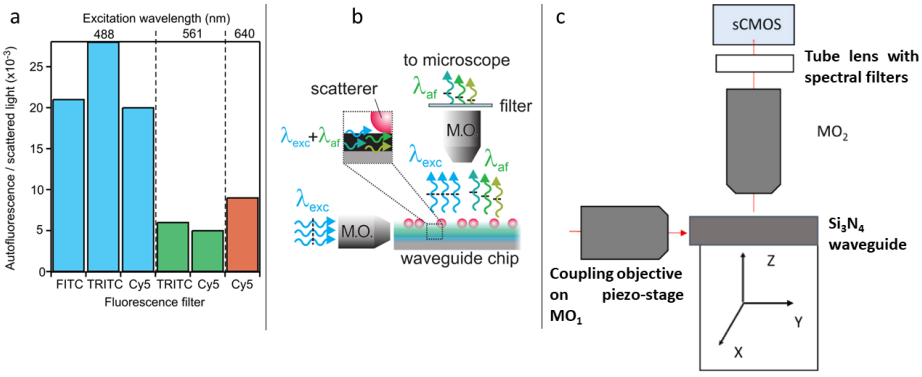

Figure 5.1: (a) Ratio of PL to scattering as a function of different excitation wavelengths is shown. The PL emission is broadband, spanning a few hundred nanometers in the visible frequency range. This broadband light can be collected using various spectral filters such as FITC, TRITC, CY5. The spectral bandwidth of these filter sets is provided in the attached manuscript, Table 2 of supplementary section. (b) Schematic of the proposed concept of EPSLON. The guided light induces PL in the Si_3N_4 core of the waveguide. The sample scatters both the guided coherent as well as the incoherent PL light into the far-field. Using appropriate filters, the coherent light is cut-off and only the incoherent light is allowed to reach the camera. (c) Schematic of the experimental setup in EPSLON. The use of spectral filters ensures that the coherent light is cut-off and only the incoherent PL reaches the camera. Thus, a label-free incoherent imaging system is developed.

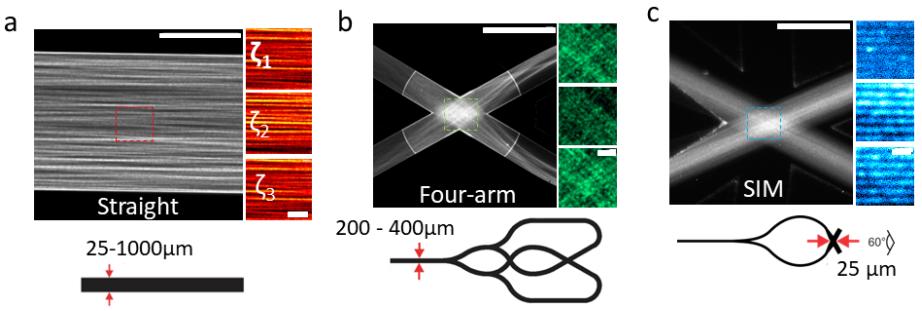

Figure 5.2: Various waveguide geometries employed in EPSLON. The images are the MMI patterns of the different geometries acquired in EPSLON configuration. (a) Straight waveguides with width 25 μm - 1000 μm are employed. τ_i showcases the different MMI patterns in the straight waveguide as the coupling objective MO_1 scans the input facet of the waveguide. (b) Four-arm crossing waveguide and its MMI patterns acquired acquired as the coupling objective oscillates along the input facet. The widths of these waveguides are in the range of 200 μm - 400 μm. (c) Single mode SIM chips used in this work. The angle of interference between the arms of the waveguide is approximately 60°. The different phase shifted frames are shown alongside. Phase shifting is generated by changing the index on one of the arms of the interfering waveguides. Scale bar in large field-of-view 20 μm and scale bar in insets 5 μm.

in contrast to the coherently scattering scenario shown alongside. This implies that fluorescence-based algorithms can now be applied to a so generated image stack to achieve label-free super-resolution. Therefore, the proposed solution EPSLON can be used to generate a label-free incoherent imaging system.

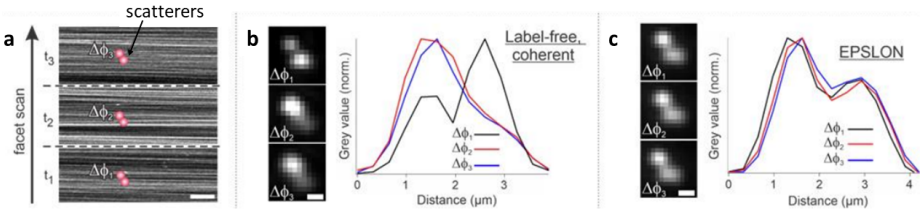

Figure 5.3: (a) Schematic of two unlabeled particles placed on top of the core-cladding interface of the waveguide. The piezo is oscillated along the input facet of the waveguide. At each time instance, a different set of modes are excited that cause a difference in phase of the scattered light off the particles. (b) In label-free coherent scattering, the different MMI patterns correspond to different phases of the illuminating field $\Delta\phi$. The differences in obliquity of the illumination as the piezo scans the input facet of the waveguide, causes differences in the experimentally captured images. The line plot corresponds to intensity variation along the beads for the different cases provided. (c) In label-free incoherent scattering EPSLON, the image registered by the camera looks identical within the same field-of-view , as evidenced by the line plots. Scale bar 10 μm.

Results: Label-free super-resolved images of 100 nm polystyrene beads (Fig. 3b in the attached paper), biological samples like extra-cellular vesicles (Fig. 4 in the attached paper), human placenta tissue (Fig. 5 in the attached paper) and rat kidney sections (Fig. 6 in the attached paper) is generated using the concepts developed in this work. Resolution gain over the experimental diffraction-limit of 1.9 times on rat kidney sections, 2.8 times on human placenta tissue sections and two-point resolution of 144 nm on 100 nm beads is demonstrated and experimentally verified using scanning electron microscope (SEM). Some of these results are shown in Fig. 5.4 and Fig. 5.5.

Conclusion and Outlook: EPSLON helps realize a label-free incoherent imaging system. The incoherent nature of the scattered light helps mitigate the speckle noise naturally. In addition, by exploiting the MMI patterns in multi-moded waveguides or well-defined interference fringes in SIM chips, image stacks exhibiting intensity fluctuations can be generated. Image stacks so acquired can then be processed using SIM [94] or BlindSIM [92] or intensity-fluctuation algorithms [27,32]. Typically, rotating diffusers are used to modify the coherence properties of the light source [88], where the speckle size is limited by the diffraction of light. Recently, artificially engineered materials have also been used to reduce the speckle size [67], again limited by the diffraction of light. However, if the tiniest independently emitting light sources available, like atoms or

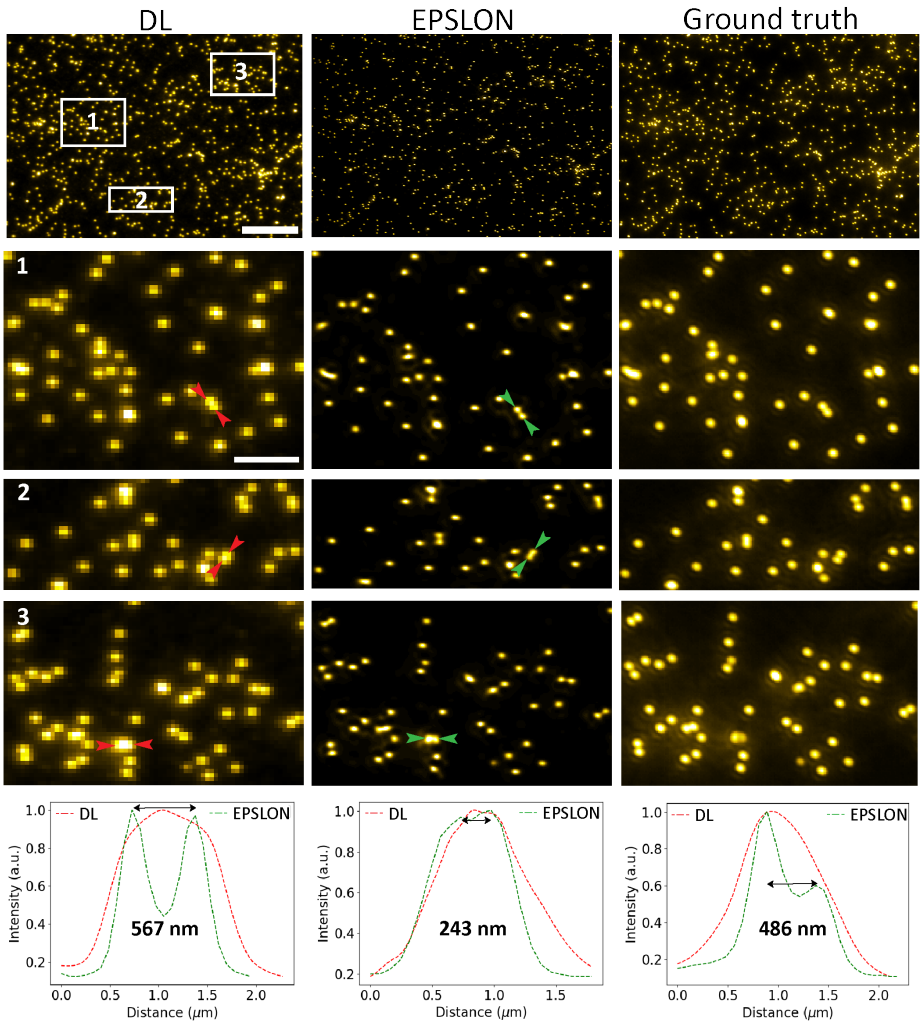

Figure 5.4: Diffraction-limited (DL), super-resolved image (EPSLON) and ground truth optical images are shown, scale bar 20 μm. Three regions of interest labeled '1', '2' and '3' are blown up and shown, scale bar 1 μm. DL images are acquired using 20X/0.75 NA objective, ground truth images are acquired using 60X/1.2 NA detection objective. Stack of images acquired using 0.75 NA are processed using BlindSIM to generate the super-resolved EPSLON image. Red arrows indicate unresolved beads in the DL image and green arrows indicate the corresponding resolved beads in the EPSLON image. EPSLON and ground truth images are in agreement. The line plots indicate intensity variation along the arrows, red dotted line in the DL image and green dotted in the EPSLON image.

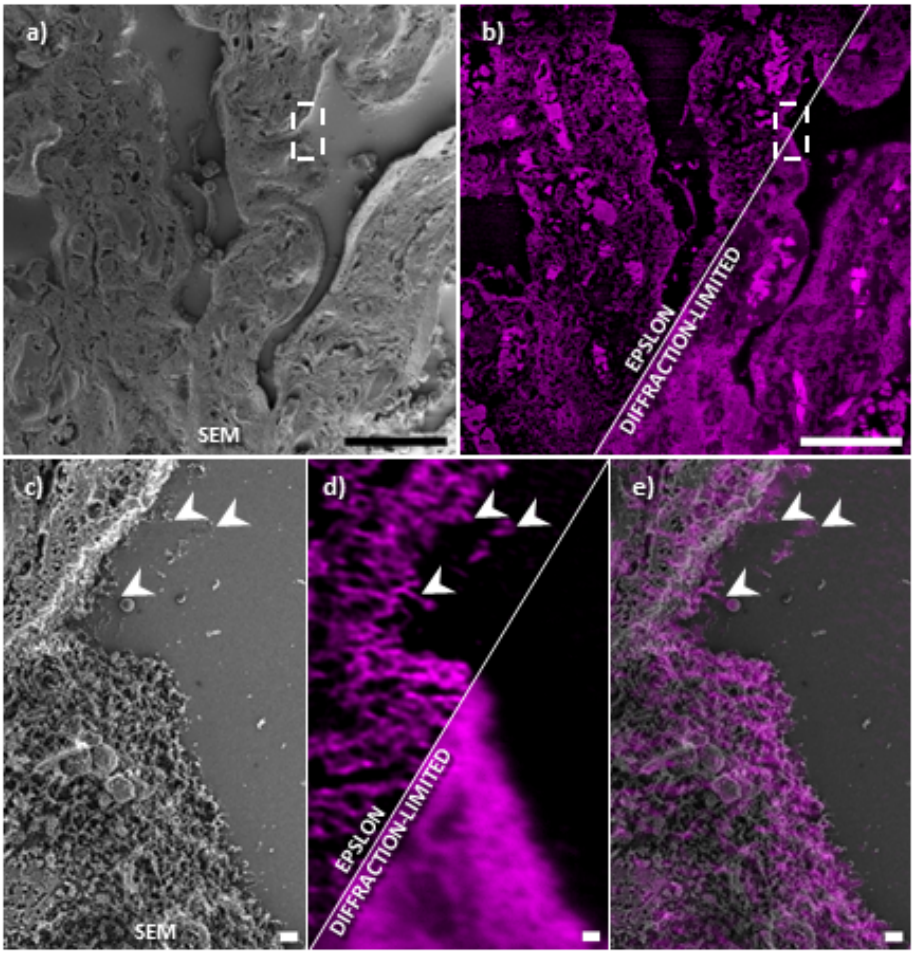

Figure 5.5: Label-free super-resolved images of human placenta tissue is shown. (a) Scanning electron microscope (SEM) image of a region of interest is shown, scale bar 50 μm. (b) The corresponding optical super-resolved EPSLON and diffraction-limited images, scale bar 50 μm. A white box in both SEM and optical images are blown up and provided. Mean resolution estimated using Fourier Ring Correlation (FRC) [93] of the diffraction-limited image is 496 nm and that of EPSLON is 176 nm. (c) SEM image of the white box is shown. (d) Corresponding EPSLON and diffraction-limited images are provied, scale bar 1 μm. The white arrows indicate areas of high correlation between the SEM and optical EPSLON image. (e) Overlay of SEM and EPSLON image allows for visualizing correlation between SEM and EPSLON imaging methods.

molecules, can be used to provide near-field illumination of samples, then each point on the sample can be regarded as emitting incoherently with respect to all other points. This is realized in EPSLON by utilizing the PL in Si_3N_4 waveguides and thus, EPSLON helps realize a two-dimensional label-free incoherent imaging system.

Interestingly, it is important to highlight that PL in waveguides is an undesirable phenomenon. This is because the guided light gets absorbed along the length of the waveguide, i.e., the waveguides become lossy. The employed waveguides are characterized and their losses are reported in Supplementary Table 1 in the attached manuscript. In addition, the transmitted PL is present as an omnipresent background. Therefore, achieving a high signal-to-background ratio in EPSLON has been challenging. Nevertheless, imaging of nanobeads and biological samples has been demonstrated in this proof-of-concept work. This work thus provides a new solution to the problem of label-free super-resolution, by catering the properties of the illuminating field.

Author contribution: NJ conceptualized the idea. NJ and BSA designed the experiments. NJ performed the initial reconstructions and was later passed onto WZ, who performed SACD and BlindSIM reconstructions. LEVH prepared the human placenta tissue and rat kidney sections on chips and imaged them along with NJ. HM and LEVH performed SEM imaging of tissue sections. FTD and JCT designed the waveguide chip and mask for fabrication. FTD also performed the FIMMWAVE simulations. KS and AL provided the extra-cellular vesicles for imaging and wrote the EV preparation protocol. NJ performed the experiments, analyzed the results and prepared the manuscript with inputs from FTD, JCT, and BSA. NJ, LEVH, HM and JCT prepared the figures. LEVH prepared the video animations in the supplementary section. All authors commented on the manuscript. BSA secured the funding and supervised the project.

Label-free incoherent super-resolution optical microscopy

Nikhil Jayakumar**[1], Luis E. Villegas-Hernández[1], Weisong Zhao[2], Hong Mao[1], Firehun T Dullo[3], Jean-Claude Tinguely[1], Krizia Sagini[4,5], Alicia Llorente[4,5,6], Balpreet Singh Ahluwalia*[1,7]

[1]*Department of Physics and Technology, UiT The Arctic University of Norway, Tromsø, 9037, Norway*
[2]*Innovation Photonics and Imaging Center, School of Instrumentation Science and Engineering, Harbin Institute of Technology, Harbin, China*
[3]*Department of Microsystems and Nanotechnology, SINTEF Digital, Gaustadalleen 23C, 0373 Oslo, Norway*
[4] *Department of Molecular Cell Biology, Institute for Cancer Research, Oslo University Hospital, The Norwegian Radium Hospital, 0379 Oslo, Norway*
[5]*Centre for Cancer Cell Reprogramming, Faculty of Medicine, University of Oslo, Montebello, 0379 Oslo, Norway*
[6]*Department for Mechanical, Electronics and Chemical Engineering, Oslo Metropolitan University, Oslo, Norway*
[7]*Department of Clinical Science, Intervention and Technology, Karolinska Institute, Sweden*

*Balpreet.singh.ahluwalia@uit.no, **nik.jay.hil@gmail.com

Abstract: The photo-kinetics of fluorescent molecules has enabled the circumvention of far-field optical diffraction-limit. Despite its enormous potential, the necessity to label the sample may adversely influence the delicate biology under investigation. Thus, continued development efforts are needed to surpass the far-field label-free diffraction barrier. The coherence of the detected light in label-free mode hinders the application of existing super-resolution methods based on incoherent fluorescence imaging. In this article, we present the physics and propose a methodology to circumvent this challenge by exploiting the photoluminescence of silicon nitride waveguides for near-field illumination of unlabeled samples. The technique is abbreviated EPSLON, Evanescently decaying Photoluminescence Scattering enables Label-free Optical Nanoscopy. We demonstrate that such an illumination has properties that mimics the photo-kinetics of nano-sized fluorescent molecules. This allows to develop a label-free incoherent system that is linear in intensity, and stable with time thereby permitting the application of techniques like structured illumination microscopy (SIM) and intensity-fluctuation based optical nanoscopy (IFON) in label-free mode to circumvent the diffraction limit. We experimentally demonstrate label-free super-resolution imaging of nanobeads (polystyrene and gold), extra-cellular vesicles, rat kidney sections and human placenta tissue. In this proof-of-concept work, two-point resolution of $\sim 144\ nm$ on nanobeads, ~176 nm mean resolution estimated using Fourier ring correlation (FRC) on human placenta tissue (~2.8 times resolution gain) and $\sim 133\ nm$ mean FRC resolution (~1.92 times resolution gain) on rat kidney tissue sections is demonstrated. We believe EPSLON is a step forward within the field of incoherent far-field label-free super-resolution microscopy that holds a key to investigate delicate biological systems in its natural state without the need for exogenous labels.

Introduction

The ability of light beams to interfere is quantified by their degree of coherence. Light beams originating from within the coherence volumes can only overlap and generate a sustained interference pattern [1, 2]. In fluorescence microscopy, the transversal coherence lengths are typically on the order of a few nanometers. This is because the fluorescent molecules, a few nanometers in size, emit independently and stochastically. It leads to a linear mapping between the sample plane fluorophore concentration and image plane intensity. This may be utilized to circumvent the far-field diffraction-limit, as in structured illumination microscopy [3, 4] or fluorescence-based IFON algorithms [5-10]. However, the absence of such exogenous molecules in label-free microscopy restricts the far-field transversal coherence lengths to a few hundreds of nanometers [11, 12]. This hinders the application of fluorescence-based super-resolution algorithms in the label-free regime for generating reliable super-resolved images [13]. Another hinderance in label-free microscopy is the lack of selectivity and specificity that results in strong scattering and multiple scattering from the entire sample. To alleviate these challenges of scattering, a near-field illumination via nano-sized light sources with stochastic photo-kinetics and sufficient quantum yield will be beneficial. Therefore, through this article, we provide the concepts and a key to unlock the challenge of generating far-field label-free super-resolved optical images using fluorescence based super-resolution algorithms: photoluminescence (PL) of silicon nitride (Si_3N_4) [14, 15] waveguide functions as exogenous nano-sized illumination sources with stochastic photo-kinetics. In addition, the photonic-chip helps in engineering the illumination to induce fluctuations in intensity via multi-mode interference (MMI) speckle-like patterns [16-18] or via well-defined interference fringes that permits the application of fluorescence based IFON algorithms [19, 20] or SIM respectively to enhance the resolution.

Poor-contrast and diffraction-limited resolution are major impediments to the development of label-free optical microscopy. To mitigate the issue of poor contrast, various approaches have emerged: phase contrast microscopy [21], differential interference contrast [22], Hoffman modulation [23], interferometric scattering microscopy [24], quantitative phase microscopy [25], holographic non-interferometric techniques [26], Fourier Ptychography [27], rotating coherent scattering microscopy [28], manipulating the coherence of light sources used for illumination [29], ultraviolet microscopy [30], optical waveguides [31, 32], among others. However, circumventing the diffraction-limit in label-free regime is still challenging in life sciences, as opposed to fluorescence microscopy [33]. This could be attributed to the ease of utilizing/manipulating the photo-kinetics of nano-sized fluorescent molecules to gain information beyond the diffraction-limit.

The different approaches developed for label-free super-resolution microscopy, albeit with their respective experimental challenges especially for life sciences applications, includes near-field scanning optical microscopy [34], super-lens [35], micro-sphere assisted super-resolution imaging [36], high-index liquid immersed microsphere assisted super-resolution [37], optical super-oscillation techniques [38], non-linear imaging systems [39], multiplexing information in polarization, wavelength or time [40], etc.

For the far field high-resolution label-free optical microscopy techniques, different concepts have been developed [41]. A short overview of different approaches is detailed in the Supplementary section 1. Broadly, these methods employ the concept of synthetic aperture or spatial frequency shifting for coherently scattering specimens using free-space optics [27, 28, 42-44] or chip-based solutions [31, 45-47], or application of fluorescence-based super-resolution algorithms to coherently scattering specimens [48]. Some of these techniques achieve sub-100 nm resolution, but the best achievable theoretical resolution is given by Abbe's diffraction-limit, $\frac{\lambda_{det}}{NA_{ill}+NA_{det}}$, where λ_{det} is the wavelength of the detected light and $NA_{ill/det}$ is the numerical aperture of the illumination and detection light paths, respectively. In addition, some methods indeed achieve label-free super-resolution by utilizing the intrinsic auto-fluorescence of biological specimens in tandem with super-resolution fluorescence-based algorithms [49, 50]. In this article, we propose the use of photoluminescence of Si_3N_4 waveguides to solve the abovementioned challenges associated with the far-field label-free super-resolution optical microscopy. The concept permits the application of fluorescence based super-resolution algorithms on unlabeled samples, generating high-contrast label-free super-resolved images, without photo-toxicity and photobleaching plaguing the imaging process. Our work helps synthesize a label-free incoherent imaging system and is termed Evanescently decaying Photoluminescence Scattering enables Label-free Optical Nanoscopy (EPSLON), which builds and extends the concepts outlined by Ruh et.al. [25], Wicker and Heinztmann [13], and previous work based on photonic-chip microscopy [29]. These concepts of EPSLON which enable circumventing the label-free far-field diffraction-limit are explained and experimentally demonstrated in Fig. 1 and Fig. 2. We describe how PL from Si_3N_4 waveguide is a solution to these challenges and validate our concepts experimentally via high-contrast label-free super-resolved images of polystyrene nanobeads, gold nanoparticles, weakly scattering specimen like extra-cellular vesicles, human placenta tissue and rat kidney sections.

Conceptual framework and Results

Problem statement

Here we describe why fluorescence based super-resolution algorithms when applied to coherently scattering samples do not yield any resolution gain beyond the diffraction-limit [13]. In label-free mode, when two particles are illuminated by a monochromatic plane wave, the intensity registered by the camera is $I(\vec{r}) = \langle \left| \left(E_1(\overrightarrow{r_1}, t) + E_2(\overrightarrow{r_2}, t) \right) \otimes h(\vec{r}) \right|^2 \rangle$, where $\langle\ \rangle$ represents time averaging by the detector, $h(\vec{r})$ is the coherent point spread function of the imaging system , $\otimes$ represents the convolution operation and $E_{1,2}$ are the scattered scalar electric fields which are linked to applied electric fields via polarizability of the two particles [51]. Due to statistical similarity or coherence between the overlapping scattered fields, the intensity registered by the camera is non-linearly related to the particle concentration and is a function of $\Delta\varphi = \vec{k}.\overrightarrow{r_2} - \vec{k}.\overrightarrow{r_1}$. It implies that the image generated by the camera varies with either a change in the illumination angle $\vec{k}$, or with the relative positions of the particles $\overrightarrow{r_2} - \overrightarrow{r_1}$.

Next, to illustrate the image formation process in fluorescence microscopy we replace the phase-objects with fluorescent molecules. Analogous to the strengths of the scattered fields, $|a_1(\overrightarrow{r_1})|^2$ and $|a_2(\overrightarrow{r_2})|^2$, are the brightness of the molecules that typically depends on the illumination intensity at the location of the molecule. The molecules can also be assumed to emit independently [52] and stochastically typically on the order of nanoseconds [53]. The

following properties of these molecules can be utilized in fluorescence microscopy by collecting only the Stoke shifted light emitted by the molecules:

(i) Stochastic emission between the molecules causes the phase difference between the emitted fields to be a function of time, $\Delta\varphi(t)$. It implies that the molecule emissions are incoherent with respect to one another, or, in other words, we can say that the transversal coherence length is determined by the size of an individual molecule. This gives rise to similar images for different illumination angles of the incident plane wave. It is this property that allows the usage of structured light in SIM [13, 54] or the intrinsic photo-kinetics of the molecules in IFON algorithms to enhance the resolution [29],

(ii) Excited lifetime on the order of nanoseconds of these molecules helps mitigate the speckle-noise and

(iii) Molecular specificity offered by these fluorescent molecules enables multi-color imaging of different cell organelles. It can be concluded that the suppression of speckle noise and molecular specificity offered by the molecules enables high-contrast imaging and the linear relationship between molecular concentration and image plane intensity helps in enhancing the resolution via fluorescence-based super-resolution algorithms.

Hence, to improve the label-free resolution via fluorescence-based algorithms, we need to ensure that there exists no statistical similarity between the scattered fields originating from different locations [51]. This calls for the spatial coherence function to be δ-function correlated, i.e.,

$$J(\overrightarrow{r_1},\overrightarrow{r_2}) = \langle E_T(\overrightarrow{r_1},t)E^*{}_T(\overrightarrow{r_2},t)\rangle = KI_T(\overrightarrow{r_1})\,\delta(\overrightarrow{r_1}-\overrightarrow{r_2}) \quad (1)$$

where $J(\overrightarrow{r_1},\overrightarrow{r_2})$ is the spatial coherence function and determines the spatial correlation of the fields, $E_T(\vec{r},t) = E_1(\vec{r},t) + E_2(\vec{r},t)$ is the total field reaching the camera, K is a real constant and I_T is the image generated by the camera. This will ensure an incoherent imaging system. Eqn. (1) can be assumed to be satisfied in fluorescence microscopy because the transversal spatial coherence length is determined by the size of the fluorescent molecules and the image generated by the camera indicates the spatial locations of the fluorescent molecules.

Thus, to circumvent the label-free diffraction-limit using fluorescence-based super-resolution algorithms, we need to develop a light source with δ-function correlations and then acquire an image stack exhibiting intensity-fluctuations to apply SIM or intensity-fluctuation based algorithms. This can be realized experimentally via the EPSLON configuration. Fig. 1(a-c) compares the conventional imaging configurations and their corresponding image plane intensity distribution with EPSLON, Fig. 1(d). EPSLON satisfies Eqn. 1 and is experimentally demonstrated in Fig. 1e-1j. In Fig. 1e-1f, schematic diagrams of waveguide-based label-free coherent and incoherent imaging systems EPSLON are shown. The coherent and corresponding EPSLON images are compared in Fig. 1g, where speckle suppression due to loss in phase information in the scattered light is clearly evidenced in the EPSLON configuration image. This loss in phase information also implies that identical images must be generated for arbitrary illumination angles in EPSLON configuration, as opposed to label-free coherent imaging. This is demonstrated experimentally in Fig. 1h-1j where the coherent and its corresponding incoherent EPSLON images are provided.

EPSLON: a solution for high-contrast far-field label-free super-resolution microscopy

To employ a light source with δ-function correlations, we resort to the high-index contrast ($\Delta n \approx 2$) Si_3N_4 optical waveguide deposited using plasma enhanced chemical vapor deposition (PECVD) scheme. Waveguide fabrication and properties of the guided modes and its spatial frequency extend is provided in Supplementary section 2 and in previous works [55, 56]. The propagation loss in these waveguides as a function of wavelength is determined and given in Table 1 in the supplementary section 2. The choice of Si_3N_4 over other high index contrast optical waveguides, such as tantalum pentoxide, Ta_2O_5, or titanium dioxide TiO_2, is attributed to the room-temperature visible PL generated inside the core during the transfer of optical power along its length.

Determining the origin and lifetime of this emission is not within the scope of this work. The origin and photophysical properties of this PL is a widely researched area [57-59]. It is found to be dependent on the waveguide fabrication scheme employed and could be attributed to intrinsic fluorescence of the material [14]. The PL emission spectrum is broad [15] and the lifetime of these states is found to vary on the order of a few nanoseconds to a few hundred microseconds depending on the origin of the PL [16, 60-61]. Such an emission could be visualized as a very large number of fluorescent molecules embedded in a material and emitting stochastically. Hence, if the PL light is used for near-field illumination of samples, then Eqn. (1) will be satisfied for the incoherently scattered fields. This helps in synthesizing a label-free incoherent system, Fig. 1.

The next problem to tackle is that of generating an image stack with intensity-fluctuations for the fluorescence-based algorithms. Structuring the illumination beam, manipulating the photophysical properties of the fluorescence molecules are some of the ways typically employed for generating image stacks with intensity-fluctuations. In EPSLON, this problem is resolved by resorting to Si_3N_4 waveguides of the following types: (1) Straight waveguides with strip geometry and large widths that supports a large number of the guided modes, generating MMI patterns (Fig. 2a) [32], (2) Four-arm junction multi-moded strip waveguides for speckle illumination from different azimuthal angles (Fig. 2b) [32] and, (3) a single moded SIM chip with rib geometry and phase modulation for one-dimensional structured illumination (Fig. 2c) [62] and four-arm junction multi-moded strip waveguide for two-dimensional structured illumination. Simulation analysis and experimental results is presented in the Supplementary Section 3 to validate how multi-moded illumination pattern when used in tandem with IFON help gain resolution. Our results in Supplementary Fig. 3-6, show that the different azimuthal illumination frequencies in four-arm junction multi-moded waveguide, helps achieve low correlation between different scatterers and thereby aid, IFON techniques like SOFI [5] and SACD [9] that exploit intensity-correlations between different emitters to generate super-resolved images.

Image formation process in EPSLON

Laser is coupled into a Si_3N_4 waveguide via a microscope objective MO_1, (Supplementary Fig. 7). The coupled optical power gets distributed among the multiple coherent guided modes, which correspond to the eigen vectors of the guiding structure. As the modes guide power along the length of the waveguide, they also induce a broadband PL along the length as shown in Fig. 2d-2e. The Si_3N_4 waveguide employed in this work demonstrated PL in all the commonly used wavelengths in bio-imaging, 488 nm, 561 nm, and 647/660 nm (Fig. 2e). This PL of Si_3N_4 waveguide does not exhibit any bleaching effect over long periods of times (Fig. 2f), as opposed to the autofluorescence in polymer waveguides [63] and varies linearly with the excitation power (Fig. 2g).

To explain the origin of fluctuations in intensity, we consider the case of a multi-moded straight waveguide. Fluctuations over time, $I_{core}^{m}(\vec{r},t)$, can be induced by oscillating MO_1 using a piezo-stage across the input facet of the waveguide (Supplementary Fig. 7) which excites different sets of modes $\psi_m(\vec{r},t)$ with relative amplitudes $0 \leq a_m(t) \leq 1$. The instantaneous PL intensity at each location in the core is dependent on the coherent superposition of the modes and can be represented mathematically as $I_{core}^{m}(\vec{r},t) = \eta(\lambda)|\sum_m a_m(t)\psi_m(\vec{r},t)|^2$, where $\eta(\lambda)$ is assumed to be a constant across the material for a specific wavelength. $\psi_m(\vec{r},t) = E_m(x,y)e^{(i\beta_m z - i\omega t)}$ corresponds to the scalar representation of the mth guided mode with fixed transversal profile $E_m(x,y)$ and propagation constant β_m. As the PL emission occurs inside a high-index core, a part of the PL light gets confined to the core due to total-internal reflection at the core-cladding interface and the remaining part gets transmitted into the far-field, which is visible as an omnipresent background or noise. This ratio is quantified experimentally and found to be about 0.01, Supplementary Fig. 8a. What this implies is that the scattered light off the sample in EPSLON configuration will be stronger than the background. This can also be understood from Supplementary Fig. 8b, where tissue scattering is predominantly due to confined light in the waveguide.

Now the presence of any index perturbation at the core-cladding interface scatters this evanescently decaying PL light into the far-field (Fig. 1d) and hence the technique is abbreviated EPSLON. That is, both the coherent as well as the Stoke shifted incoherent PL light gets scattered into the far-field. By invoking a first order Born approximation for evanescent field excitation of biological specimens $S(\vec{r}) = \iint_S \alpha(\vec{r}_k)\delta(\vec{r} - \vec{r}_k)\, d\vec{r}_k$ with α being the polarizability, it is seen that these scattered fields contain the information of the sample. Only these scattered fields are collected by the microscope objective MO_2 and relayed onto the camera via tube lens because of the decoupled illumination and detection scheme offered by waveguides (Supplementary Fig. 7). Through the usage of appropriate bandpass filters, the coherently scattered light is filtered out and only the incoherent light gets detected. The oscillation of MO_1 is synchronized with the detector in such a way that an image is acquired at each excitation point of the waveguide. By invoking Eqn. (1) and neglecting noise, an EPSLON image (Fig. 1d) at the camera plane in general may be described mathematically as

$$I^m(\vec{r}) = \eta|S(\vec{r}) \sum_m a_m(t)\psi_m(\vec{r},t)|^2 \otimes |h(\vec{r})|^2 \quad (2)$$

The abovementioned concepts and experimental results can be summarized into the following: (i) Speckle noise is mitigated in EPSLON images as opposed to label-free waveguide based coherent images due to stochastic fluctuations between the scattered fields, Fig. 1g. (ii) Stochastic fluctuations implies that phase relationships between the scattered fields are lost in EPSLON images as opposed to label-free coherent images. This also leads to identical images for different illumination angles, Fig. 1(h-j) and (iii) Intensity-fluctuations are induced over

time due to time dependence of $a_m(t)$ and $\psi_m(\vec{r},t)$. This is evident in the line plots in Fig. 1j and in the MMI patterns shown as insets in Fig. 2a-2c. This is also validated using simulations in Supplementary section 5, Fig. 9. Thus, EPSLON when used in tandem with fluorescence-based super-resolution algorithms helps develop a high-contrast label-free super-resolution imaging system.

Applications of EPSLON

The potential of EPSLON is first demonstrated on 195 nm polystyrene beads. For brevity, the diffraction-limited label-free image and its corresponding reconstructed super-resolved image in the following sections are termed DL and EPSLON. 2D label-free SIM is demonstrated using four-arm junction waveguide as shown in Fig. 3a and in Supplementary Fig. 10. The use of such a waveguide geometry helps in introducing additional illumination frequencies (Supplementary Fig. 2). 50 images each are acquired using a 0.75 NA detection objective (Fig. 3a) and a 0.9 NA detection objective (Supplementary Fig. 10). The corresponding pixel sizes at the sample plane are for 0.75 NA and 0.9 NA detection objectives are 325 nm and 108 nm respectively. The EPSLON images are then generated using BlindSIM reconstruction algorithm [64]. The EPSLON images of 0.75 NA are validated using a 1.2 NA detection objective which serves as the ground truth optical image. Three insets in the DL image labeled '1', '2' and '3' are blown up and shown. The line plots correspond to intensity variations along the red and green arrows in the DL and EPSLON image respectively. It is seen that the use of such a waveguide geometry helps to resolve beads oriented along different azimuthal directions. EPSLON resolves beads separated by 567 nm, 243 nm and 486 nm in insets '1', '2' and '3' respectively as shown in Fig. 3a. The EPSLON and ground truth images are in good agreement. Then a region within this same field-of-view is then imaged with a 0.9 NA detection objective and the corresponding EPSLON image is shown in Fig. 10 in the supplementary section. Next, in the supplementary Fig. 11, we demonstrate label-free 1-D SIM in EPSLON configuration using three phase shifted frames as input to FairSIM [65]. The nanobeads are deposited directly on the core of SIM structure shown in Fig. 2c. The angle between the interfering waveguides used in the experiment is 60º. This will create an interference pattern with a fringe period $f = \frac{\lambda_{ex}}{2n_f \sin\frac{\theta}{2}}$ where λ_{ex} is the excitation wavelength, $n_f \approx 1.7$ is the refractive index of the guided mode and θ is the angle between the interfering waveguides. For better visualization purposes, the interference fringe pattern shown in Fig. 2c is generated by waveguides interfering at an angle $\theta = 20^{o}$. In supplementary section 8 (supplementary Fig. 12 – Fig. 15), the dependence of speckle size and resolution on λ_{ex}, θ and λ_{det} is experimentally demonstrated. It is experimentally verified that the period of the fringes generated in EPSLON configuration depends on λ_{ex} and θ and the resolution of the final DL image depends in addition also on λ_{det}.

Next, the potential of EPSLON is demonstrated on 100 nm polystyrene beads, Fig. 3b. A straight waveguide is employed, and the images of beads placed directly on top of waveguide core are acquired using a detection MO with numerical aperture NA = 0.9. The acquired image stack of 100 frames is given as input to a fluorescence-based super-resolution algorithm called as Super-resolution method based on Auto-Correlation two-step Deconvolution (SACD) [9]. The choice of SACD over other IFON algorithms is based on the simulation studies shown in supplementary section 3 and due to better performance of the algorithm at low signal to background ratios [66]. Now to validate the super-resolved images generated by SACD, the same sample is imaged by a scanning electron microscope (SEM), which serves as the ground truth image. In Fig. 3b, the line profiles indicate the intensity variations across the particles in the insets. The line profile of the green inset clearly indicates that EPSLON resolves the unresolved nanobeads shown in the red inset in the DL image. The peak-to-peak distance between the beads is 144 nm. It is seen that EPSLON, and the ground truth image (SEM) agree well.

Next, to showcase the potential of EPSLON for life sciences, we choose biological samples such as extra-cellular vesicles (EVs), human placental tissue and rat kidney sections. The first of them, e.g., small EVs, are gaining attention due to their role in intercellular communication and possible clinical applications, especially for targeted drug delivery. Nevertheless, their molecular biology, as well as their therapeutic potential, is far to be completely understood. Further understanding of the spatiotemporal aspects of EVs rely on the ability to image processes such as EV secretion, uptake and biodistribution. However, imaging and tracking of small EVs has been challenging due to their small sizes (50-200 nm), and often require the use of labeling strategies, that may alter EV release and structure, prior to visualization [67]. These problems are mitigated in EPSLON: the decoupled speckle-illumination and detection paths helps visualize these structures beyond the diffraction-limit with high-contrast and without photobleaching as demonstrated in Fig. 4a. The EVs used in this experiment have a size distribution of 75-250 nm, Supplementary Fig. 16, and are fluorescently labeled. EPSLON and total-internal reflection

fluorescence (TIRF) imaging of the same region of interest is performed. Fluorescent dyes are chosen in a way to ensure that there is no fluorescent signal reaching the camera during EPSLON imaging. 50 images are acquired in both EPSLON and TIRF mode using a detection MO with NA = 0.45. It is seen in Fig. 4a and Fig. 4b that the EPSLON and TIRF images are in good agreement. The line profile in the red and green insets in Fig. 4b show a blob of light and therefore, unable to clearly resolve the EV particles. To resolve these particles, the DL image stack is given as input to the reconstruction algorithm to generate the EPSLON image. From Fig. 4b it is seen that in the EPSLON image the EVs are clearly resolved as shown by the line profiles. To validate the EPSLON result, the same region of interest is imaged with a higher NA = 0.9 detection MO. The EPSLON matches well with the line profile of the ground truth optical image.

We now showcase the potential of EPSLON for the evaluation of human placental tissue sections using straight waveguides in tandem with SACD. The human placenta is a pregnancy-specific organ that plays a key role in mediating the gas and nutrient exchange between the mother and the fetus. Moreover, scientific evidence suggests a relationship between ultrastructural changes in placentas and pregnancy-related diseases such as preeclampsia ([68]). Traditionally, the visualization of such changes was made possible through complex, costly, and slow methods such as electron microscopy. Although recent advances in fluorescence-based super-resolution microscopy have successfully enabled detailed visualizations of such ultrastructural features [18, 69], the fluorescent markers used in these imaging methods exhibit practical limitations for routine histological practice. These include (1) low stability, in the sense that the fluorescence imaging must be carried out in a relatively short period of time after sample labeling, e.g. less than a week, to avoid the issues with the decay of the fluorescent dyes; (2) a special handling of the fluorescently-labeled sample, particularly to avoid light exposure that might render the dyes photobleached; and (3) extended sample preparation, in terms of cost and time, associated with the fluorescence labeling. Thus, a label-free method for achieving ultrastructural visualizations of the placental morphology would prove advantageous for the field of placental research. Here, the proposed EPSLON method alleviate these issues, enabling a fast, simple, and repeatable route for observing, for example, sub-diffraction sized placental features. We illustrate the potential of EPSLON for placental histology in Fig. 5. First, 250 optical images of a region of interest were acquired using a detection MO with NA = 1.2, and subsequently averaged to obtain a diffraction-limited image (DL), as shown in Fig. 5a. The corresponding super-resolved EPSLON image is also shown in Fig. 5a. Next, to serve as a ground truth, a scanning electron microscope image of the same sample region is performed, as illustrated in Fig. 5b. The white dotted boxes in Fig. 5a and Fig. 5b are respectively expanded in Fig. 5c and Fig. 5d. The former, Fig. 5c, reveals the enhanced contrast and super-resolution provided by EPSLON in comparison to the DL method. The latter, Fig. 5d, offers a complementary view of the same region, where the white arrows indicate features of fine correlation between EPSLON and SEM images. The resolution of optical images acquired is quantified using FRC, Fourier Ring Correlation [70]. Mean FRC of DL image is 496 nm and of EPSLON is 176 nm, ~2.8 times resolution gain. A Supplementary Movie 1 is provided to show correlation between EPSLON and SEM images in Fig. 5. One of the inherent advantages of photonic chip-based microscopy is large field-of-view (FOV) super-resolution imaging. Therefore, a larger FOV image of a human placenta section acquired using a 10X/0.25 NA and its corresponding EPSLON image, which is essential for histopathology applications, is shown in Supplementary Fig. 17.

Next, we demonstrate the utility of EPSLON as an attractive method for super-resolution imaging of kidney tissue. Particularly, the ultrastructural analysis of this organ is of great importance for the identification of several renal pathologies such as, for example, the minimal change disease [71]. While in recent years significant attention has been given to fluorescence-based super-resolution optical methods for kidney research and diagnosis [72], the exploration of label-free optical super-resolution approaches in these cases remain largely unexplored. In this work, we employed rat kidney sections as a test sample as shown in Fig. 6. 250 frames of rat kidney sections are imaged first in label-free mode, then in waveguide TIRF mode (i.e., using fluorescence markers) and finally using SEM. Fig. 6a shows the label-free DL and EPSLON images of a rat kidney section acquired using a detection MO with NA = 1.42. The central portion of the image labeled ‘G’ in yellow font represents a kidney glomerulus, while regions labeled ‘PT’ in yellow font correspond to the proximal tubuli in the kidney section. Three regions of interest labeled ‘b’, ‘c’ and ‘d’ in Fig. 6a are blown-up and shown. Fig. 6b1 and Fig. 6c1 are TIRF-DL images of regions enclosed in ‘b’ and ‘c’. Its corresponding TIRF-SACD images are shown in Fig. 6b2 and Fig. 6c2 respectively. Label free DL images of regions enclosed in ‘b’ and ‘c’ are shown in Fig. 6b3 and Fig. 6c3. Its corresponding EPSLON images are shown in Fig. 6b4 and Fig. 6c4 respectively. Fig. 6d1 and Fig. 6d2 are TIRF-DL and TIRF-SACD images of the region labeled ‘d’. Label-free DL and EPSLON images of the region labeled ‘d’ are shown in Fig. 6d3 and Fig. 6d4 respectively. A SEM image of the same region is shown in Fig. 6d5. Also, a Supplementary Movie 2 is added to show the correlation between DL and EPSLON at different regions of interest

in Fig. 6. The mean resolution of label-free DL image is 256 nm and for EPSLON is 133 nm, which implies a ~1.92 fold resolution gain. Local FRC plot of the whole field-of-view in Fig. 6 is shown in supplementary Fig. 18.

Discussion and Outlook

Fluorescence based algorithms have been previously applied to coherently scattering specimens [47, 73]. However, the reconstructed images generated must be interpreted with caution with regards to resolution beyond the diffraction-limit as coherence of the scattered light cannot be neglected [13, 32]. In our proof-of-concept work EPSLON, we circumvent this issue for two-dimensional samples by realizing a light source with δ-function correlations, i.e., by using the PL property of Si_3N_4 waveguides for near-field illumination of unlabeled samples. In addition, PL emission takes place within the core matrix and a part of it gets transmitted into the far-field, which prevents realizing an ideal chip-based imaging system where only the scattered light off the sample reaches the camera. As a result, the signal to background ratio of weakly scattering specimens is poor and. Despite the limited photon budget, we have demonstrated proof-of-concept label-free super-resolution results on nanobeads, EVs, human placenta tissue and rat kidney sections. The experimental particulars are provided in Table 2 and Table 3 in the supplementary material. In future works, we propose novel chip designs as in Ref. [74, 75] which will improve the signal to background ratio. The other challenge of lack of specificity in label-free imaging can be mitigated by resorting to machine learning based tools [76].

This work lays the foundation for synthesizing a label-free incoherent imaging system that is compatible with the myriad of fluorescence based super-resolution algorithms to circumvent the spatial diffraction-limit. We believe that EPSLON will trigger further developments of label-free super-resolution incoherent optical microscopy methods and its application in biology, with particular attention to histological analyses where a fast, simple, cost-effective, and high-resolution imaging method is beneficial for medical guidance and diagnosis. Future studies will also investigate the role of intrinsic autofluorescence of tissue sections in label-free imaging. Expanding the concepts of EPSLON to be applied in tandem with other fluorescence-based super-resolution algorithms like Non-linear SIM [77], STED [78] and expansion microscopy [79] is currently in progress. This work could also initiate further developments within integrated optics to harness the PL properties of different materials. Interestingly, PL in waveguides is an undesirable phenomenon as it increases the propagation losses of the guiding structures. However, here we demonstrated that PL of Si_3N_4 waveguide can be harnessed for near-field illumination to develop an incoherent imaging system for surpassing the diffraction limit in label-free regime.

References

1. Wolf, E., 2007. *Introduction to the Theory of Coherence and Polarization of Light*. Cambridge university press.
2. Fujimoto, J.G., Pitris, C., Boppart, S.A. and Brezinski, M.E., 2000. Optical coherence tomography: an emerging technology for biomedical imaging and optical biopsy. *Neoplasia*, *2*(1-2), pp.9-25.
3. Heintzmann, R. and Cremer, C.G., 1999, January. Laterally modulated excitation microscopy: improvement of resolution by using a diffraction grating. In *Optical biopsies and microscopic techniques III* (Vol. 3568, pp. 185-196). SPIE.
4. Gustafsson, M.G., 2000. Surpassing the lateral resolution limit by a factor of two using structured illumination microscopy. *Journal of microscopy*, *198*(2), pp.82-87.
5. Dertinger, T., Colyer, R., Iyer, G., Weiss, S. and Enderlein, J., 2009. Fast, background-free, 3D super-resolution optical fluctuation imaging (SOFI). *Proceedings of the National Academy of Sciences*, *106*(52), pp.22287-22292.
6. Gustafsson, N., Culley, S., Ashdown, G., Owen, D.M., Pereira, P.M. and Henriques, R., 2016. Fast live-cell conventional fluorophore nanoscopy with ImageJ through super-resolution radial fluctuations. *Nature communications*, *7*(1), pp.1-9.
7. Yahiatene, I., Hennig, S., Müller, M. and Huser, T., 2015. Entropy-based super-resolution imaging (ESI): From disorder to fine detail. *Acs Photonics*, *2*(8), pp.1049-1056.
8. Cox, S., Rosten, E., Monypenny, J., Jovanovic-Talisman, T., Burnette, D.T., Lippincott-Schwartz, J., Jones, G.E. and Heintzmann, R., 2012. Bayesian localization microscopy reveals nanoscale podosome dynamics. *Nature methods*, *9*(2), pp.195-200.

9. Zhao, W., Zhao, S., Han, Z., Ding, X., Hu, G., Qu, L., Huang, Y., Wang, X., Mao, H., Jiu, Y. and Hu, Y., 2023. Enhanced detection of fluorescence fluctuations for high-throughput super-resolution imaging. *Nature Photonics*, pp.1-8.
10. Agarwal, K. and Macháň, R., 2016. Multiple signal classification algorithm for super-resolution fluorescence microscopy. *Nature communications*, *7*(1), pp.1-9.
11. Ryabukho, V.P., Lyakin, D.V., Grebenyuk, A.A. and Klykov, S.S., 2013. Wiener–Khintchin theorem for spatial coherence of optical wave field. *Journal of Optics*, *15*(2), p.025405.
12. Goodman, J.W., 2007. *Speckle phenomena in optics: theory and applications*. Roberts and Company Publishers.
13. Wicker, K. and Heintzmann, R., 2014. Resolving a misconception about structured illumination. *Nature Photonics*, *8*(5), pp.342-344.
14. Kistner, J., Chen, X., Weng, Y., Strunk, H.P., Schubert, M.B. and Werner, J.H., 2011. Photoluminescence from silicon nitride—no quantum effect. *Journal of Applied Physics*, *110*(2), p.023520.
15. Coucheron, D.A., Helle, Ø.I., Wilkinson, J.S., Murugan, G.S., Domínguez, C., Angelskår, H. and Ahluwalia, B.S., 2021. Study of waveguide background at visible wavelengths for on-chip nanoscopy. *Optics Express*, *29*(13), pp.20735-20746.
16. Diekmann, R., Helle, Ø.I., Øie, C.I., McCourt, P., Huser, T.R., Schüttpelz, M. and Ahluwalia, B.S., 2017. Chip-based wide field-of-view nanoscopy. *Nature Photonics*, *11*(5), pp.322-328.
17. Jayakumar, N., Helle, Ø.I., Agarwal, K. and Ahluwalia, B.S., 2020. On-chip TIRF nanoscopy by applying Haar wavelet kernel analysis on intensity fluctuations induced by chip illumination. *Optics Express*, *28*(24), pp.35454-35468.
18. Villegas-Hernández, L.E., Dubey, V., Nystad, M., Tinguely, J.C., Coucheron, D.A., Dullo, F.T., Priyadarshi, A., Acuña, S., Ahmad, A., Mateos, J.M. and Barmettler, G., 2022. Chip-based multimodal super-resolution microscopy for histological investigations of cryopreserved tissue sections. *Light: Science & Applications*, *11*(1), pp.1-17.
19. Kim, M., Park, C., Rodriguez, C., Park, Y. and Cho, Y.H., 2015. Superresolution imaging with optical fluctuation using speckle patterns illumination. *Scientific reports*, *5*(1), p.16525.
20. Choi, Y., Kim, M., Park, C., Park, J., Park, Y. and Cho, Y.H., 2022. Wide-field super-resolution optical fluctuation imaging through dynamic near-field speckle illumination. *Nano letters*, *22*(6), pp.2194-2201.
21. Zernike, F., 1955. How I discovered phase contrast. *Science*, *121*(3141), pp.345-349.
22. Munro, P.R. and Török, P., 2005. Vectorial, high numerical aperture study of Nomarski's differential interference contrast microscope. *Optics Express*, *13*(18), pp.6833-6847.
23. Hoffman, R., 1977. The modulation contrast microscope: principles and performance. *Journal of microscopy*, *110*(3), pp.205-222.
24. Taylor, R.W., Mahmoodabadi, R.G., Rauschenberger, V., Giessl, A., Schambony, A. and Sandoghdar, V., 2019. Interferometric scattering microscopy reveals microsecond nanoscopic protein motion on a live cell membrane. *Nature Photonics*, *13*(7), pp.480-487.
25. Park, Y., Depeursinge, C. and Popescu, G., 2018. Quantitative phase imaging in biomedicine. *Nature photonics*, *12*(10), pp.578-589.
26. Baek, Y. and Park, Y., 2021. Intensity-based holographic imaging via space-domain Kramers–Kronig relations. *Nature Photonics*, *15*(5), pp.354-360.
27. Zheng, G., Horstmeyer, R. and Yang, C., 2013. Wide-field, high-resolution Fourier ptychographic microscopy. *Nature photonics*, *7*(9), pp.739-745.
28. Ruh, D., Mutschler, J., Michelbach, M. and Rohrbach, A., 2018. Superior contrast and resolution by image formation in rotating coherent scattering (ROCS) microscopy. *Optica*, *5*(11), pp.1371-1381.
29. Redding, B., Choma, M.A. and Cao, H., 2012. Speckle-free laser imaging using random laser illumination. *Nature photonics*, *6*(6), pp.355-359.
30. Ojaghi, A., Fay, M.E., Lam, W.A. and Robles, F.E., 2018. Ultraviolet hyperspectral interferometric microscopy. *Scientific reports*, *8*(1), pp.1-6.
31. Liu, X., Kuang, C., Hao, X., Pang, C., Xu, P., Li, H., Liu, Y., Yu, C., Xu, Y., Nan, D. and Shen, W., 2017. Fluorescent nanowire ring illumination for wide-field far-field subdiffraction imaging. *Physical Review Letters*, *118*(7), p.076101.
32. Jayakumar, N., Dullo, F.T., Dubey, V., Ahmad, A., Ströhl, F., Cauzzo, J., Guerreiro, E.M., Snir, O., Skalko-Basnet, N., Agarwal, K. and Ahluwalia, B.S., 2022. Multi-moded high-index contrast optical waveguide for super-contrast high-resolution label-free microscopy. *Nanophotonics*, *11*(15), pp.3421-3436.

33. Schermelleh, L., Ferrand, A., Huser, T., Eggeling, C., Sauer, M., Biehlmaier, O. and Drummen, G.P., 2019. Super-resolution microscopy demystified. *Nature cell biology*, *21*(1), pp.72-84.
34. Betzig, E. and Chichester, R.J., 1993. Single molecules observed by near-field scanning optical microscopy. *Science*, *262*(5138), pp.1422-1425.
35. Pendry, J.B., 2000. Negative refraction makes a perfect lens. *Physical review letters*, *85*(18), p.3966.
36. Wang, Z., Guo, W., Li, L., Luk'Yanchuk, B., Khan, A., Liu, Z., Chen, Z. and Hong, M., 2011. Optical virtual imaging at 50 nm lateral resolution with a white-light nanoscope. *Nature communications*, *2*(1), pp.1-6.
37. Darafsheh, A., Limberopoulos, N.I., Derov, J.S., Walker Jr, D.E. and Astratov, V.N., 2014. Advantages of microsphere-assisted super-resolution imaging technique over solid immersion lens and confocal microscopies. *Applied Physics Letters*, *104*(6), p.061117.
38. Rogers, E.T., Lindberg, J., Roy, T., Savo, S., Chad, J.E., Dennis, M.R. and Zheludev, N.I., 2012. A super-oscillatory lens optical microscope for subwavelength imaging. *Nature materials*, *11*(5), pp.432-435.
39. Barsi, C. and Fleischer, J.W., 2013. Nonlinear abbe theory. *Nature Photonics*, *7*(8), pp.639-643.
40. Zalevsky, Z. and Mendlovic, D., 2004. *Optical superresolution* (Vol. 91). Springer Science & Business Media.
41. Astratov, V. ed., 2019. *Label-free super-resolution microscopy* (p. 371). Cham: Springer.
42. Cotte, Y., Toy, F., Jourdain, P., Pavillon, N., Boss, D., Magistretti, P., Marquet, P. and Depeursinge, C., 2013. Marker-free phase nanoscopy. *Nature Photonics*, *7*(2), pp.113-117.
43. Maire, G., Giovannini, H., Talneau, A., Chaumet, P.C., Belkebir, K. and Sentenac, A., 2018. Phase imaging and synthetic aperture super-resolution via total internal reflection microscopy. *Optics letters*, *43*(9), pp.2173-2176.
44. Yurdakul, C., Avci, O., Matlock, A., Devaux, A.J., Quintero, M.V., Ozbay, E., Davey, R.A., Connor, J.H., Karl, W.C., Tian, L. and Unlu, M.S., 2020. High-throughput, high-resolution interferometric light microscopy of biological nanoparticles. *ACS nano*, *14*(2), pp.2002-2013.
45. Ströhl, F., Opstad, I.S., Tinguely, J.C., Dullo, F.T., Mela, I., Osterrieth, J.W., Ahluwalia, B.S. and Kaminski, C.F., 2019. Super-condenser enables labelfree nanoscopy. *Optics express*, *27*(18), pp.25280-25292.
46. Tang, M., Han, Y., Ye, D., Zhang, Q., Pang, C., Liu, X., Shen, W., Ma, Y., Kaminski, C.F., Liu, X. and Yang, Q., 2022. High-Refractive-Index Chip with Periodically Fine-Tuning Gratings for Tunable Virtual-Wavevector Spatial Frequency Shift Universal Super-Resolution Imaging. *Advanced Science*, *9*(9), p.2103835.
47. Pang, C., Li, J., Tang, M., Wang, J., Mela, I., Ströhl, F., Hecker, L., Shen, W., Liu, Q., Liu, X. and Wang, Y., 2019. On-Chip Super-Resolution Imaging with Fluorescent Polymer Films. *Advanced Functional Materials*, *29*(27), p.1900126.
48. Lee, Y.U., Li, S., Wisna, G.B.M., Zhao, J., Zeng, Y., Tao, A.R. and Liu, Z., 2022. Hyperbolic material enhanced scattering nanoscopy for label-free super-resolution imaging. *Nature communications*, *13*(1), pp.1-8.
49. Lin, C., Peñaranda, J.S.D., Dendooven, J., Detavernier, C., Schaubroeck, D., Boon, N., Baets, R. and Le Thomas, N., 2022. UV photonic integrated circuits for far-field structured illumination autofluorescence microscopy. *Nature Communications*, *13*(1), pp.1-9.
50. Dong, B., Almassalha, L.M., Stypula-Cyrus, Y., Urban, B.E., Chandler, J.E., Nguyen, T.Q., Sun, C., Zhang, H.F. and Backman, V., 2016. Superresolution intrinsic fluorescence imaging of chromatin utilizing native, unmodified nucleic acids for contrast. *Proceedings of the National Academy of Sciences*, *113*(35), pp.9716-9721.
51. Goodman, J. W. *Introduction to Fourier Optics* (Roberts & Company, 2005).
52. Gustafsson, M.G., 2005. Nonlinear structured-illumination microscopy: wide-field fluorescence imaging with theoretically unlimited resolution. *Proceedings of the National Academy of Sciences*, *102*(37), pp.13081-13086.
53. Berezin, M.Y. and Achilefu, S., 2010. Fluorescence lifetime measurements and biological imaging. *Chemical reviews*, *110*(5), pp.2641-2684.
54. Chowdhury, S., Dhalla, A.H. and Izatt, J., 2012. Structured oblique illumination microscopy for enhanced resolution imaging of non-fluorescent, coherently scattering samples. *Biomedical optics express*, *3*(8), pp.1841-1854.

55. Prieto, F., Sepúlveda, B., Calle, A., Llobera, A., Domínguez, C., Abad, A., Montoya, A. and Lechuga, L.M., 2003. An integrated optical interferometric nanodevice based on silicon technology for biosensor applications. *Nanotechnology*, *14*(8), p.907.
56. Tinguely, J.C., Helle, Ø.I. and Ahluwalia, B.S., 2017. Silicon nitride waveguide platform for fluorescence microscopy of living cells. *Optics express*, *25*(22), pp.27678-27690.
57. Dhakal, A., Wuytens, P., Raza, A., Le Thomas, N. and Baets, R., 2017. Silicon nitride background in nanophotonic waveguide enhanced Raman spectroscopy. *Materials*, *10*(2), p.140.
58. Aydinli, A., Serpengüzel, A. and Vardar, D., 1996. Visible photoluminescence from low temperature deposited hydrogenated amorphous silicon nitride. *Solid state communications*, *98*(4), pp.273-277.
59. Vlasukova, L.A., Komarov, F.F., Parkhomenko, I.N., Milchanin, O.V., Leont'ev, A.V., Mudryi, A.V. and Togambaeva, A.K., 2013. Optical properties of silicon nitride films formed by plasma-chemical vapor deposition. *Journal of Applied Spectroscopy*, *80*(1), pp.89-92.
60. Giorgis, F., Vinegoni, C. and Pavesi, L., 2000. Optical absorption and photoluminescence properties of a− Si 1− x N x: H films deposited by plasma-enhanced CVD. *Physical Review B*, *61*(7), p.4693.
61. Smith, J., Monroy-Ruz, J., Rarity, J.G. and C. Balram, K., 2020. Single photon emission and single spin coherence of a nitrogen vacancy center encapsulated in silicon nitride. *Applied Physics Letters*, *116*(13), p.134001.
62. Helle, Ø.I., Dullo, F.T., Lahrberg, M., Tinguely, J.C., Hellesø, O.G. and Ahluwalia, B.S., 2020. Structured illumination microscopy using a photonic chip. *Nature Photonics*, *14*(7), pp.431-438.
63. Engdahl, A.K., Belle, S., Wang, T.C., Hellmann, R., Huser, T. and Schüttpelz, M., 2021. Large Field-of-View Super-Resolution Optical Microscopy Based on Planar Polymer Waveguides. *ACS Photonics*, *8*(7), pp.1944-1950.
64. Mudry, E., Belkebir, K., Girard, J., Savatier, J., Le Moal, E., Nicoletti, C., Allain, M. and Sentenac, A., 2012. Structured illumination microscopy using unknown speckle patterns. *Nature Photonics*, *6*(5), pp.312-315.Müller, M., Mönkemöller, V., Hennig, S., Hübner, W. and Huser, T., 2016. Open-source image reconstruction of super-resolution structured illumination microscopy data in ImageJ. *Nature communications*, *7*(1), pp.1-6.
65. Müller, M., Mönkemöller, V., Hennig, S., Hübner, W. and Huser, T., 2016. Open-source image reconstruction of super-resolution structured illumination microscopy data in ImageJ. *Nature communications*, *7*(1), pp.1-6.
66. Opstad, I.S., Acuña, S., Hernandez, L.E.V., Cauzzo, J., Škalko-Basnet, N., Ahluwalia, B.S. and Agarwal, K., 2020. Fluorescence fluctuations-based super-resolution microscopy techniques: an experimental comparative study. *arXiv preprint arXiv:2008.09195*.
67. Chuo, S.T.Y., Chien, J.C.Y. and Lai, C.P.K., 2018. Imaging extracellular vesicles: current and emerging methods. *Journal of biomedical science*, *25*(1), pp.1-10.
68. Redman, C.W.G., Tannetta, D.S., Dragovic, R.A., Gardiner, C., Southcombe, J.H., Collett, G.P. and Sargent, I.L., 2012. Does size matter? Placental debris and the pathophysiology of pre-eclampsia. *Placenta*, *33*, pp.S48-S54.
69. Villegas-Hernández, L.E., Nystad, M., Ströhl, F., Basnet, P., Acharya, G. and Ahluwalia, B.S., 2020. Visualizing ultrastructural details of placental tissue with super-resolution structured illumination microscopy. *Placenta*, *97*, pp.42-45.
70. Zhao, W., Huang, X., Yang, J., Qiu, G., Qu, L., Zhao, Y., Zhao, S., Luo, Z., Wang, X., Jiu, Y. and Mao, H., 2022. Quantitatively mapping local quality of super-resolution microscopy by rolling Fourier ring correlation. *bioRxiv*, pp.2022-12.
71. Patrakka, J., Lahdenkari, A.T., Koskimies, O., Holmberg, C., Wartiovaara, J. and Jalanko, H., 2002. The number of podocyte slit diaphragms is decreased in minimal change nephrotic syndrome. *Pediatric research*, *52*(3), pp.349-355.
72. Siegerist, F., Drenic, V., Koppe, T.M., Telli, N. and Endlich, N., 2023. Super-Resolution Microscopy: A Technique to Revolutionize Research and Diagnosis of Glomerulopathies. *Glomerular Diseases*, *3*(1), pp.19-28.
73. Chang, B.J., Lin, S.H., Chou, L.J. and Chiang, S.Y., 2011. Subdiffraction scattered light imaging of gold nanoparticles using structured illumination. *Optics letters*, *36*(24), pp.4773-4775.
74. Chazot, C.A., Nagelberg, S., Rowlands, C.J., Scherer, M.R., Coropceanu, I., Broderick, K., Kim, Y., Bawendi, M.G., So, P.T. and Kolle, M., 2020. Luminescent surfaces with tailored angular emission for compact dark-field imaging devices. *Nature photonics*, *14*(5), pp.310-315.

75. Kuai, Y., Chen, J., Fan, Z., Zou, G., Lakowicz, J. and Zhang, D., 2021. Planar photonic chips with tailored angular transmission for high-contrast-imaging devices. *Nature communications*, *12*(1), pp.1-9.
76. Kandel, M.E., He, Y.R., Lee, Y.J., Chen, T.H.Y., Sullivan, K.M., Aydin, O., Saif, M.T.A., Kong, H., Sobh, N. and Popescu, G., 2020. Phase imaging with computational specificity (PICS) for measuring dry mass changes in sub-cellular compartments. *Nature communications*, *11*(1), pp.1-10.
77. Gustafsson, M.G., 2005. Nonlinear structured-illumination microscopy: wide-field fluorescence imaging with theoretically unlimited resolution. *Proceedings of the National Academy of Sciences*, *102*(37), pp.13081-13086.
78. Hell, S.W. and Wichmann, J., 1994. Breaking the diffraction resolution limit by stimulated emission: stimulated-emission-depletion fluorescence microscopy. *Optics letters*, *19*(11), pp.780-782.
79. Chen, F., Tillberg, P.W. and Boyden, E.S., 2015. Expansion microscopy. *Science*, *347*(6221), pp.543-548.

Ethical statement

Full-term placentae from 10 different Caucasian healthy patients were collected anonymously immediately after delivery at the University Hospital of North Norway. Written consent was obtained from the participants according to the protocol approved by the Regional Committee for Medical and Health Research Ethics of North Norway (REK Nord reference no. 2010/2058–4).

Acknowledgements

We wish to acknowledge the fruitful discussions with Prof. Olav Gaute Helleso (UiT), Dr. Florian Strohl (UiT) and Prof. Krishna Agarwal (UiT). Also acknowledgments to Prof. Ganesh Acharya and Associate Prof. Mona Nystad (UiT) for providing us with the tissue placenta sections and Assoc. Prof. Neoma Tove Boardman and Nirgun Basnet for providing rat kidney tissue sections. We are grateful to Fernando Cázarez-Márquez for assisting with the rat kidney embedding and sectioning.

This project has received funding from the European Union's Horizon 2020 research and innovation program under the Marie Skłodowska-Curie Grant Agreement No. 766181, project "DeLIVER". BSA acknowledges the funding from the Research Council of Norway, projects # NANO 2021–288565 and # BIOTEK 2021–285571, and from the European Innovation Council (EIC), EIC-Transition project # 101058016.

Authors and Affiliations

Dept. of Physics and Technology, UiT The Arctic University of Norway, Tromsø 9037, Norway

Nikhil Jayakumar, Luis E. Villegas-Hernández, Hong Mao Jean-Claude Tinguley, Balpreet Singh Ahluwalia

Dept. of Microsystems and Nanotechnology, SINTEF Digital, Gaustadalleen 23C, 0373 Oslo, Norway

Firehun T Dullo

Dept. of Molecular Cell Biology, Institute for Cancer Research, Oslo University Hospital, Oslo, Norway

Krizia Sagini, Alicia Llorente

Centre for Cancer Cell Reprogramming, Faculty of Medicine, University of Oslo, Montebello, 0379 Oslo, Norway

Krizia Sagini, Alicia Llorente

Dept. for Mechanical, Electronics and Chemical Engineering, Oslo Metropolitan University, Oslo, Norway

Alicia Llorente

Innovation Photonics and Imaging Center, School of Instrumentation Science and Engineering, Harbin Institute of Technology, Harbin, China

Weisong Zhao

Author Contribution

NJ conceptualized the idea. NJ and BSA designed the experiments. WZ performed SACD and BlindSIM reconstructions. LEVH prepared the human placenta tissue and rat kidney sections on chip and imaged along with NJ. HM and LEVH performed SEM imaging of tissue sections. FTD and JCT designed the waveguide chip and mask for fabrication. FTD also performed the FIMMWAVE simulations. KS and AL provided the extra-cellular vesicles for imaging and wrote the EV preparation protocol. NJ performed the experiments, analyzed the results and prepared the manuscript with inputs from FTD, JCT, and BSA. NJ, LEVH, HM and JCT prepared the figures. LEVH prepared the video animations in the supplementary section. All authors commented on the manuscript. BSA secured the funding and supervised the project.

Conflict of interest statement: B.S.A. have applied for patent for chip-based optical nanoscopy. B.S.A is the co-founder of the company Chip NanoImaging AS, which commercializes on-chip super-resolution microscopy systems. All other authors declare no conflicts of interest regarding this article.

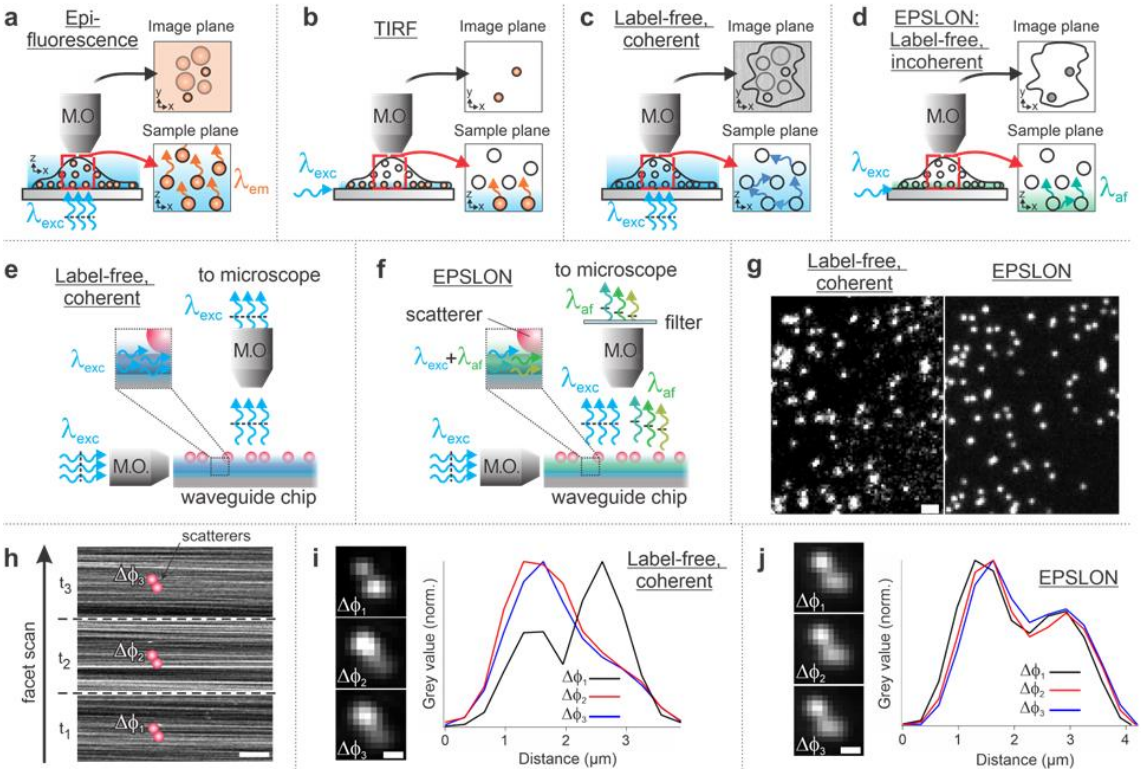

Figure 1 **Overview of ELSPON:** (**a-d**) Comparison between fluorescence and label-free microscopy. (**a**) Epifluorescence: coherent light λ_{exc} is used for excitation of fluorescent molecules and the camera detects the Stoke shifted incoherent light emitted by the molecules λ_{em}. Stochastic fluctuations of the Stoke shifted light and specificity offered by the molecules helps suppress speckle noise enabling high-contrast imaging. (**b**) TIRF: coherent light for near-field illumination of fluorescently labeled samples and incoherent light gets detected by the camera. Near-field illumination helps to further improve the contrast as compared to the epifluorescence by illuminating thin sections of the sample. (**c**) Label-free coherent imaging: coherent light for illumination and coherent light gets detected by the camera. Multiple scattering and coherent nature of the scattered light leads to speckle noise, (**d**) EPSLON: incoherent light for near-field illumination of unlabeled samples and incoherent light scattered by the sample, λ_{af}, forms the image. The incoherent nature of the detected light in addition to the near-field illumination helps generate high-contrast label-free images. (**e**) Schematic of optical waveguide-based label-free coherent imaging. The guided coherent light generates an evanescent field that interacts with the sample placed at the core-cladding interface,. (**f**) Schematic of EPSLON imaging using Si_3N_4 waveguide. The guided coherent light induces incoherent photoluminescence (PL) in the core of the waveguide that interacts with the sample and gets transmitted into the far-field. (**g**) 200 nm gold nanoparticles imaged in coherent and EPSLON mode, scale bar 100 μm. The issues of coherent noise, poor-contrast associated with conventional label-free techniques is mitigated in EPSLON due to δ-function correlations existing in the detected light. (**h**) To induce fluctuations in image intensity over time, different modes of the waveguide are excited by scanning the coupling objective along the input facet of the waveguide. At each instance of time t_1, t_2, t_3 etc. the scatterers get excited by different MMI patterns, and an image is acquired. Scale bar 10 μm. (**i**) Experimental demonstration of coherence of scattered light using two 200 nm gold nanoparticles, scale bar 10 μm. The excitation of different modes causes the phase difference $\Delta\varphi$ between the scattered light off the particles to change, leading to different images at different instances of time in label-free coherent imaging. This is demonstrated by the line profile of the bead images provided alongside. (**j**) Experimental realization of stochastic nature of the detected light in label-free imaging. The same nanoparticles shown in (i) are imaged in EPSLON mode, scale bar 10 μm. In EPSLON, stochastic fluctuations between the scattered incoherent PL light reaching the camera leads to identical images at different instances of time. This can be seen from the line profiles of the bead images provided alongside.

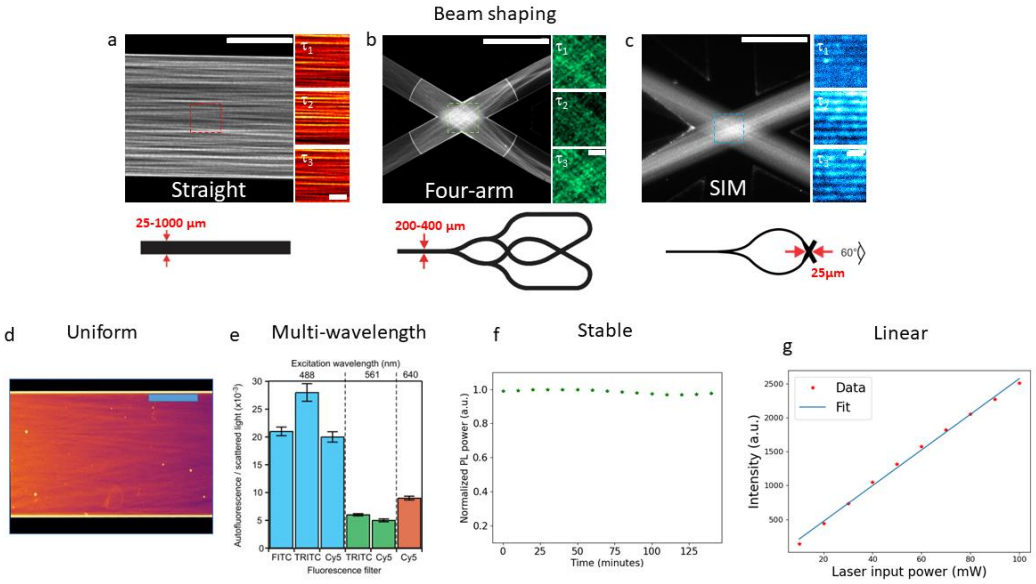

Figure 2: Structuring the incoherent photoluminescent illumination using Si_3N_4 waveguides and its properties. (**a-c**) Structuring photoluminescence using different waveguide geometries. (**a**) Straight waveguide that supports multiple modes in the core, scale bar 20 µm. The red insets are a part of the imaging region on the straight waveguide that is blown up to show the MMI pattern at different instances of time, scale bar 5 µm. Schematic diagram shows the geometry and width of the straight waveguide fabricated on a wafer. (**b**) Four-arm crossing waveguide provides more illumination spatial frequencies, scale bar 20 µm. The green inset is the blown-up region of the imaging area on the four-arm crossing waveguide, showing different speckle patterns at different instances of time, scale bar 5 µm. Schematic diagram shows the geometry and width of the four-arm crossing waveguide. (**c**) SIM chip where two single-mode waveguides are made to overlap at the imaging area enclosed by the blue inset, scale bar 20 µm. The blown-up regions show the interference fringe pattern at three different phases, 2 µm. Schematic diagram shows the geometry of the SIM chip for two-dimensional SIM works. (**d**) By averaging out several MMI patterns, an illumination profile devoid of speckle patterns, as shown in supplementary Fig. 2b, over large field-of-view can be generated, scale bar 100 µm. The color grading visible from left to right is attributed to propagation loss (Supplementary Table 1). (**e**) Ratio of incoherent PL scattering to coherent scattering for a single waveguide at three different wavelengths is plotted. Here the waveguide is excited at 488 nm, 561 nm and 640 nm and the corresponding emissions may be detected in FITC, TRITC and CY5 channels. (**f**) Normalized PL emission with a root mean squared value of 1007 a.u. is plotted here as a function of time. No bleaching was observed for about 2 hours of imaging indicating a stable emission that is suitable for long-term cell imaging. (**g**) PL emission varies linearly with the input coupling power, implying a linear system.

a **2D label-free SIM**

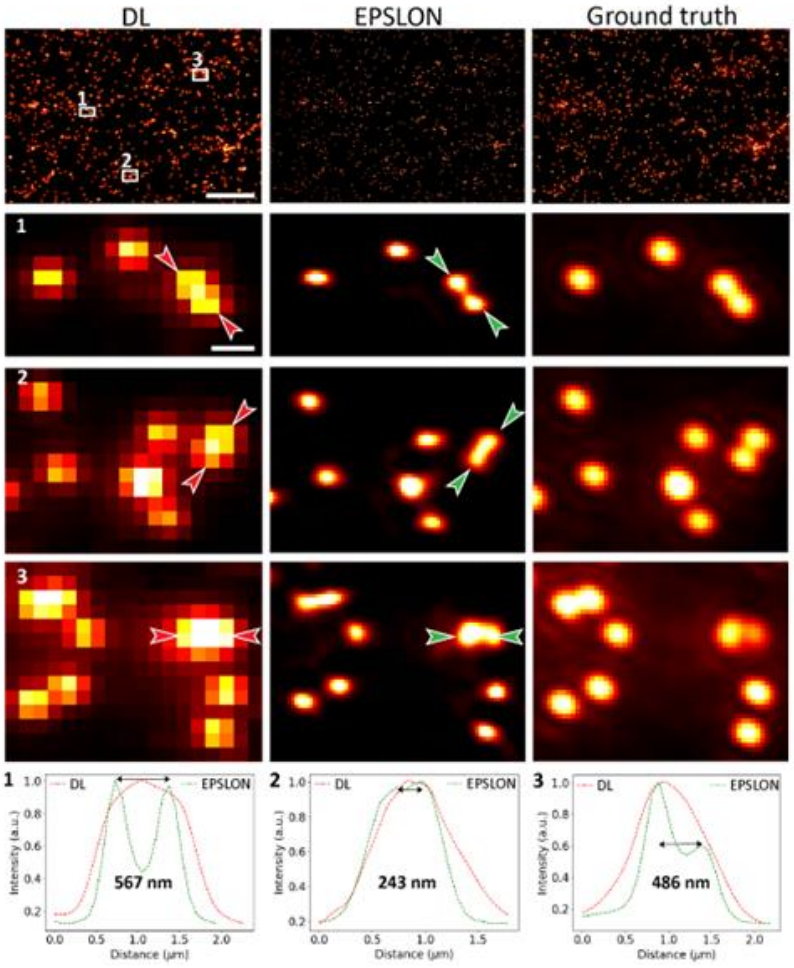

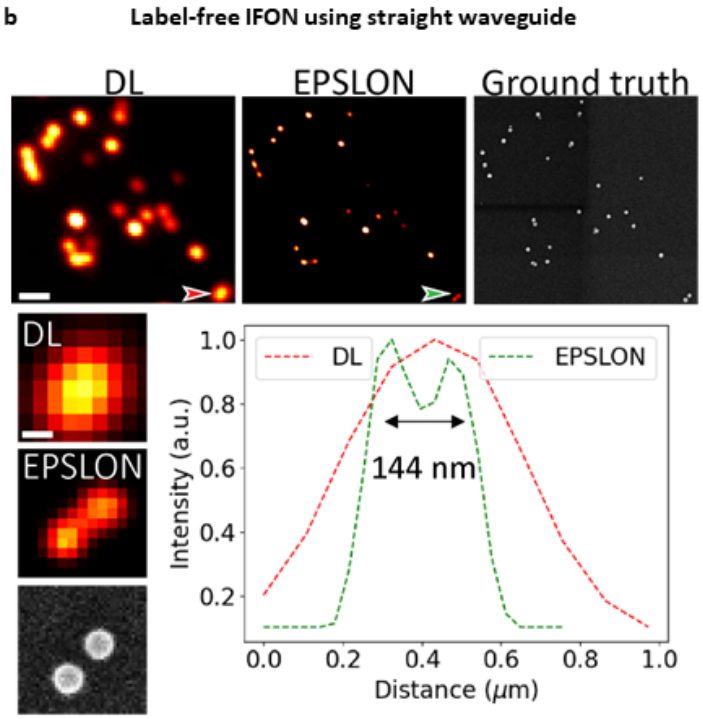

Figure 3: (a) EPSLON for label-free 2D SIM of 195 nm polystyrene beads using four-arm junction waveguide. Large field-of-view diffraction-limited (DL), super-resolved (EPSLON) and ground-truth images are shown, scale bar 20 μm. The DL images are acquired using 0.75 NA and ground truth optical image with 60X 1.2 NA objective lens. Three regions of interest enclosed in white boxes in DL image are blown up and shown, scale bar 1 μm. The corresponding EPSLON and ground-truth large images are also blown up and shown alongside which agree. The red arrows indicate unresolved beads in the DL images and the green arrows indicate the resolved beads in the EPSLON images. The line plots corresponding to normalized intensity variations along these arrows show the resolution improvement in EPSLON. **(b) EPSLON for label-free super-resolution imaging of 100 nm polystyrene beads using straight waveguides**. Diffraction-limited DL image, super-resolved EPSLON image and scanning electron microscope (SEM) ground truth image are shown, scale bar 1 μm. The red and green line plot corresponds to intensity variation along the red and green arrows in the DL and EPSLON images respectively, scale bar 100 nm. The EPSLON and SEM ground truth image agree.

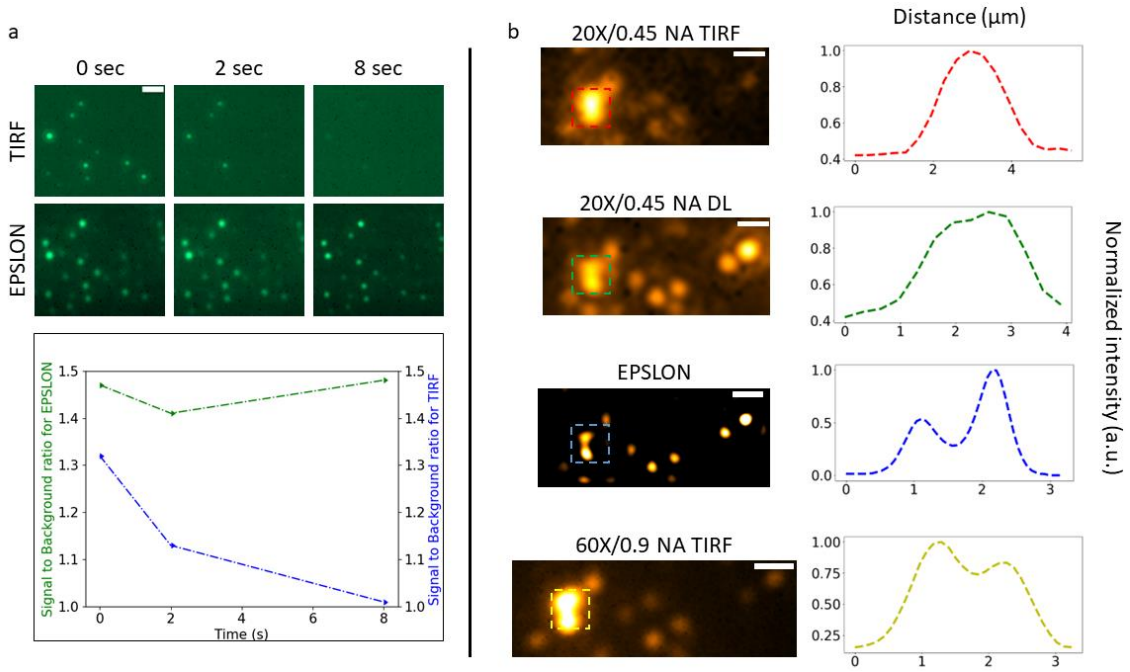

Figure 4: EPSLON for circumventing photobleaching and for label-free super-resolution imaging of EVs (**a**) Time-lapse imaging comparison of extra-cellular vesicles between TIRF and EPSLON configurations. EPSLON helps to image nanosized EVs over long periods of time without photobleaching and with better signal-to-background ratio as opposed to TIRF, scale bar 5 μm. This fact is quantified in the graph where signal-to-background ratio as a function of time is plotted. (**b**) Super-resolution imaging of EVs in label-free regime using EPSLON configuration. EVs are imaged in both TIRF and EPSLON mode, scale bar 2 μm. The red, green, blue, and yellow insets correspond to EVs in diffraction-limited TIRF image, label-free diffraction-limited image termed DL, label-free super-resolved EPSLON image and TIRF ground truth image. The line profiles corresponding to each of these insets showing the intensity variation are also shown alongside. EPSLON resolves the unresolved EVs in the diffraction-limited images and this result is validated by the TIRF ground truth image acquired with a higher NA objective.

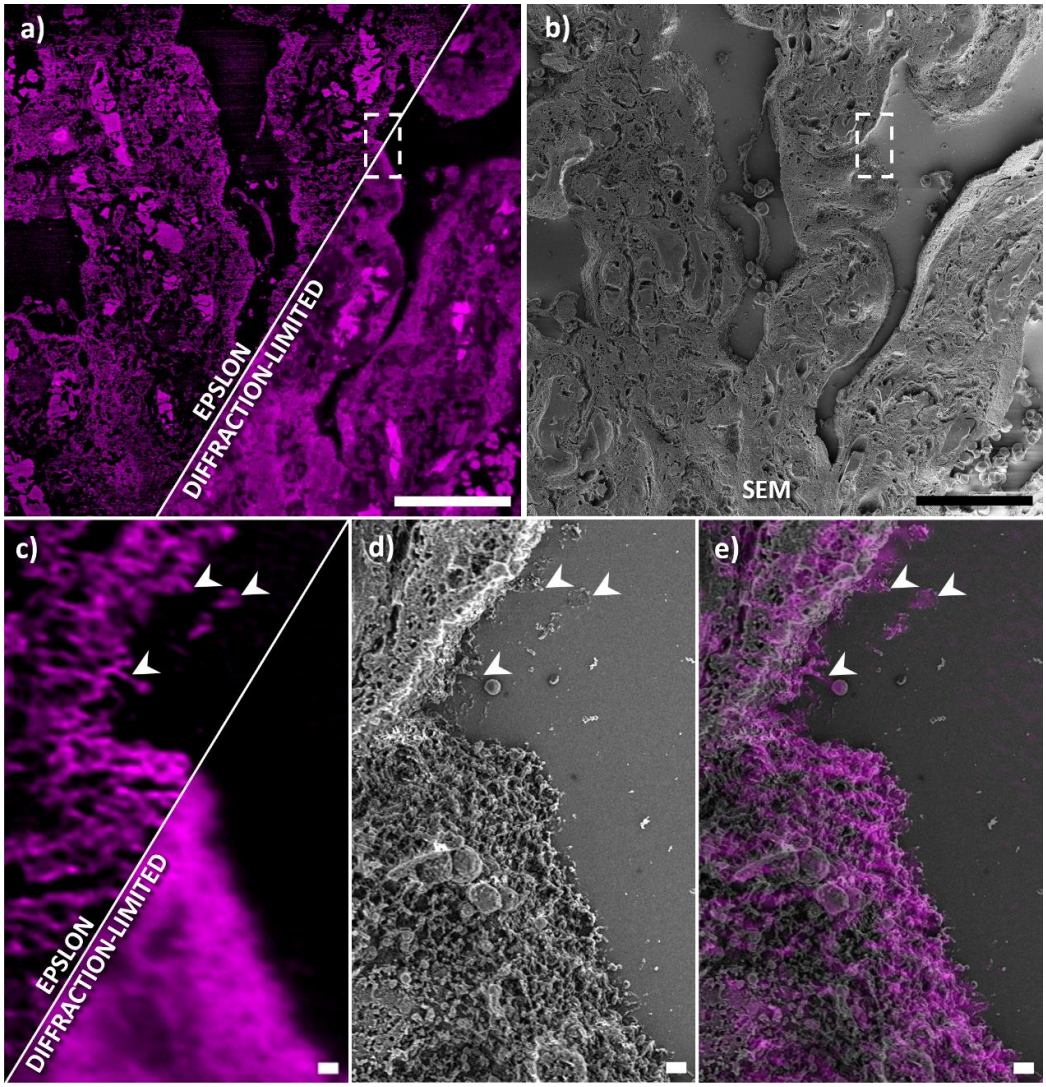

Figure 5: EPSLON for label-free super-resolution imaging of human placenta tissue sections and benchmarking with correlative microscopy: EPLSON-SEM. (a) A large FOV visualization of a human placental tissue section on a Si_3N_4 chip and imaged using a MO with detection NA = 1.2. Both DL and its corresponding super-resolved EPSLON images are shown, exhibiting a mean FRC resolution of 496 nm and 176 nm, respectively. **(b)** Same sample region acquired in a scanning electron microscope (SEM). **(c)** A zoomed-in view of the white-dotted box in (a) reveals the enhanced contrast and super-resolution provided by EPSLON in comparison to its DL counterpart. The white arrow heads denote the location of ultrastructural features with a high correlation with the SEM method. **(d)** Complementary SEM view of the same region in (c), illustrating with white arrow heads the correspondence with those seen via EPSLON. **(e)** An overlay view of (c) and (d) allows for visualizing correlation between EPSLON and SEM imaging methods. Scale bars a-b 50 µm, c-e 1 µm.

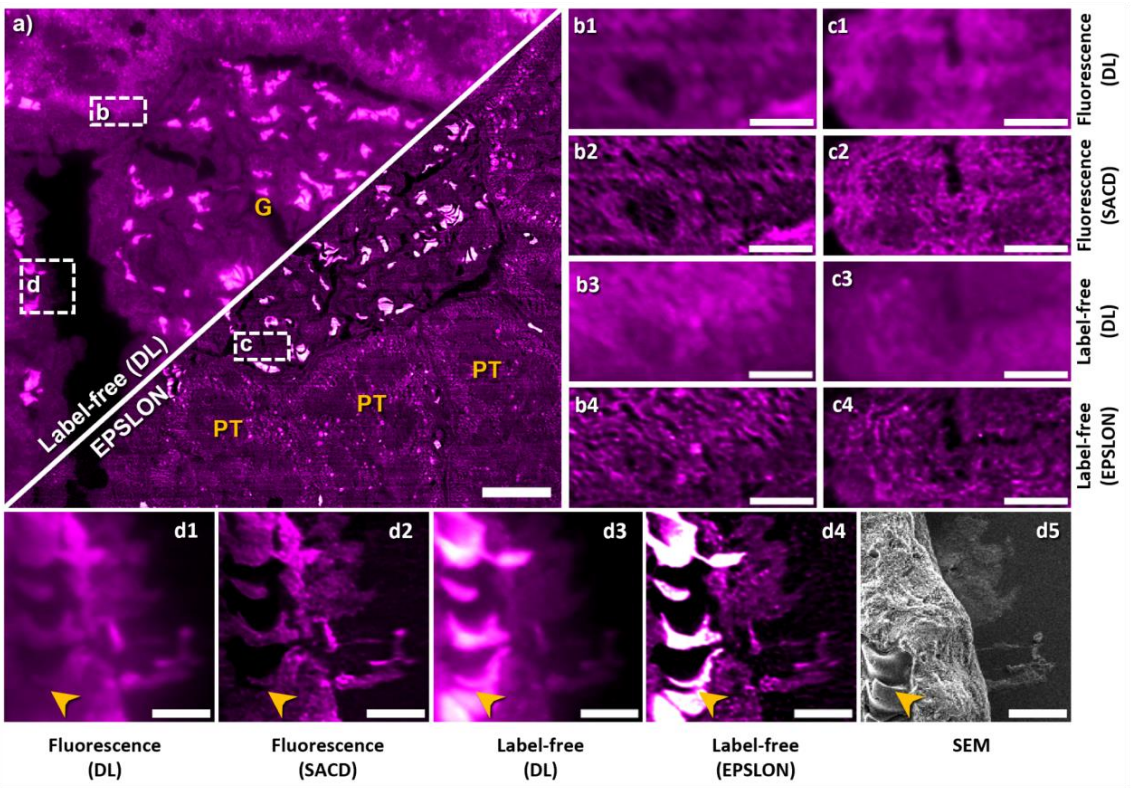

Figure 6: EPSLON for label-free super-resolution imaging of rat kidney tissue sections and benchmarking via correlative microscopy: EPSLON-TIRF and ELSON-SEM: (a) Label-free diffraction-limited (DL) and its corresponding super-resolved EPSLON images are shown. The region 'G' labeled in yellow font indicates Glomerulus and the regions labeled 'PT' in yellow font indicates Proximal Tubuli of the kidney section. Three regions of interest enclosed in white dotted boxes are labeled 'b', 'c' and 'd'. Scale bar 25 µm. **(b1, c1, d1)** Diffraction-limited TIRF images of the regions enclosed by white dotted boxes in (a) are blown-up and shown, scale bar 5 µm. **(b2, c2, d2,)** Corresponding super-resolved TIRF images of regions in (b1, c1, d1) are shown, scale bar 5 µm. **(b3, c3, d3)** Label-free DL images of regions enclosed by the white dotted boxes in (a) are shown magnified, scale bar 5 µm. **(b4, c4, d4)** Super-resolved EPSLON images of regions corresponding to (b3, c3, d3) are shown, scale bar 5 µm. **(d5)** SEM image of region enclosed by white dotted box labeled 'd' is shown. The yellow arrow heads denote the location of red blood cells, being imaged throughout all the microscopy methods. Scale bar 5 µm. Mean FRC resolution of label-free DL image is 256 nm and Mean FRC resolution of EPSLON image is 133 nm.

Label-free incoherent super-resolution optical microscopy

Nikhil Jayakumar**[1], Luis E. Villegas-Hernández[1], Weisong Zhao[2], Hong Mao[1], Firehun T Dullo[3], Jean-Claude Tinguley[1], Krizia Sagini[4,5], Alicia Llorente[,4,5,6], Balpreet Singh Ahluwalia*[1,7]

[1]*Department of Physics and Technology, UiT The Arctic University of Norway, Tromsø, 9037, Norway*
[2]*Innovation Photonics and Imaging Center, School of Instrumentation Science and Engineering, Harbin Institute of Technology, Harbin, China*
[3]*Department of Microsystems and Nanotechnology, SINTEF Digital, Gaustadalleen 23C, 0373 Oslo, Norway*
[4] *Department of Molecular Cell Biology, Institute for Cancer Research, Oslo University Hospital, The Norwegian Radium Hospital, 0379 Oslo, Norway*
[5]*Centre for Cancer Cell Reprogramming, Faculty of Medicine, University of Oslo, Montebello, 0379 Oslo, Norway*
[6]*Department for Mechanical, Electronics and Chemical Engineering, Oslo Metropolitan University, Oslo, Norway*
[7]*Department of Clinical Science, Intervention and Technology, Karolinska Institute, Sweden*

*Balpreet.singh.ahluwalia@uit.no, **nik.jay.hil@gmail.com

1. Label-free high-resolution microscopic techniques

Below we have categorized the state-of-the-art high-resolution label-free techniques into three categories:
Technique 1: Techniques that use the concept of synthetic aperture/spatial frequency shift for coherently scattering samples
Technique 2: Synthetic aperture/Spatial-frequency shift concepts for coherently scattering samples using chip-based solutions
Technique 3: Techniques that apply fluorescence-based algorithms to coherently scattering samples.

Technique 1: High-resolution techniques that use the concept of synthetic aperture for label-free microscopy

Abbe's resolution-limit when considering oblique illumination for elastically scattered light is $\frac{\lambda_{ill}}{NA_{ill}+NA_{det}}$. And in fluorescent microscopy, because of the emission properties of fluorescent molecules, the Abbe resolution limit is $\frac{\lambda_{det}}{2NA_{det}}$. Below we highlight the state-of-the-art label-free optical techniques and briefly elucidate their working principles. This will help to understand the differences between EPSLON and label-free state-of-the-art optical techniques.

a. Cotte, Yann, et al. "Marker-free phase nanoscopy." *Nature Photonics* 7.2 (2013): 113-117.
b. Zheng, Guoan, Roarke Horstmeyer, and Changhuei Yang. "Wide-field, high-resolution Fourier ptychographic microscopy." *Nature photonics* 7.9 (2013): 739-745.
c. Maire, Guillaume, et al. "Phase imaging and synthetic aperture super-resolution via total internal reflection microscopy." *Optics letters* 43.9 (2018): 2173-2176.
d. Jünger, Felix, Philipp V. Olshausen, and Alexander Rohrbach. "Fast, label-free super-resolution live-cell imaging using rotating coherent scattering (ROCS) microscopy." *Scientific reports* 6.1 (2016): 30393.
e. Yurdakul, Celalettin, et al. "High-throughput, high-resolution interferometric light microscopy of biological nanoparticles." *ACS nano* 14.2 (2020): 2002-2013.

Ref. [a]: different holograms corresponding to different illumination directions on the sample plane are recorded. After post-processing, a high-resolution image is obtained which is diffraction-limited in Abbe's sense. The best theoretical resolution after post-processing will be $\lambda_{ill}/(NA_{illu} + NA_{det})$, where λ is the wavelength of the detected light, NA_{illu} is the numerical aperture of the illumination objective and NA_{det} is the numerical aperture of the detection objective.

Ref. [b]: typically, in Fourier Ptychography, an LED array is used to provide oblique illumination at the sample plane. Then using a phase retrieval algorithm from the intensity images, a high-resolution final image is generated. The final image is still limited by Abbe's diffraction limit.

Ref. [c]: several azimuthally varying illuminations at the sample plane is provided to perform synthetic aperture reconstruction of the sample. The final resolution is determined by Abbe's diffraction limit.

Ref. [d]: a 2π azimuthal scan of a laser beam at the back-focal plane of the illumination objective within the integration time of the camera generates a high-contrast image. The final resolution is limited by Abbe's diffraction limit.

Ref. [e]: sample is illuminated via a series of oblique illuminations. The scattered light off the sample and specular reflection from the SiO_2 substrate helps create a common-path interferometry configuration. Via post-processing a two times resolution over head-on illumination λ_{ill}/NA_{det} is obtained. The final resolution is within Abbe's diffraction limit.

Techniques 2: High-resolution label-free chip-based techniques with concepts like synthetic aperture microscopy
The concepts elaborated in Technique 1 are translated to chip-based platforms here. Hence, an even higher resolution in principle is possible due to the higher refractive-index of the material employed. The resolution achievable is given by Abbe, $\frac{\lambda_{ill}}{NA_{ill}+NA_{det}}$. All these techniques mitigate coherent speckle noise, either by summing up different speckle patterns on intensity-basis at the camera plane or by using a broadband light source

a. Ströhl, Florian, et al. "Super-condenser enables label free nanoscopy." *Optics express* 27.18 (2019): 25280-25292.
b. Liu, Xiaowei, et al. "Fluorescent nanowire ring illumination for wide-field far-field subdiffraction imaging." *Physical Review Letters* 118.7 (2017): 076101.
c. Tang, Mingwei, et al. "High-Refractive-Index Chip with Periodically Fine-Tuning Gratings for Tunable Virtual-Wavevector Spatial Frequency Shift Universal Super-Resolution Imaging." *Advanced Science* 9.9 (2022): 2103835.
d. Pang, Chenlei, et al. "On-Chip Super-Resolution Imaging with Fluorescent Polymer Films." *Advanced Functional Materials* 29.27 (2019): 1900126.

Ref. [a]: samples are illuminated in multiple azimuthal directions via evanescent waves generated by a Si_3N_4 waveguide. A post-processing algorithm is then applied to generate a high-resolution label-free image. This resolution is determined by Abbe's diffraction limit of $\lambda_{ill}/(NA_{illu} + NA_{det})$.

Ref. [b]: In this work, broadband light emitted by the nanowire ring (NWR) is coupled into the film waveguide via a single mode. The shortest Stoke shifted wavelength emitted by the NWR will then determine the smallest coherence length. What it essentially implies is that the scattered light will have a constant phase relationship between different locations excited by this mode. Or in other words, the phase information is still preserved in the scattered light. Hence, in principle this technique is not suitable to be applied to in tandem with fluorescence based super-resolution algorithms like structured-illumination microscopy. This is contrary to EPSLON where incoherent imaging system is proposed.

Ref. [c]: a photonic-chip made of Gallium Phosphide (refractive index > 3) is used in this work. Evanescent waves are used for illuminating the sample. Using a reconstruction algorithm a very high-resolution image limited by Abbe's diffraction-limit can be generated. However, the technique is still coherent in nature and therefore, fluorescence based super-resolution algorithms cannot be applied to circumvent the far-field diffraction-limit. This paper demonstrates $\boldsymbol{\lambda}/4.7$ resolution in the label-free mode. Here, authors used objective lens of $N.A._{det}$= 1.49 and GaP chip is used for illumination, i.e., refractive index 3.3 = $N.A._{illum}$. Then Abbe's resolution limit is $\lambda_{ill}/(NA_{illu} + NA_{det}) = \boldsymbol{\lambda}_{ill}/4.79$.

Ref. [d]: This is also a coherent imaging technique where the sample is illuminated from multiple directions using evanescent waves generated by a waveguide. The broadband light emitted by F8BT is efficiently coupled into waveguides. The guided light then provides evanescent wave illumination for the sample. By illuminating the sample from multiple orientations, a high-resolution image is generated. The resolution of the final image is still limited by Abbe's diffraction limit. This paper demonstrates $\boldsymbol{\lambda}/3$ resolution in the label-free mode. Here, authors

used objective lens of $N.A._{det}$= 0.85 and TiO_2 chip is used for illumination, i.e. refractive index 2.2 = $N.A._{illum}$. Abbe's resolution limit is therefore $\lambda/(NA_{illu} + NA_{det}) = \boldsymbol{\lambda}/3.05$.

Techniques 3: Techniques that apply fluorescence-based algorithms to coherently scattering samples.

a. Lee, Yeon Ui, et al. "Hyperbolic material enhanced scattering nanoscopy for label-free super-resolution imaging." *Nature communications* 13.1 (2022): 6631.

Here, fluorescence-based super-resolution algorithm BlindSIM is applied in label-free mode. In this work, organic hyperbolic materials are employed to create sub-diffraction sized speckles. The illuminating field is passed through a vibrating multi-mode fiber to create temporal variations. Multiple oblique illuminations in the azimuthal plane are applied at the sample plane. Then Blind-SIM is applied to generate a super-resolved image. The technique resolution is given by Abbe's limit for elastically scattered light, $\lambda_{ill}/(NA_{ill} + NA_{det})$. Here NA_{ill} is exceptionally high due to the high-index organic hyperbolic material used which leads to a super-resolution. A true incoherent system is imperative to avoid the caveats linked to the application of fluorescence based super-resolution algorithms for the coherent imaging [Wicker, Kai, and Rainer Heintzmann. *Nature Photonics* 8.5 (2014): 342-344, Jayakumar et al. *Nanophotonics* 11.15 (2022): 3421-3436].

b. Dong, Biqin, et al. "Superresolution intrinsic fluorescence imaging of chromatin utilizing native, unmodified nucleic acids for contrast." *Proceedings of the National Academy of Sciences* 113.35 (2016): 9716-9721.

In this work, the intrinsic autofluorescence of the cells mimic the stochastic fluctuations from a fluorescent molecule and therefore, a fluorescence-based localization technique is applied to circumvent the diffraction-limit. This work depends on samples that have unique intrinsic autofluorescence and it is thus not universal to diversified specimens.

The novelty in EPSLON is in using incoherent point-like light sources for near-field illumination of unlabeled samples, i.e., photoluminescence of Si_3N_4. It implies that each location of the sample, within the penetration depth of the incoherent evanescent field, scatters the non-propagating incoherent field into the far-field. This permits the application of fluorescence-based algorithms like SIM and IFON in the label-free regime to circumvent Abbe's diffraction-limit. Such an illumination technique is imperative to avoid the caveats linked with the coherent imaging [Wicker, Kai, and Rainer Heintzmann. *Nature Photonics* 8.5 (2014): 342-344, Jayakumar et al. *Nanophotonics* 11.15 (2022): 3421-3436].

2. Waveguide fabrication

A 2 µm thick oxide layer was thermally grown on a silicon wafer, followed by the deposition of 150 nm thick Si3N4 layer using plasma enhanced chemical vapor deposition (PECVD). The 2D channel waveguides were defined by photolithography process and etched using reactive ion etching (RIE). Then, silicon oxide layer was deposited using PECVD on the patterned nitride layer for protection. Finally, the oxide layer was patterned and removed from certain regions of each waveguide to create the imaging regions. The oxide layer was removed using combination of both dry and wet etching [1]. Thus, at the imaging region the specimen is in direct contact with the waveguide core layer, accessing the evanescent field.

Waveguide modes

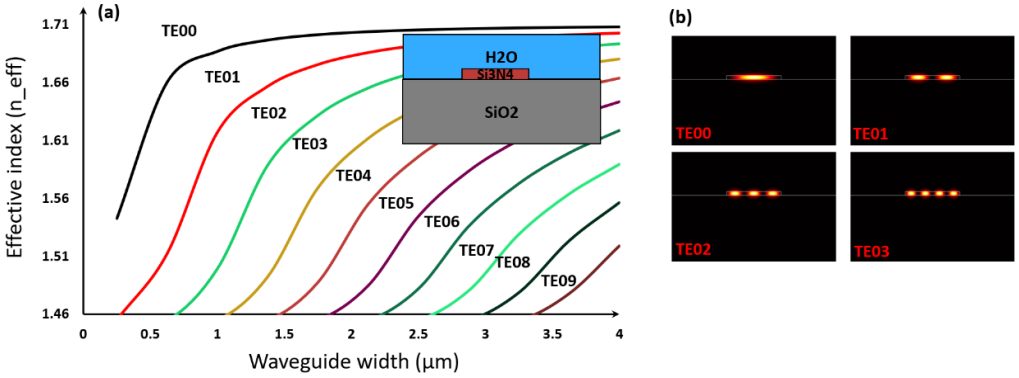

Figure. 1: (a) Effective indices of the guided modes for various Si_3N_4 waveguide widths. A schematic diagram of the cross-section of the waveguide is provided as an inset in the plot. (b) Mode profiles for the fundamental and higher-order TE - modes. The geometry of the waveguide in the simulation model is 150 nm thick and 0.25 - 4 µm wide. The guided modes for a strip Si3N4 waveguide were simulated using the commercial software FIMMWAVE (Photon Design, Oxford, UK), and its effective indices were calculated using the full-vectorial film mode matching (FMM) method.

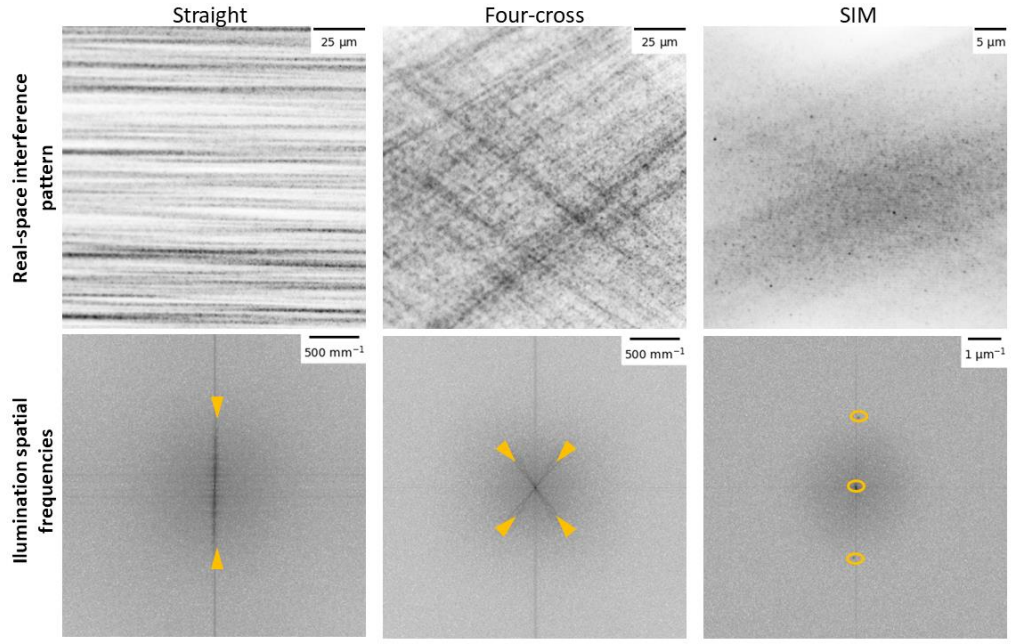

Figure. 2a: Waveguide geometries employed in EPSLON for beam shaping and their corresponding illumination frequencies. The multi-moded interference (MMI) pattern of straight and four-crossing waveguide is captured using a 20X/0.45 NA objective, scale bar 25 µm, while that of the SIM chip is captured using a 60X/1.2 NA objective, scale bar 5 µm. To see the well-defined fringe patterns in case of SIM chips, the interference angle between the overlapping single moded waveguides is chosen to be 20 degrees. The orange markers on the figures indicate the extend and orientation of the illuminating frequencies. Scale bar 500 mm^{-1} for the straight and four-arm junction waveguide and 1 μm^{-1} for the SIM chip.

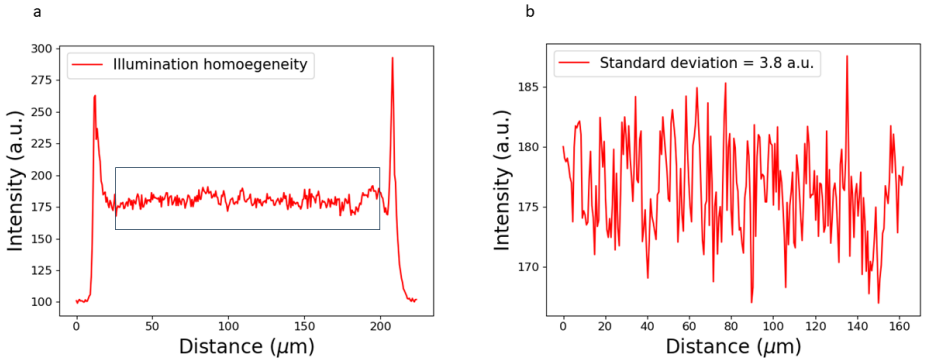

Figure. 2b: (a) Intensity variation along the width of a 200 μm waveguide is plotted. The two peaks in the plot correspond to the edges of the waveguide. (b) The black box in (a) is zoomed in and shown for better visualization purposes. The standard deviation of intensity over approximately 160 μm is 3.8 a.u.

Table 1:

Sl. No.	Excitation wavelength	Propagation loss
1	488 nm	≈ 10 dB/cm
2	561 nm	≈ 2.5 dB/cm
3	660 nm	≈ 1dB/cm

Table1: Propagation loss of a straight waveguide at different excitation wavelengths.

3. Simulation study and experimental verification of influence of multi-mode illumination patterns for usage in IFON

The following simulation studies elucidate how the multi-moded illumination pattern-induced correlation is mitigated to generate the super-resolved images in EPSLON.

Simulation1: The raw-image stack consists of three synthetic ring-like structures (220 nm, 260 nm and 300 nm from left to right). The data stack is then convolved with a PSF (220 nm) and down-sampled six times. Various types of noise (mixture noise with cytosol background, Poisson noise, Gaussian noise, out-of-focus light and baseline background) are then added to generate the final raw image stack. The emitters have an on/off fluctuating behavior. The fluctuation rate (On Time ζ_{on}/Off Time ζ_{off}) is to $\zeta_{on} = 1.67 \times 200$ frames and $\zeta_{off} = 2.5 \times 200$ frames, i.e., $\zeta_{on}/\zeta_{off} \approx 2/3$. The label density is set as 10000/μm^2 and all emitters have the same intrinsic brightness. An image stack of 100 frames is then reconstructed using 2nd order SOFI (SOFI^2) and 2nd order SACD (SACD^2). The structural similarity (SSIM) score is provided alongside each of the reconstructions as well.

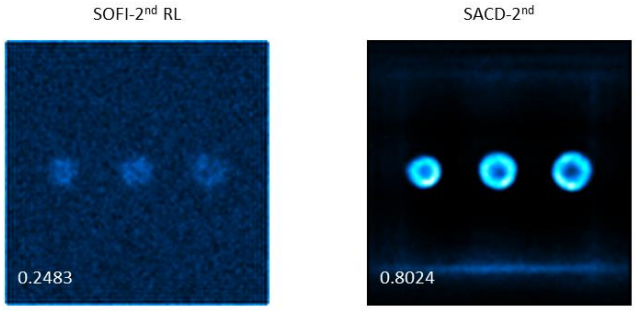

Figure. 3: Comparison of reconstructions using 2nd order SOFI and 2nd order SACD on the synthetic data set having slow intrinsic fluctuations ($\zeta_{on} = 1.67 \times 200$ frames and $\zeta_{off} = 2.5 \times 200$ frames).

It is seen that SACD^2 has been able to achieve a higher SSIM score than SOFI^2 for the slow fluctuation rate scenario we have chosen here, Fig. 3. The higher SSIM score of SACD is attributed to the pre-deconvolution steps

involved in its reconstruction pipeline. This behavior is documented in Ref. [Zhao, Weisong, et al. "Enhanced detection of fluorescence fluctuations for high-throughput super-resolution imaging." *Nature Photonics* (2023): 1-8.] where SACD^2 is shown to have a high convergence even with just 20 frames.

Simulation2: The difference as opposed to Simulation1 is that the raw image stack is now multiplied with multi-moded illumination pattern. This will correspond to the situation where these very slowly fluctuating emitters are placed on top of the core-cladding interface of the waveguide. Therefore, these emitters get illuminated by the mode patterns of the waveguide. Then the final image at the camera plane is the product of the waveguide mode pattern and slowly fluctuating emitters convolved with the PSF (220 nm).

For simplicity, the mode patterns for the straight waveguide considered here are assumed to have a single spatial frequency and oriented only along the vertical-axis as shown in the figure below. Then each image in the image stack is multiplied with a phase-shifted fringe pattern. The phase shift is to mimic for the piezo stage oscillating along the input facet of the waveguide. The phase shift of the interferogram is chosen to change by 2π radians over 10 frames. SOFI^2 and SACD^2 reconstructions along with the SSIM scores are given below.

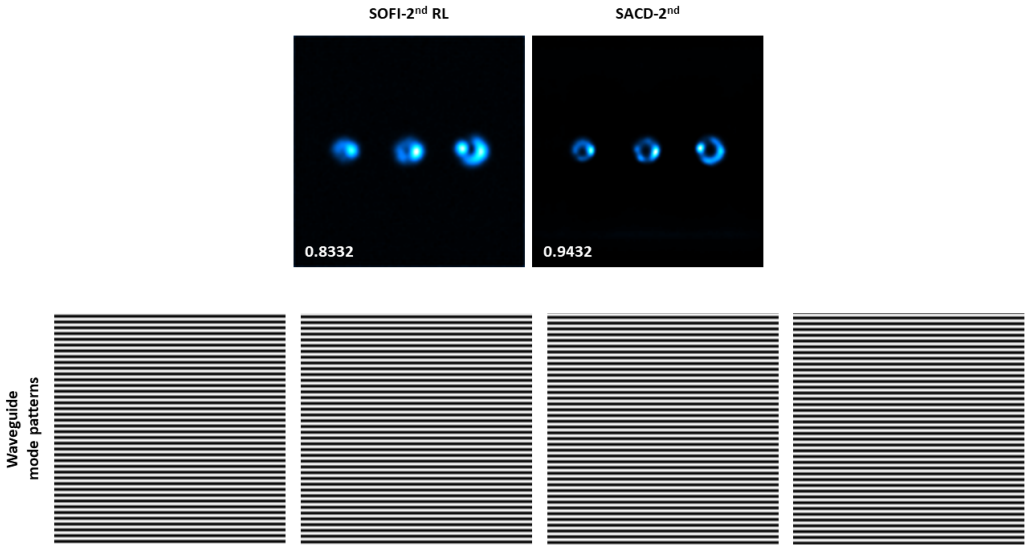

Figure. 4: Influence of mode patterns of a straight waveguide on reconstructions using 2nd order SOFI and 2nd order SACD on the synthetic data set with slow intrinsic fluctuations ($\zeta_{on} = 1.67 \times 200$ frames and $\zeta_{off} = 2.5 \times 200$ frames). A few of the phase-shifted mode patterns used for illuminating the sample is also shown.

The SSIM score has improved from 0.2483 to 0.8332 for SOFI^2 and from 0.8024 to 0.9432 for SACD^2. This implies that the intensity-fluctuations induced by the waveguide mode patterns have helped achieve a better reconstruction. An important observation is that the non-uniform waveguide illumination induces artifacts (unresolved regions) in the image. This can be seen as bright points in the reconstructed synthetic structures in Fig. 4. These points lie along the fringes, i.e., horizontally. This arises due to the correlation between the different emitters.

Simulation3: The experimental particulars used for the emitters are the same as in the previous two cases. Here the difference arises solely because a four-arm waveguide is used to illuminate the slowly fluctuating emitters. The use of a four-arm waveguide helps mitigate the correlation between the emitters due to the random nature of the sub-diffraction sized speckle patterns. This is because these waveguides are highly multi-moded and all the four waveguides overlap in the imaging area as shown in Fig. 2b of the main text. Therefore, as the piezo stage oscillates the coupling objective along the input facet of the waveguide, a different set of modes get excited in the overlapping waveguides and thereby, induces stochasticity in the illumination pattern which helps to mitigate the illumination induced correlation.

A few of the different mode patterns used for illuminating the emitters are provided in the figure below. For simplicity, we have considered mode patterns with a single spatial frequency but with different azimuthal

orientations for each frame as shown below in Fig. 5. To introduce the effect of the piezo stage oscillation along the input facet of the waveguide, these interferograms are given a phase shift of 2π radians over 10 frames. During the experiments, there will be multiple spatial frequencies and the mode patterns will be more chaotic due to the multi-moded waveguides employed.

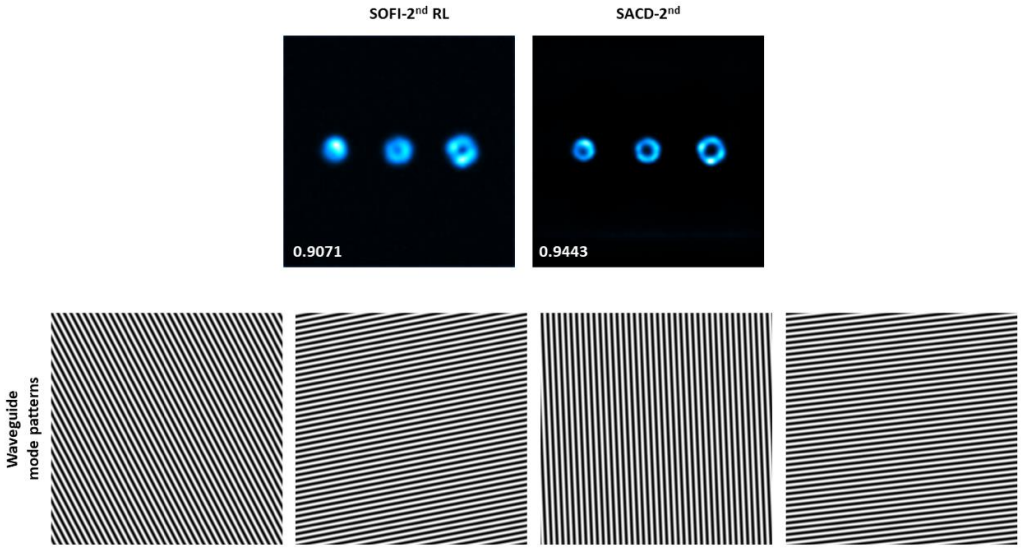

Figure. 5: Influence of mode patterns of a four-arm waveguide on reconstructions using 2nd order SOFI and 2nd order SACD on the synthetic data set with slow intrinsic fluctuations ($\zeta_{on} = 1.67 \times 200$ frames and $\zeta_{off} = 2.5 \times 200$ frames). A few of the phase-shifted mode patterns with different azimuthal orientations is also shown.

The main finding is that using a four-arm waveguide, we obtained the highest SSIM score for SOFI^2 and SACD^2. SSIM score for SOFI^2 is 0.9071 and for SACD^2 is 0.9443. The artifacts (unresolved areas) have been mitigated due to reduced correlation arising due to different orientations of the illumination patterns in each frame.

Experimental validation: The simulation studies concluded that a four-arm waveguide geometry is ideal for mitigating the correlation value between the different emitters so that SOFI^2 and SACD^2 can generate super-resolved images. Therefore, in this experiment a four-arm waveguide geometry is employed to illuminate 195 nm polystyrene beads placed on top of its core-cladding interface. An image stack of 100 frames is captured by oscillating the coupling objective mounted on the piezo stage and is given as input to SOFI^2 and SACD^2. The reconstructed EPSLON images are shown and the correlation values between the emitters at 4 different regions of interest (ROI) are also provided in Fig. 6.

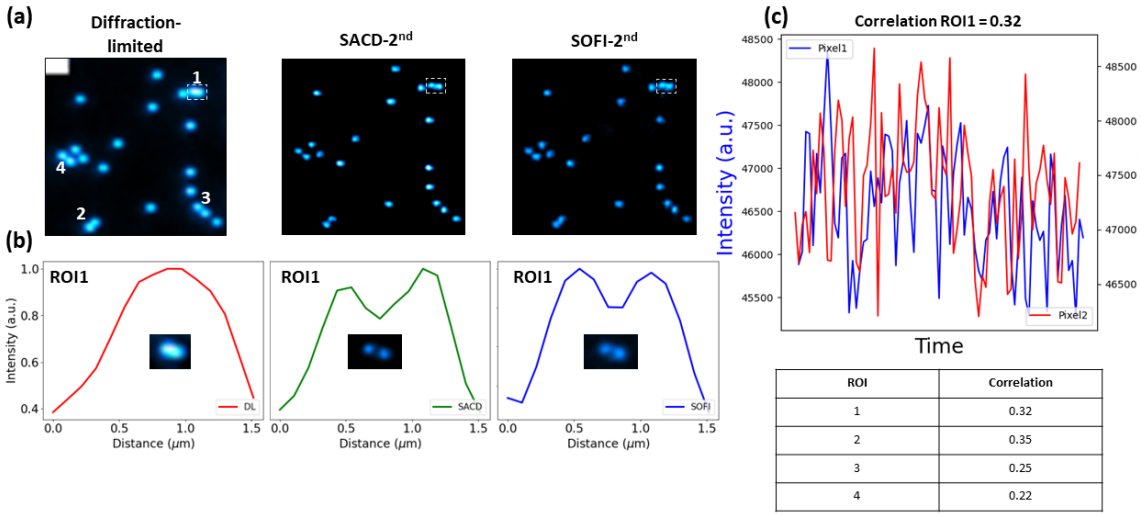

ROI	Correlation
1	0.32
2	0.35
3	0.25
4	0.22

Figure. 6: **Experimental demonstration of low correlation value in four-arm waveguide geometry for EPSLON**. (a) Diffraction-limited (DL) image and its corresponding 2nd order SACD and 2nd order SOFI reconstructions are shown, scale bar 2 μm. DL image is the averaged intensity image of 100 frames as the piezo stage oscillates along the input facet of the four-arm waveguide. Four different regions of interest (ROI) labeled '1', '2', '3' and '4' are shown in the DL image. (b) The red, green and blue line plots correspond to the intensity variation (normalized) in ROI1 of DL, SACD^2 and SOFI^2 images. The insets in the plots provide a magnified view of ROI1 in the DL (unresolved beads) and reconstructed images (super-resolved beads). (c) Line plot shows correlation between the two pixels hosting the unresolved emitters in region '1' in the DL image. The correlation value is 0.32 and the correlation plot is shown. SACD^2 and SOFI^2 resolve the beads due to the low correlation in the DL image. (d) The correlation values in ROI2, ROI3 and ROI4 are given in the table.

Thus, in our manuscript to avoid the influence of the correlation arising due to active modulation of the PL, two strategies have been adopted:

(i) straight waveguide (Fig. 2a in main text) and SACD^2. The high-index core material and interference between the multiple modes in straight waveguide helps generate sub-diffraction sized speckle patterns that is further employed by SACD^2.

(ii) four-arm waveguide (Fig. 2b in main text) and SOFI^2 or SACD^2. The high-index core material plus the counter propagating highly multi-moded waveguides creates sub-diffraction sized speckles that vary stochastically due to the piezo scanning along the input facet of the waveguide. Such a strategy helps generate sub-diffraction sized speckle patterns that can be employed by SACD^2, SOFI^2 and BlindSIM.

4. Schematic diagram of the imaging setup for EPSLON

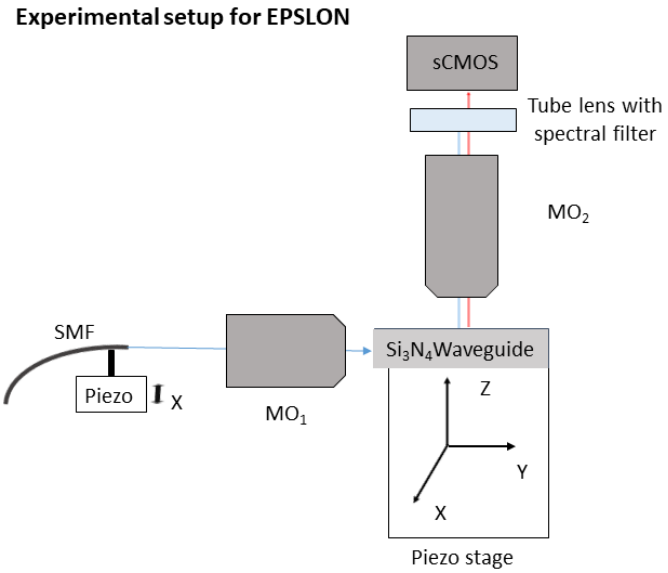

Figure. 7. Schematic diagram of experimental setup for EPSLON. Laser guided by a single mode fiber (SMF) held on a XY piezo stage by vacuum chuck is collimated and directed to the back-focal plane of coupling objective Olympus LMPanFL N 50×/0.5 NA MO_1. The light is focused by MO_1 and coupled into Si_3N_4 waveguide mounted on a XYZ piezo stage. The coupled laser light in the waveguide, induces a broadband photoluminescence in the core. Any index perturbation scatters the PL light, shown in red, into the far-field via detection objective MO2, tube lens with spectral filters onto a sCMOS Hamamatsu C13440-20CU camera**.** The spectral filters are chosen to reject the coherent laser light and transmit only the incoherent photoluminescent light.

Investigation of the PL: Experiment to measure the ratio of transmitted to confined photoluminescence

In the first experiment, the ratio of PL light that is confined inside the waveguide to the PL light transmitted into the far-field is quantified and found to be more than two orders of magnitude. The experimental configuration is shown below in Fig. 8 below. Laser light (488 nm) is coupled into a 400 µm wide Si_3N_4 waveguide using a coupling objective. This guided light will induce broadband incoherent photoluminescence (PL) inside the core. PL emitted inside the core will be both transmitted into the far-field and confined inside the core. The confined light will get guided along the length of the waveguide, attenuated by the propagation loss for that wavelength (see Table 1 above). At the output facet of the waveguide, a detection objective 2 is used to collect the guided confined light.

A combination of long-pass and band-pass filter ensures that the coherent coupling laser light is blocked and only the incoherent PL guided light reaches the camera. The PL light collected by Detection Objective 2 is shown as inset in Camera which is the experimentally obtained image of the PL emanating from the output facet of the waveguide.
Now, the transmitted at the imaging area is also captured by Detection Objective 1. The same combination of long-pass and band-pass filters ensure that only the transmitted incoherent PL light reaches the camera, and the coherent laser light is blocked. The inset in camera shows the multiple modes overlapping at the imaging area of the waveguide. This experiment is repeated multiple times and the counts reaching the cameras are measured. The ratio of PL transmitted (Detection objective 2) to PL confined (Detection objective 1) is approximately 0.01.

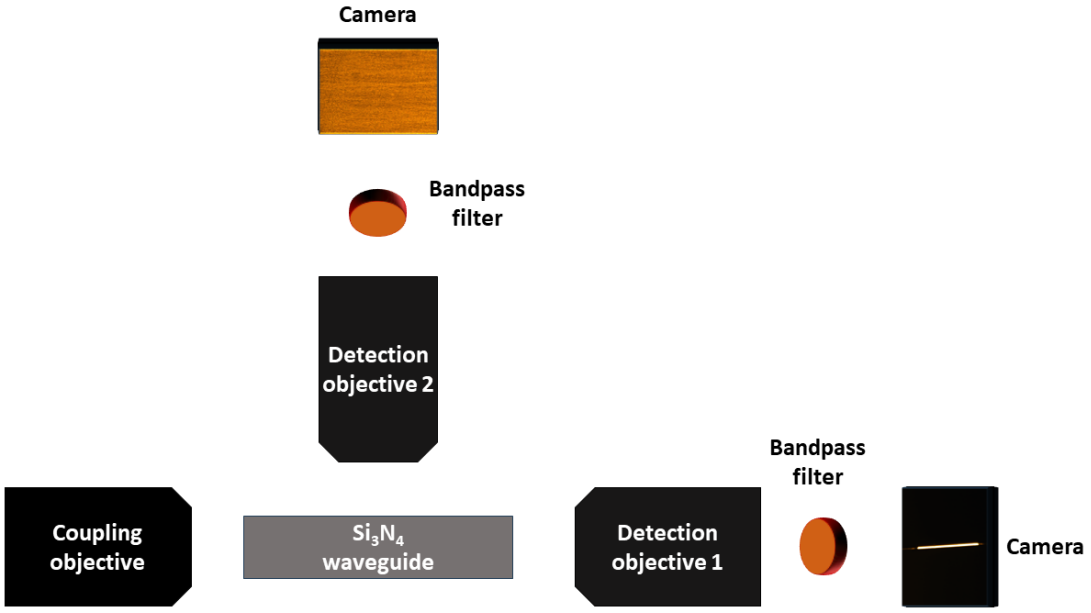

Figure. 8a: Schematic of the experimental setup to measure the ratio of transmitted photoluminescence to the confined photoluminescence. A coupling objective is used to guide laser (488 nm vacuum wavelength) along the length of the Si_3N_4 waveguide. A combination of long-pass (561 nm EdgeBasic LWP) and bandpass filter (592/43 nm EOTECH SPEC 67034) ensures that the coherent guided light is blocked and only the incoherent photoluminescence reaches the camera. Two identical detection objectives are used: Detection objective 1 for detecting the guided light along the length of the waveguide and Detection objective 2 for detecting the transmitted (unguided light) in the waveguide. Light is detected finally by identical scientific cameras. Actual images detected in the experiment are provided as insets in the cameras. The ratio of light collected by objective 1 and object 2 is found to be more than two orders of magnitude.

Investigation of the PL: Experimental verification of evanescent nature of EPSLON

This experiment is extended using rat kidney section to validate that it is indeed the evanescently decaying PL light that contributes to the signal. For this experiment, a rat kidney section (embedded in glycerol) is placed on the waveguide. The kidney section lies on top of both Si_3N_4-SiO_2 layer and in the imaging area (Si_3N_4 core) where no SiO_2 layer is present. As can be seen in Fig. 8b below, only those portions of the rat kidney section which are placed directly on top of Si_3N_4 core-cladding interface scatter light into the camera. The epi-illumination image shows the presence of the tissue section on top of the SiO_2 cladding layer. This experimentally proves that the evanescent field of the waveguide core contributes predominantly to image formation in EPSLON.

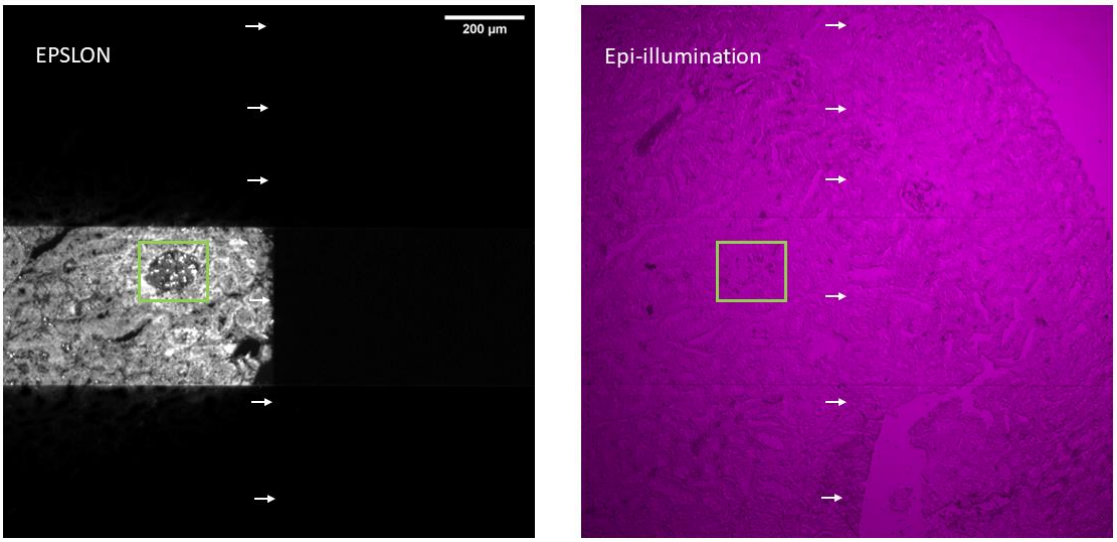

Figure. 8b: Comparison between EPSLON and epi-illumination. The green box simply serves as a landmark to correlate between EPSLON and epi-illumination images. The white arrows indicate the boundary where SiO_2 cladding layer stops on the waveguide. As can be seen from the EPSLON image, signal reaches the camera from tissue sections lying directly over the Si_3N_4 core and no signal is obtained from tissue sections lying over the SiO_2 cladding, scale bar 200 µm.

5. Optical modes of the waveguide to induce intensity-fluctuations: simulation study

Two identical square particles, 150 nm in size, are placed on top of a 10 µm rectangular waveguide. The center-to-center separation between the particles is 350 nm. The refractive index of the core is set as 2 and refractive index of cladding is set as 1. This waveguide is excited at 500 nm vacuum wavelength. The detection objective numerical aperture is set to NA = 1. Then the coherent transfer function is defined as $h_c = \frac{j_1(\psi)}{\psi}$, where $\psi = \frac{2\pi\, r\, NA}{\lambda}$, where a circular aperture is assumed. Here r is the radial coordinates and λ is the vacuum wavelength of light. For simplicity, emission and detection wavelength is set to be equal, λ=500 nm. Then the spatial cut-off frequency of the system for EPSLON is defined to be twice the abovementioned coherent cut-off frequency, which corresponds to the incoherent case.

The electric field (modes of the waveguide) interacts with these particles. The scattered field is defined as the product of the electric field distribution of the guided mode and the particle. The sample space is defined as an array of zeros except at the location of the two particles, where the value is set to 1. This ensures that only the scattered fields off the two particles propagate into the far-field because in a waveguide-based illumination scheme, only the scattered fields reach the camera plane. Since identical particles are considered, phase difference between the scattered fields arises only due to different locations of the particles as mentioned in the main text. As the piezo stage oscillates the coupling objective along the input facet of the waveguide, different modes get excited with different amplitudes.

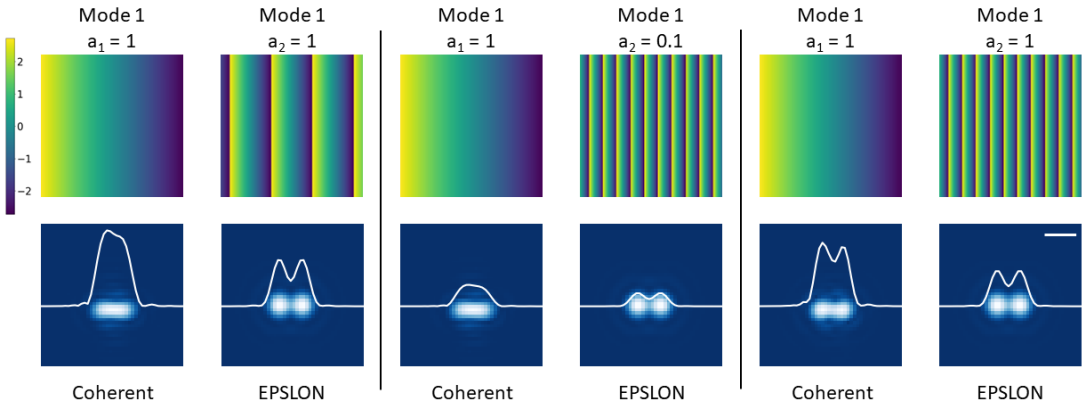

Figure. 9: Two particle resolution comparison between waveguide-based coherent and incoherent (EPSLON) imaging. Three separate cases are considered for comparison between coherent and incoherent EPSLON imaging. For brevity, only the fundamental mode with amplitude a_1 and higher-order mode with amplitude a_2 are considered interacting with the sample in each case. The colorbar provided alongside indicates the phase variation of the field across the cross-section or width of the waveguide. The sample consists of two 150 nm sized particles which are placed with a center-to-center distance of 350 nm apart on the core-cladding interface of a 10 μm Si_3N_4 waveguide. The particles scatter 500 nm wavelength light into a detection objective with NA = 1. The image generated at the camera plane for the coherent and EPSLON cases are shown, scale bar 500 nm. The loss in phase information in EPSLON imaging leads to similarity in images for the different excitation cases.

6. Structured illumination microscopy using a four-arm junction waveguide

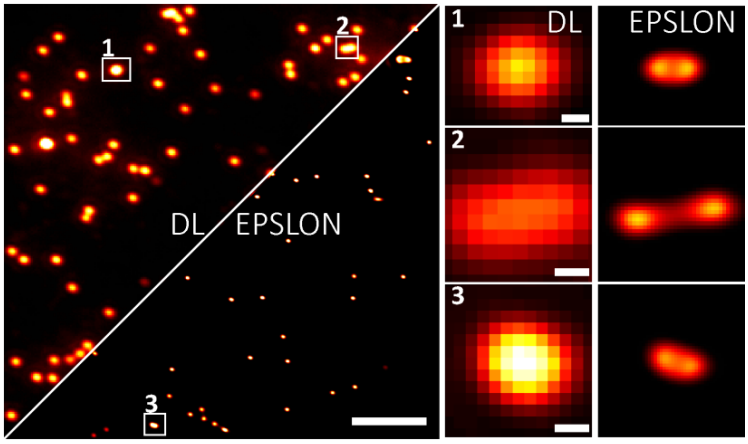

Figure. 10: Label-free 2D SIM of 195 nm polystyrene beads is demonstrated using 60X/0.9 NA objective. Diffraction-limited (DL) and super-resolved (EPSLON) images are shown, scale bar 5 µm. Three regions of interest labeled '1', '2' and '3' in DL and its corresponding EPSLON images are blown up and shown alongside, scale bar 125 nm.

7. One-dimensional structured illumination microscopy using a SIM chip

For the 1-D SIM experiment, images are acquired using a detection MO with NA = 1.2. Phase shifted frames required for the SIM reconstruction is generated by temporarily changing the index on one of the arms of the interfering waveguides. The three phase shifted frames are then given as input to the Fiji plugin of FairSIM. The reconstructed images and its Fourier spectra are provided in Fig. 11 below. The SIM reconstruction can clearly resolve the beads enclosed in the red inset in the DL image. The beads in the green inset in the EPSLON image are separated by 274 nm, shown in the line profile. Due to aberrations in the system, the experimental diffraction-limit of the SIM microscope is quantified to be 500 nm while the theoretical Abbe diffraction limit is $\frac{\lambda_{det}}{2NA_{det}} \approx 272 - 287\ nm$.

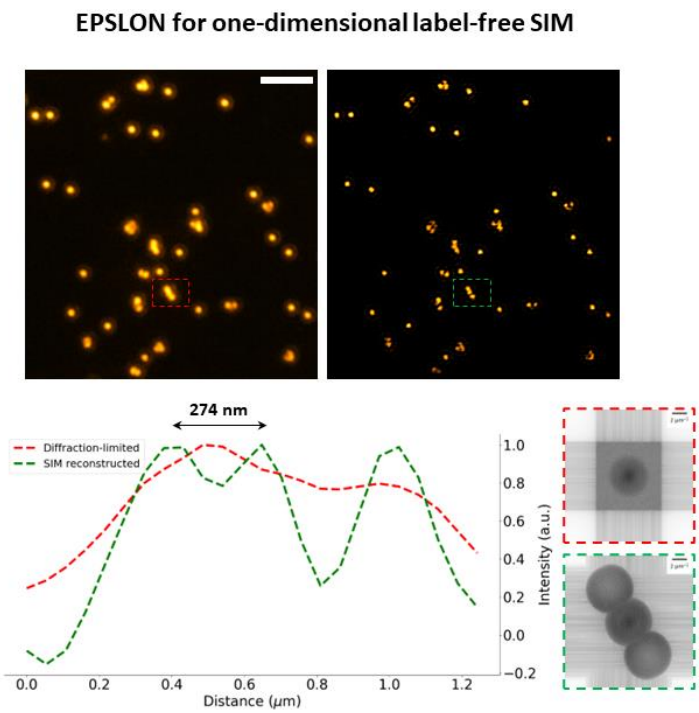

Figure. 11: Label-free 1-D SIM of 200 nm gold nanoparticles is demonstrated, scale bar 5 μm. The line profile indicates the intensity variations in the red and green insets in the diffraction-limited DL and FairSIM reconstructed EPSLON images respectively. The line profile clearly shows the separation of two particles spaced 274 nm, which is beyond the diffraction-limit of the imaging system. The Fourier domain representation of the diffraction-limited and reconstructed image are also provided alongside, scale bar 2 μm^{-1}.

8. Investigation of the PL: Speckle size determination

A structured illumination microscopy (SIM) waveguide chip and modes are excited at 640 nm vacuum wavelength (coupled light). The period *f* of the fringes generated is given by

$$f = \frac{\lambda_{ex}}{2n_f \sin\frac{\theta}{2}}$$

where λ_{ex} is the excitation wavelength, $n_f \approx 1.7$ is the refractive index of the guided mode for the Si_3N_4 waveguide used here and θ is the angle between the interfering waveguides.

First, we experimentally measure the fringe period generated in photoluminescence (PL) configuration. The angle between the interfering waveguides in the SIM chip is ≈25°. The period of the fringes is show in Fig. 12 below in the line plot.

Then we coat the imaging area with a very thin layer of cell mask deep red fluorescent stain and excite the waveguide at the same wavelength 640 nm, i.e., acquire a TIRF image of a layer of fluorescent stain. The period of the fringes generated in fluorescence mode (TIRF) is also shown in Fig. 1 below.

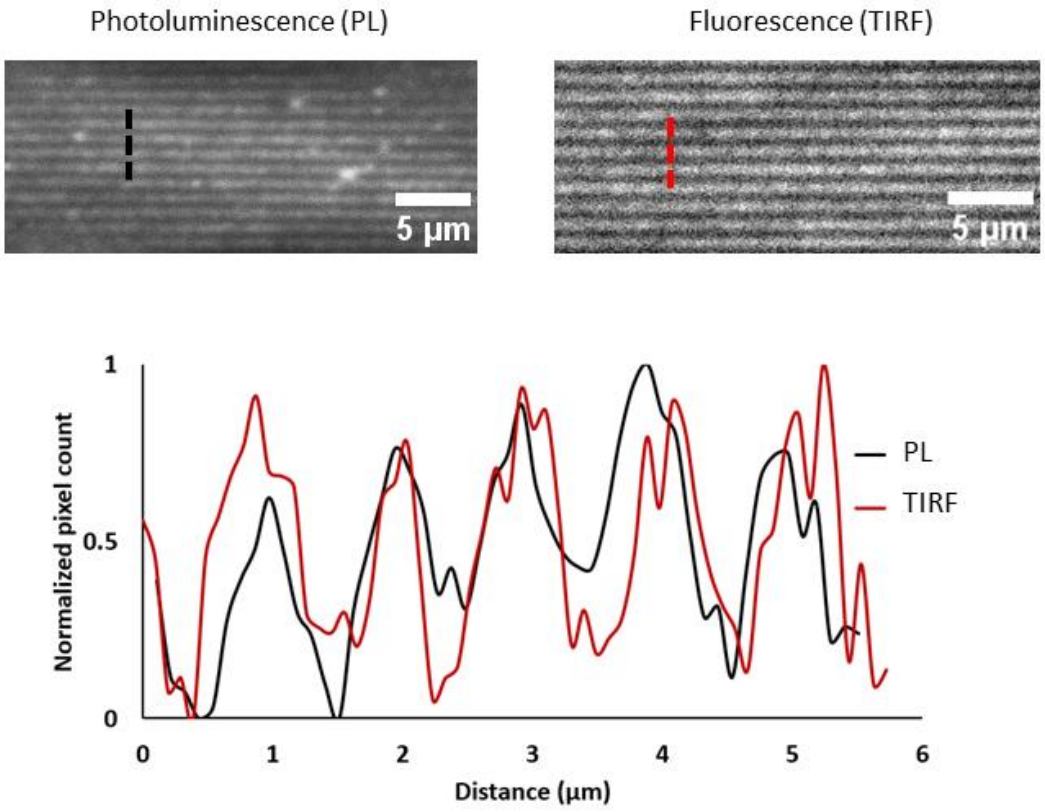

Figure. 12: Periodicity of fringe patterns in PL and TIRF mode using a ≈25° SIM chip when $\lambda_{ex} = 640\ nm$. The line plots show the normalized modulation in intensity across the black and red dotted lines in the PL and TIRF images respectively. White scale bar 5 µm.

The period of the fringes (≈ 870 nm) match in both PL and fluorescence mode and closely match with the theoretical value predicted by the equation above. This implies that period generated by the SIM chip in PL and TIRF mode is dependent only on the excitation wavelength λ_{ex}, index of the guided mode and angle between the interfering waveguides as mentioned in the formula above. The period in the SIM chips is not dependent on the emission autofluorescence wavelength λ_{af}.

Next, to show fringe period dependence on the excitation wavelength dependence λ_{ex}, the same SIM chip used above is excited in PL configuration at 640 nm and 561 nm. The periodicity and contrast of the fringe patterns are also provided alongside in Fig. 13.

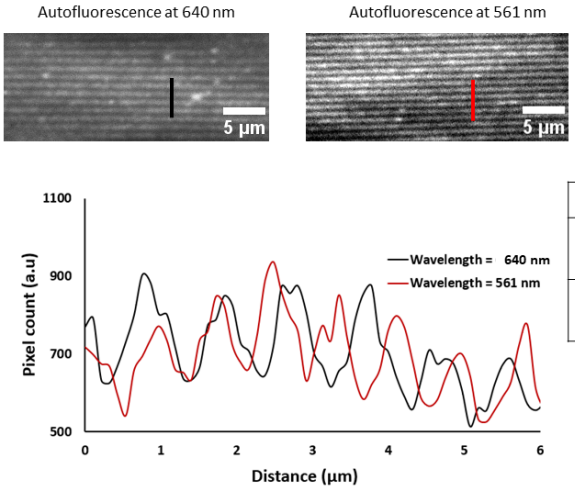

Sl. No.	Mode	Period	Contrast
1	Autofluorescence at 640 nm	≈ 870 nm	≈ 0.14
2	Autofluorescence at 561 nm	≈ 756 nm	≈ 0.15

Figure. 13: Fringe period in PL mode using a ≈25° SIM chip when $\lambda_{ex} = 640\ nm$ and $\lambda_{ex} = 561\ nm$. The line plot shows the modulation in intensity across the black and red lines in the fringe patterns. Black curve and red curve show the modulation in intensity in PL mode at $\lambda_{ex} = 640\ nm$ and $\lambda_{ex} = 561\ nm$ respectively. The table shown alongside mentions the fringe period and its corresponding contrast at $\lambda_{ex} = 640\ nm$ and $\lambda_{ex} = 561\ nm$. White scale bar 5 µm.

From Fig. 13, it is seen that the fringe period scales with λ_{ex} as mentioned by the formula earlier. The implication of the experimental results in Fig. 12 and Fig. 13 shown above are that, for a fixed interference angle between the chips, fringe period is determined by λ_{ex} and its corresponding effective mode index. The fringe period is ≈ 870 nm and contrast is ≈ 0.14 at $\lambda_{ex} = 640\ nm$. At $\lambda_{ex} = 561\ nm$, the fringe period is ≈ 756 nm and contrast is ≈ 0.15 and these periods closely match with the theoretical value given by the formula.

To verify that indeed we have a single spatial frequency corresponding to the excitation wavelength λ_{ex}, Fig. 14 is provided. As can be seen from the Fourier domain representation of the fringe pattern, the first order peaks, encircled within the red and green regions in Fig. 14, have a single spatial frequency component. Therefore, the fringe period in these SIM chips correspond to the excitation wavelength (monochromatic coupling laser light) and not with multiple frequencies corresponding to the polychromatic emission of PL.

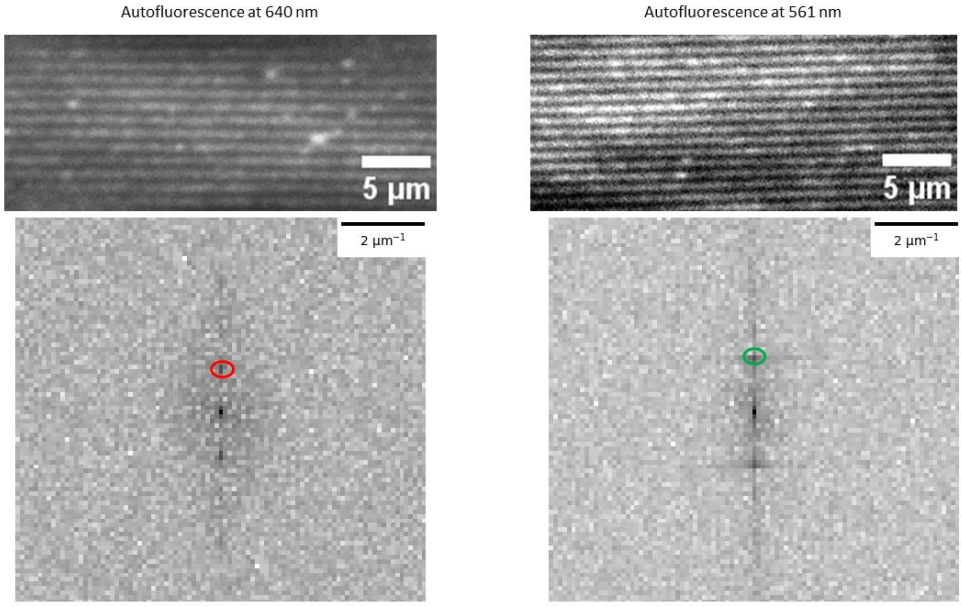

Figure. 14: Fringe period in PL mode using a ≈25° SIM chip when $\lambda_{ex} = 640\ nm$ and $\lambda_{ex} = 561\ nm$, scale bar 5 µm. The corresponding Fourier spectrum is shown. The red and green circle indicates the first order component which corresponds to $\lambda_{ex} = 640\ nm$ and $\lambda_{ex} = 561\ nm$. Scale bar 2 µm^{-1}.

Finally, to demonstrate the influence of detection wavelength λ_{det}, the following experiment is carried out and the results are shown in Fig. 15. As shown in Fig. 2(e) of the main paper, the PL emission spectrum is very broad spanning more than a few hundred nanometers. Therefore, if we excite the waveguide at 488 nm, we can choose any of the filters, (FITC, TRITC, CY5), provided in Table 2 in the supplementary section. The choice of filters during experiments in this manuscript was based on maximizing the signal at the camera plane, so that the fluorescence-based super-resolution algorithms generated super-resolved images with fidelity.

To experimentally demonstrate that the influence in changing the emission filter (FITC, TRITC, CY5) is in the resolution of the final diffraction-limited image, a straight waveguide is excited at 488 nm. The scattering image and the PL images in FITC, TRITC and CY5 channels are shown alongside. As seen, the speckle patterns in all the images match well. The resolution in each channel is computed using Fourier ring correlation (FRC) and shown in the table alongside.

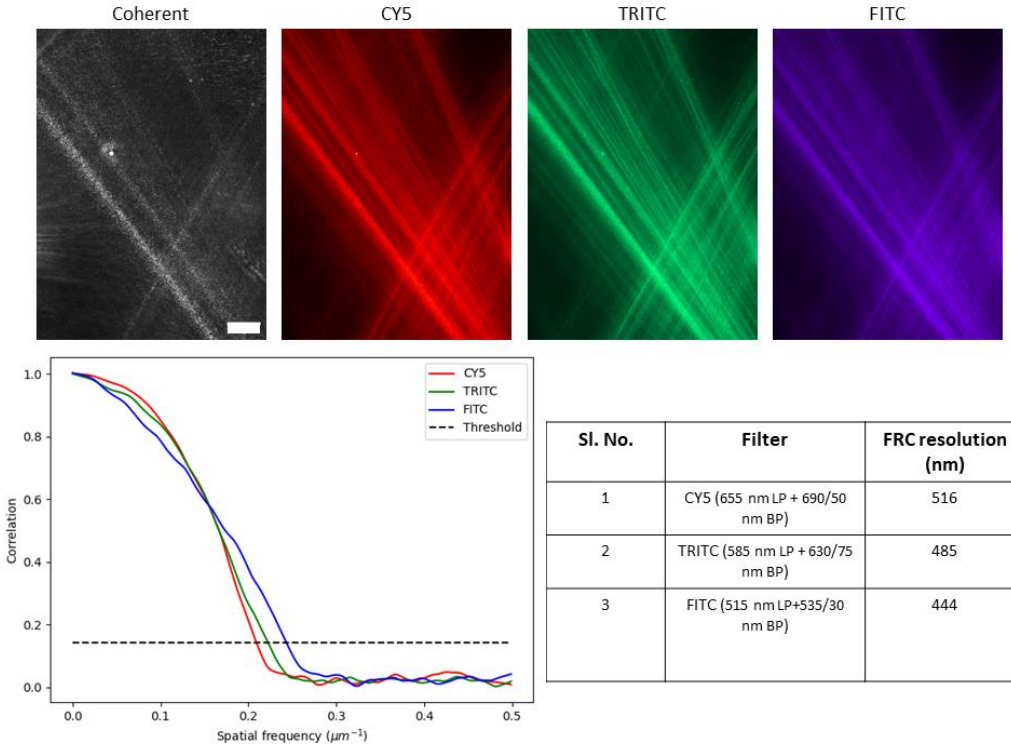

Sl. No.	Filter	FRC resolution (nm)
1	CY5 (655 nm LP + 690/50 nm BP)	516
2	TRITC (585 nm LP + 630/75 nm BP)	485
3	FITC (515 nm LP+535/30 nm BP)	444

Figure. 15: Speckle patterns, in a straight waveguide excited at 488 nm, in different filter channels and the corresponding resolution in each of the channels computed using Fourier Ring Correlation. Scale bar 25 µm.

9. Small EV preparation and characterization

Small EVs were isolated from fresh urine samples collected in the morning from healthy donors. The collection of urine samples was approved by the Norwegian Regional Committees for Medical and Health Research Ethics and the participants gave informed written consent. Small EVs were isolated by differential centrifugation as previously described [2]. Briefly, urine (around 200 ml) was centrifuged at 2000×g for 15 min at room temperature (RT) to remove cells and cell debris, and then at 10,000×g for 30 min at RT to separate large particles/vesicles. The resulting supernatant was centrifuged at 100,000×g for 70 min at RT in a Ti70 fixed-angle rotor (Beckmann Coulter, IN, USA) to pellet small particles. The pellet was washed with 20 ml phosphate-buffered saline (PBS) and centrifuged again at 100,000×g for 70 min at 4°C in a Ti70 rotor. The pellet was then resuspended in 6.5 ml PBS, vortexed and centrifuged at 100,000×g for 70 min at 4°C in an MLA-80 fixed-angle rotor (Beckmann Coulter, IN, USA). The supernatant was then removed, and the pellet resuspended in 200 µl PBS (filtered through a 0.02-µm Anotop 25 filter) and stained with CellMask™ Deep Red plasma membrane dye (C10046, Invitrogen, MA, USA) according to manufacturer's instructions. Briefly, small EVs were incubated with CellMask™ Deep Red (diluted 1:500) for 10 min at 37°C, then the unbounded dye was removed and stained EVs washed with filtered PBS using ultrafiltration devices (Amicon Ultra 0.5 mL - 3K, UFC5003234, Millipore, MA, USA) at RT. The sample was then stored at 4°C until further use. A small aliquot of the sample was used to measure the size and number of particles in the 100,000×g pellets using a Nanosight NS500 instrument (Malvern Panalytical, Malvern, UK). The sample was diluted to the optimal working concentration of the instrument (2×10^8 to 1×10^9 particles per ml) with filtered PBS, and then measured. Five videos of 60 sec were acquired and subsequently analyzed with the NTA 3.4 software, which identifies and tracks the center of each particle under Brownian motion to measure the average distance the particles move on a frame-by-frame basis. As shown in Fig. 5, the majority of the small EVs has a diameter between 100-175 nm (65,9% of the total) with a mode of 101 nm.

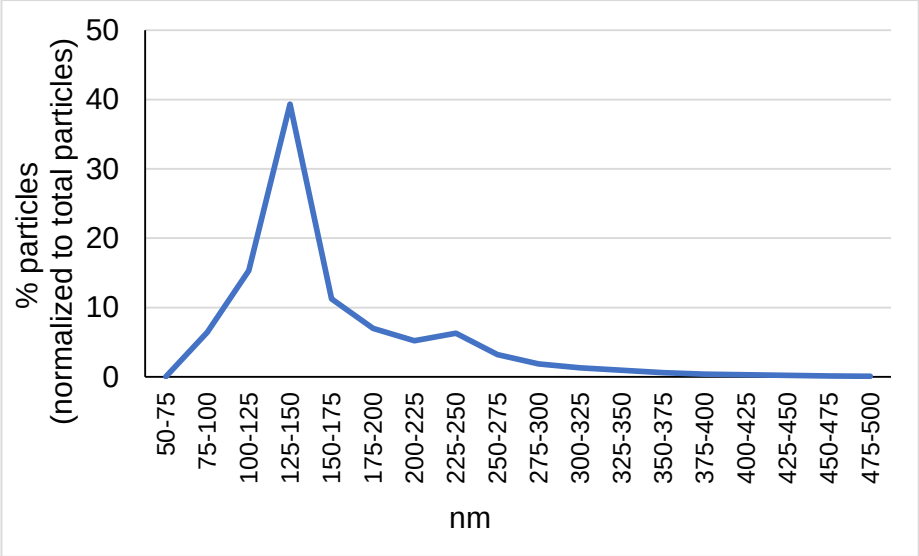

Figure. 16: Small EVs were isolated by sequential centrifugation from healthy donor urine and their size was measured by NTA. The size distribution of small EVs is shown as percentage of particles having the indicated size normalized by the total number of particles.

10.Human-placenta tissue preparation and characterization

Placental tissue samples are first fixed in formalin and then embedded in paraffin [3]. 4 μm sections of the tissue samples are then cut from these paraffin blocks using microtome (HM 355S Automatic Microtome, Thermo Fisher Scientific, Waltham, Massachusetts, USA). The cut sections are then placed on poly-L-lysine coated Si_3N_4 waveguide chips, and deparaffinized in xylene (3 × 5 min), followed by rehydration in descendent series of ethanol: 100% (2 × 10 min), 96% (2 × 10 min) and 70% (10 min).

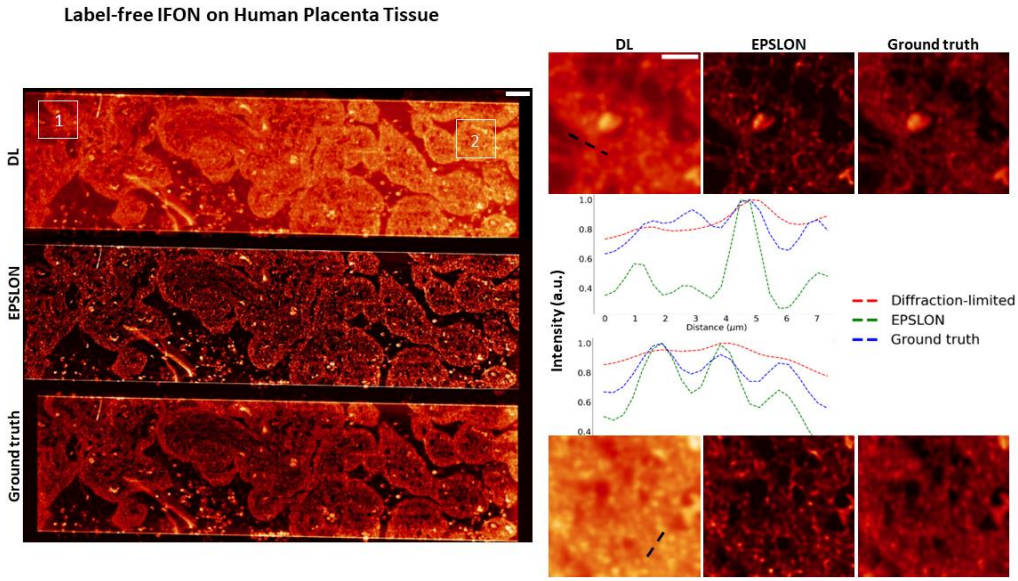

Figure. 17: EPSLON for label-free super-resolution imaging of human placenta tissue sections: Large field-of-view label-free diffraction-limited image termed DL, super-resolved EPSLON image and ground truth images are shown, scale bar 25 μm. Two regions marked ‘‘1’’ and ‘‘2’’ in the DL image are blown-up and shown alongside. The corresponding regions in the EPSLON and ground truth images are also magnified and shown, scale bar 10 μm. Line profiles along the white dotted lines in the magnified boxes of the DL image fails to resolve any intricate features as shown by the line plots. EPSLON images provide more details as seen in the images and they are validated by the ground truth images, which are also evidenced by the line plots.

11. Rat kidney sections

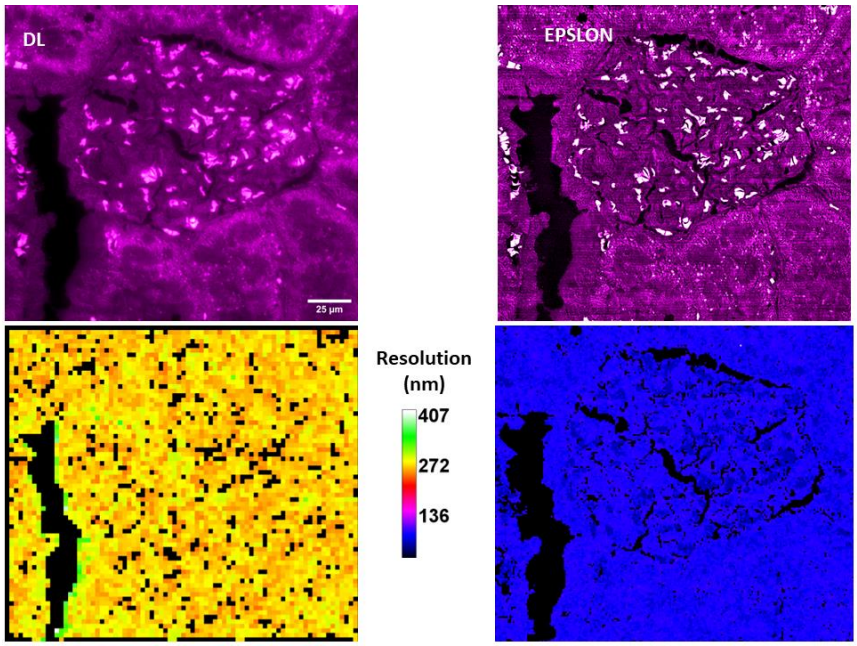

Figure. 18: Local FRC plot of rat kidney sections shown in Fig. 6 in main text. Label-free diffraction-limited (DL) and its corresponding super-resolved EPSLON images are shown, scale bar 25 µm. Local FRC resolution is computed and shown below for both DL and EPSLON images. The colorbar indicates the spatial resolution in nanometers.

12. Experimental details

The following spectral filters are used in this work:

Table 2:

Sl. No.	Filter Name	Spectral range (LP: LongPass, BP: BandPass)
1	FITC	515 nm LP + 535\30 nm BP
2	TRITC	585 nm LP \ 630\75 nm BP
3	CY5	655 nm LP \ 690\50 nm BP

Table 3:

Figure #	Sample	λ_{ill}	Spectral filter \ MO_2	Exposure	Reconstruction Algorithm	# Images	Comments
3a	195 nm polystyrene beads	561 nm	TRITC \ 0.75 NA	100 ms	BlindSIM[5]	50	
3b	100 nm Polystyrene beads	405 nm	FITC \ 0.9 NA	100 ms	SACD [4]	100	Order 2 used for reconstruction
4	(75 –250) nm Extracellular vesicles	488 nm for PL	TRITC \ 0.45 NA	1 sec	SACD	50	Order 2 used for reconstruction
		640 nm for TIRF	CY5 \ 0.45 NA, 1.2 NA	100 ms		50	
5	Human placenta tissue	488 nm	TRITC \ 1.2 NA	100 ms	SACD	250	Order 2 used for reconstruction
6	Rat kidney sections	488 nm	FITC\ 1.42 NA	100 ms	SACD	250	Order 2 used for reconstruction.
Supplementary Fig. 10	195 nm polystyrene beads	561 nm	TRITC \ 0.9 NA	100 ms	BlindSIM	50	
Supplementary Fig. 11	200 nm gold nanoparticles	640 nm	CY5\ 1.2 NA	100 ms	FairSIM[6]	3	
Supplementary Fig. 17	Human placenta tissue	488 nm	TRITC\ 0.25 NA (PL image) and 0.45 NA (Ground truth)	50 ms	SACD	20	Order 2 used for reconstruction. Each image is acquired for 50 ms and 20 images are averaged to create (50 ms*20 = 1sec) to create one input image for SACD.

13.References

1. Prieto, F., Sepúlveda, B., Calle, A., Llobera, A., Domínguez, C., Abad, A., Montoya, A. and Lechuga, L.M., 2003. An integrated optical interferometric nanodevice based on silicon technology for biosensor applications. *Nanotechnology*, *14*(8), p.907.
2. Ramirez-Garrastacho, M., Berge, V., Linē, A. and Llorente, A., 2022. Potential of miRNAs in urinary extracellular vesicles for management of active surveillance in prostate cancer patients. *British journal of cancer*, *126*(3), pp.492-501.
3. Slaoui, M. and Fiette, L., 2011. Histopathology procedures: from tissue sampling to histopathological evaluation. In *Drug safety evaluation* (pp. 69-82). Humana Press.
4. Zhao, Weisong, et al. "Enhanced detection of fluorescence fluctuations for high-throughput super-resolution imaging." *Nature Photonics* (2023): 1-8.
5. Mudry, Emeric, et al. "Structured illumination microscopy using unknown speckle patterns." *Nature Photonics* 6.5 (2012): 312-315.
6. Müller, M., Mönkemöller, V., Hennig, S., Hübner, W. and Huser, T., 2016. Open-source image reconstruction of super-resolution structured illumination microscopy data in ImageJ. *Nature communications*, *7*(1), pp.1-6.

Chapter 6

Conclusion and outlook

Two major challenges in optical microscopy of biological specimens are that of poor-contrast and diffraction-limited resolution. Poor-contrast arises due to weak absorption of light in the visible frequency regime by biological specimens, while diffraction-limited resolution arises due to diffraction of light. In this thesis, these two problems are attacked using optical waveguides and the physical mechanism behind the developed solutions are provided. The results in this thesis can be summed up as follows:

Paper 1:

- Aim: Use artificially induced intensity-fluctuations for generation of super-resolved fluorescence images.
- Idea: Use temporally varying speckle/multi-mode interference (MMI) patterns in multi-moded waveguides.
- Challenge: MMI patterns introduce artifacts in the super-resolved SOFI images.
- Solution: Pre-process the acquired image stacks using HAWK algorithm. This helps introduce sparsity to break correlation between emitters arising out of the illumination pattern.
- Result: Super-resolved fluorescence images devoid of artifacts are generated using SOFI.

Paper 2:

- Aim: (i) Use multi-moded waveguides to generate high-contrast label-free images. (ii) Use artificially introduced intensity-fluctuations for generation of label-free super-resolved images.
- Idea: (i) Add many speckle/MMI patterns within the integration time of the camera to generate an image with reduced speckle noise. (ii) Apply fluorescence-based intensity-fluctuation techniques like in Paper 1 to generate label-free super-resolved images.

- Challenge: The challenge is with respect to gaining resolution, as coherent scattering prevents resolution gain over the diffraction-limit.
- Solution: If the particles can be made to scatter incoherently, then super-resolution can be achieved. This idea is explored in the subsequent work in Paper 3.
- Result: High-contrast label-free images are generated using high-index contrast multi-moded waveguides. The developed technique is abbreviated cELS. Resolution gain using fluorescence-based intensity-fluctuation techniques is not feasible. In addition, due to coherent scattering off the particles, the algorithm can generate artifacts in the reconstructed image.

Paper 3:

- Aim: Generate label-free super-resolved images using fluorescence-based algorithms.
- Idea: Use incoherent light sources to illuminate the sample.
- Challenge: The smallest coherent area that can be generated is still limited by diffraction, i.e., all regions of the sample within the coherent area will scatter coherently.
- Solution: Use photoluminescence in Si_3N_4 for near-field illumination of unlabeled samples.
- Result: Label-free super-resolution in 2D is achieved. The developed technique is abbreviated EPSLON.

This thesis provides a physical understanding of employing optical waveguides in microscopy. Optical waveguides are employed for both fluorescence and label-free super-resolution imaging. The decoupled illumination/detection path offered by waveguides permits only the scattered light off the sample to reach the camera. This property can be utilized to perform high-contrast imaging of biological specimens over large field-of-view. For resolution gain, the same waveguides can induce intensity fluctuations which can be harnessed by fluorescence-based super-resolution algorithms in both fluorescence and label-free microscopy. In addition, complex beam shaping can be performed on-chip, which helps reduce cost and complexity and aids in miniaturizing conventional microscopes to smaller footprints.

Label-free imaging offers non-invasive methods to study life. Though specificity is one of the hallmarks of fluorescence microscopy, if high-contrast super-resolved images can be generated in label-free mode, and tools developed in machine learning be employed to introduce specificity in the unlabeled structures, then label-free microscopy could become a competitor for fluorescence microscopy. The concepts developed in this thesis could be used as a step in this direction. By exploring materials that have room-temperature PL and a higher refractive than Si_3N_4, even higher resolutions in principle can be achieved. A

higher refractive index will also confine more light to the core, and thereby, help in reducing the background. In future, efforts to apply the concepts of Non-linear SIM [24] or STED [22] in label-free mode will be interesting to push the resolution well below the 100 nm mark.

Bibliography

[1] Fulvio Melia. *Electrodynamics*. University of Chicago Press, 2001. 1, 18

[2] Lukas Novotny and Bert Hecht. *Principles of nano-optics*. Cambridge university press, 2012. 2, 9

[3] Emil Wolf. *Introduction to the Theory of Coherence and Polarization of Light*. Cambridge university press, 2007. 2, 12

[4] Helmut Wiedemann. *Particle accelerator physics*. Springer Nature, 2015. 8

[5] Amalia Torre. *Linear ray and wave optics in phase space: bridging ray and wave optics via the Wigner phase-space picture*. Elsevier, 2005. 9

[6] Rainer Heintzmann. Answers to fundamental questions in superresolution microscopy. *Philosophical Transactions of the Royal Society A*, 379(2199):20210105, 2021. 10, 27, 29

[7] Joseph W Goodman. *Introduction to Fourier optics*. Roberts and Company publishers, 2005. 11, 12, 14, 15, 16

[8] Joseph W Goodman. *Statistical optics*. John Wiley & Sons, 2015. 12, 72

[9] Stephane Perrin and Paul Montgomery. Fourier optics: basic concepts. *arXiv preprint arXiv:1802.07161*, 2018. 15

[10] Emil Wolf. A macroscopic theory of interference and diffraction of light from finite sources ii. fields with a spectral range of arbitrary width. *Proceedings of the Royal Society of London. Series A. Mathematical and Physical Sciences*, 230(1181):246–265, 1955. 15, 16

[11] Emil Wolf. Three-dimensional structure determination of semi-transparent objects from holographic data. *Optics communications*, 1(4):153–156, 1969. 17

[12] Sigal Trattner, Micha Feigin, Hayit Greenspan, and Nir Sochen. Validity criterion for the born approximation convergence in microscopy imaging. *JOSA A*, 26(5):1147–1156, 2009. 18, 23

[13] Eric Akkermans and Gilles Montambaux. *Mesoscopic physics of electrons and photons*. Cambridge university press, 2007. 19

[14] Ajoy K Ghatak and K Thyagarajan. *An introduction to fiber optics*. Cambridge university press, 1998. 19, 20, 21

[15] Y Ben-Aryeh. Superresolution observed from evanescent waves transmitted through nano-corrugated metallic films. *Applied Physics B*, 109:165–170, 2012. 23

[16] Bjorn Agnarsson, Anders Lundgren, Anders Gunnarsson, Michael Rabe, Angelika Kunze, Mokhtar Mapar, Lisa Simonsson, Marta Bally, Vladimir P Zhdanov, and Fredrik Hook. Evanescent light-scattering microscopy for label-free interfacial imaging: from single sub-100 nm vesicles to live cells. *ACS nano*, 9(12):11849–11862, 2015. 23, 29, 33, 39

[17] Jeff W Lichtman and José-Angel Conchello. Fluorescence microscopy. *Nature methods*, 2(12):910–919, 2005. 24

[18] Michael J Sanderson, Ian Smith, Ian Parker, and Martin D Bootman. Fluorescence microscopy. *Cold Spring Harbor Protocols*, 2014(10):pdb–top071795, 2014. 23

[19] Rainer Heintzmann and Gabriella Ficz. Breaking the resolution limit in light microscopy. *Briefings in Functional Genomics*, 5(4):289–301, 2006. 25

[20] Dominic A Helmerich, Gerti Beliu, Danush Taban, Mara Meub, Marcel Streit, Alexander Kuhlemann, Sören Doose, and Markus Sauer. Photoswitching fingerprint analysis bypasses the 10-nm resolution barrier. *Nature Methods*, 19(8):986–994, 2022. 25

[21] Lothar Schermelleh, Alexia Ferrand, Thomas Huser, Christian Eggeling, Markus Sauer, Oliver Biehlmaier, and Gregor PC Drummen. Superresolution microscopy demystified. *Nature cell biology*, 21(1):72–84, 2019. 25

[22] Stefan W Hell and Jan Wichmann. Breaking the diffraction resolution limit by stimulated emission: stimulated-emission-depletion fluorescence microscopy. *Optics letters*, 19(11):780–782, 1994. 25, 166

[23] Eric Betzig, George H Patterson, Rachid Sougrat, O Wolf Lindwasser, Scott Olenych, Juan S Bonifacino, Michael W Davidson, Jennifer Lippincott-Schwartz, and Harald F Hess. Imaging intracellular fluorescent proteins at nanometer resolution. *science*, 313(5793):1642–1645, 2006. 25

[24] Mats GL Gustafsson. Nonlinear structured-illumination microscopy: wide-field fluorescence imaging with theoretically unlimited resolution. *Proceedings of the National Academy of Sciences*, 102(37):13081–13086, 2005. 25, 166

[25] Peter Dedecker, Johan Hofkens, and Jun-ichi Hotta. Diffraction-unlimited optical microscopy. *Materials Today*, 11:12–21, 2008. 25

[26] Monika Pawlowska, Ron Tenne, Bohnishikha Ghosh, Adrian Makowski, and Radek Lapkiewicz. Embracing the uncertainty: the evolution of sofi into a diverse family of fluctuation-based super-resolution microscopy methods. *Journal of Physics: Photonics*, 4(1):012002, 2021. 25

[27] Thomas Dertinger, Ryan Colyer, Gopal Iyer, Shimon Weiss, and Jörg Enderlein. Fast, background-free, 3d super-resolution optical fluctuation imaging (sofi). *Proceedings of the National Academy of Sciences*, 106(52):22287–22292, 2009. 25, 41, 117

[28] Nils Gustafsson, Siân Culley, George Ashdown, Dylan M Owen, Pedro Matos Pereira, and Ricardo Henriques. Fast live-cell conventional fluorophore nanoscopy with imagej through super-resolution radial fluctuations. *Nature communications*, 7(1):12471, 2016. 25

[29] Idir Yahiatene, Simon Hennig, Marcel Muller, and Thomas Huser. Entropy-based super-resolution imaging (esi): From disorder to fine detail. *Acs Photonics*, 2(8):1049–1056, 2015. 25

[30] Susan Cox, Edward Rosten, James Monypenny, Tijana Jovanovic-Talisman, Dylan T Burnette, Jennifer Lippincott-Schwartz, Gareth E Jones, and Rainer Heintzmann. Bayesian localization microscopy reveals nanoscale podosome dynamics. *Nature methods*, 9(2):195–200, 2012. 25

[31] Krishna Agarwal and Radek Macháň. Multiple signal classification algorithm for super-resolution fluorescence microscopy. *Nature communications*, 7(1):13752, 2016. 25, 72

[32] Weisong Zhao, Shiqun Zhao, Zhenqian Han, Xiangyan Ding, Guangwei Hu, Liying Qu, Yuanyuan Huang, Xinwei Wang, Heng Mao, Yaming Jiu, et al. Enhanced detection of fluorescence fluctuations for high-throughput super-resolution imaging. *Nature Photonics*, pages 1–8, 2023. 25, 44, 115, 117

[33] Rainer Heintzmann and Christoph G Cremer. Laterally modulated excitation microscopy: improvement of resolution by using a diffraction grating. In *Optical biopsies and microscopic techniques III*, volume 3568, pages 185–196. SPIE, 1999. 25, 26

[34] Mats GL Gustafsson. Surpassing the lateral resolution limit by a factor of two using structured illumination microscopy. *Journal of microscopy*, 198(2):82–87, 2000. 25, 26

[35] Stefan Geissbuehler, Noelia L Bocchio, Claudio Dellagiacoma, Corinne Berclaz, Marcel Leutenegger, and Theo Lasser. Mapping molecular statistics with balanced super-resolution optical fluctuation imaging (bsofi). *Optical Nanoscopy*, 1(1):1–7, 2012. 26

[36] MinKwan Kim, ChungHyun Park, Christophe Rodriguez, YongKeun Park, and Yong-Hoon Cho. Superresolution imaging with optical fluctuation using speckle patterns illumination. *Scientific reports*, 5(1):16525, 2015. 26

[37] Young Choi, MinKwan Kim, ChungHyun Park, Jongchan Park, YongKeun Park, and Yong-Hoon Cho. Wide-field super-resolution optical fluctuation imaging through dynamic near-field speckle illumination. *Nano letters*, 22(6):2194–2201, 2022. 26

[38] Nikhil Jayakumar, Øystein I Helle, Krishna Agarwal, and Balpreet Singh Ahluwalia. On-chip tirf nanoscopy by applying haar wavelet kernel analysis on intensity fluctuations induced by chip illumination. *Optics Express*, 28(24):35454–35468, 2020. 26, 33, 39, 43, 44

[39] Thomas Dertinger, Alessia Pallaoro, Gary Braun, Sonny Ly, Ted A Laurence, and Shimon Weiss. Advances in superresolution optical fluctuation imaging (sofi). *Quarterly reviews of biophysics*, 46(2):210–221, 2013. 27

[40] Amit Lal, Chunyan Shan, and Peng Xi. Structured illumination microscopy image reconstruction algorithm. *IEEE Journal of Selected Topics in Quantum Electronics*, 22(4):50–63, 2016. 27, 28, 30

[41] YongKeun Park, Christian Depeursinge, and Gabriel Popescu. Quantitative phase imaging in biomedicine. *Nature photonics*, 12(10):578–589, 2018. 29

[42] Wonshik Choi, Christopher Fang-Yen, Kamran Badizadegan, Seungeun Oh, Niyom Lue, Ramachandra R Dasari, and Michael S Feld. Tomographic phase microscopy. *Nature methods*, 4(9):717–719, 2007. 29

[43] Claire L Curl, Catherine J Bellair, Trudi Harris, Brendan E Allman, Peter J Harris, Alastair G Stewart, Ann Roberts, Keith A Nugent, and Lea MD Delbridge. Refractive index measurement in viable cells using quantitative phase-amplitude microscopy and confocal microscopy. *Cytometry Part A: The Journal of the International Society for Analytical Cytology*, 65(1):88–92, 2005. 29

[44] Chenfei Hu and Gabriel Popescu. Physical significance of backscattering phase measurements. *Optics Letters*, 42(22):4643–4646, 2017. 29

[45] Frits Zernike. How i discovered phase contrast. *Science*, 121(3141):345–349, 1955. 29

[46] Peter RT Munro and Peter Török. Vectorial, high numerical aperture study of nomarski's differential interference contrast microscope. *Optics Express*, 13(18):6833–6847, 2005. 29

[47] Dominic Ruh, Julius Mutschler, Moritz Michelbach, and Alexander Rohrbach. Superior contrast and resolution by image formation in rotating coherent scattering (rocs) microscopy. *Optica*, 5(11):1371–1381, 2018. 29

[48] Richard W Taylor and Vahid Sandoghdar. Interferometric scattering microscopy: seeing single nanoparticles and molecules via rayleigh scattering. *Nano letters*, 19(8):4827–4835, 2019. 29

[49] Xiaowei Liu, Cuifang Kuang, Xiang Hao, Chenlei Pang, Pengfei Xu, Haifeng Li, Ying Liu, Chao Yu, Yingke Xu, Di Nan, et al. Fluorescent nanowire ring illumination for wide-field far-field subdiffraction imaging. *Physical Review Letters*, 118(7):076101, 2017. 29, 33, 39

[50] Mokhtar Mapar, Mattias Sjöberg, Vladimir P Zhdanov, Björn Agnarsson, and Fredrik Höök. Label-free quantification of protein binding to lipid vesicles using transparent waveguide evanescent-field scattering microscopy with liquid control. *Biomedical Optics Express*, 14(8):4003–4016, 2023. 29, 39

[51] Florian Ströhl, Ida S Opstad, Jean-Claude Tinguely, Firehun T Dullo, Ioanna Mela, Johannes WM Osterrieth, Balpreet S Ahluwalia, and Clemens F Kaminski. Super-condenser enables labelfree nanoscopy. *Optics express*, 27(18):25280–25292, 2019. 29, 33, 39

[52] Nikhil Jayakumar, Firehun T Dullo, Vishesh Dubey, Azeem Ahmad, Florian Ströhl, Jennifer Cauzzo, Eduarda Mazagao Guerreiro, Omri Snir, Natasa Skalko-Basnet, Krishna Agarwal, et al. Multi-moded high-index contrast optical waveguide for super-contrast high-resolution label-free microscopy. *Nanophotonics*, 11(15):3421–3436, 2022. 29, 30, 33, 39, 73, 74

[53] Pavan Chandra Konda, Lars Loetgering, Kevin C Zhou, Shiqi Xu, Andrew R Harvey, and Roarke Horstmeyer. Fourier ptychography: current applications and future promises. *Optics express*, 28(7):9603–9630, 2020. 29

[54] Hiroshi Ueno, So Nishikawa, Ryota Iino, Kazuhito V Tabata, Shouichi Sakakihara, Toshio Yanagida, and Hiroyuki Noji. Simple dark-field microscopy with nanometer spatial precision and microsecond temporal resolution. *Biophysical journal*, 98(9):2014–2023, 2010. 29

[55] Eric Betzig and Robert J Chichester. Single molecules observed by near-field scanning optical microscopy. *Science*, 262(5138):1422–1425, 1993. 29

[56] John Brian Pendry. Negative refraction makes a perfect lens. *Physical review letters*, 85(18):3966, 2000. 29

[57] Biqin Dong, Luay M Almassalha, Yolanda Stypula-Cyrus, Ben E Urban, John E Chandler, The-Quyen Nguyen, Cheng Sun, Hao F Zhang, and Vadim Backman. Superresolution intrinsic fluorescence imaging of chromatin utilizing native, unmodified nucleic acids for contrast. *Proceedings of the National Academy of Sciences*, 113(35):9716–9721, 2016. 29

[58] Christopher Barsi and Jason W Fleischer. Nonlinear abbe theory. *Nature Photonics*, 7(8):639–643, 2013. 29

[59] Zengbo Wang, Wei Guo, Lin Li, Boris Luk'Yanchuk, Ashfaq Khan, Zhu Liu, Zaichun Chen, and Minghui Hong. Optical virtual imaging at 50 nm lateral resolution with a white-light nanoscope. *Nature communications*, 2(1):218, 2011. 29

[60] Edward TF Rogers, Jari Lindberg, Tapashree Roy, Salvatore Savo, John E Chad, Mark R Dennis, and Nikolay I Zheludev. A super-oscillatory lens optical microscope for subwavelength imaging. *Nature materials*, 11(5):432–435, 2012. 29

[61] Yann Cotte, Fatih Toy, Pascal Jourdain, Nicolas Pavillon, Daniel Boss, Pierre Magistretti, Pierre Marquet, and Christian Depeursinge. Marker-free phase nanoscopy. *Nature Photonics*, 7(2):113–117, 2013. 29

[62] Guoan Zheng, Roarke Horstmeyer, and Changhuei Yang. Wide-field, high-resolution fourier ptychographic microscopy. *Nature photonics*, 7(9):739–745, 2013. 29, 39

[63] Guillaume Maire, Hugues Giovannini, Anne Talneau, Patrick C Chaumet, Kamal Belkebir, and Anne Sentenac. Phase imaging and synthetic aperture super-resolution via total internal reflection microscopy. *Optics letters*, 43(9):2173–2176, 2018. 29

[64] Celalettin Yurdakul, Oguzhan Avci, Alex Matlock, Alexander J Devaux, Maritza V Quintero, Ekmel Ozbay, Robert A Davey, John H Connor, W Clem Karl, Lei Tian, et al. High-throughput, high-resolution interferometric light microscopy of biological nanoparticles. *ACS nano*, 14(2):2002–2013, 2020. 29

[65] Mingwei Tang, Yubing Han, Dehao Ye, Qianwei Zhang, Chenlei Pang, Xiaowei Liu, Weidong Shen, Yaoguang Ma, Clemens F Kaminski, Xu Liu, et al. High-refractive-index chip with periodically fine-tuning gratings for tunable virtual-wavevector spatial frequency shift universal super-resolution imaging. *Advanced Science*, 9(9):2103835, 2022. 29, 39

[66] Chenlei Pang, Jingxi Li, Mingwei Tang, Jianpu Wang, Ioanna Mela, Florian Ströhl, Lisa Hecker, Weidong Shen, Qiulan Liu, Xiaowei Liu, et al. On-chip super-resolution imaging with fluorescent polymer films. *Advanced Functional Materials*, 29(27):1900126, 2019. 29, 39, 75

[67] Yeon Ui Lee, Shilong Li, G Bimananda M Wisna, Junxiang Zhao, Yuan Zeng, Andrea R Tao, and Zhaowei Liu. Hyperbolic material enhanced scattering nanoscopy for label-free super-resolution imaging. *Nature communications*, 13(1):6631, 2022. 29, 117

[68] Kai Wicker and Rainer Heintzmann. Resolving a misconception about structured illumination. *Nature Photonics*, 8(5):342–344, 2014. 30, 31, 39, 113

[69] Robin Diekmann, Øystein I Helle, Cristina I Øie, Peter McCourt, Thomas R Huser, Mark Schüttpelz, and Balpreet S Ahluwalia. Chip-based wide field-of-view nanoscopy. *Nature Photonics*, 11(5):322–328, 2017. 33, 35, 38, 39, 44

[70] Øystein Ivar Helle, Firehun Tsige Dullo, Marcel Lahrberg, Jean-Claude Tinguely, Olav Gaute Hellesø, and Balpreet Singh Ahluwalia. Structured illumination microscopy using a photonic chip. *Nature photonics*, 14(7):431–438, 2020. 33, 39

[71] Jean-Claude Tinguely, Øystein Ivar Helle, and Balpreet Singh Ahluwalia. Silicon nitride waveguide platform for fluorescence microscopy of living cells. *Optics express*, 25(22):27678–27690, 2017. 33, 39

[72] Anna Archetti, Evgenii Glushkov, Christian Sieben, Anton Stroganov, Aleksandra Radenovic, and Suliana Manley. Waveguide-paint offers an open platform for large field-of-view super-resolution imaging. *Nature communications*, 10(1):1267, 2019. 33, 39

[73] Björn Agnarsson, Saevar Ingthorsson, Thorarinn Gudjonsson, and Kristjan Leosson. Evanescent-wave fluorescence microscopy using symmetric planar waveguides. *Optics express*, 17(7):5075–5082, 2009. 33, 39

[74] Hao Shen, Eric Huang, Tapaswini Das, Hongxing Xu, Mark Ellisman, and Zhaowei Liu. Tirf microscopy with ultra-short penetration depth. *Optics express*, 22(9):10728–10734, 2014. 33

[75] HM Grandin, B Städler, M Textor, and Janos Vörös. Waveguide excitation fluorescence microscopy: A new tool for sensing and imaging the biointerface. *Biosensors and Bioelectronics*, 21(8):1476–1482, 2006. 33

[76] Srinivasan Ramachandran, Daniel A Cohen, Arjan P Quist, and Ratnesh Lal. High performance, led powered, waveguide based total internal reflection microscopy. *Scientific reports*, 3(1):2133, 2013. 33

[77] Anish Priyadarshi, Firehun Tsige Dullo, Deanna Lynn Wolfson, Azeem Ahmad, Nikhil Jayakumar, Vishesh Dubey, Jean-Claude Tinguely, Balpreet Singh Ahluwalia, and Ganapathy Senthil Murugan. A transparent waveguide chip for versatile total internal reflection fluorescence-based microscopy and nanoscopy. *Communications Materials*, 2(1):85, 2021. 33, 39

[78] Mattias Sjoberg, Mokhtar Mapar, Antonius Armanious, Vladimir P Zhdanov, Bjorn Agnarsson, and Fredrik Hook. Time-resolved and label-free evanescent light-scattering microscopy for mass quantification of protein binding to single lipid vesicles. *Nano Letters*, 21(11):4622–4628, 2021. 33

[79] Daniel Axelrod. Total internal reflection fluorescence microscopy in cell biology. *Traffic*, 2(11):764–774, 2001. 37

[80] Øystein I Helle, David A Coucheron, Jean-Claude Tinguely, Cristina I Øie, and Balpreet S Ahluwalia. Nanoscopy on-a-chip: super-resolution imaging on the millimeter scale. *Optics express*, 27(5):6700–6710, 2019. 37

[81] Benedict Diederich, Øystein Helle, Patrick Then, Pablo Carravilla, Kay Oliver Schink, Franziska Hornung, Stefanie Deinhardt-Emmer, Christian Eggeling, Balpreet Singh Ahluwalia, and Rainer Heintzmann. Nanoscopy on the chea (i) p. *bioRxiv*, pages 2020–09, 2020. 39

[82] Nikhil Jayakumar, Firehun T Dullo, Jean-Claude Tinguley, Krizia Sagini, Alicia Llorente, and Balpreet Singh Ahluwalia. Label-free incoherent super-resolution optical microscopy. *arXiv preprint arXiv:2301.03451*, 2023. 39

[83] David A Coucheron, Øystein I Helle, James S Wilkinson, Ganapathy Senthil Murugan, Carlos Domínguez, Hallvard Angelskår, and Balpreet S Ahluwalia. Study of waveguide background at visible wavelengths for on-chip nanoscopy. *Optics Express*, 29(13):20735–20746, 2021. 39

[84] Anders Kokkvoll Engdahl, Stefan Belle, Tung-Cheng Wang, Ralf Hellmann, Thomas Huser, and Mark SchuHERE!HERE!ttpelz. Large field-of-view super-resolution optical microscopy based on planar polymer waveguides. *ACS Photonics*, 8(7):1944–1950, 2021. 39

[85] Shwetadwip Chowdhury, Al-Hafeez Dhalla, and Joseph Izatt. Structured oblique illumination microscopy for enhanced resolution imaging of non-fluorescent, coherently scattering samples. *Biomedical optics express*, 3(8):1841–1854, 2012. 39

[86] Richard J Marsh, Karin Pfisterer, Pauline Bennett, Liisa M Hirvonen, Mathias Gautel, Gareth E Jones, and Susan Cox. Artifact-free high-density localization microscopy analysis. *Nature methods*, 15(9):689–692, 2018. 42

[87] Jennifer Cauzzo, Nikhil Jayakumar, Balpreet Singh Ahluwalia, Azeem Ahmad, and Nataša Škalko-Basnet. Characterization of liposomes using quantitative phase microscopy (qpm). *Pharmaceutics*, 13(5):590, 2021. 71

[88] Azeem Ahmad, Nikhil Jayakumar, and Balpreet Singh Ahluwalia. Demystifying speckle field interference microscopy. *Scientific Reports*, 12(1):10869, 2022. 71, 117

[89] Joseph W Goodman. Some fundamental properties of speckle. *JOSA*, 66(11):1145–1150, 1976. 73

[90] J Kistner, X Chen, Y Weng, HP Strunk, MB Schubert, and JH Werner. Photoluminescence from silicon nitride—no quantum effect. *Journal of Applied Physics*, 110(2), 2011. 114

[91] Atilla Aydinli, Ali Serpengüzel, and Didem Vardar. Visible photoluminescence from low temperature deposited hydrogenated amorphous silicon nitride. *Solid state communications*, 98(4):273–277, 1996. 114

[92] Emeric Mudry, Kamal Belkebir, J Girard, Julien Savatier, Emmeran Le Moal, C Nicoletti, Marc Allain, and Anne Sentenac. Structured illumination microscopy using unknown speckle patterns. *Nature Photonics*, 6(5):312–315, 2012. 115, 117

[93] Robert PJ Nieuwenhuizen, Keith A Lidke, Mark Bates, Daniela Leyton Puig, David Grünwald, Sjoerd Stallinga, and Bernd Rieger. Measuring image resolution in optical nanoscopy. *Nature methods*, 10(6):557–562, 2013. 119

[94] Marcel Müller, Viola Mönkemöller, Simon Hennig, Wolfgang Hübner, and Thomas Huser. Open-source image reconstruction of super-resolution structured illumination microscopy data in imagej. *Nature communications*, 7(1):10980, 2016. 117

Acknowledgement

Firstly, I wish to express my gratitude towards my supervisor Prof. Balpreet Singh Ahluwalia for giving me an opportunity to work in this lab. Thank you for all the help.
Azeem, Krishna, Olav, Firehun: For all those discussions, thank you. Many a times, your way of thinking gave new insights.
Thank you Daada for all your help.
Seba: always a pleasure to go on those long hikes and engage in discussions, be it life, music or research.
Deanna: you have helped me immensely. Thank you from my heart.
JC: Thank you for all your help, you always make me feel welcome in a group.
Vishesh: from cell culture to bank loans, I know whom to approach.
Florian: I learnt a lot from our discussions and I hope to work with you more.
David: for the discussions, proof-reading of my thesis, and for those times when you and Vilde made me at ease here in Tromsø.
Yingying: for helping everytime I got stuck. Thank you for sparing time to look into my doubts and proof-reading my thesis.
Hong: lunch, labs, discussions thank you. It's fun when you are around.
Abhishek: Nansenvegen, Utsikten, Gimle... journey still continues...
Luis: enjoyed sharing office and lab space with you over the last few years. Thank you for all your help.
Daniel: thank you for troubleshooting setups or softwares, it really helped to expedite. Ankit, Joy, Komal, Rohit: weekends were fun with you guys. Cheers.
Oliver, Farhad, Pawel, Jon-Richard: its always nice to catch up with you guys during a lunch or coffee break and discuss something random.
Øystein, Ida: thank you, it was nice working with you guys.
Priya, Dishiti: thank you guys.
ITN members: especially Matteo, Jennifer and Prof. Peter McCourt thank you guys.
I am forever thankful to my supervisors and colleagues in Jena. Thank you Prof. Dr. Christian Spielmann, Prof. Dr. Ulf Peschel, Dr. Martin Wimmer, Dr. Rudrakant Sollapur and Dr. Álvaro Rodríguez.
Thank you Abhinanda for your constant encouragement and support. Last but not the least, I would like to acknowledge the support of my parents, Jayakumar and Latha, and my younger brother, Rahul. Thank you so much for supporting my interests.
Namaskaram.